Diss. ETH No. 21742

ENGINEERING ARTIFICIAL GRAPHENE WITH AN ULTRACOLD FERMI GAS

A thesis submitted to attain the degree of

DOCTOR OF SCIENCES of ETH ZURICH

(Dr. sc. ETH Zurich)

presented by

THOMAS UEHLINGER

Dipl. Phys., ETH Zurich

born on 12.09.1983

citizen of

Zurich and Neunkirch SH, Switzerland

accepted on the recommendation of

Prof. Dr. Tilman Esslinger, examiner

Prof. Dr. Gianni Blatter, co-examiner

2014

THOMAS UEHLINGER
Engineering Artificial Graphene with an Ultracold Fermi Gas
Diss. ETH No. 21742

Digital Object Identifier DOI:10.3929/ethz-a-010150075

E-MAIL:
uehlinger@phys.ethz.ch

GROUP WEBSITE:
http://www.quantumoptics.ethz.ch

To my family and friends.

ABSTRACT

This thesis reports on the realization of an artificial graphene system using an ultracold Fermi gas of ^{40}K atoms loaded into an optical lattice. In contrast to the situation in a real solid, where the properties are defined by the rigid crystal structure, in our system both the lattice geometry as well as the inter-particle interactions can be tuned over a wide range. For the honeycomb geometry, the two lowest electronic bands are connected at two single points, with a linear dispersion relation in their vicinity. These conical band crossings, called Dirac points, are the origin of phenomena as diverse as the backscattering-free conduction or the quasi-relativistic behavior of the particles. We detect and characterize the Dirac points by dynamically probing them using momentum-resolved Bloch-Zener transitions between the two bands. By introducing an energy offset between the two sublattices, the transition from massless to massive Dirac fermions is studied. When imbalancing the tunnel couplings, equivalent to applying linear strain, we observe a movement of the Dirac points. Beyond a critical imbalance, the two points are found to merge and to annihilate, indicating a topological transition of the Fermi surface. The transfer efficiency is modeled analytically using the Landau-Zener formula and numerically by a time evolution of the trapped many-body system. The results of both calculations agree well with the measurements.

Using an effective spin-$1/2$ system, realized by two Zeeman substates of ^{40}K, the effect of interaction is studied. By tuning from weak to strong repulsion using a Feshbach resonance, we observe the transition from a semimetallic to a Mott-insulating state, both in independent two-dimensional artificial graphene layers as well as in coupled systems. It is signaled by a strong reduction of the double occupancy of the system, in good agreement with predictions from a high-temperature series expansion assuming experimentally realistic entropies. Furthermore, we investigate the gapped excitation spectrum in the Mott-insulating state by amplitude modulation of the lattice.

Approaching the regime of quantum magnetism, we have developed methods for obtaining and detecting short-range magnetic correlations in dimerized and anisotropic lattice structures. The dependence of the correlations on lattice geometry and entropy is investigated experimentally. The results are in good agreement with predictions from a high-temperature series expansion and a dynamical cluster approximation. Moreover, a method for detecting density correlations based on the fluctuations in the measured momentum distributions is successfully implemented and tested for various lattice geometries. In the future, this method should allow for the detection of long-range spin and density correlations in the lattice.

ZUSAMMENFASSUNG

Die vorliegende Arbeit berichtet über die Realisierung eines künstlichen Graphen-Systems mittels ultrakalter Quantengase. Dazu werden fermionische ^{40}K-Atome in ein optisches Gitter mit hexagonaler Geometrie geladen. Im Gegensatz zur Situation in echten Festkörper-Systemen, deren Eigenschaften durch die starre Gitterstruktur definiert sind, können in unserer Implementation sowohl die Geometrie des Gitters als auch die Wechselwirkung über einen grossen Bereich variiert werden. In der hexagonalen Gittergeometrie sind die untersten beiden Energiebänder an zwei einzelnen Punkten verbunden. Diese konischen Kreuzungspunkte werden aufgrund der linearen Dispersionsrelation in ihrer Umgebung Dirac-Punkte genannt. Sie sind der Ursprung von Phänomenen wie der rückstreungsfreie Transport oder das quasi-relativistische Verhalten der Teilchen in ihrer Nähe. Wir detektieren und charakterisieren die beiden Dirac-Punkte mit Hilfe von dynamisch induzierten, impulsaufgelösten Bloch-Zener-Übergängen zwischen den beiden Energiebändern. Die Erzeugung eines Energie-Offsets zwischen den zwei Untergittern der hexagonalen Struktur ermöglicht die Beobachtung des Übergangs zwischen masselosen und massebehafteten Dirac-Fermionen. Für ungleiche Tunnel-Kopplungen, was einer linearen Deformation der Geometrie entspricht, beobachten wir eine Verschiebung der Dirac-Punkte. Wird ein kritisches Ungleichgewicht zwischen den Tunnel-Kopplungen erreicht, verschmelzen die beiden Dirac-Punkte und eine Band-Lücke öffnet sich. Dies entspricht einem topologischen Übergang der Fermi-Fläche. Die Transfer-Effizienz wird analytisch mittels der Landau-Zener-Formel und numerisch mit einer Zeitevolution des Vielkörpersystems in der Falle modelliert. Die Resultate beider Methoden stimmen gut mit den Messungen überein.

Mit einem effektiven Spin-$^1/_2$ System, realisiert durch zwei Zeeman-Zustände von ^{40}K, wird der Effekt der Wechselwirkung untersucht. Wird diese mittels einer Feshbach-Resonanz erhöht, beobachten wir einen Übergang von einem halbmetallischen zu einem Mott-isolierenden Zustand, sowohl im Falle von unabhängigen künstlichen Graphen-Schichten als auch für gekoppelte Systeme. Der Übergang manifestiert sich durch eine starke Unterdrückung der Doppelbesetzung im Gitter, in guter Übereinstimmung mit den Resultaten einer Hochtemperatur-Entwicklung des grosskanonischen Potentials unter Annahme von experimentell realistischen Entropien. Zudem untersuchen wir mittels Gitteramplituden-Modulation das Anregungsspektrum des Systems, welches im Mott-isolierenden Zustand eine Energielücke aufweist.

Um in das Regime des Quanten-Magnetismus vorzudringen, haben wir Methoden zur Erzeugung und Detektion von kurzreichweitigen magnetischen Korrelationen in dimerisierten und anisotropischen Gitterstrukturen entwickelt. Die Abhängigkeit der Korrelationen von der Gittergeometrie und der Entropie wird experimentell untersucht. Die Resultate stimmen gut mit den theoretischen Vorhersagen einer Hochtemperatur-Entwicklung sowie einer dynamischen Cluster-Approximation überein. Zudem implementieren wir eine Methode zur Detektion von Dichte-Korrelationen im optischen Gitter. Diese basiert auf einer Analyse der Fluktuationen in den gemessenen Impulsverteilungen. Tests der Methode für verschiedene Gittergeometrien zeigen, dass damit zukünftig langreichweitige Spin- oder Dichte-Korrelationen in unserem System nachgewiesen werden können.

CONTENTS

Detailed tables of contents can be found at the beginning of each chapter.

INTRODUCTION

1

The development of new materials is one of the major drivers of today's technological progress. For example, the discovery of semiconductors and the development of techniques to dope them has lead to the invention of the transistor by John Bardeen, Walter Brattain, and William Shockley in 1947, which has become the foundation of information technology. Superconductors, discovered by Kamerlingh Onnes in 1911, have allowed for the construction of more powerful electromagnets, which are essential for medical imaging applications or mass spectrometers. In the future, superconducting materials might play an important role for energy transport and storage. Compared to these two examples, graphene, a two-dimensional (2D) material consisting of single atomic layers of graphite, is a much younger material, studied for the first time in 2004 by Konstantin Novoselov and Andre Geim [Novoselov *et al.*, 2004], who were already in 2010 awarded with the Nobel price for their ground breaking work on this first truly 2D physical system. Despite being only in its infancy, graphene has already proved its potential for future technological applications, be it for ultrafast transistors, new types of sensors or for composite materials [Novoselov *et al.*, 2012].

Graphene, a single atomic layer of hexagonally arranged carbon atoms

The origin of many of its fascinating properties is found in its unusual band structure, with its valence and conduction bands connected by two conical intersections, where the dispersion relation becomes linear. In Fig. 1.1 a typical band structure of our specific implementation of a graphene system is shown. The band crossings gives rise to a largely suppressed back-scattering of the charge carriers, making graphene a particularly good conductor. It also leads to the unconventional quantum Hall effect [Novoselov *et al.*, 2005], where the Hall plateaux are shifted with respect to the conventional quantum Hall effect. In graphene, this effect can even be observed at room temperature, allowing for practical applications such as ultra-precise metrology [Novoselov *et al.*, 2007].

On a more fundamental level, the linear dispersion relation in the vicinity of the two band crossings has attracted interest in its own right. In these regions, the electrons and holes behave like massless Weyl-Dirac fermions similar to neutrinos or free electrons moving at nearly the speed of light. For this reason the two band crossings are called Dirac points, and the band structure of graphene can serve as a testbed for relativistic physics. This has for example allowed for the study of Klein tunneling [Katsnelson *et al.*, 2006], a reflection-free transmission through a potential barrier, which is a hallmark phenomenon of relativistic physics.

Conical band crossings: the Dirac points

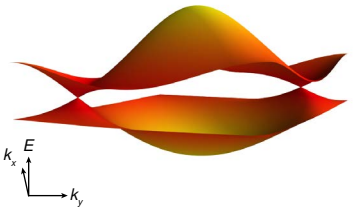

Figure 1.1: *Typical band structure.* A three-dimensional view of the energy spectrum shows the linear intersection of the bands at the two Dirac points. The band structure of our specific implementation is shown in the first Brillouin zone (B.Z.) for typical experimental parameters. Up to a rescaling of one axis and the convention for choosing the B.Z. boundaries, it corresponds to that of graphene.

Despite the tremendous progress in the exploration of this new material, many questions are yet to be answered, especially concerning the role of interactions. They give rise to effects which do not appear on a single-particle level but only in the collective behavior of an ensemble of particles. It is precisely these many-body

effects that lead on one hand to fascinating new phenomena but on the other hand complicate the investigation of their underlying mechanisms. This is because for describing an interacting quantum mechanical system not only the separate states of its constituents have to be taken into account, but also their correlations. These are intrinsically hard to measure in experiments, and many of the experimental techniques required to do so are yet to be developed. Apart from the most simple cases, the emerging correlations also render an exact analytical treatment or computer simulation of such systems impossible for realistic sizes, owing to the exponentially increasing number of quantum mechanical states.

Quantum simulation

Therefore, within the scientific methodology, the step of finding models which include all the necessary features to describe the experimentally observed phenomena, but are still simple enough to allow for new predictions, has become ever more important. In the last decade a new approach, termed *quantum simulation* by Richard Feynman [1982, 1986], has emerged to complement the traditional analytic and computational methods used for testing and studying these models. The principal idea of this new approach is to implement a certain model Hamiltonian using a different physical system that is more accessible for experimental investigation than the original system. By now a variety of physical realizations of quantum simulators exist [Georgescu *et al.*, 2014], ranging from dilute atomic gases at temperatures close to absolute zero (the system used in this thesis), to trapped ions, superconducting chips, patterned surfaces, quantum dots or single spins in bulk solids, to photonic systems in the optical or microwave range.

Artificial graphene systems

Specifically addressing the physics of graphene, several implementations of *artificial graphene* systems have been realized recently [Polini *et al.*, 2013]. First emulations of the band structure were performed by confining light in photonic crystals [Peleg *et al.*, 2007] and using hexagonal assemblies of microwave resonators [Kuhl *et al.*, 2010]. A system of strongly localized electrons on a hexagonal lattice has been realized by nano-patterning of a two-dimensional electron gas (2DEG) [Singha *et al.*, 2011]. Also on a 2DEG, the effect of doping and strain was simulated by assembling single molecules on the surface using a scanning tunneling microscope [Gomes *et al.*, 2012].

In this thesis, an implementation of an artificial graphene system using a gas of ultracold fermionic ^{40}K atoms trapped in a novel type of a highly tunable optical lattice is presented. Triggered by the first experimental observation of Bose-Einstein condensation in a dilute gas of bosonic ^{87}Rb and ^{23}Na atoms in 1995 [Anderson *et al.*, 1995; Davis *et al.*, 1995], followed by the production of a quantum degenerate gas of fermionic ^{40}K four years later [DeMarco *et al.*, 1999], ultracold quantum gases have since then evolved into a versatile tool for studying a large variety of phenomena. Topics as diverse as superfluidity, the effects of strong inter-particle or matter-light interactions, and static or dynamic properties of phase transitions in different dimensions have been addressed so far[1]. Furthermore, quantum gases have also found practical applications, for example in ultra-precise clocks [Derevianko *et al.*, 2011]. The tremendous success of the field can largely be attributed to the unique flexibility in preparing, controlling and probing these systems by means of laser beams, magnetic fields and radio frequency (rf) radiation [Ketterle *et al.*, 1999, 2008].

Mimicking solids using cold atoms loaded into optical lattices

The atom-light interaction [Cohen-Tannoudji *et al.*, 2008] has led to yet another application: by trapping the atoms in the standing wave potential of counter-propagating laser beams, crystal structures alike those of solid materials can be constructed. In such a system, the role of the electrons in solids is taken by the quantum degenerate fermionic atoms, and the periodic potential is realized by means of the laser beams mimicking the Coulomb interaction with the nuclei. The Coulomb repulsion of the charged electrons is on the other hand replaced by the

1 Jaksch *et al.*, 2005; Lewenstein *et al.*, 2007; Bloch *et al.*, 2008; Giorgini *et al.*, 2008; Ritsch *et al.*, 2013.

van der Waals interaction between the neutral atoms, which reduces to a contact interaction for low enough temperatures [Castin, 2006]. By means of Feshbach resonances [Chin *et al.*, 2010], which are most commonly accessed by an externally applied magnetic field, the effective scattering potential can be adjusted all the way from repulsive to non-interacting or even attractive. Based on this analogy, which is the focus of Chapter 2 of this thesis, Jaksch *et al.* [1998] proposed the implementation of Hubbard models [1963] using cold atoms. The Hubbard model describes the hopping of particles between neighboring sites in a lattice as well as local interactions between the particles. It is thus one of the simplest models for a solid that includes the interplay between kinetic and interaction energy. Jaksch *et al.* found that, despite the fact that the typical temperatures in cold atoms system (100 nK) are up to a million times colder than in real solids and that the lattice spacings (typically 0.5 µm) are about a factor of thousand larger, the realized parameter regimes of the model systems match in fact those of real solids. The experimental realization of his theoretical proposal for bosonic [Greiner *et al.*, 2002] and fermionic atoms [Jördens *et al.*, 2008; Schneider *et al.*, 2008] set the stage for studying more complex solids using cold atoms [Lewenstein *et al.*, 2007, 2012].

The optical lattice

Key to the realization of the artificial graphene system using cold atoms is the optical lattice with tunable geometry. The lattice is constructed from two perpendicular and mutually interfering retro-reflected laser beams. Additionally, a third retro-reflected beam co-propagates with one of the former beams, see Fig. 1.2a. However, owing to a small detuning in frequency, this beam only interferes with itself, but not with the others[2]. By adjusting the intensities of the laser beams, the resulting optical potential can be set to various geometries, ranging from honeycomb, triangular, dimerized, one-dimensional (1D) chain, to checkerboard or square geometry, as shown in Fig. 1.2b. A fourth independent standing wave, perpendicular to the shown lattice plane, allows for the creation of several independent or coupled layers of any of these geometries. The details on the experimental implementation of the optical lattice as well as the preparation and probing of the cold samples are the topic of Chapter 3.

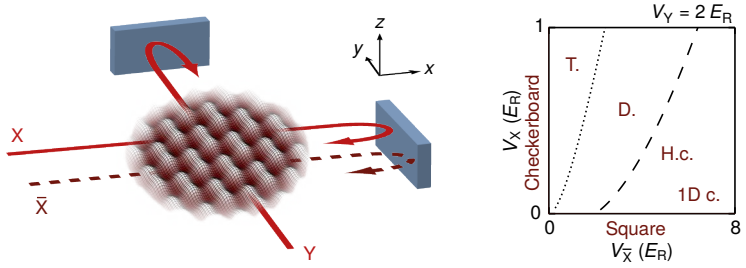

a. Setup of the optical lattice

b. Diagram of lattice geometries

Figure 1.2: *The optical lattice of tunable geometry.* a. The optical lattice is constructed from two retro-reflected and mutually interfering laser beams X and Y (solid red) and a third beam $\bar{X}$ (dashed dark red), co-propagating with X, which does not interfere with the other beams. A forth beam along z (not shown) is used to create layered systems. b. Different lattice potentials can be realized depending on the intensities of the lattice beams. The diagram shows the accessible geometries as a function of the lattice depths $V_{\bar{X}}$ and V_X. The transition between triangular (T.) and dimer (D.) lattices is indicated by a dotted line. When crossing the dashed line into the honeycomb (H.c.) regime, Dirac points appear in the band structure. The limit $V_{\bar{X}} \gg V_{X,Y}$ corresponds to weakly coupled one-dimensional chains (1D c.).

2 In fact it does interfere with the other beams but the atomic motion cannot follow the potential resulting from the interference term, which oscillates at a frequency of several 100 MHz.

Investigating the band structure

As compared to the situation in free space, the motion of the particles is profoundly altered by the presence of a periodic potential. The quadratic dispersion relation of the free particles transforms into a band structure containing allowed and forbidden energy regions. The peculiarities of the band structure in the honeycomb lattice implemented in our system are discussed in Chapter 4. This is followed by the presentation of the experimental evidence and the characterization of the Dirac points, in Chapter 5. Using non-interacting particles, we probe the band structure by momentum-resolved interband transitions induced by Bloch oscillations, similar to a method used for the characterization of the linear crossings of excited bands in a 1D system [Salger *et al.*, 2007]. This experimental technique allows for a precise determination of the position of the Dirac points within the band structure as well as for a characterization of the band structure in their vicinity.

Exploiting the tunability of the lattice, we have studied the effect of breaking the energy degeneracy of the two interleaved triangular lattices forming the honeycomb structure. Lifting this degeneracy corresponds to breaking the inversion symmetry of the lattice. The resulting transition from massless to massive Dirac fermions is characterized by a gap opening in the band structure. Moreover, we observe a movement of the Dirac points as the ratio of the tunneling amplitudes along the two spatial directions is varied. This corresponds to the effect observed when applying linear strain to real graphene. As the imbalance reaches a certain critical value, the two Dirac points are found to merge, a situation which is beyond the accessible regime for graphene. At this point, the two points annihilate and a gap opens, signaling the transition from a semimetallic to an insulating state of the material. We map out this transition for a range of lattice geometries and find excellent agreement with theoretical predictions. The corresponding experiments are discussed in Chapter 6.

The role of interactions

In the second part of this thesis, the emerging phenomena in the presence of repulsive inter-particle interactions are studied. In Chapter 7, the mapping of our system to the Fermi-Hubbard model is discussed, including methods for a theoretical treatment of this model. Since the Fermi level in real graphene lies exactly at the two Dirac points, it is a semimetal. This is a class of materials for which the top of the valence band is connected to the conduction band, but with a vanishing density of states at the Fermi energy. While insulating behavior can occur as a consequence of a filled band, it can also be induced by strong repulsive interactions, an effect first described by Mott [1949]. While in real graphene the kinetic and interaction energy are of similar magnitude, the tunability of the interactions in our system via a Feshbach resonance also allows for the exploration of the strongly interacting regime. In Chapter 8, we study the transition from a semimetallic to a Mott-insulating state using an interaction dependent rf spectroscopy method [Jördens *et al.*, 2008] to measure the fraction of atoms on doubly occupied lattice sites. A strong suppression of the double occupancy is found, signaling the transition to the Mott-insulating state, similar as in previous studies of simple cubic lattices [Jördens *et al.*, 2008; Jördens *et al.*, 2010]. The measured double occupancies are found to be in agreement with numerical predictions obtained from a high-temperature series expansion (HTSE) up to second order. By amplitude modulation of the lattice beam intensity excitations in the form of additional double occupancies can be created. This allows for an observation of the gapped excitation spectrum in the Mott-insulating state and for a verification of the methods employed to establish the mapping to the Hubbard model.

The Mott insulator transition

Despite the ultra-low temperatures now routinely achieved in cold atom experiments, the temperature normalized to the relevant energy scales of these systems is in fact usually higher than that of real solids. The systems are therefore comparably far from their true ground state, where previously unstudied phases of matter are expected. For example, in honeycomb lattices, the existence of a spin liquid, an

exotic quantum phase in which the spins remain in a disordered state even at zero temperature, has been debated [Meng *et al.*, 2010; Sorella *et al.*, 2012; Assaad *et al.*, 2013]. To access this regime, the temperature limitations imposed by the currently used cooling and trapping schemes need to be overcome. To this end, we have developed a method for a local redistribution of entropy in the lattice, which we use to obtain short-range magnetic order in dimerized and anisotropic square lattice geometries. Moreover, a specifically tailored detection procedure based on coherent oscillations between the singlet and a triplet state of pairs of the effective spin-½ particles has been developed. These methods as well the characterization of the emerging correlations as a function of lattice geometry and entropy are the topic of Chapter 9.

Obtaining short-range magnetic ordering by means of local entropy redistribution

Many of the low-temperature states are in fact characterized by long-range ordering of their spins, as is the case for large repulsive interactions in the honeycomb lattice. In Chapter 10 the implementation and verification of a measurement technique which can be used to extract information about the correlations in the momentum distribution of an atomic cloud is discussed [Altman *et al.*, 2004]. The method relies on the analysis of the density fluctuations of the atom cloud after a short time of free expansion, as obtained by recording the amount of absorbed light when illuminating the cloud with a resonant laser beam. Owing to Pauli's principle, every available quantum state can only be occupied by one particle, leading to characteristic dips in the autocorrelation function of the momentum distribution for distances corresponding to multiples of the lattice momentum. As illustrated by the measurements presented in this chapter, the method also allows for the detection of ordering patterns in the lattice, making it a viable tool for the characterization of long-range ordered magnetic states.

Noise correlation measurements

The results presented in this thesis set the grounds for further studies of artificial graphene systems using cold atoms. Our experimental setup can be readily enhanced to allow for sophisticated lattice amplitude or phase modulation schemes, which can be employed to mimic (staggered) magnetic fields [Dalibard *et al.*, 2011]. Under these conditions, a topological insulator is predicted to emerge, a state of matter in which the bulk of the material is insulating but the edges show backscattering-free conduction. In the presence of interactions, the ionic Hubbard model [Egami *et al.*, 1993] or magnetic ordering in the honeycomb lattice could be studied in the future.

Outlook

The work during the course of this thesis was carried out in collaboration with Daniel Greif, Leticia Tarruell, Gregor Jotzu, Michael Messer, Robert Jördens, Niels Strohmaier and Tilman Esslinger.

HOW ULTRACOLD ATOMS MIMIC ELECTRONS IN SOLIDS

2

In this chapter I will briefly discuss the key ingredients required to mimic a solid state system: a particle that behaves similar to an electron, means of providing a periodic potential structure for that particle, inter-particle interactions and probes for the system.

CHAPTER CONTENTS

Concept of quantum simulation

The concept of emulating the properties of a certain physical system with a different, more accessible one was already discussed by Richard Feynman in his keynote lecture "Simulating Physics with Computers" held at the Massachusetts Institute of Technology (MIT) in Cambridge more than 30 years ago [Feynman, 1982, 1986].

The need for such a *quantum simulator* can be derived from the fact that already for one of the most simple quantum mechanical system imaginable, the spin-½ system, the dimension of the Hilbert space and with that the number of matrix elements of the description of such a state grows as 2^N when considering an ensemble of N such spins. The number of required coefficients easily exceeds the amount of memory available to even the most advanced supercomputers already for $N < 100$. The same holds obviously for the computing power required to manipulate such a state. For realistic system sizes, the number of states even exceeds the number of atoms in the universe. To put it in Feynman's words:

> *"Nature isn't classical, dammit, and if you want to make a simulation of Nature, you'd better make it quantum mechanical, and by golly it's a wonderful problem, because it doesn't look so easy."*
>
> — Richard Feynman

But only recently have implementations of the at the time of Feynman's lecture unimaginable quantum simulators reached a state where problems beyond the capabilities of current experimental, theoretical and numerical simulations can be attacked. Experiments are now even reaching out to explore regimes in solid state systems which are not, or not yet, accessible to research in currently existing materials, with the aim of testing new materials before they can even be produced.

Implementations of quantum simulators

Implementations of quantum simulators have been brought forward using various types of physical systems [Georgescu *et al.*, 2014]. The most advanced systems

are nowadays based on atomic or molecular dilute gases at almost zero temperature [Bloch *et al.*, 2012] as will be presented in this thesis, on arrays of trapped ions [Blatt *et al.*, 2012], on photonic systems [Aspuru-Guzik *et al.*, 2012], on superconducting circuits etched into chips [Houck *et al.*, 2012] as well as implementations using the nuclear and electronic spins in bulk solids or in quantum dots and similar microstructures, making for example use of nuclear magnetic resonance (NMR) techniques.

Addressing solid state physics questions using quantum simulation

Solid state physics is without question one of the most fruitful fields to address using quantum simulation. With today's advancement of technology, many problems addressed by solid state research are of direct importance for everyday life, be it on a personal scale (e. g. faster and more compact portable electronic devices) or with a more global relevance (e. g. in the area of energy transport and storage). The ultra-fast timescales, the predominantly global probes as well as sample preparation processes prone to introducing unwanted contaminations challenge researchers in the field. Offering complementary approaches, quantum simulators of solids may help answering some of the open questions.

Ingredients for a simulation of a solid

Key to a wide range of phenomena in solids is undoubtedly the interaction of the electrons subject to the band structure given by the potential of the periodically arranged nuclei. The ingredients for a most basic emulation of a condensed matter system can therefore be summarized as:

- A particle that is an effective spin-1/2 system and therefore obeys fermionic spin statistics. Temperatures need to be such that the particle system is at a similar level of quantum degeneracy as the electron system to be studied, i. e. in most cases well below the Fermi temperature T_F.
- The particles need to be exposed to a periodic potential.
- Inter-particle interactions are required to emulate effects beyond single-particle physics.
- Probes are needed to characterize the system in a meaningful way.
- The system needs to be validated in order to assess the applicability of the obtained results to the original system.

In our implementation, the role of the electrons is taken by atoms as a whole, and the periodic potential is created by forces exerted onto the atoms by light. Inter-particle interactions are realized by the van der Waals force between the atoms. Table 2.1 on the next page gives a comparison between a typical solid state system and a corresponding cold atom based emulation. The following sections will address the ingredients in more detail.

2.1 THE PARTICLE

Neutral atoms as particles that mimic the behavior of electrons

As outlined above, the cold-atom based approach to emulating solid state physics is based on atoms mimicking the behavior of electrons. This may seem as an odd approach first, but as will be shown in the following sections, the properties of electrons seemingly missing in atoms (that is probably most notably a natural spin 1/2 and Coulomb interactions) can be emulated by other physical effects.

The choice of element is actually mostly based on technical grounds (most notably the ability to laser cool the element, see Section 3.1.1 on page 37). A popular choice are alkali elements due to their simple electronic structure: they have one valence electron very much similar to hydrogen. For many effects, the electrons in the lower lying shells can be treated together with the atomic core as one entity. They therefore tend to have closed electronic transitions which can be easily addressed using laser light. Quantum degenerate Fermi gases have so far been produced using the two possible candidates of the alkali metals, ^{40}K [DeMarco *et al.*,

Elements used to produce dilute quantum degenerate Fermi gases

Table 2.1: *Comparison between a solid state system and a cold atom based emulation.* Some of the key properties of electrons in a solid are compared with are compared to those of an ultracold quantum gas loaded into an optical lattice, with the element ^{40}K used as an example.

	ELECTRONS IN SOLIDS	COLD ATOMS (^{40}K)
spin statistics	fermionic	fermionic
mass	9.1×10^{-31} kg	6.6×10^{-26} kg
interactions	Coulomb	van der Waals
lattice	Coulomb potential of the nuclei	optical dipole potential
lattice spacing	$\approx$ Å $= 1 \times 10^{-10}$ m	$\approx 5 \times 10^{-7}$ m
density	10^{21} to 10^{23} cm^{-3}	10^{12} to 10^{13} cm^{-3}
energies	$\approx$ 10 eV	$\approx 10 \times 10^{-11}$ eV
timescales	$\approx$ 1 fs	$\approx$ 1 ms
T	$\approx$ 300 K	$\approx$ 30 nK
T_F	$\approx 1 \times 10^4$ K	$\approx$ nK – µK
T/T_F	< 1%	10%

1999] and ^{6}Li [Truscott *et al.*, 2001; Schreck *et al.*, 2001], the earth-alkali metal ^{87}Sr [DeSalvo *et al.*, 2010; Tey *et al.*, 2010], using ^{3}He* [McNamara *et al.*, 2006], and with ^{173}Yb [Fukuhara *et al.*, 2007] as well as the strongly dipolar ^{161}Dy [Lu *et al.*, 2012] and ^{167}Er [Aikawa *et al.*, 2014] from the lanthanide series.

2.1.1 SPIN AND QUANTUM STATISTICS

To quantum mechanically treat an alkali atom the same method as for the hydrogen atom can be applied [Haken *et al.*, 2003] by adapting the nuclear charge in the problem. The Hamiltonian for the electron-nucleus system is given by:

Hamiltonian of the electron-nucleus system

$$\begin{aligned}\hat{H}_0 &= \hat{H}_{\text{kin}} + \hat{H}_{\text{Coulomb}} + \hat{H}_{\text{FS}} + \hat{H}_{\text{HFS}} \\ &= -\frac{\hbar^2}{2m_0}\Delta + \frac{Ze^2}{4\pi\varepsilon_0 r} + \propto \hat{L}\cdot\hat{S} + \propto \hat{I}\cdot\hat{J}\end{aligned} \tag{2.1}$$

with m_0 being the electron mass, Z the number of protons in the nucleus, r the distance of the electron from the nucleus and e the elementary charge. $\hat{L}$, $\hat{S}$, $\hat{I}$ and $\hat{J}$ are the total orbital angular momentum, the electron spin angular momentum, the nuclear spin angular momentum and the total electronic angular momentum $\hat{J} = \hat{L} + \hat{S}$ respectively.

$\hat{H}_{\text{kin}}$ and $\hat{H}_{\text{Coulomb}}$ account for the kinetic energy of the electron and the Coulomb interaction between the nucleus and the valence electron, respectively. $\hat{H}_{\text{FS}}$ is the fine structure term describing the spin-orbit coupling. Effects of the spin and electric quadrupole moment of the nucleus are included in the hyperfine structure term $\hat{H}_{\text{HFS}}$.

Spin ½

Most crucial to the relevant physics in cold gases is the total spin $I + S$ of the system as it determines the quantum statistics of the atom. If $I + S$ assumes a half-integer value as is the case for ^{6}Li and ^{40}K of the alkalis, the atom behaves as a fermion and thus observes Fermi-Dirac statistics, while it will show bosonic behavior otherwise. To emulate electrons, a fermionic particle is obviously the way to go. To choice of the exact element then again is largely based on technically relevant parameters such as the mass determining the required laser powers for trapping, or the accessibility of inter-particle scattering resonances for control of the interactions.

When solving for the eigenenergies of the Hamiltonian given in Eq. (2.1) on page 19, a clever choice of the quantum numbers has to be made. Because neither $\hat{L}$ nor $\hat{S}$ commutate with the Hamiltonian and are therefore not good quantum numbers, one introduces the total electron angular momentum $J = \hat{L} + S$. As a result of the spin-orbit coupling the energy levels are split up in what is called the fine structure. The eigenvalues of the new operator can be calculated using

Fine structure

$$\hat{L} \cdot \hat{S} = \frac{1}{2}\left(J^2 - L^2 - S^2\right) \tag{2.2}$$

to be

$$E_{\mathrm{FS}} \propto \frac{1}{2}\left[j(j+1) - l(l+1) - s(s+1)\right]. \tag{2.3}$$

Here l and s are the orbital angular momentum and spin quantum numbers. As one can easily see, only energy levels with $l \neq 0$ are split up.

Hyperfine structure

Taking also the so called hyperfine splitting into account, that is the coupling of the total angular momentum of the electrons $\hat{J}$ to the nuclear spin $\hat{I}$, the new eigenvalues can be calculated in a similar way by introducing the new total angular momentum $\hat{F} = \hat{J} + \hat{I}$:

$$E_{\mathrm{HFS}} \propto \left[f(f+1) - j(j+1) - i(i+1)\right]. \tag{2.4}$$

Now levels with $l = 0$ are also split up and one gets for example for the ground state of ^{40}K two levels with

$$F = |I - J|, ..., |I + J| = {}^{9}/_{2}, {}^{7}/_{2}. \tag{2.5}$$

Zeeman effect

When now applying an external magnetic field **B**, the new term

$$\hat{H}_B = -\hat{\mu} \cdot \mathbf{B} \tag{2.6}$$

breaks the spherical symmetry of the Hamiltonian. Here, $\hat{\mu}$ is the magnetic dipole operator. For weak magnetic fields the new term can be treated as a perturbation and F is still a good quantum number. In this so-called Zeeman regime the energy shifts caused by the magnetic field are linear, see Fig. 2.1. In the intermediate regime an additional quadratic Zeeman shift appears, while for high fields (the Paschen-Back regime) the dipole term governs the energy eigenstructure. The new eigenstates in the external magnetic field are denoted with the additional quantum number $m_F = -|F|, ..., |F|$.

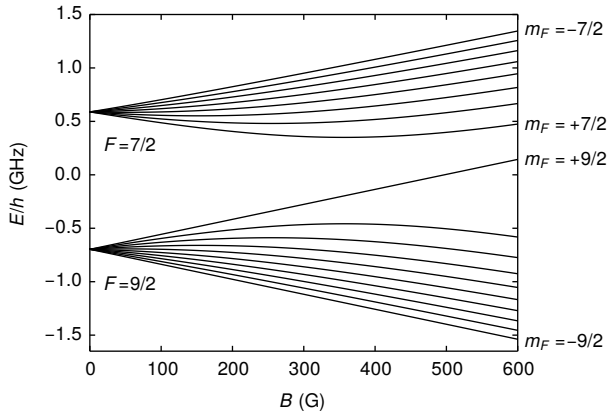

Figure 2.1: *Hyperfine structure of the ground state of ^{40}K.* The energy of the magnetic sublevels of the ground state $4^2S_{1/2}$ fine structure manifold of ^{40}K are plotted as a function of the magnetic field. The crossover from the Zeeman to the Paschen-Back regime is visible. The eigenenergies were calculated by exact diagonalization of the Hamiltonian.

While the excited states of the atom are mostly relevant in the preparation process, be it for laser or evaporative cooling, states close to the absolute ground state

are usually desired for the actual experiments in order to minimize unwanted relaxation processes. In our experiment we typically use an ensemble containing an incoherent 50:50 mixture of atoms in two low-lying Zeeman m_F states to mimic the spin-½ system of electrons in real solids, where $s_z = -|S|, +|S| = -1/2, +1/2$. In contrast to a condensed matter system, we can also realize a completely spin-polarized system by preparing all atoms in the same m_F state. In this case interparticle interactions are fully suppressed because the fermionic atoms will not interact due to the Pauli exclusion principle. This situation may be desirable to study effects originating from the non-interacting band structure separately from other influences.

Spin mixture

2.1.2 QUANTUM DEGENERACY

The electron gas in real solids is already at room temperature highly quantum degenerate as its Fermi temperature T_F is typically on the order of 1×10^4 K. Some quantitative arguments about the requirements for quantum degeneracy in our system can be given based on its density and the achievable temperatures.

A metastable system: density and collisions

The densities in our systems are on the order of $n \approx 1 \times 10^{13}\,\mathrm{cm}^{-3}$ as compared to solid state systems with densities larger than $1 \times 10^{23}\,\mathrm{cm}^{-3}$. While these densities coincidentally result in an average occupation of one atom per site for an optical lattice created by readily available solid state lasers, they are also in the ideal range for an optimal lifetime of the ultracold quantum gas, which is by nature actually in a metastable state. If the densities were just one to two orders of magnitude larger, three-body collisions resulting in deeply bound molecules would start to dominate over elastic collisions which are essential for the rethermalization during the preparation of the samples. For lower densities on the other hand ($n < 1 \times 10^{12}\,\mathrm{cm}^{-3}$) the energy scales would become extremely small and the experimental timescales thus so long that they would exceed the lifetime of the gas, which is ultimately limited by background collisions in the vacuum chamber.

Energy scales

A natural energy scale for the system is given by the Fermi energy

Fermi energy

$$E_\mathrm{F} = \frac{\hbar^2 k_\mathrm{F}^2}{2m} \tag{2.7}$$

where

Fermi wave vector

$$k_\mathrm{F} = (6\pi^2 n)^{1/3} \tag{2.8}$$

is the Fermi wave vector. In our system, $k_\mathrm{F} \approx 100\,\mathrm{nm}^{-1}$, resulting in $E_\mathrm{F}/h \approx 7$ kHz, which corresponds to 3×10^{-11} eV or 300 nK. Here, h denotes Planck's constant.

From the temperature T of the gas the typical momentum of an atom can be estimated to be

$$p \approx \sqrt{m k_\mathrm{B} T}\,, \tag{2.9}$$

where k_B is the Boltzmann constant. Using the de Broglie relation the extent of the wave function of such an atom can be expressed as

$$\lambda = h/p\,. \tag{2.10}$$

Correctly taking into account the mean energy per particle, the thermal de Broglie wavelength is obtained,

Thermal de Broglie wavelength

$$\lambda_T = \sqrt{\frac{2\pi\hbar^2}{m k_\mathrm{B} T}}\,. \tag{2.11}$$

Condition for quantum degeneracy

In a simplified picture the wave functions of the independent atoms start to overlap when this wavelength becomes comparable or smaller than the interparticle spacing $\lambda_T \lesssim n^{1/3}$ (or alternatively $k_B T \lesssim E_F$). At this point, the underlying quantum statistics governing the occupation of the available quantum states starts to play a role. For fermions, the occupation probability of a state with energy E is then given by the Fermi distribution

Fermi distribution

$$f(E) = \frac{1}{\exp\left[(E-\mu)/k_B T\right] + 1}, \tag{2.12}$$

where μ is the chemical potential. As Fig. 2.2 shows, states with energies well below the chemical potential are then occupied with almost unity probability, while the probability crosses smoothly to zero around the chemical potential, with the width of the transition defined by the temperature.

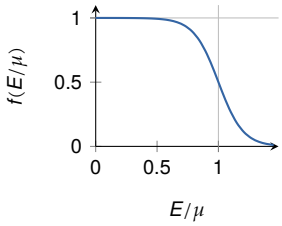

Figure 2.2: *Fermi distribution.* The occupation probability of a state with energy E crosses smoothly from 1 to 0 in the vicinity of the the chemical potential μ. The width of the crossover region is defined by the temperature.

Given the criterion and densities from above, one calculates that the temperatures to achieve quantum degeneracy need to be well below one microkelvin. These ultra-low temperatures required to bring a dilute atomic gas to quantum degeneracy cannot be achieved in the dilution refrigerators currently used at the forefront of research in solid state physics, where temperatures of a few millikelvin can be obtained. Only with the arrival of cooling techniques such as laser- and evaporative cooling, quantum degeneracy of dilute atomic gases was achieved for the first time in 1995 for ^{87}Rb and ^{23}Na [Anderson *et al.*, 1995; Davis *et al.*, 1995]. Paradoxically, in relative units of the respective degeneracy temperatures $k_B T/E_F$, solids cooled in dilution refrigerators are still much "colder" at $k_B T/E_F \lesssim 10^{-6}$, while in cold gases presently 10^{-1} can be reached.

Laser- and evaporative cooling as requirements to produce dilute quantum degenerate gases

2.2 CRYSTAL STRUCTURES

Exerting forces onto atoms

Since atoms are neutral particles, crystal structures cannot be realized in the the same way as they are in real solids, i. e. via the Coulomb interaction. The remaining options would be the realization of either periodic magnetic fields or, alternating current (AC) electric fields that can exert forces via a permanent or induced electric polarization of the atom. Forming these fields via periodic patterning of some surface structure, however, apart from a few very special cases, mostly falls out of question. This is because the interactions of ultracold atoms with surfaces are hard to control with the required accuracy, leading to instabilities of the system that results in excess heating or collapse with atoms crashing into the surface. A viable option however is the use of the atom-light interaction.

While the dissipative light force, i. e. the force exerted onto an atom as a result of photon scattering, is nowadays an essential tool for cooling and trapping atoms at very low temperatures [Hänsch *et al.*, 1975; Dalibard *et al.*, 1989; Adams *et al.*, 1997] and is also employed for sample preparation in the setup used in this thesis, it is unsuitable for creating static potentials as momentum is permanently exchanged between the atoms and the light field. In contrast, the conservative light force allows for using optical projection technologies to impart potentials of almost arbitrary shape onto the atoms to trap and manipulate them [Grimm

et al., 2000], even from the outside of the containing vacuum system. In today's cold atom experiments state-of-the-art projection techniques using high numerical aperture (NA) microscopes, phase masks or spatial light modulators (SLMs) such as digital mirror devices (DMDs)[1] are employed.

When letting several laser beams interfere, the resulting periodic fringe pattern can be used to confine the ultracold atoms to a periodic arrangement resembling that of real solids. This concept of an "optical lattice" was first proposed in the field of laser spectroscopy [Letokhov, 1968; Letokhov *et al.*, 1977; Letokhov *et al.*, 1978]. First experiments in the context of cold atoms focused on the investigation of the band structure [Verkerk *et al.*, 1992; Jessen *et al.*, 1992; Grynberg *et al.*, 1993] and on a direct verification of the periodic arrangement of the atoms via optical Bragg diffraction [Birkl *et al.*, 1995; Weidemüller *et al.*, 1995].

2.2.1 LIGHT FORCES

A two-level atom in a coherent light field

The conservative light force, also called dipole force, is easiest understood in a model considering a two-level atom in a coherent light field [Dalibard *et al.*, 1985]. The state of the system can be written as either $|g, N\rangle$ (if the atom is in the ground state) or $|e, N\rangle$ (atom in the excited state) with N being the photon number in the light field. The two states $|g, N\rangle$ and $|e, N-1\rangle$ are coupled to each other via stimulated absorption and emission of a photon induced by the electric dipole-field interaction $\hat{H}_d = -\hat{d}\hat{E}$) with $\hat{d}$ and $\hat{E}$ being the dipole and electric field operator, respectively. The eigenenergies of the coupled system are then

$$E_\pm = \pm\hbar\sqrt{\Omega_1^2 + \delta_L^2} \tag{2.13}$$

with the Rabi frequency $\Omega_1 = \frac{2}{\hbar}\langle e, N|\hat{H}_d|g, N-1\rangle$ and the detuning between the laser and atomic transition frequency $\delta_L = \omega_L - \omega_0$. In the case of a far-detuned laser $\delta_L \gg \Omega_1$ spontaneous emission from the excited state can neglected and the laser intensity-dependent energy shift of the ground state can be formulated as a conservative potential:

Conservative light potential

$$V_d \approx \frac{\hbar\Omega_1^2}{2\delta_L} = \frac{3\pi c^2\Gamma}{2\omega_0^3\delta_L} I. \tag{2.14}$$

Here, $\Gamma = \omega_L^3/3\pi\varepsilon_0\hbar c^3 \left|\langle e|\hat{d}|g\rangle\right|^2$ is the decay rate of the excited state, c is the speed of light and $I = 2\varepsilon_0 c|E|^2$ is the (position dependent) light intensity, and ε_0 is the dielectric constant. The dipole force $F_d = \mathrm{d}V_d/\mathrm{d}\mathbf{r}$, where $\mathbf{r}$ is the spatial position, therefore has the same sign as δ_L and acts as an attractive force for red detuning and repulsively for blue detuning. The energies of the dressed atomic states for a red detuned laser beam with an gaussian spatial intensity profile are shown in Fig. 2.3.

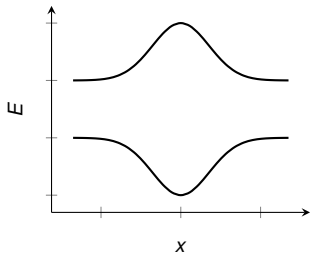

Figure 2.3: *Energies of the ground and excited state of an atom in a laser beam with a gaussian intensity profile.* The laser is far red-detuned by $\delta_L < 0$, giving rise to a potential that lowers the energy of the ground state $|g, N\rangle$ at the intensity maximum of a red-detuned laser beam, while it increases the energy of the excited state $|e, N-1\rangle$. In contrast, for a blue-detuned beam the potential acts repulsively for the ground state.

1 This is an SLM technique based on tilting micro-mirrors invented by Texas Instruments in 1987 and nowadays widely used in video projectors.

2.2.2 OPTICAL LATTICES

A 1D optical lattice can be created by two counter-propagating laser beams as outlined above. The interference between the two beams with equal linear polarization and wavelength λ leads to a standing wave and produces a potential with a periodicity of $d = \lambda/2$ along the beam axis. In a red-detuned lattice the atoms are attracted to the intensity maxima of the interference pattern. The potential depth V_X is controlled by the light intensity and is usually expressed in units of the atom's recoil energy, $E_R = \hbar^2 k_L^2/2m$. Here, $k_L = 2\pi/\lambda$ is the wave vector of the lattice laser and m the atomic mass. The resulting optical potential in the focus of the beam is an array of potential wells, see Fig. 2.4 (left),

$$V(r,x) = V_X \cos^2(k_L x)\, e^{-2r^2/w_r^2}\,. \tag{2.15}$$

The radial envelope is given by the cylindrical symmetric gaussian beam profile with a waist ($1/e^2$ radius) of w_r. Since the waists are usually much larger than the wavelength, the Rayleigh range is also much larger than the size of the atomic cloud. Therefore intensity profile variations along the propagation direction of the beams can be neglected.

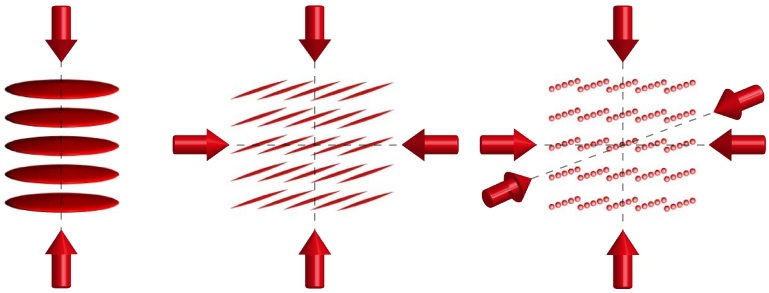

Figure 2.4: *Illustration of the potentials formed by one, two and three pairs of counter-propagating laser beams.* A single pair of red-detuned interfering beams gives rise to a stack of round and almost flat systems. If two pairs are used, an array of tubes is created, which allow only for movement of the atoms in one dimension. The created systems can be considered 2D or 1D if the chemical potential and the kinetic energy of the particles is smaller than the spacing of the first and second harmonic oscillator level along the transverse direction. In the case of three pairs of crossing laser beams, a three-dimensional (3D) crystal structure is created. Adapted from [Stöferle, 2005].

Creating lattice structures by overlapping perpendicular laser beams

When an additional independent orthogonal standing wave is superimposed, $V(x,y,z) = V(r,x) + V(r,y)$, the resulting intensity pattern becomes a planar array of cigar-shaped tubes with simple square periodicity. Adding another orthogonal standing wave $V(x,y,z) = V(r,x) + V(r,y) + V(r,z)$, the resulting potential resembles a simple cubic crystal structure, see Fig. 2.4 (right). By modifying the respective intensities of the standing waves, the dimensionality of the system can be changed on-the-fly and thus, for example, quenches in the dimensionality can be realized.

External confinement

Besides the periodic potential the standing waves of an optical lattice also produce an overall external potential, which is due to the radial intensity profile of the beams. The inhomogeneity of the potential breaks the translational lattice symmetry and therefore alters the situation with respect to a solid state system, where the energy on every lattice site is equal and only falls off abruptly at the edge of the sample (it is box-like, see Fig. 2.5 on the next page). However, if the length scale of the additional confinement is much larger than the lattice spacing, the system can still be considered to be locally homogeneous. This approximation is usually called the local density approximation (LDA) in the cold atom community, see Section 7.3.2 on page 145.

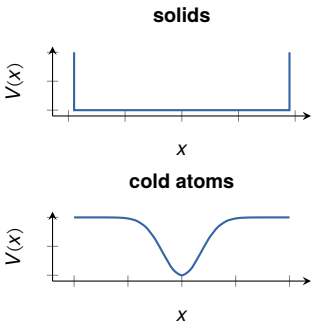

Figure 2.5: *External trapping potential.* Schematic drawing of the confining potential in real solids and for typical cold atom systems. In solids the confining potential is nearly constant over the whole extent of the bulk material, with a sharp boundary at its edge that keeps the electrons confined within the material. Therefore, the energy on every lattice site is essentially the same for the whole system. In implementations of solids using ultracold atoms, the laser beams needed to form the periodic potential and/or hold the atoms against gravity typically give rise to a gaussian envelope of the confining potential. The energy at the bottom of the lattice wells therefore smoothly changes within the system. The systems are typically also much smaller than their real equivalents.

2.3 INTERACTIONS

Interactions between neutral particles: van der Waals potential

Inter-particle interactions are the "spice in the life" of any quantum mechanical system. While the physics resulting from placing non-interacting particles into a periodic potential discussed so far can be fully treated on a single particle level, complex quantum many-body behavior only emerges as interactions are included, leading to a mixing of the single-particle states.

As atoms are neutral particles, they are – in contrast to real electrons – not subject to the Coulomb interaction between each other. In atomic gases interactions are usually only mediated via the short-ranged two-atom molecular potential, which has an effective range of only a few Å. While one might think that this discrepancy between the two systems might fundamentally break their analogy, this is not actually the case since the Coulomb interactions among mobile electrons are usually screened at long distances and are therefore effectively also only short-range.

2.3.1 INTERATOMIC SCATTERING POTENTIAL

Because of the low densities, the interactions in cold atomic gases can usually be treated as a pure two-atom quantum mechanical scattering problem [Sakurai, 1994; Schwabl, 2002].

The scattering potential $V(\mathbf{r})$ is the result of a strong repulsion at short distances due to the overlap of the electron wave functions, and the attractive van der Waals force. Here, $\mathbf{r}$ is the relative spatial coordinate of the two atoms. The range of the potential is r_0. The Schrödinger equation for the problem is then

$$\left[-\frac{\hbar^2}{2m}\nabla^2 + V(\mathbf{r})\right]\psi_{\mathbf{k}}(\mathbf{r}) = E\psi_{\mathbf{k}}(\mathbf{r})\,. \tag{2.16}$$

Treatment as a pure two-atom quantum mechanical scattering problem

The wave vector of the incoming wave is $\mathbf{k}$ with an associated energy $E = \hbar^2k^2/2m$. For large distances $|\mathbf{r}| \gg r_0$ the wave function can be written as a sum of an incoming plane wave and a scattered spherical wave

$$\psi_{\mathbf{k}}(\mathbf{r}) = e^{i\mathbf{k}\mathbf{r}} + \frac{e^{ikr}}{r} f(\mathbf{k},\mathbf{k}')\,. \tag{2.17}$$

The wave vector of the outgoing wave is given by $\mathbf{k}' = k\mathbf{r}/r$. The scattering cross section σ_0 describes the effective spatial extent of the potential seen by the scattering partner. It can be calculated by integrating over the whole sphere:

$$\sigma_0 = \int \mathrm{d}\Omega\, |f(\mathbf{k},\mathbf{k}')|^2\,. \tag{2.18}$$

For a weak interaction potential $V(\mathbf{r})$ the scattering amplitude $f(\mathbf{k},\mathbf{k}')$ can be calculated in the Born approximation, with the result

$$f(\mathbf{k},\mathbf{k}') = -\frac{m}{2\pi\hbar^2}\widetilde{V}(\mathbf{k}-\mathbf{k}')\,, \tag{2.19}$$

where the Fourier transform of the interaction potential is denoted by $\widetilde{V}(\mathbf{k}-\mathbf{k}')$.

Radial Schrödinger equation

To obtain a closed expression for the scattering amplitude, we assume a spherically symmetric interaction potential $V(r)$. The wave function can then be written in spherical coordinates $\psi_{\mathbf{k}}(\mathbf{r})$. It consists of partial waves $Y_{l,m}(\theta,\varphi)$ constructed from Legendre polynomials $P_l(\cos\theta)$ of order $l \in \{0, 1, ...\}$ and a radial wave function $R_l(r)$. The Schrödinger equation for the radial part for a given l then reads

$$\left[-\frac{\hbar^2}{2m}\left(\frac{\partial}{\partial r^2}+\frac{2}{r}\frac{\partial}{\partial r}\right)+V_{\text{eff}}(r)\right]R_l(r)=E\,R_l(r)\,. \tag{2.20}$$

For this, the potential $V(r)$ is replaced by an effective potential

$$V_{\text{eff}}(r)=V(r)+\frac{\hbar^2 l(l+1)}{2mr^2} \tag{2.21}$$

that includes a centrifugal barrier for angular momenta $l > 0$, see Fig. 2.6. This barrier cannot be overcome in the limit of low scattering energies i. e. $k \to 0$ (corresponding to low temperatures).

Inspecting the spatial wave function in the above form one notices that it is symmetric for even values of l and antisymmetric for odd l. The fermionic quantum statistics thus forbids collisions of two fermions with the same spin in the s-wave channel as the combined spatial and spin wave function needs to be antisymmetric. Contributions from the allowed p-wave channel are on the other hand negligibly small at low k. Therefore a spin-polarized Fermi gas can be considered to be essentially non-interacting.

Spin-polarized Fermi gases are essentially non-interacting.

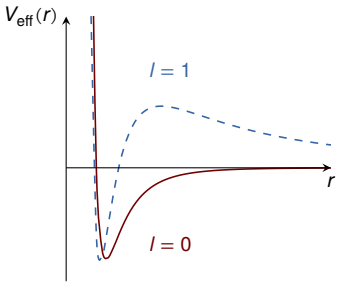

Figure 2.6: *Centrifugal barrier in the interatomic scattering potential.* The potential barriers for the scattering of two different partial waves are drawn. In the limit of low energies $k \to 0$ the centrifugal barrier suppresses scattering in the p-wave ($l = 1$, blue dotted line) and higher partial waves. Only s-wave scattering ($l = 0$, red solid line) is allowed in this case.

The only remaining partial wave is then the radially symmetric s-wave ($l = 0$) term. In this case the asymptotic solution of Eq. (2.20) is $R_0(r) = (r-a)/r$ leading to

$$\psi_{\mathbf{k}\to 0}(\mathbf{r}) \propto \frac{r-a}{r}. \tag{2.22}$$

The s-wave scattering length a

The entire scattering problem can thus be described by a single parameter, the s-wave scattering length a, which corresponds to the intercept of the asymptotic (i. e. $r \gg r_0$) scattering wave function. The sign of a distinguishes two cases, see Fig. 2.7 on the next page. If the attractive potential does not support a bound state, the change to the wave function is small and $a < 0$. In fact, a diverges when a new bound state is just supported by $V(r)$. A potential supporting a bound state ($a > 0$) results in an outgoing wave function $rR_0(r)$ that bends downwards and is associated with a positive scattering length. In the former case, the interaction is said to be *attractive*, whereas in the latter case it is *repulsive*.

Expanding for low energies, the scattering length can be related to the scattering amplitude by

$$f_0(k)=-\frac{1}{1/a+ik-k^2 r_e/2}, \tag{2.23}$$

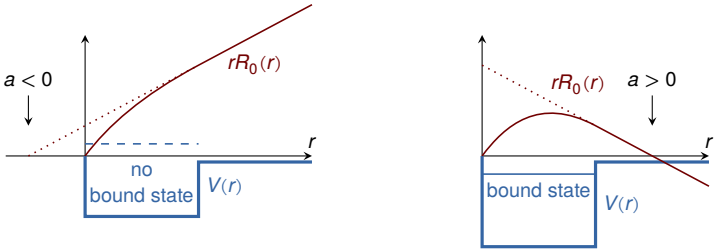

Figure 2.7: *Positive and negative scattering lengths in an attractive potential.* For *s*-wave scattering, the scattering length a is defined as the intercept of the asymptotic slope of the radial scattering wave function $rR_0(r)$ with the r axis. As the depth of the attractive potential is increased, the scattering length a tends to $-\infty$. It diverges exactly when a new bound state is supported by the potential, and becomes positive as the energy of the bound state is lowered further. Adapted from [Jördens, 2010].

where the effective range r_e of the interaction potential was introduced [Gao, 1998; Diener *et al.*, 2004]. The scattering cross section is obtained from the optical theorem:

Optical theorem

$$\sigma_0 \doteq \frac{4\pi}{k}\,\Im\mathrm{m}\, f_0(k) = \frac{4\pi a^2}{1+a^2k^2}\,. \tag{2.24}$$

At the low densities of cold atom systems, the interaction potential between two atoms is given by the van der Waals potential

Van der Waals potential

$$V(r) = -\frac{C_6}{r^6}\,. \tag{2.25}$$

The effective range can be calculated from the van der Waals parameter C_6 as $r_e = \beta_6 = \left(C_6 m/\hbar^2\right)^{1/4}$. As this effective range is much smaller than the typical inter-particle spacing $\beta_6 \ll 1/k_\mathrm{F}$, the scattering formalism introduced above is indeed applicable and the outgoing wave function can be replaced by its asymptotic behavior. This assumption holds for all but the most extreme cases, where the scattering lengths are very large or the atoms are confined in deep optical lattices.

As the inter-atomic potential is in many cases too complicated for analytical calculations, it is usually replaced by a zero-range potential [Castin, 2006] (i. e. a potential which satisfies $k^2 r_e \ll |1/a + ik|$):

$$V_\mathrm{pseudo}(r) = g\delta(r)\frac{\partial}{\partial r}r\,, \tag{2.26}$$

with the interaction parameter g proportional to the scattering length

$$g = \frac{4\pi\hbar^2}{m}a\,. \tag{2.27}$$

In contrast to the real potential, this pseudo-potential can be treated in the Born approximation and allows for a mean-field description of the interacting many-body system as long as $k_\mathrm{F}|a| \ll 1$.

2.3.2 FESHBACH RESONANCES

Feshbach resonances have been originally studied as a phenomenon in nuclear physics [Feshbach, 1958] but have since emerged to one of the key tools in cold atom physics. They allow for tuning the effective interactions over wide ranges, often all the way from strongly attractive through non-interacting to strongly repulsive [Tiesinga *et al.*, 1993; Moerdijk *et al.*, 1995; Giorgini *et al.*, 2008; Ospelkaus

et al., 2010]. While Feshbach resonances are most commonly accessed via magnetic fields [Inouye *et al.*, 1998; Chin *et al.*, 2010], optical [Fedichev *et al.*, 1996; Theis *et al.*, 2004; Jones *et al.*, 2006] as well as rf [Tscherbul *et al.*, 2010] accessing techniques have been explored as well. Their dynamical tunability has allowed to explore the crossover between very different types of quantum many-body states, e. g. from a Bose-Einstein condensate (BEC) state in a Fermi gas, where the atoms are bound together to form repulsively interacting bosonic molecules, to a Bardeen-Cooper-Schrieffer (BCS) state where the fermions form Cooper pairs, which are attractively bound over long distances [Bartenstein *et al.*, 2004; Bourdel *et al.*, 2004; Zwierlein *et al.*, 2005].

BEC-BCS crossover

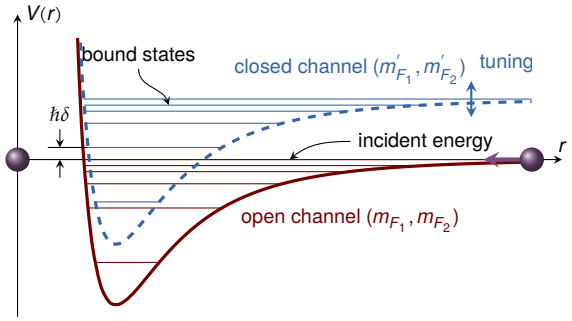

Figure 2.8: *Feshbach resonance.* Two atoms in Zeeman states m_{F_1} and m_{F_2} collide in the so called *open channel*. The coupling to other states m'_{F_1} and m'_{F_2} (*closed channel*) during the scattering process can lead to an effective change in scattering length. If the detuning $\hbar\delta$ between two bound states in the open and closed channel becomes exactly zero, the scattering between the two states is resonantly enhanced ($a \to \pm\infty$). Adapted from [Jördens, 2010].

Coupling between open and closed channels

In the treatment so far, the internal degrees of freedom of the scattering atoms, i. e. the spin, have so far been neglected. Since the electron wave functions of the two atoms 1 and 2 with quantum numbers $|F_1, m_{F_1}\rangle$ and $|F_2, m_{F_2}\rangle$ overlap during the scattering process, their electronic spins couple via the spin-spin interaction $S_1 \cdot S_2$. This in turn couples channels with different total angular momentum $F' = F'_1 + F'_2$ of the unperturbed two-body Hamiltonian used in Eq. (2.20) on page 26. The total magnetic quantum number $m_F = m_{F_1} + m_{F_2}$ however is conserved. The incoming atoms in states $|F_1, m_{F_1}\rangle$ and $|F_2, m_{F_2}\rangle$ are called to be colliding in the *open channel*, see Fig. 2.8. The spin-spin coupling leads to an admixture of other states with $|F'_1, m'_{F_1}\rangle$ and $|F'_2, m'_{F_2}\rangle$ that conserve m_F (i. e. $m'_F = m_F$). These are called the *closed channels*. Since their magnetic moments $\mu_{\text{open}} - \mu_{\text{closed}} = \Delta\mu$ are different as compared to the open channel states, a varying external magnetic field can be used to change the energy difference between the channels by means of the Zeeman effect.

The highest vibrationally excited bound state of the open channel determines the background scattering length a_{bg}, i. e. the scattering length away from any Feshbach resonance. As the magnetic field is tuned to B_{res}, such that a bound state in the closed channel matches the energy of the two incoming atoms in the open channel (that is the energy at the continuum threshold), the coupling to the closed channel becomes relevant and leads to an resonantly enhanced scattering process. The detuning from the resonance is given by $\hbar\delta = \Delta\mu(B - B_{\text{res}})$. The scattering length close to a Feshbach resonance is then given by [Moerdijk *et al.*, 1995]

Scattering length close to a Feshbach resonance

$$a(B) = a_{\text{bg}}\left(1 - \frac{\Delta B}{B - B_0}\right), \tag{2.28}$$

where B_0 is the resonance position (which does not exactly coincide with B_{res} due to an avoided crossing of the weakest bound state in the open channel [Szymańska *et al.*, 2005]) and $\Delta B = 2\hbar^2/(m r_e a_{\text{bg}} \Delta\mu)$ is its width [Castin, 2006]. At the resonance position the scattering length diverges and the only remaining length scale is the inter-particle spacing $\sim 1/k_{\text{F}}$. In this limit, called the *unitarity regime* [Giorgini *et al.*, 2008], the thermodynamics of the system becomes universal and is analogous to the description of neutron stars or quark-gluon plasmas.

In the experiments presented in this thesis, two Feshbach resonances between the states $|F = 9/2, m_F = -9/2\rangle$ and $|F = 9/2, m_F = -7/2\rangle$ (denoted by $m_F = (-9/2, -7/2)$) and between $|F = 9/2, m_F = -9/2\rangle$ and $|F = 9/2, m_F = -5/2\rangle$ (denoted by $m_F = (-9/2, -5/2)$) are employed for controlling the scattering length. Their parameters are listed in Table 2.2 and the scattering length is plotted as a function of the magnetic field in Fig. 2.9.

Table 2.2: *Parameters of the Feshbach resonances used in this thesis.* Position and width of the two Feshbach resonances for the used Zeeman states in the $F = 9/2$ hyperfine manifold of ^{40}K are listed. The background scattering length is $a_{bg} = 174a_0$ [Regal *et al.*, 2004a], where a_0 denotes the Bohr radius. Data either taken from the cited sources or measured in the experiment [Jördens, 2010].

CONFIGURATION	POSITION B_0	WIDTH ΔB
$m_F = (-9/2, -7/2)$	202.10(7) G [1]	7.5(1) G [3]
$m_F = (-9/2, -5/2)$	224.21(5) G [2]	7.6(1) G [3]

1 From [Regal *et al.*, 2004b]. While writing this thesis, we became aware of additional evidence [Zhang, 2013] that suggests using 202.20(2) G [Gaebler *et al.*, 2010] as the accepted position, also slightly changing the width measured in the experiment to 7.4(1) G.
2 From [Regal *et al.*, 2003].
3 Measured in the experiment [Jördens, 2010].

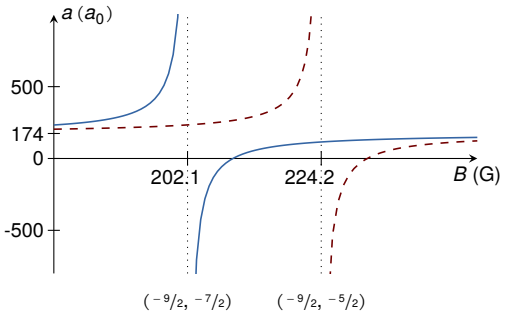

Figure 2.9: *The scattering length in the vicinity of the two relevant Feshbach resonances.* The scattering length was calculated according to Eq. (2.28) using the parameters given in Table 2.2. For most experiments, either a $(-9/2, -7/2)$ or $(-9/2, -5/2)$ spin mixture with a magnetic field located in between the two Feshbach resonance positions is used.

INTERACTIONS IN OPTICAL LATTICES

Under the assumption that the harmonic oscillator length on a lattice site $a_{ho} = \sqrt{\hbar/m\omega_{site}}$ is larger than the effective range of the van der Waals potential β_6, interactions of particles in an optical lattice can be treated in much the same way as in free space.

Treating the lattice sites as harmonic oscillators

One possible approach is to approximate the localized states on the lattice sites by the harmonic oscillator levels of a single well. Under this assumption and using the regularized contact interactions pseudo-potential given in Eq. (2.26) on page 27, the two-particle problem has been solved analytically [Busch *et al.*, 1998]. The modified energies of the harmonic oscillator levels are shown in Fig. 2.10 on the next page.

The lowest branch in the plot on the $a > 0$ side, i. e. for repulsive interactions, corresponds to the solution of the scattering problem in free space. Both in free space and in a lattice the two atoms can be converted from free particles to a Feshbach molecule when sweeping the scattering length close to $a = +0$. The binding energy of these molecules in the vicinity of the Feshbach resonance is given by the Wigner formula [Sakurai, 1994]

$$E_{bind} = -\frac{\hbar^2}{ma^2}\,. \tag{2.29}$$

For $a < 0$ bound states only appear in the presence of confinement, and – in contrast to the free space situation, where deeply bound molecule can be created by sweeping to $a = -\infty$ – their binding energy remains bounded.

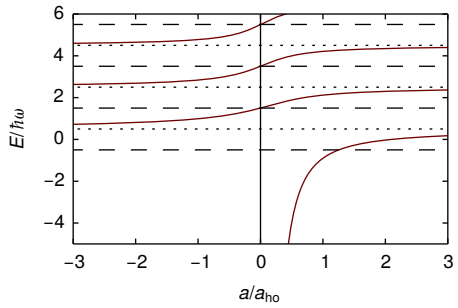

Figure 2.10: *Two-particle states in a harmonic potential.* The energy of the two-particle system is drawn as a function of the inter-particle scattering length (solid red line). The energies of the non-interacting harmonic oscillator states are located at $\hbar\omega(2n + 3/2)$ ($n \in \mathbb{N}$) and are drawn as dashed lines. On resonance, the energies are $\hbar\omega(2n + 1/2)$ (dotted lines). Additionally, a confinement-independent true bound state exists below the lowest harmonic oscillator level.

2.4 PROBES AND MANIPULATION

Despite of the aim of simulating solid state systems, the probes employed in cold atoms experiments are quite dissimilar to those used in solid state research. This is however, most often not a disadvantage, but rather an enrichment as the probes available for cold atomic gases may be complementary to what is available in condensed matter physics. Using tools like fluorescence imaging or absorptive or dispersive imaging techniques, as well as Bragg diffraction [Birkl *et al.*, 1995; Weidemüller *et al.*, 1995, 1998], in combination with techniques like time-of-flight (TOF) (see below), rf pulses, laser beams for manipulation such as stirring, heating or deformation, magnetic field gradients or spectroscopy techniques (such as Bragg or modulation spectroscopy) the state of the system can be characterized in different ways.

Imaging techniques

While recording the fluorescence of the atoms excited by a laser beam resonant with an electronic transition offers the advantage of a background-free signal, it is in practice hard to implement because the atoms are severely heated up by the photon scattering and thus expelled from the trap before enough scattered photons can be collected. Using appropriate freezing lattices and re-cooling schemes, this method has however been used to detect atoms on single sites of optical lattices [Bakr *et al.*, 2010; Sherson *et al.*, 2010]. In absorptive or dispersive imaging techniques the "shadow" of the atoms in a resonant laser beam is recorded on a CCD camera or the phase shift induced by the atoms is measured in an interferometer-like setup, with both methods offering the advantage of better signal-to-noise ratio as compared to fluorescence imaging. All these imaging methods are in some way used to obtain information about the density distribution (or higher order density correlations) of the atoms integrated along one spatial axis[2], either while they are still trapped or after time-of-flight (TOF). In this technique the traps usually required to hold the atomic cloud in a fixed region in space are switched off and the cloud is allowed to evolve freely during a certain amount of time (usually a few milliseconds) under the influence of gravity (or commonly also magnetic field gradients to separate or levitate the atomic cloud), before it is imaged. In this way information about the momentum distribution of the atoms in the trap can be gained as momentum is converted into position information during TOF.

Time-of-flight

Bragg scattering

Used in the same way as in neutron scattering for solid state systems, Bragg scattering gives insight about the a periodic arrangement of the atoms in the sample.

All of the above techniques can be exponentiated by combing them with preparatory steps, during which the state of the system is encoded in other degrees of freedom, which can then be measured using one of these techniques. For example, single atoms can be selectively manipulated or removed from the system using laser or microwave fields [Weitenberg *et al.*, 2011] or electron beams [Würtz *et al.*, 2009]. Several applications of this general scheme will be discussed in this

2 This is commonly called *column-integration*.

thesis. For details on how measurements are performed in our experimental setup, see Section 3.4 on page 63.

Destructiveness of the imaging techniques

In contrast to most solid state measurement techniques, all the mentioned detection methods are in fact destructive to the system already on rather short time scales – that is within the time required to obtain a satisfying signal-to-noise ratio – as they provide the sample with so much energy by momentum impaired via photon scattering that the atoms leave the trap or the imaging region. The destructiveness however varies considerably: while typical absorption imaging usually destroys the sample already when obtaining one single image of the 2D density distribution, other techniques such as the one used in Ref. [Freilich *et al.*, 2010], where only a fraction of the atoms in the cloud is destructively imaged and the rest left intact, allow for taking many images of the same atomic cloud.

Observing dynamics

The destructiveness of the imaging techniques makes it intrinsically hard to observe time-dependent dynamics in these systems. However, the high degree of control over the sample production process and the resulting reproducibility of the experiments helps to overcome this issue: time-series measurements can be constructed by the measurement of many samples at different times relative to the start of the dynamic process (e. g. an excitation created by an instantaneously applied force).

THE EXPERIMENTAL SETUP

3

In this chapter I will discuss the apparatus which was used to perform the experiments described in this thesis. After a brief historical review, I will first describe the steps required to obtain an ultracold Fermi gas in the optical dipole trap, which is the starting point for the actual experiments. Then the main experimental tool of this thesis will be discussed, the tunable-geometry optical lattice. Then, the different lattice geometries which can be achieved using the optical lattice will be studied. To close the chapter, the employed detection methods are presented.

CHAPTER CONTENTS

Brief history of the apparatus

The construction of the setup began in 2001 and allowed for the preparation of the first Bose-Einstein condensate (BEC) of rubidium 87 in Switzerland towards the end of 2002. Since then, the apparatus has been continuously modernized to allow for various kinds of experiments such as the study of Bose gases in optical lattices of different dimensionality[1]. Details on these experiments can be found in the theses of Thilo Stöferle [2005] and Henning Moritz [2006].

After adapting the setup in order to also cool potassium 40 to quantum degeneracy in 2003/2004, the experiment was the first to study ultracold Fermi gases in 3D optical lattices [Köhl, Moritz, Stöferle, Günter, *et al.*, 2005]. This allowed further studies addressing the band structure and interactions [Köhl, Moritz, Stöferle, Günter, *et al.*, 2005; Günter *et al.*, 2005] and Feshbach- [Stöferle *et al.*, 2006; Köhl *et al.*, 2006] and confinement-induced molecules [Moritz *et al.*, 2005], dynamics [Köhl, Moritz, Stöferle, Günter, *et al.*, 2005; Strohmaier *et al.*, 2007] and mixtures of Bose and Fermi gases [Günter *et al.*, 2006]. Details on these experiments can be found in the theses of Henning Moritz [2006] and Kenneth Günter [2007]. Refinement of the experimental techniques, namely the precise measurement of the atomic double occupancies in the optical lattice, and enhancements to the experimental setup allowed for the first observation [Jördens *et*

1 Moritz *et al.*, 2003; Stöferle *et al.*, 2004; Köhl, Moritz, Stöferle, Schori, *et al.*, 2005; Köhl *et al.*, 2004; Schori *et al.*, 2004.

al., 2008] and subsequent characterization of the metal to Mott insulator transition [Jördens *et al.*, 2010] with ultracold fermions. In this context, both the equilibrium [Greif *et al.*, 2011] and non-equilibrium properties [Strohmaier *et al.*, 2010; Sensarma *et al.*, 2010] of the Mott-insulating state were studied using lattice modulation [Stöferle *et al.*, 2004]. This work is detailed in the theses of Niels Strohmaier [2010], Robert Jördens [2010] and Daniel Greif [2013]. A major addition was the tunable-geometry optical lattice installed in 2011, allowing for the exploration of more complex structures such as hexagonal lattices similar to those of graphene [Tarruell *et al.*, 2012; Uehlinger, Greif, Jotzu, Tarruell, Esslinger, *et al.*, 2013; Uehlinger, Jotzu, *et al.*, 2013]. For dimerized and anisotropic lattices, quantum magnetism of ultracold fermions was studied for the first time in 2012 [Greif *et al.*, 2013]. Details on the tunable-geometry optical lattice and the observation of short-range quantum magnetism can be found in the thesis of Daniel Greif [2013].

Main parts of the experimental setup

The experiment in its current state fills a temperature-stabilized and vibration-isolated room of 40 m^2. It consists of four main parts:

- An optical table where the laser light required for cooling, trapping, and imaging is generated and prepared.
- A second optical table holding a stainless steel vacuum chamber where the actual experiment is performed. It holds the required optics and magnetic coils for manipulating the atoms and charge-coupled device (CCD) cameras to acquire images of the atom cloud.
- Electronics for laser stabilization, generation of rf signals, and the control of electric currents.
- Five personal computers connected in a client-server architecture to control the experiment and acquire data.

3.1 PREPARATION OF THE ULTRACOLD FERMI GAS

The used alkali elements

Some of the properties relevant for the two alkali elements used in the preparation, the bosonic ^{87}Rb and the fermionic ^{40}K are listed in Table 3.2 and Table 3.1 on the next page. Potassium builds together with lithium, sodium, rubidium, cesium and francium the first group in the periodic table, which is called the group of alkali metalsİt is a soft silvery-white metal that occurs naturally bound to other elements in for example seawater and many minerals. It oxidizes rapidly in air and is very reactive with water. Potassium is the seventh abundant element on the earth's crust.

Vacuum chamber

A schematic drawing of the vacuum chamber in which the Fermi gas is prepared is shown together with the timing of the main experimental steps in Fig. 3.2 on page 36. In contrast to many other research fields, the "samples" produced and investigated in our experiment are one-time use only, i. e. the measurement process destroys them. Luckily, the generation of a new sample takes only less than one minute (for all-optical experiments this can even be less than 10 s). In order to minimize thermal drifts, this process is continuously repeated during normal operation, even when no measurements are to be taken.

Both the sample preparation process as well as the final samples are in fact highly sensitive to external magnetic fields, electromagnetic radiation and even other particles hitting the atoms in the sample. Therefore the apparatus is well shielded against magnetic fields by *Mu-metal*[2] and is held in an ultra-high vacuum chamber at pressures $< 1 \times 10^{-11}$ mbar. These extremely low pressures are maintained by two ion pumps, which trap particles from the vacuum by ionizing and accelerating them towards one of the electrodes, where they get buried

2 This is the brand name for a nickel-iron alloy with an exceptionally high magnetic permeability.

Table 3.1: *Fermionic potassium ^{40}K.* This table lists some of the relevant properties of the element.

natural abundance [Haynes, 2013]	0.0117(1)	%
abundance in the enriched source material	14	%
radioactive lifetime [Haynes, 2013]	1.2×10^9	y
atomic mass m [Haynes, 2013]	39.9639985	u
vapor pressure at 50 °C [Haynes, 2013]	3.8×10^{-7}	mbar
nuclear spin I [Haynes, 2013]	4	
nuclear g_I factor [Arimondo *et al.*, 1977]	0.000176490(34)	[1]
g_J factor ($4^2S_{1/2}$) [Arimondo *et al.*, 1977]	2.00229421(24)	
wavelength of D_2 line [Tiecke, 2013]	766.700674872(173)	nm
wavelength of D_1 line [Tiecke, 2013]	770.108136507(144)	nm
natural line width Γ of D_2 transition [Tiecke, 2013]	$2\pi \times 6.035(11)$	MHz
ground state hyperfine splitting [Arimondo *et al.*, 1977]	$2\pi \times 1285.8$	MHz
background scattering length a_{bg} [Ticknor *et al.*, 2004]	174	a_0
^{40}K–^{87}Rb interspecies background scattering length ($B = 0$) [Ferlaino *et al.*, 2006a,b]	-185 ± 7	a_0

1 The nuclear gyromagnetic ratio is defined through the nuclear magnetic moment $\boldsymbol{\mu}_{\text{nucl}} = -g_I \mu_B \mathbf{I}$, where μ_B is the Bohr magneton.

Table 3.2: *Bosonic rubidium ^{87}Rb.* This table lists some of the relevant properties of the element.

natural abundance [Haynes, 2013]	27.83(2)	%
radioactive lifetime [Haynes, 2013]	4.9×10^{10}	y
atomic mass m [Haynes, 2013]	86.90918053	u
vapor pressure at 20 °C [Haynes, 2013]	3.1×10^{-7}	mbar
nuclear spin I [Haynes, 2013]	3/2	
nuclear g_I factor [Arimondo *et al.*, 1977]	−0.0009951414(10)	
g_J factor ($5^2S_{1/2}$) [Arimondo *et al.*, 1977]	2.00233113(20)	
wavelength of D_2 line (vacuum) [Steck, 2013]	780.241209686(13)	nm
wavelength of D_1 line (vacuum) [Steck, 2013]	794.978851156(23)	nm
natural line width of D_2 transition Γ [Steck, 2013]	$2\pi \times 6.0666(18)$	MHz
ground state hyperfine splitting [Arimondo *et al.*, 1977]	$2\pi \times 6834.6823$	MHz
background scattering length a_{bg} [Theis *et al.*, 2004]	100	a_0

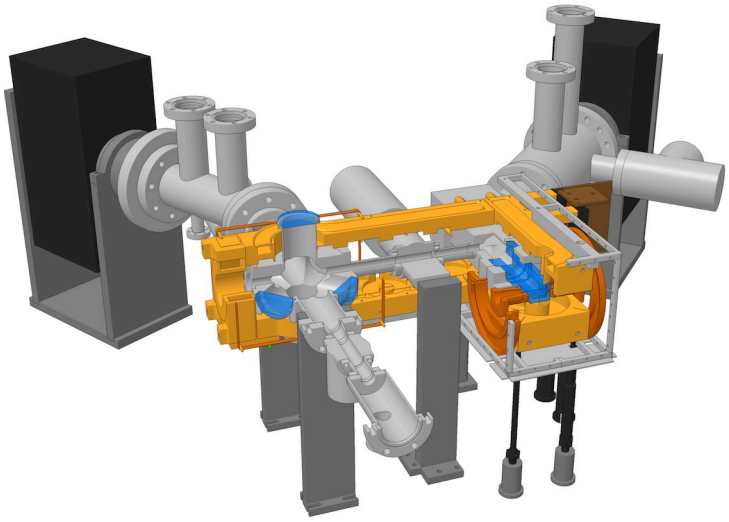

Figure 3.1: *Computer-aided design (CAD) drawing of the apparatus.* A cut through the main parts of the vacuum chamber including magnetic coil supports and ion pumps is shown.

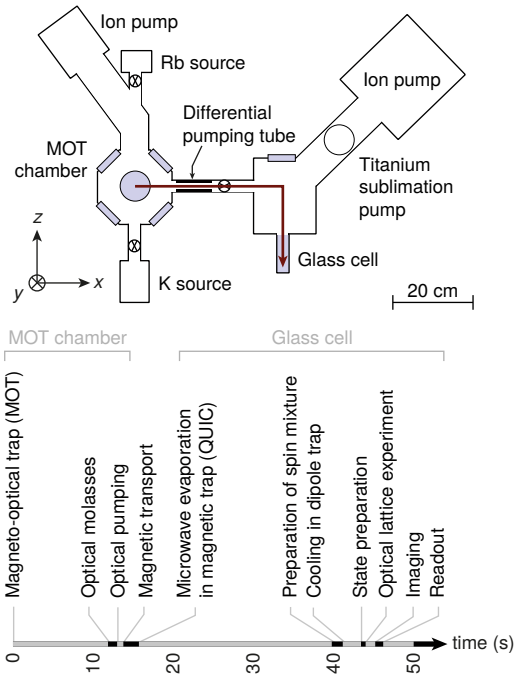

Figure 3.2: *Preparation steps.* During the experimental cycle lasting roughly 50 s, the atoms are captured from the background pressure in the magneto-optical trap (MOT) chamber established by the two atom reservoirs. After magnetic transport through the differential pumping stage to the glass cell the atoms are cooled on quantum degeneracy in a magnetic quadrupole-Ioffe-configuration (QUIC) trap. Following the transfer to a crossed-beam optical dipole trap the optical lattice beams are ramped up in intensity and the actual experiment is performed. Cloud sizes and profiles are afterwards recorded using absorption imaging on CCD cameras. The laboratory coordinate system used throughout this thesis is also introduced. Gravity points along *y*. Drawing adapted from [Stöferle, 2005].

in the surface. A titanium sublimator can be used to coat the inner surface of the vacuum chamber with the very reactive titanium which binds particles from the remaining background gas by a chemical reaction.

Atom sources

The atoms to be prepared for the actual experiment are sourced from to ampuls brought into the vacuum chamber and then cracked to allow some of the atoms to diffuse into the MOT chamber. To avoid unnecessary contamination of the vacuum system, the source material has been purified and for the case of potassium also enriched and then distilled into the ampul. The bosonic ^{87}Rb was obtained as a > 98% pure metal from *Sigma-Aldrich* at a fill-in-weight of 2 g. The ^{40}K has been enriched to 14% and was obtained as a salt (KCl) from *Trace Sciences International, USA*[3]. This compound has been then distilled into the ampul as a pure metal by *Precision Glassblowing, Centennial, CO* at a quantity of 30 mg.

Then, the atoms need to be prepared at the required temperature, density and in the desired internal state to be able to load them into the optical lattice where the actual experiment is performed. To this end, several different types of traps, combined with various cooling techniques are used, with an overview shown in Fig. 3.3.

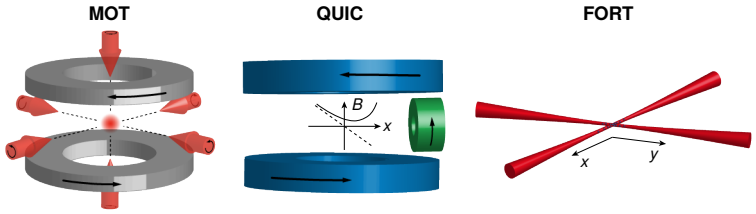

Figure 3.3: *Atom traps.* The different types of traps used in the experiment are shown. First, the atoms are cooled and trapped in a MOT, which is built from six crossed laser beams and a magnetic quadrupole field. Next, the atoms a transported in a quadrupole trap (not shown) to the glass cell, where they are evaporatively cooled in a quadrupole-Ioffe-configuration (QUIC) trap. In a final step, they are transferred to a crossed-beam optical dipole trap (far-off resonance trap (FORT)), where a second step of evaporative cooling is performed. Adapted from [Günter, 2007].

3.1.1 LASER COOLING

First cooling step: the magneto-optical trap

The first preparation step is based on the principle of laser cooling proposed by Hänsch *et al.* The atoms are caught and cooled in a MOT from the background gas built up by diffusing ^{87}Rb and ^{40}K atoms, see Fig. 3.4 on the following page. The background pressure of ^{87}Rb is 3.1×10^{-7} mbar at room temperature, enough for an efficient loading into the MOT. For ^{40}K it is only 1.3×10^{-8} mbar and thus needs to be enhanced to a similar pressure as for ^{87}Rb by heating the area of the vacuum chamber close to the ampul to 50 °C. By simultaneously applying a magnetic field in a quadrupole configuration generated by two switchable magnetic coils and three pairs of perpendicular counter-propagating laser beams addressing the D_2 electronic transition lines, the atoms can be cooled and trapped in the center of the coil and beam arrangement. The exact laser frequencies can be found in the energy level scheme displayed in Fig. 3.5 on the next page.

Addressed atomic transitions: cooler and repumper laser

In order to achieve a cooling effect, the *cooler* lasers are slightly red detuned (i. e. their frequency is slightly lower) with respect to the transition to be addressed. Because the used transitions are not fully closed, an additional laser frequency (the *repumper*) has to be employed to pump the atoms back into the relevant ground

3 Recently, ^{40}K seems not to be available from this company in highly enriched quality anymore. However, we are aware of another company, *American Elements*, which is still offering ^{40}K enriched to $\geq$ 10%.

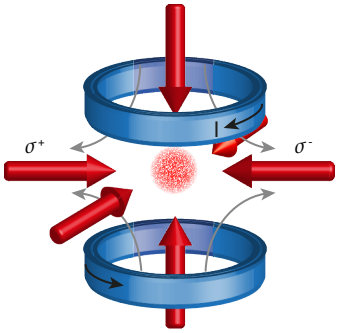

Figure 3.4: *Magneto-optical trap.* Six circularly polarized laser beams with a frequency which is red-detuned with respect to the atomic transition cross at the center of a magnetic quadrupole field. This gives rise to a momentum- and position-dependent photon scattering rate, leading to both a cooling and trapping effect.

state. The fact that an electronic transition in an atom or molecule can actually be cycled through in a continuous fashion using only these two *cooler* and *repumper* laser frequencies is actually not at all trivial. This is only the case for very few elements and transitions, for example for those of alkali atoms as used here. Both the cooling and trapping effect in the MOT can be understood in the picture of dissipative light forces: by the combination of the laser detuning and the detuning resulting from a position dependent Zeeman splitting in the quadrupole field, photons are only scattered from atoms propagating away from the trap center towards one of the six beams, see Fig. 3.4. The directed transferred momentum acquired during absorption of a photon is subsequently lost by the isotropic emission of the photon. This repeated process leads to a net reduction of the momentum of the atoms in the center of the trap combined with a net force directed towards the center.

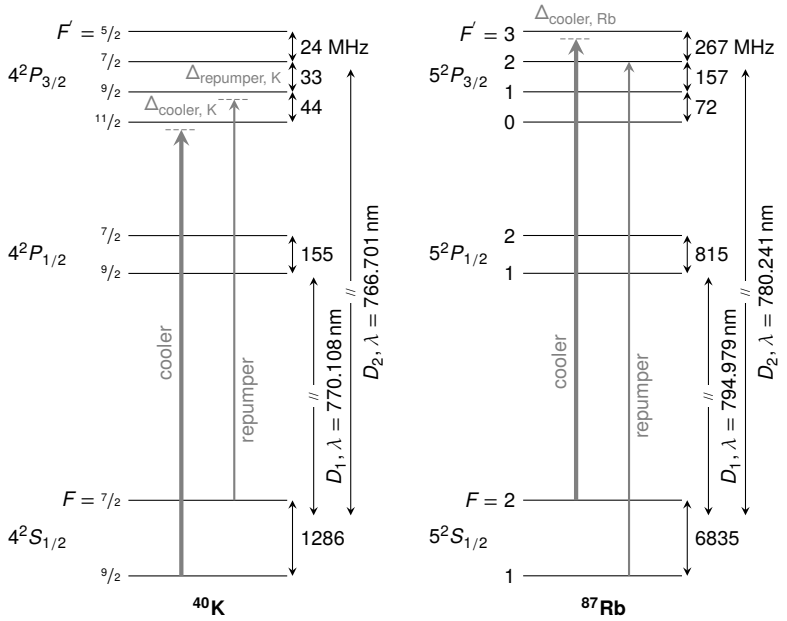

Figure 3.5: *Level schemes for ^{40}K and ^{87}Rb including both the D_1 and D_2 transitions.* The cooling and repumper transitions are addressed by slightly red-detuned laser frequencies. The linewidths of the D_2 transitions used in the experiment are 6.04 MHz and 6.07 MHz for ^{40}K and ^{87}Rb, respectively. The D_1 transition is not directly involved in the laser cooling process. Adapted from [Jördens, 2010]. Data from [Steck, 2013; Tiecke, 2013].

In the experiment, we first load about 20×10^6 potassium atoms into the MOT. In a second step, ^{87}Rb is loaded, with a final atom number of about 1×10^9. Both species are captured and cooled in the same place, with the cooling laser beams for both elements co-propagating along all six spatial directions. To avoid collisional losses of potassium atoms induced by the rubidium, ^{87}Rb is only collected during

the last 3 s of the MOT stage lasting 12 s in total. The essential parameters of this cooling step are listed in Table 3.3.

Table 3.3: *Summary of the parameters for the MOT and the optical molasses cooling.* Adapted from [Günter, 2007].

PARAMETER	^{40}K	^{87}Rb
cooling power (fiber output)	200 mW	250 mW
repumping power (fiber output)	100 mW	5 mW
cooler detuning Δ_{cool}	$-5.5\,\Gamma$	$-3\,\Gamma$
repumper detuning Δ_{repump}	$-5.5\,\Gamma$	$0\,\Gamma$
magnetic field gradients	(−5, −5, 10) G/cm	(−5, −5, 10) G/cm
loading duration	12 s	3 s
atom number	$\sim 20\times10^6$	$\sim 10^9$
molasses detuning	$-3\,\Gamma$	$-10\,\Gamma$
molasses duration	6 ms	6 ms

At the end of this cooling step, temperatures on the order of a mK are reached. To achieve a further reduction of temperature, the magnetic field is switched off and molasses cooling is performed during 6 ms, with a final detuning of -10Γ and -3Γ for ^{87}Rb and ^{40}K, respectively. We then optically pump the ^{87}Rb into the $|F = 2, m_F = +2\rangle$ state and ^{40}K into $|F = 9/2, m_F = {}^{+}9/2\rangle$, respectively, by a short sequence of laser pulses (total duration: 1.8 ms) of the resonant cooling and repumper light followed by a controlled switch-off of first the cooler and then the repumper. The two Zeeman states are chosen because of their favorable interspecies scattering properties required for efficient sympathetic cooling.

Molasses cooling and optical pumping

3.1.2 MAGNETIC TRAPPING AND TRANSPORT

The above-mentioned states of both elements have a positive magnetic moment and are thus low-field seekers, i. e. their energy is minimized in magnetic field minima. They can thus be trapped in a magnetic quadrupole field which we in the following employ to transport the atoms through the differential pumping stage into the glass cell. The transport is achieved by subsequently ramping the currents in the 11 coil pairs arranged along the transport path outside of the vacuum chamber on and off. In this way, the magnetic field minimum is smoothly moved along the transport path to the glass cell within 1.5 s, allowing the atoms to follow like in a conveyor belt. About 20% of the atoms initially trapped in the MOT are finally captured in a magnetic trap in the glass cell. This includes losses during the molasses cooling, optical pumping, the transport and loading into the final magnetic trap. In the glass cell, the atoms are transferred into a QUIC trap [Esslinger *et al.*, 1998]. This type of magnetic trap avoids the problem of Majorana losses [Petrich *et al.*, 1995] due to the magnetic field minimum present in the trap center of pure quadrupole traps. This is achieved by adding the additional Ioffe coil, which produces an overall offset field of in our case about 3 G. In this trap, the atomic cloud assumes the shape of a cigar, with the axis aligned with that of the Ioffe coil.

Magnetic transport through a conveyor belt arrangement of coils

3.1.3 EVAPORATIVE COOLING

When arriving in the glass cell, the atoms are roughly at a temperature on the order of some 10 µK, which is – even though these temperatures are already on the order of those achieved in today's best cryostats – still much higher than the Fermi temperature of some 100 nK of this extremely dilute gas. Even lower tem-

Magnetic cooling in the QUIC trap within the glass cell

peratures can be achieved by a slow removal of the hottest atoms in the trap, while allowing for a continuous rethermalization of the atoms by interactions, a method called forced evaporative cooling. In our setup, we use microwave radiation to address the $5^2S_{1/2}$ $|F = 2, m_F = 2\rangle \rightarrow |F = 1, m_F = 1\rangle$ transition of ^{87}Rb in order to transfer atoms from a magnetically trapped to an untrapped state. Due to the Zeeman effect, the transition frequency has a spatial dependence, which allows for addressing only the outside, i. e. the hottest atoms. During a total time of 23 s atoms are continuously removed with a lowering frequency accounting for the decreasing size of the cloud. This process is performed slowly enough for allowing rethermalization of the rubidium gas by collisions. The *s*-wave scattering length of ^{87}Rb resulting from the underlying van der Waals interactions is 100 a_0, where a_0 denotes the Bohr radius.

The microwave frequencies are generated by mixing a commercial microwave source operating at 6.630 000 000 GHz[4] with a signal generated from a computer-controlled direct digital synthesizer (DDS) developed in our group [Jördens, 2006].

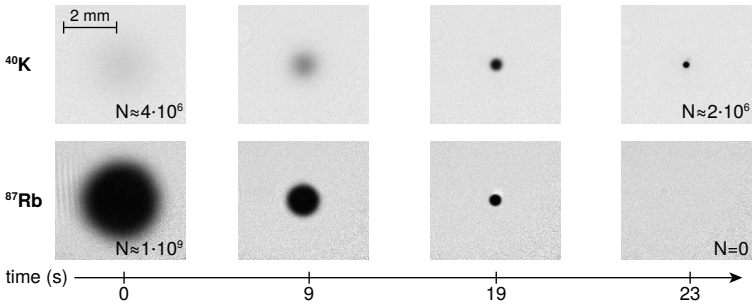

Figure 3.6: *Evaporative cooling.* Absorption images of ^{40}K and ^{87}Rb at different times during the evaporation stage. The potassium atoms are only visible at a later stage of the evaporation as their initial density is very low. The forced evaporation on ^{87}Rb is performed until all atoms are completely removed, leaving only the sympathetically cooled ^{40}K at a relative temperature down to $T/T_F \approx 20\%$. Images were taken on a temporarily installed low-magnification imaging system along the *x* axis using a *Point Grey Flea2* CCD camera. Adapted from [Greif, 2013].

Currents in the QUIC coils

Usually both the quadrupole pair as well as the additional Ioffe coil in the QUIC trap are driven by the same current. In our experiment, the atoms would in this configuration partially get in contact with the inner glass cell wall at the beginning of the evaporation process. Therefore we use during 7 s a modified configuration, in which the current through the Ioffe coils is increased in order to push the trap minimum away from the glass cell wall. In this configuration 20 A of current are run through the quadrupole coils and 30 A are used for the Ioffe coil[5]. The evaporation frequency is ramped from 6.8945 GHz to 6.8695 GHz. This step is followed by 23 s evaporation in a normal QUIC configuration. During this time the current is ramped from 30 A to 25 A using an exponential ramp to lessen three-body losses, and the frequency is tuned from 6.8745 GHz to 6.8415 GHz, depending on the atom number required in the final configuration. The power of the microwave radiation is decreased by 14 dB as well to counteract power broadening.

For ^{40}K, the situation is different: Due to the fermionic spin of ^{40}K, collisions between particles are not allowed if a spin-polarized gas (i. e. only containing

4 The absolute frequency stability of all frequency generators used in the experiment is ensured by a phase-locked loops (PLLs) referenced to a long-time stable 10 MHz signal obtained from a global positioning system (GPS) receiver, which additionally ensures short-time stability via quartz oscillator locked to the GPS time signal.

5 The offset field needs to be decreased in this configuration by an additional coil in order to stiffen the trap. This however increases the sensitivity to spurious rf at low frequencies which can cause spin-flips to untrapped states.

only particles in one spin state) is used. Therefore one cannot cool spin-polarized fermionic potassium by evaporative cooling in magnetic traps just by itself due the lack of thermalization. We circumvent this problem by making use of the inter-species collisions between the overlapped ^{40}K and ^{87}Rb clouds, allowing for a continuous re-thermalization of the potassium atoms while microwave evaporation is performed on rubidium. This technique is called sympathetic cooling. The relevant inter-species background scattering length is $a = -185(7)a_0$. Images of the atomic clouds at different times during the evaporation are shown in Fig. 3.6 on page 40. As the actual experiments are to be performed with only ^{40}K, the ^{87}Rb atoms are usually completely removed during the evaporation process.

3.1.4 OPTICAL TRAPPING

While magnetic traps are the ideal choice to create both very deep and large traps for cold atoms, they do not allow for an arbitrary choice of a homogenous external magnetic field, which is needed when a precise control of the inter-particle interactions via Feshbach resonances (see Section 2.3.2 on page 27) is required. Optical dipole traps – also called FORTs –, based on the AC-Stark effect, are a much better choice in this case as they do not involve static magnetic fields. The forces resulting from these traps are conservative, i. e. do not transfer any energy, and are therefore ideally suited to hold or manipulate the ultracold samples created in these types of experiments. A brief introduction to the origin of the light forces is given in Section 2.2.1 on page 23. Details on their working principle and applications can for example be found in [Grimm *et al.*, 2000].

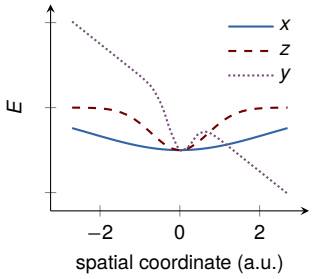

Figure 3.7: *Trap potential of a single beam dipole trap.* The potential in the focus of a laser beam with an elliptic gaussian intensity profiles propagating along x is drawn for the three spatial directions. Along the propagation direction x the confinement is very weak, leading to an elongated cloud. Along y, gravity counteracts the confinement, requiring a narrower beam along this direction.

Crossed beam optical dipole trap

In Fig. 3.7 we schematically plot the potential from a single gaussian laser beam along the three spatial axes. Gravity points along y. In such a potential the atomic cloud would assume a very elongated shape along the axial direction of the laser beam. To obtain a round cloud profile in the $x - z$ plane, we use two horizontal FORT beams crossing at 90°. To avoid interference between the two beams, their frequencies are detuned with respect to each other by approximately 160 MHz by means of two acousto-optic modulators (AOMs). About 1% of the light is picked up after the fiber output coupler on the experimental table via an anti-reflection (AR) plate and sent to high-bandwidth photodiodes. This signal as well as the analog setpoint voltage signal output by the computer control card are fed to a proportional-integral-derivative (PID) controller. The processed error signal is then fed back into the AOM for intensity stabilization. As the dipole trap also has to hold the cloud against gravity, the confinement is increased along this axis by an elliptic beam profile created by means of an anamorphic prism pair. The parameters of the dipole trap configuration used in the experiment can be found in Table 3.4 on the following page. We use a titanium-sapphire (Ti:Sa) laser (*Coherent MBR110* pumped by a *Coherent Verdi V18*) operating at a wavelength of $\lambda = 826.05$ nm, resulting in a red-detuning with respect to the atomic transition frequency of 59 nm. The exact wavelength of the FORT laser is in principle not crucial. Measurements at different wavelengths showed however a close-by loss fea-

Parameters of the dipole trap

ture centered at 826.10 nm caused by a photo-association resonance [Strohmaier, 2010].

Table 3.4: *Dipole trap parameters.* The two beams propagate horizontally in the x and z direction. The typical final parameters correspond to the usual recompression endpoint after evaporation where laser powers of about 43 mW per beam are used. Adapted from [Jördens, 2010].

wavelength	$\lambda_F = 826.05\,\text{nm}$
horizontal waist	$w_h = 150\,\mu\text{m}$
vertical waist	$w_v = 50\,\mu\text{m}$
typical gravitational sag	$y_0 \approx -11\,\mu\text{m}$
typical final trap depth with gravity	$\Delta V_F \approx 2.4\,E_\text{R} \approx k_\text{B} \times 0.5\,\mu\text{K}$
typical final trap frequencies	$\omega_{F(x,y,z)}/2\pi = [31.3(2), 97(1), 33.0(2)]\,\text{Hz}$
typical mean trap frequency	$\omega_F/2\pi = 46.6\,\text{Hz}$

TRAP FREQUENCIES

Together with the gravitational potential the two beams form the potential

$$V_F(x,y,z) = -V_{Fx}\exp\left(-2\frac{z^2}{w_h^2} - 2\frac{y^2}{w_v^2}\right) - V_{Fz}\exp\left(-2\frac{x^2}{w_h^2} - 2\frac{y^2}{w_v^2}\right) + mgy\,, \tag{3.1}$$

where w_h and w_v are the horizontal and vertical $1/e^2$ waists, respectively. The potential depth at the center of the two beams is V_{Fx} and V_{Fz}.

The gravitational potential pulls the atoms downwards and leads to a sag in their equilibrium position with respect to the symmetric position in the intensity maximum. For deep traps, where the sag is small compared to the waist, the new equilibrium position lies at $y_0 \approx -mgw_v^2/4(V_{Fx}+V_{Fz})$. Close to its minimum, the potential shape can be well approximated by that of a purely harmonic potential around $(x,y,z) = (0,y_0,0)$:

$$V_F(x,y,z) \approx \frac{1}{2}m\left(\omega_{Fx}^2x^2 + \omega_{Fz}^2z^2 + \omega_{Fy}^2(y-y_0)^2\right) \tag{3.2}$$

Harmonic trapping frequencies of the FORT

with the oscillator frequencies

$$\begin{aligned}
\omega_{Fx}^2 &= \frac{4V_{Fz}\exp(-2y_0^2/w_v^2)}{w_h^2 m}\,,\\
\omega_{Fz}^2 &= \frac{4V_{Fx}\exp(-2y_0^2/w_v^2)}{w_h^2 m}\,, \quad \text{and}\\
\omega_{Fy}^2 &= \frac{4(V_{Fx}+V_{Fz})(1-4y_0^2/w_v^2)\exp(-2y_0^2/w_v^2)}{w_v^2 m}\,.
\end{aligned} \tag{3.3}$$

These harmonic oscillator frequencies, called the trap frequencies, can be experimentally measured. For this, dipole oscillations of the ^{40}K atomic cloud with interactions tuned close to zero are induced by magnetic field gradients (for the x and z direction) or a sudden change of the FORT intensity (for the y direction). The oscillation frequency is then measured by recording the center of mass of the cloud after TOF.

LOADING

In order to transfer the atoms from the magnetic trap to the optical dipole trap, the intensity of the two FORT beams is first ramped up to a value between 120 mW and 200 mW per beam within 100 ms, followed by a ramp-down of the magnetic field within another 100 ms. We then make use of the large coil-pair mounted in Helmholtz configuration along the x axis to create a homogenous offset field of about 10 G at the position of the atoms. As this coil pair is later used to control the Feshbach field, these coils are aptly called the "Feshbach coils" (see Fig. 3.29 on page 62 for an overview of the relevant magnetic coils). An rf frequency sweep using an rf antenna located within the *Mu-metal* shielding close to the glass cell then induces subsequent Landau-Zener transfers taking the atoms from the $|F = 9/2, m_F = +9/2\rangle$ to $|F = 9/2, m_F = -9/2\rangle$ (see Fig. 3.8, step ①), i. e. the absolute electronic ground state of the system. Following this procedure, the magnetic field is increased to several 100 G, where the degeneracy of the m_F states is lifted due to the increasing quadratic Zeeman shift. In this crossover regime between the Zeeman and Paschen-Back effect different $m_F \rightarrow m_F \pm 1$ transitions can be selectively addressed for further preparation. Depending on the Feshbach resonance or magnetic fields to be accessed, either of the two evaporative cooling procedures in the FORT outlined below is followed.

Preparation of the atoms in the absolute ground state

PREPARATION ON THE LOW-FIELD SIDE OF THE (−9/2,−7/2) FESHBACH RESONANCE

For accessing magnetic fields at the low-field side of the $(-9/2, -7/2)$ Feshbach resonance, the magnetic offset field is ramped to 186 G (see Fig. 3.8), where an incoherent, balanced (i. e. with a ratio 0.50(5)) mixture of the two Zeeman states $|F = 9/2, m_F = -9/2\rangle$ and $|F = 9/2, m_F = -7/2\rangle$ is created by a sequence of fast Landau-Zener transfers between the two states lasting for a total of 200 ms (step ②). The magnetic field is then ramped to a value of 197.5 G resulting in a scattering length of $a = 460a_0$ ③. At this scattering length allowing for a continuous re-thermalization, the ^{40}K is then further evaporatively cooled by ramping the intensity of the FORT beams down to 37 mW–45 mW within 2.5 s using an exponential ramp with a time constant $\tau = 450$ ms. Typically, the FORT is then recompressed to an intensity of 43 mW–45 mW to avoid further evaporation and to have a well-defined starting point for the actual experiment. From here, scattering lengths in the range of 200 to $650a_0$ can be set Ⓣ.

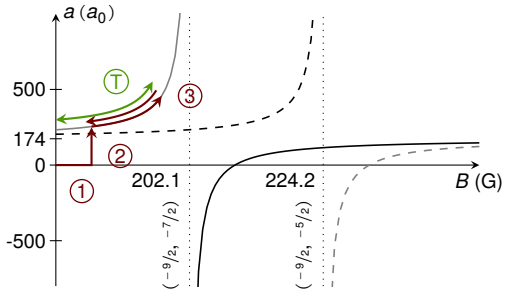

Figure 3.8: *Spin mixture preparation and cooling on the left of the $(-9/2, -7/2)$ Feshbach resonance.* Both the spin-mixture preparation ② and the cooling ③ are performed on the repulsive side of the Feshbach resonance.

PREPARATION ON THE HIGH-FIELD SIDE OF THE (−9/2,−7/2) FESHBACH RESONANCE

The preparation procedure on the "right" (i. e. high-field) side of the $(-9/2, -7/2)$ resonance is mostly analogous to that on the "left" side. To create the $|F = 9/2, m_F = -9/2\rangle$ — $|F = 9/2, m_F = -7/2\rangle$ spin mixture, the offset field is ramped to 232 G ②. The scattering length is then tuned to $-1600(200)a_0$ by setting

$B = 202.8\,\mathrm{G}$ for the evaporative cooling ③. The evaporation ramp starts from a FORT intensity of 120 mW and has an exponential shape with a duration of 1.7 s and a time constant $\tau = 700\,\mathrm{ms}$. After the evaporation, the scattering length is tuned close to its zero-crossing at $B = 216.6\,\mathrm{G}$. The FORT is then recompressed. At this point, we either drive a Landau-Zener transition using a frequency sweep ④ to transform the $|F = 9/2, m_F = -9/2\rangle$ — $|F = 9/2, m_F = -7/2\rangle$ mixture into a $|F = 9/2, m_F = -9/2\rangle$ — $|F = 9/2, m_F = -5/2\rangle$ mixture in order to have access to large positive scattering lengths in the range of 200 to $650a_0$ (blue Ⓣ) or keep the $|F = 9/2, m_F = -9/2\rangle$ — $|F = 9/2, m_F = -7/2\rangle$ spin mixture already used for evaporation to access scattering lengths in the range of -650 to $110a_0$ (green Ⓣ).

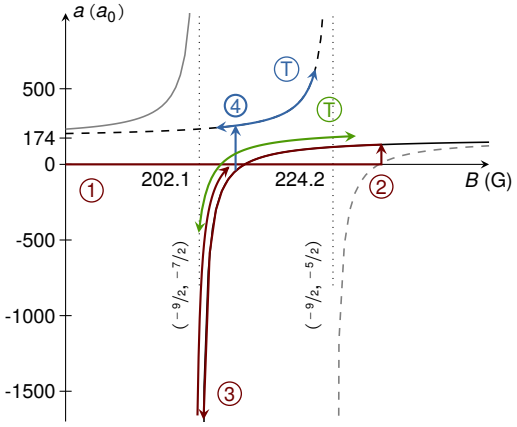

Figure 3.9: *Spin mixture preparation and cooling on the right of the $(-9/2, -7/2)$ Feshbach resonance.* Here, the spin mixture ② is prepared on the right of the Feshbach resonance and the cooling is performed at a large attractive scattering length ③. A Landau-Zener transition ④ can be used to obtain a $(-9/2, -5/2)$ spin mixture.

Choice of the evaporation side

The choice of the evaporation side depends on the requirements of the actual experiment to be performed. The use of a $(-9/2, -7/2)$ mixture is in principle preferred in all cases, as losses due to spin-changing collisions and the attributed heating are lower. However, large repulsive interactions with $(-9/2, -7/2)$ mixtures can only be accessed when evaporating on the left side of the respective Feshbach resonance, where in our experiment the evaporation does not work as efficiently as on the high-field side and thus only temperatures on the order of $T/T_\mathrm{F} = 20\%$ can be reached. On the right side, we typically reach temperatures below $T/T_\mathrm{F} = 10\%$ for the $(-9/2, -7/2)$ mixture, which translate into temperatures on the order of $T/T_\mathrm{F} = 14\%$ after transferring to $(-9/2, -5/2)$.

3.2 THE TUNABLE-GEOMETRY OPTICAL LATTICE

The tunable-geometry optical lattice scheme developed in our setup is the key to the experiments presented in this thesis. The lattice was originally planned to allow for a dynamic tuning between a lattice with simple cubic geometry and a configuration where every two wells in the original lattice are merged to one for the detection of spin order (*cf.* [Pedersen *et al.*, 2011]). Only later we realized that the setup would also allow for various other geometries like triangular, dimerized and honeycomb lattices, as well as certain types of coupled chain arrangements.

Interference between detuned optical lattice beams

One of the most simple ways of constructing an optical lattice in one dimension is letting a laser beam (which is far detuned from the electronic transition of the atom) interfere with itself after retro-reflection on a mirror. This results in a periodic potential of $\cos^2(x)$ shape. The scheme can be easily extended to higher dimensions by combing several perpendicular retro-reflected beams interfering with themselves, but not with each other. Interference between the beams is suppressed in such a scheme by either a perpendicular polarization direction and/or frequency detunings of at least several MHz, leading to a quickly varying interference term. This term averages out in the effective potential seen by the atoms

since its frequency is much higher than the harmonic oscillator frequency of the atoms in the lattice wells [Greiner, 2003].

Schemes for complex lattice geometries

More complex geometries can be obtained by not only letting two counter-propagating beams interfere as when retro-reflecting the laser beams, but by allowing beams of the same frequency to interfere at angles $\neq 180°$, combined with a clever choice of polarization [Petsas *et al.*, 1994]. Pioneering experiments using such a scheme [Hemmerich and Hänsch, 1993; Grynberg *et al.*, 1993; Hemmerich, Zimmermann, *et al.*, 1993] were limited by their susceptibility to fluctuations of the relative phase between interfering beams. Using a combination of electro-optic modulators (EOMs) to phase-shift the light between the mirrors used for retro-reflecting and diverting the beam to the perpendicular lattice axis, a 2D double well lattice relying on passive stability was realized [Sebby-Strabley *et al.*, 2006]. Later, triangular and hexagonal geometries were constructed using actively phase stabilized laser beams at an angle of 120° [Becker *et al.*, 2010; Soltan-Panahi *et al.*, 2011].

Using different laser frequencies, 1D lattices with a complex band structure could be realized in a setup using AOMs to derive the required laser frequencies [Ritt *et al.*, 2006]. A 1D double-well lattice could also be realized using two entirely different laser frequencies [Fölling *et al.*, 2007]. Also employing two different laser frequencies and beams angled at 120°, lattices of *kagome* geometry were recently implemented [Jo *et al.*, 2012].

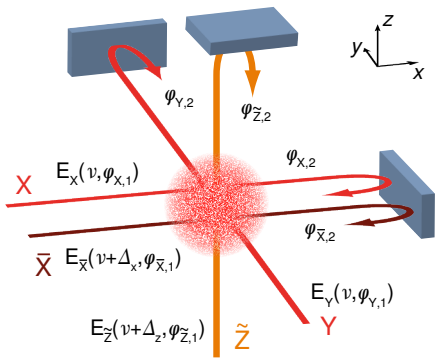

Figure 3.10: *Schematic drawing of the optical lattice beam arrangement.* Four retro-reflected laser beams at a wavelength of $\lambda = 1064\,\text{nm}$ are used. The polarization and exact frequency of the perpendicular X and Y beams are chosen such that they interfere with each other. The $\bar{X}$ beam is collinear with X, but only interferes with itself, as is the case for the forth beam $\tilde{Z}$. The corresponding electric fields, laser frequencies and light-phase pickups are labeled for each beam.

General idea of the optical lattice of tunable geometry

Our scheme is an extension of the classical lattice beam arrangement used for simple cubic 3D geometries illustrated in the very beginning of this section. It is conceptually simple and also relatively straightforward to implement even in existing setups because it requires only adding one additional laser beam superimposed with one of the three beams, see Fig. 3.10. The trick is now to let this beam interfere with one of the beams perpendicular to it, by choice of the same laser frequency and polarization. The resulting interference pattern has to be kept locked to that of the original beam configuration by an active phase stabilization.

3.2.1 CONCEPT

Arrangement of the optical lattice beams

The lattice is built from four linearly polarized laser beams X, $\bar{X}$, Y and $\tilde{Z}$, which are red-detuned with respect to the atomic transition and operate at a wavelength of $\lambda \approx 1064\,\text{nm}$, see Fig. 3.10. All of them are retro-reflected into themselves and cross at the center position of the atomic cloud. X and Y both operate at the same frequency ν and have the same polarization. This therefore leads to a standing wave pattern resulting from the interference between the two beams. $\bar{X}$ and $\tilde{Z}$ are detuned from this frequency by Δ_x and Δ_z respectively, both on the order of 100 MHz. The resulting cross-interference terms vary therefore with this frequency difference. This fast oscillation of the potential depth, however, cannot be followed by the atomic motion. These interference terms can therefore be ne-

glected. Moreover, since the polarization of the $\tilde{\mathrm{Z}}$ beam is orthogonal to that of the $\bar{\mathrm{X}}$, X and Y beams, the z direction actually decouples from the rest and can thus be treated separately.

Electric fields

Following the derivations in [Mottl, 2009], neglecting the spatial intensity profile of the laser beams and the overall phase $e^{i2\pi\nu t}$, the electric fields of the beams sum up to

$$\begin{aligned}
\mathbf{E} &= \mathbf{E}_{\bar{\mathrm{X}}} + \mathbf{E}_{\mathrm{X}} + \mathbf{E}_{\mathrm{Y}} + \mathbf{E}_{\tilde{\mathrm{Z}}} \quad \text{with} \\
\mathbf{E}_{\bar{\mathrm{X}}} &= E_{\bar{\mathrm{X}}}\,\mathbf{e}_z \left[\exp\left(i(k'_{\mathrm{L}}x + \varphi_{\bar{\mathrm{X}},1})\right) + \exp\left(i(-k'_{\mathrm{L}}x + \varphi_{\bar{\mathrm{X}},1} + \varphi_{\bar{\mathrm{X}},2})\right)\right] e^{i2\pi\Delta_x t} \\
\mathbf{E}_{\mathrm{X}} &= E_{\mathrm{X}}\,\mathbf{e}_z \left[\exp\left(i(k_{\mathrm{L}}x + \varphi_{\mathrm{X},1})\right) + \exp\left(i(-k_{\mathrm{L}}x + \varphi_{\mathrm{X},1} + \varphi_{\mathrm{X},2})\right)\right] \\
\mathbf{E}_{\mathrm{Y}} &= E_{\mathrm{Y}}\,\mathbf{e}_z \left[\exp\left(i(k_{\mathrm{L}}y + \varphi_{\mathrm{Y},1})\right) + \exp\left(i(-k_{\mathrm{L}}y + \varphi_{\mathrm{Y},1} + \varphi_{\mathrm{Y},2})\right)\right] \\
\mathbf{E}_{\tilde{\mathrm{Z}}} &= E_{\tilde{\mathrm{Z}}}\,\mathbf{e}_y \left[\exp\left(i(k''_{\mathrm{L}}z + \varphi_{\tilde{\mathrm{Z}},1})\right) + \exp\left(i(-k''_{\mathrm{L}}y + \varphi_{\tilde{\mathrm{Z}},1} + \varphi_{\tilde{\mathrm{Z}},2})\right)\right] e^{i2\pi\Delta_z t}\,.
\end{aligned} \tag{3.4}$$

The detuning Δ_x is set to a value close to 400 MHz and can be used to adjust the lattice geometry, see Section 3.2.5 on page 53. The detuning Δ_z of the $\tilde{\mathrm{Z}}$ lattice beam is set to −70.1 MHz. As the interference caused by the detuned beams does not affect the atomic motion (see above), the atomic potential can be written in the form

$$V(x,y,z) \propto |\mathbf{E}_{\bar{\mathrm{X}}}|^2 + |\mathbf{E}_{\mathrm{X}} + \mathbf{E}_{\mathrm{Y}}|^2 + |\mathbf{E}_{\tilde{\mathrm{Z}}}|^2\,. \tag{3.5}$$

When additionally setting $k_{\mathrm{L}} \equiv 2\pi/\lambda = k'_{\mathrm{L}} \equiv 2\pi/\lambda' = k''_{\mathrm{L}} \equiv 2\pi/\lambda''$, where λ, λ' and λ'' are the wavelengths associated to the slightly different laser frequencies involved, one finds

$$\begin{aligned}
V(x,y,z) = &- V_{\bar{\mathrm{X}}} \cos^2(k_{\mathrm{L}}x + \theta/2) \\
&- V_{\mathrm{X}} \cos^2(k_{\mathrm{L}}x) - V_{\mathrm{Y}} \cos^2(k_{\mathrm{L}}y) \\
&- 2\sqrt{V_{\mathrm{X}} V_{\mathrm{Y}}} \cos(k_{\mathrm{L}}x)\cos(k_{\mathrm{L}}y)\alpha\cos\varphi \\
&- V_{\tilde{\mathrm{Z}}} \cos^2(k_{\mathrm{L}}z)\,.
\end{aligned} \tag{3.6}$$

Here, $V_{\bar{\mathrm{X}},\mathrm{X},\mathrm{Y},\tilde{\mathrm{Z}}}$ are the lattice depths of the independent beams. An additional parameter α is introduced to account for a reduced contrast of the interference between X and Y, caused for example by not perfectly matched polarization directions. The phases in Eq. (3.4) are reduced to the two more intuitive phases for the $x-y$ plane,

Relevant phases

$$\text{interference phase} \quad \varphi = \varphi_{\mathrm{Y},1} - \varphi_{\mathrm{X},1} + \frac{\varphi_{\mathrm{Y},2} - \varphi_{\mathrm{X},2}}{2} \tag{3.7}$$

$$\text{symmetry phase} \quad \theta = \varphi_{\mathrm{X},2} - \varphi_{\bar{\mathrm{X}},2}\,. \tag{3.8}$$

The control over the lattice depths $V_{\bar{\mathrm{X}},\mathrm{X},\mathrm{Y},\tilde{\mathrm{Z}}}$ as well as the phases φ and θ allows for creating a multitude of different lattice geometries as will be detailed in Section 3.3.1 on page 54. The setup required for the generation of the beams and the control of the phases is described in the following sections. The technical details on the stabilization schemes employed for the optical lattice can be found in the thesis of Daniel Greif [2013].

3.2.2 OPTICAL SETUP

An overview of the setup required to prepare the optical lattice beams is shown in Fig. 3.11 on the next page, with the relevant frequency offset given in Table 3.5. The laser light for all beams is derived from a neodymium-doped yttrium aluminum garnet (Nd:YAG) laser (*Coherent Mephisto MOPA 36W NE*) with a maximum output power of 40 W. The specified line width is 1 kHz when integrating over 100 ms and the relative intensity noise is < −130 dB/Hz for frequencies above 10 kHz.

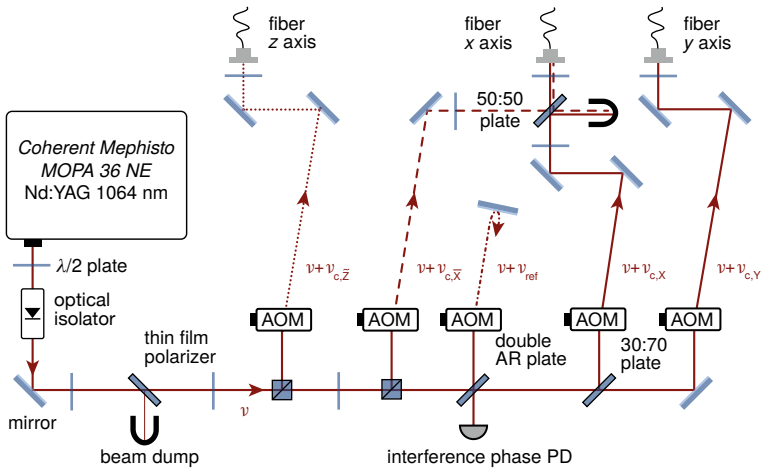

Figure 3.11: *Optical lattice beam preparation.* The light from the Nd:YAG laser first passes through an optical isolator to avoid back-reflections into the laser. It is then split into four main paths, where AOMs regulate the light intensity for each of the lattice beams. The light for the $\bar{X}$ and X beam is recombined using a 50:50 plate and coupled into the same optical fiber. A double AR plate is used to split off a small fraction of the light used for the reference arm of the phase stabilization interferometer. Adapted from [Greif, 2013].

AOMs for intensity regulation

The light is then distributed to four AOMs (models *IntraAction ATM2001A2 and ATM1351A2*, containing TeO_2 crystals) which are used for frequency shifting and intensity stabilization of the lattice beams. The first order diffraction is then coupled into polarization maintaining single mode fibers (*Schäfter-Kirchhoff*, 6.4 µm mode-field diameter (MFD)). An additional AOM running at 138.4 MHz is used in double-pass configuration to generate a reference beam which will be needed for the stabilization of the interference phase φ, see Section 3.2.3 on page 49. The X and Y beams are combined by means of a 50:50 splitting plate and are then coupled into the same optical fiber. The optical fibers are used to transport the light to the experimental table and also to clean the mode of the beam in order to achieve perfect gaussian intensity profiles at the output.

Single mode fibers for transport and cleaning

Table 3.5: *Frequencies of the rf sources used in the optical lattice setup.* The sign of the frequency indicates the first positive or negative diffraction order of the AOM.

LABEL	DESCRIPTION	FREQ. (MHz)
$\nu_{c,X}$	carrier X	195.1
$\nu_{c,Y}$	carrier Y	195.1
$\nu_{c,\bar{X}}$	carrier $\bar{X}$	−189.7
$\nu_{c,\tilde{Z}}$	carrier $\tilde{Z}$	125.0
ν_{ref}	reference beam	138.4

Optical setup on the optical table holding the vacuum chamber

Combining the laser beams

The optical setup close to the glass cell holding the atomic cloud is shown for the x and y axes in Fig. 3.12 and for z in Fig. 3.13 on page 49. Gravity points along y. The schematics include all laser beams in the actual experiment as well as the optical setup for the detection of the atoms. As the optical access to the glass cell is essentially limited to the three spatial axes, multi-chromatic mirrors are required to combine the beams emanating from several fibers onto the same optical axis. On each axis there is a lattice beam and a beam for imaging to be combined. On the two horizontal axes, x and z, additionally a FORT and deconfinement beam are installed to provide and control the overall harmonic confinement for the atomic cloud, see Section 3.3.3 on page 58. After polarization cleaning, about 1% of the FORT, lattice and deconfinement beams is split off by means of AR plates or by the residual transmission through a mirror and sent to a photodiode for intensity stabilization. While the imaging beam is collimated at the position of the atoms,

the other beams are focused by achromats with a focal length on the order of $f = 400\,\mathrm{mm}$.

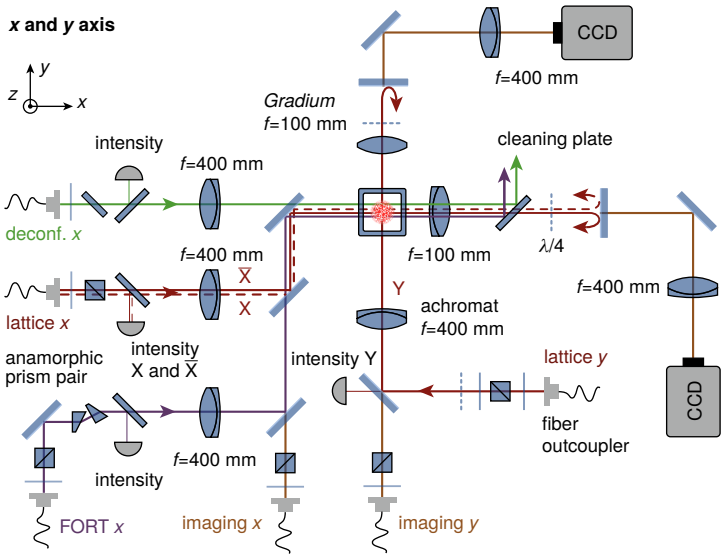

Figure 3.12: *Optical lattice beam arrangement on the x and y axis.* On every axis, the beams (depending on the direction these are the FORT, optical lattice, deconfinement and imaging beams) are after initial preparation combined using several dichromatic mirrors before they propagate almost colinearly through the atom cloud located inside the glass cell. Lenses, which act both as the objective lens for the imaging system and to re-collimate the lattice beams, are installed at a distance of 10 cm after the position of the atoms. The FORT and deconfinement beams are reflected off using multi-chromatic cleaning plates to avoid any back-reflections.

After having passed through the glass cell, the beams are re-collimated by either achromats or a *Gradium*[6] lens of focal length $f = 100\,\mathrm{mm}$. Before the lattice beams are retro-reflected by 0° multi-chromatic mirrors, the FORT and deconfinement beams are reflected off by another multi-chromatic mirror to avoid the creation of weak optical lattices by the residual reflection on the 0° mirror. After retro-reflection, the lattice beams pass in the opposite direction through the setup and are coupled back into the respective fibers. To compensate for intensity losses due to reflection on optical elements for the incoming and retro-reflected lattice beams, a $\lambda/4$ plate is installed in front of the 0° mirror. Additional $f = 400\,\mathrm{MHz}$ achromatic lenses result, combined with the lenses just after the glass cell, into telescopes with a magnification for the imaging system of about 4.

The parameters of the optical lattice are summarized in Table 3.6.

Table 3.6: *Parameters of the optical lattice.*

wavelength	$\lambda = 1064\,\mathrm{nm}$
beam waists	$w_{x,y,z} = [190, 180, 180]\,\mu\mathrm{m}$
available power per axis	2 W
maximum lattice depth per axis	$V \approx 40\,E_\mathrm{R}$
power per E_R[1]	$P_{x,y,z} = [20.5, 15.1, 15.8]\,\mathrm{mW}$

1 Measured behind the $f = 100\,\mathrm{mm}$ lens located after the glass cell.

6 This is the brand name of a singlet lens produced from material with a gradual variation of the refractive index, produced by *LightPath Technologies*.

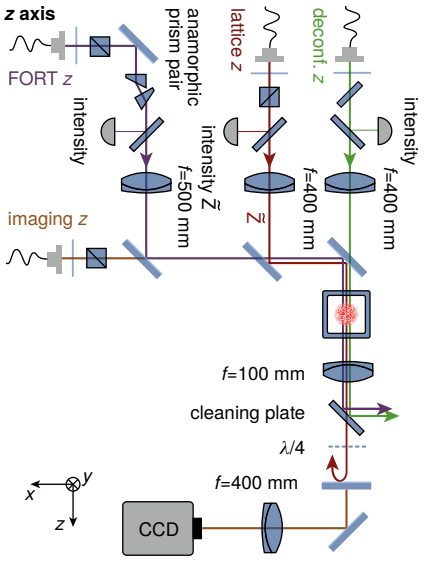

Figure 3.13: *Optical lattice beam arrangement on the z axis.* On this axis, the FORT, optical lattice, deconfinement and imaging beams are, after initial preparation, combined using several dichromatic mirrors, before they propagate almost colinearly through the atom cloud, located inside the glass cell. A lens, which acts both as the objective lens for the imaging system and to re-collimate the lattice beam, is installed at the distance of 10 cm after the position of the atoms. The FORT and deconfinement beams are reflected off using multi-chromatic cleaning plates to avoid any back-reflections.

3.2.3 INTERFERENCE PHASE STABILIZATION

The interference phase φ in Eq. (3.6) on page 46 is defined as the light phase difference picked up between the place where the source laser beam is split into the X and Y beams on the laser table and the respective retro-reflecting mirror on the experimental table. Fluctuations in this phase can arise from small variations in the optical path length within the optical fibers due to thermal effects or vibrations, from path length variations in the free space part close to the glass cell or from vibrations of the optical elements such as the retro-reflecting mirror. These effects can lead to a change of φ by more than 2π on timescales typically below 10 kHz. While passive stability improvements such as a guiding the optical fibers using damping mounting material separately from vibration inducing devices have helped to limit the fluctuations to the frequency range below 1 kHz, the remaining variations still need to be eliminated by an active stabilization scheme.

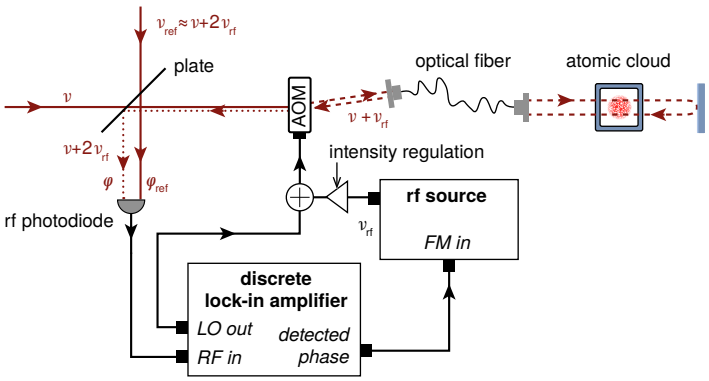

Figure 3.14: *Principle of the interference phase stabilization scheme.* The laser light of the interfering laser beams is tagged with a sideband frequency using the intensity regulation AOM. The retro-reflected light, which is subject to phase jitter, is, after passing back through the optical fiber, overlapped with a reference beam on a photodiode. The phase of the photodiode signal with respect to the original sideband signal is then detected using a lock-in amplifier built from discrete parts. This phase difference signal is then fed into the frequency modulation (FM) input of the AOM rf source in order to correct for the measured phase deviation. Adapted from [Greif, 2013].

The basic principle of the lock is similar to that used for the phase stabilization required for synchronizing distant clocks [Ma *et al.*, 1994] and is displayed

in Fig. 3.14 on page 49. The beam, whose phase is to be stabilized, passes through the AOM, where its frequency is shifted to $\nu + \nu_{\mathrm{rf}}$. The light is guided via the optical fiber to the experiment table, where it is retro-reflected after passing through the glass cell. It couples back into the fiber and is partially reflected onto a rf photodiode by a beam splitting plate. A reference beam deduced from the same laser at frequency $\nu_{\mathrm{ref}} \approx \nu + 2\nu_{\mathrm{rf}}$ enters the plate from the top and thus interferes with the retro-reflected beam on the photodiode. The photodiode can therefore be used to record the phase of the two beams with respect to each other. Variations in the measured phase can then be compensated by slightly changing the frequency (or alternatively directly the phase[7]) of the rf signal which is sent to the AOM, similar to the method used to implement PLLs in electronics [Horowitz *et al.*, 1989].

As the AOM is not only used for the loop feedback but also to change the intensity of the lattice and thus the lattice depth, the power of one of the interfering beams on the photodiode would vary accordingly. While the lock point is actually set to the zero-crossing of the interference fringe pattern and would thus not change, the amplitude of the error signal still scales with the lattice depth leading to an undesired change of the lock gain. Therefore, the phase detection is actually not done at direct current (DC), but at a frequency on the order of 1 MHz, modulated onto the lattice beam, similar to the scheme used by lock-in amplifiers [Michels *et al.*, 1941; Cosens, 1934]. This also allows for detecting the phase of both X and Y on the same photodiode as slightly different frequencies are added to the two beams. The added frequency component can also be seen as an additional beam co-propagating with the main beam in the fiber and on the atoms. The frequency components of the main and this additional, so called *phase tag* beam, are actually at slightly different angles after the AOM. To still achieve reasonable coupling efficiencies into the fibers, the frequency difference is limited to a few MHz. The power in the phase tag beams is held usually at a constant level, but can also be varied to dynamically change the lock characteristic by computer control. Typical powers in the tag beams of about 5 mW lead to a permanent residual lattice of about 0.1 E_{R}, which is accounted for when determining the effective lattice depths produced in the experiment.

Use of a lock-in amplifier scheme for phase stabilization

Phase tag beams

By changing the phase of the reference oscillator that is used to mix down the rf input with respect to that which is sent to the local oscillator (LO) port in the lock-in amplifier[8], the phase of the lattice beams can be dynamically tuned from the computer.

As both the phase of X and Y are being stabilized to that of the same reference beam, they are then also stable with respect to each other. Stabilizing the beams with respect to a reference beam has the additional advantage of allowing for an independently adjustable reference beam power: it can be increased to about 100 mW without affecting the atomic cloud in order to obtain a better signal-to-noise ratio of the interference fringe pattern on the photodiode.

Phase stabilization with respect to an independent strong reference beam

The effectiveness of the lock can be assessed by comparing the frequency spectrum of the beat between the reference oscillator of the lock-in amplifier and the rf signal input in the locked to the unlocked state, see Fig. 3.15 on the facing page. The large reduction of phase noise becomes immediately apparent from these measurements.

Stability of the phase lock

MEASURING THE INTERFERENCE PHASE

In the experiment, the phase φ can be measured using Kapitza-Dirac scattering in the Raman-Nath regime [Kapitza *et al.*, 1933; Gould *et al.*, 1986; Cahn *et al.*, 1997;

Kapitza-Dirac scattering

7 Changing the frequency result in a lock that regulates only using the integral part of the error signal, while regulating the phase results in a proportional regulation.

8 This *lock-in amplifier* is in our setup built from discrete band-pass (or low- or high-pass) filters and mixers.

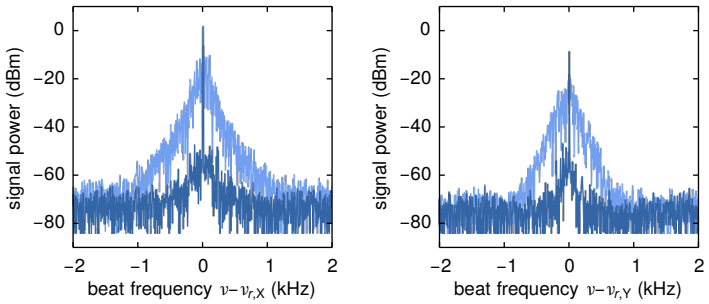

a. x axis b. y axis

Figure 3.15: *Interference phase stability.* The frequency spectrum of the detected phase difference between the lattice and the reference beams ($\nu_{r,X}$ and $\nu_{r,Y}$, respectively) is shown for the two axes with the phase stabilization deactivated (light blue) and activated (dark blue). Data from [Greif, 2013].

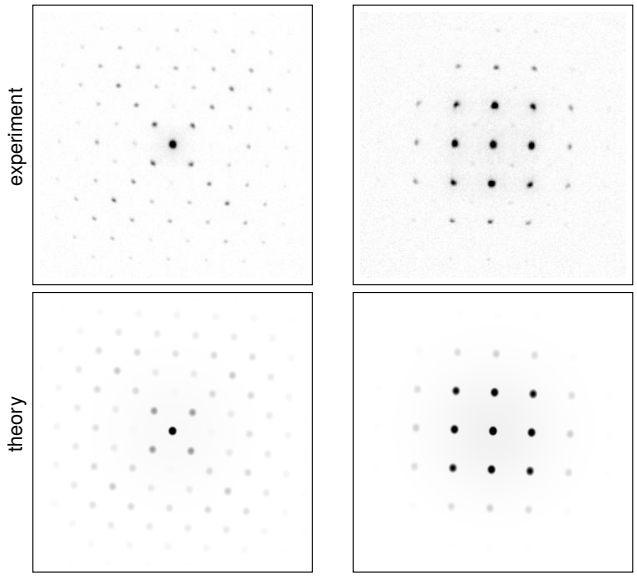

a. $\varphi \approx 0$ b. $\varphi \approx \pi/2$

Figure 3.16: *Raman-Nath diffraction.* Experimental (top) and fitted (bottom) diffraction patterns are shown for the case of maximally interfering beams X and Y ($\varphi = 0$) and at the setting where they do not interfere ($\varphi = \pi/2$). The lock settings are usually first optimized close to the $\varphi = \pi/2$ point such that the diagonal interference peaks vanish, since the optical potential is most sensitive to changes of φ at this point (because of the zero-crossing in the cosine term). We then switch to $\varphi = 0$ for the actual measurements. The fitting can be used to extract φ or α and is performed using a numerical time evolution of the single-particle lattice Hamiltonian.

Freimund *et al.*, 2002]. A BEC is exposed during typically a few µs to the lattice generated by X and Y with a depth of roughly 30 E_R. During this time, the atoms are subject to the time evolution under the single-particle Hamiltonian

Raman-Nath diffraction

$$\hat{H}_{\text{lat}} = -\frac{\hbar^2}{2m}\nabla^2 + V(x,y), \tag{3.9}$$

where $V(x,y)$ is the lattice potential. Under its influence higher lattice momentum modes are being populated, which can be seen by performing TOF after switching off the lattice beams, see Fig. 3.16 on page 51.

If φ is stabilized to 0 (Fig. 3.16a on page 51), additional momentum components located at multiples of $(\pm\hbar k_L, \pm\hbar k_L)$ appear as a result of the interference term $\cos(k_L x)\cos(k_L y)$, compared to the situation with $\varphi \approx \pi/2$, where the two beams do not interfere and thus only components at multiples of $(\pm 2\hbar k_L, \pm 2\hbar k_L)$ are present.

Inferring the phase stability

The time evolution under the Hamiltonian can be numerically computed and fitted to the experimentally recorded momentum distributions in order to extract the phase φ. By repeating the experiment with the phase stabilized to the same point, the lock stability can be inferred to be around 5°.

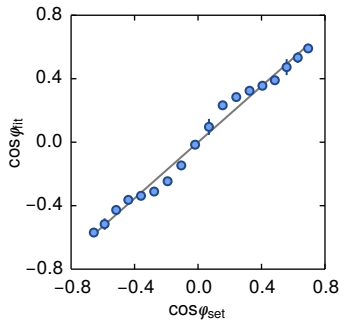

Figure 3.17: *Visibility calibration.* By fitting the Raman-Nath diffraction patterns obtained by setting different interference phases φ_{set} and comparing these with the phase obtained from the fit, φ_{fit}, the visibility of the interference can be determined, since $\cos\varphi_{\text{fit}} = \alpha\cos\varphi_{\text{set}}$. The average over two independent measurements gave a visibility $\alpha = 0.90(5)$.

Once the point of minimal interference is found, this method can be additionally used to calibrate the visibility of the interference α between X and Y. We vary the phase setpoint systematically and record the resulting momentum distribution pattern. By plotting the cosine of the set phase with respect to the reference point versus that of the fitted phase, the visibility can be extracted as the slope, see Fig. 3.17. This is because the numerical model assumes perfect visibility $\alpha_{\text{num}} = 1$ while the experiment has $\alpha < 1$ and $\alpha_{\text{num}}\cos\varphi_{\text{fit}} = \cos\varphi_{\text{fit}} \overset{!}{=} \alpha\cos\varphi_{\text{set}}$). In our experiment, we have found $\alpha = 0.90(5)$.

3.2.4 INTENSITY STABILIZATION

Intensity stabilization of a single beam propagating through a fiber

The intensity stabilization of the optical lattice beams generally adheres to the following scheme: the actual intensity of the beam is measured by directing about 1% of the light outcoupled from the optical fiber to a photodiode. Both the output voltage of the photodiode and the demanded power signal output by the control computer are sent to a PID controller. The two signals are subtracted to create the error signal which is then, after multiplication with a fixed gain and integration or differentiation (not used in our setup), sent as the control output to the AOM which sets the amplitude of the AOM rf drive signal accordingly.

Scheme to stabilize two beams propagating through a single fiber

For the $\bar{X}$ and $\bar{Z}$ beams this scheme can be implemented as is. For X and Y, a more involved approach is necessary, as the two beams are perfectly overlapped, have the same polarization and are only separated by roughly 400 MHz in frequency. Here again, a lock-in technique is used to distinguish the two beams, see Fig. 3.18 on the facing page. The AOM drive signal is mixed with the local oscillator of the discretely set up lock-in amplifiers running at about 1 MHz, but at

slightly different frequencies for the two beams. This *intensity tag* signal is then picked up in the usual location close to the glass cell and fed to the rf input of the lock-in amplifier. The detected amplitude is then used as the signal input for the PID controller. The rest of the regulation loop works as in the usual scheme.

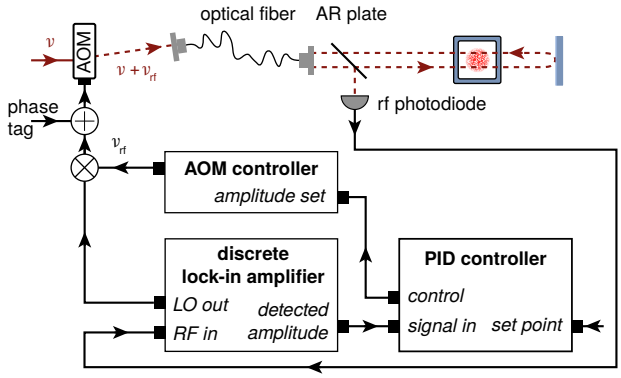

Figure 3.18: *Lattice beam intensity stabilization on the x axis.* Similar as for the interference phase stabilization, the rf signal fed to the intensity regulation AOM is tagged with different sidebands for the $\bar{\text{X}}$ and X beams. A photodiode records the intensity of the two tags on the laser table, of which the separate amplitudes are determined using two lock-in amplifiers built from discrete parts. The detected amplitude is then used as the signal input of the PID laser intensity controllers. Adapted from [Greif, 2013].

The combination of the lock-in amplifier and the PID controller limits the regulation bandwidth to about 1 kHz. Additionally, because the AOM diffraction efficiency does not scale linearly with the input rf power, the regulated light intensity will also not be linear in the set point voltage, particularly for high rf powers. Linearity can however be restored by a non-linear calibration of the computer analog output channel used to control the set point. The calibration of the lattice depth itself, i. e. the relation between the set point entered on the computer and actual depth of the lattice as felt by the atoms in energy units (E_R) is performed using Raman-Nath diffraction (see Section 3.2.3 on page 49) of a BEC on 1D lattices, as for example described in [Jördens, 2010].

3.2.5 SYMMETRY PHASE

The symmetry phase θ is the difference in phase picked up by the X and $\bar{\text{X}}$ lattice beams on the path starting from the atoms' position to the retro-reflecting mirror and back to the atoms. This phase difference originates from the frequency difference $\Delta_x = \nu_{\text{c},\bar{\text{X}}} - \nu_{\text{c,X}}$ between the two beams. It can be easily calculated from the distance between the atoms and the mirror $L \approx 20$ cm,

$$\theta = \frac{4\pi L}{c}\Delta_x, \tag{3.10}$$

where c is the speed of light in air. The detuning Δ_x was chosen such that the phase difference $\theta \approx \pi$, i. e. that the standing wave patterns of the independent $\bar{\text{X}}$ and X beams differ by about half a lattice period. By changing the carrier frequency $\nu_{\text{c},\bar{\text{X}}}$ of $\bar{\text{X}}$, this shift can be tuned without affecting the rest of the lattice potential. Changing the rf drive frequency of the AOM controlling the $\bar{\text{X}}$ light, however, requires a realignment of the fiber input coupling as the angle of diffraction in the AOM changes. Using the AOM in a double-pass configuration, in combination with an EOM to create the side band for intensity stabilization, could help to amend this situation.

Tuning the symmetry phase

Contrary to the interference phase, θ does not need to be actively stabilized. Fluctuations can only arise from thermal drifts in the mirror position or changes

in the refractive index of air caused by room temperature or pressure drifts. All of these effects, however, are found to cause relative changes of θ which are smaller than 10^{-4}. The same holds for the spatial variation of the phase over the cloud size due to the varying path length and the slightly different wave vectors.

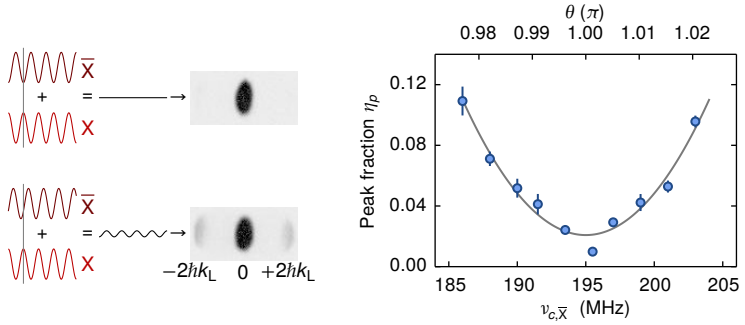

a. Principle b. Data and quadratic fit

Figure 3.19: *Symmetry phase calibration.* The longitudinal offset of the $\bar{\text{X}}$ and X standing waves can be obtained by recording the Raman-Nath diffraction pattern of the combined potential. When the two patterns are exactly shifted by half a period and have the same power, no diffraction should occur. This can be used to determine the frequency difference of the two beams necessary to obtain $\theta = \pi$. The fraction of atoms in the first diffraction peaks scales quadratically with the frequency deviation from the $\theta = \pi$ setting, $\eta_p \propto (\nu_{c,\bar{\text{X}}} - \nu^0_{c,\bar{\text{X}}})^2 + b$. We find $\nu^0_{c,\bar{\text{X}}} = 195.0(2)$ MHz as the setting corresponding to $\theta = \pi$. Schematics adapted from [Greif, 2013].

Figure 3.19a illustrates the method used to find the carrier frequency $\nu^0_{c,\bar{\text{X}}}$ where $\theta = \pi$. Raman-Nath diffraction (see Section 3.2.3 on page 49) using a BEC is performed on the combination of the $\bar{\text{X}}$ and X lattice, both at the same power and thus with the same lattice depth $V_{\bar{\text{X}}} = V_{\text{X}}$. The two beams are flashed onto the atoms for typically 20 µs and the resulting momentum distribution is recorded afterwards. When the two lattices are exactly out of phase by $\theta = \pi$, they cancel each other and no momentum is transferred into the $\pm 2\hbar k_{\text{L}}$ modes. For $\theta \neq \pi$ a net lattice results from the combination of the two beams and a fraction of atoms η_p is transferred into higher momenta. This fraction is expected to scale quadratically in the frequency offset $\nu_{c,\bar{\text{X}}} - \nu^0_{c,\bar{\text{X}}}$, as reproduced nicely in the experiment, see Fig. 3.19b. We find $\nu^0_{c,\bar{\text{X}}} = 195.0(2)$ MHz resulting in $\Delta^0_x = \nu^0_{c,\bar{\text{X}}} - \nu_{c,\text{X}} = 384.8(2)$ MHz.

3.3 MANIPULATION

3.3.1 TUNING THE LATTICE POTENTIAL

Decomposing the lattice potential into a square and checkerboard contribution

As outlined in Section 3.2 on page 44, the lattice potential can be tuned by the four lattice depths $V_{\bar{\text{X}},\text{X},\text{Y},\tilde{\text{Z}}}$ and the two relevant phases φ and θ, all of which can be accessed in the experiment. The influence of the separate parameters on the lattice potential is best understood when rewriting the potential (Eq. (3.6) on page 46) in a different form (along the lines presented in [Greif, 2013]),

$$V(x,y) = \underbrace{-\widehat{V_{\text{X}}}\cos^2(k_{\text{L}}x + \beta/2) - V_{\text{Y}}\cos^2(k_{\text{L}}y)}_{\text{square}} \underbrace{-2\sqrt{V_{\text{X}}V_{\text{Y}}}\cos(k_{\text{L}}x)\cos(k_{\text{L}}y)\cos\varphi}_{\text{checkerboard}} \tag{3.11}$$

with

$$\widehat{V_{\mathrm{X}}} = \pm\sqrt{V_{\bar{\mathrm{X}}}^2 + 2V_{\bar{\mathrm{X}}}V_{\mathrm{X}}\cos\theta + V_{\mathrm{X}}^2}\,, \quad \pm \text{ for } V_{\bar{\mathrm{X}}}\cos\theta + V_{\mathrm{X}} \gtrless 0 \tag{3.12}$$

$$\tan\beta = \frac{\sin\theta}{\cos\theta + V_{\mathrm{X}}/V_{\bar{\mathrm{X}}}}\,. \tag{3.13}$$

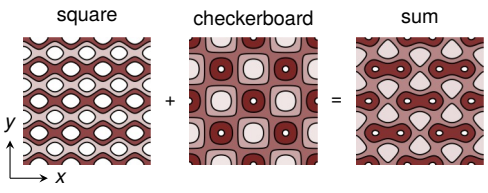

Figure 3.20: *Checkerboard and square contributions.* For a more intuitive understanding, the lattice potential can be split into two contributions, a square and checkerboard lattice. Parameters: $V_{\bar{\mathrm{X}},\mathrm{X},\mathrm{Y}} = [1.5, 0.1, 2]\,E_{\mathrm{R}}$, $\varphi = 0$, $\theta = \pi/2$.

The potential can therefore be viewed as the sum of a potential of square geometry, i. e. containing only terms that would result from lattice beams that do not interfere with each other, and one of checkerboard geometry that results from interference terms, has a larger spacing and is rotated by 45° with respect to the square potential, see Fig. 3.20. For this, we introduced the new lattice depth $\widehat{V_{\mathrm{X}}}$ and the *position phase* β. The origin of the checkerboard term can be understood from the trigonometric equality

$$\begin{aligned}-4\cos(k_{\mathrm{L}}x)\cos(k_{\mathrm{L}}y)\cos(\varphi) = {}& \cos\left(k_{\mathrm{L}}(x-y)-\varphi\right) + \cos\left(k_{\mathrm{L}}(x+y)-\varphi\right)\\ & + \cos\left(k_{\mathrm{L}}(x-y)+\varphi\right) + \cos\left(k_{\mathrm{L}}(x+y)+\varphi\right).\end{aligned} \tag{3.14}$$

The interference term can thus be seen as being created by two perpendicular interfering laser beams propagating along the $x+y$ and $x-y$ direction, respectively.

Diagram of lattice geometries

By varying the lattice depths $V_{\bar{\mathrm{X}}}$ and V_{X} (or alternatively V_{Y}) the contribution of the square term with respect to that of the checkerboard term can changed, see Fig. 3.21 on the following page. In the figure, we plot – for illustration purposes – the lattice potential with a spatial dependence on $V_{\bar{\mathrm{X}}}$ and V_{X}, using $\varphi = 0$ and $\theta = 0$. When starting from $V_{\mathrm{X}} \neq 0$ and $V_{\bar{\mathrm{X}}} = 0$, the potential evolves from pure checkerboard geometry (with a lattice spacing $\sqrt{2}\lambda/2 = 752\,\mathrm{nm}$) through triangular, dimerized, honeycomb to 1D chains. Pictorially, this is because of the increasing square contribution which starts to split every well of the checkerboard lattice into two wells along the x axis. When $V_{\mathrm{X}} = 0$, the lattice has a pure square geometry with lattice spacing $\lambda/2 = 532\,\mathrm{nm}$.

The transition line between the triangular and dimerized geometry is defined by the appearance of two potential minima within the unit cell. It can be calculated by finding the lattice parameters at which the saddle point between the two sites A and B becomes a minimum,

$$\frac{\partial^2 V(x,0)}{\partial x^2} = 0\,. \tag{3.15}$$

Using this condition, the location of the transition line is found to be

$$\begin{aligned}V_{\mathrm{X}} = {}& \frac{1}{2}\alpha^2\cos^2(\varphi)V_{\mathrm{Y}} - V_{\bar{\mathrm{X}}}\cos\theta\\ & - \sqrt{\alpha^2\cos^2\varphi V_{\mathrm{Y}}\left(\frac{1}{4}\alpha^2\cos^2\varphi V_{\mathrm{Y}} - V_{\bar{\mathrm{X}}}\cos\theta\right)}.\end{aligned} \tag{3.16}$$

Location of the triangular – dimer transition line

The separation line between a dimerized and the honeycomb structure is based

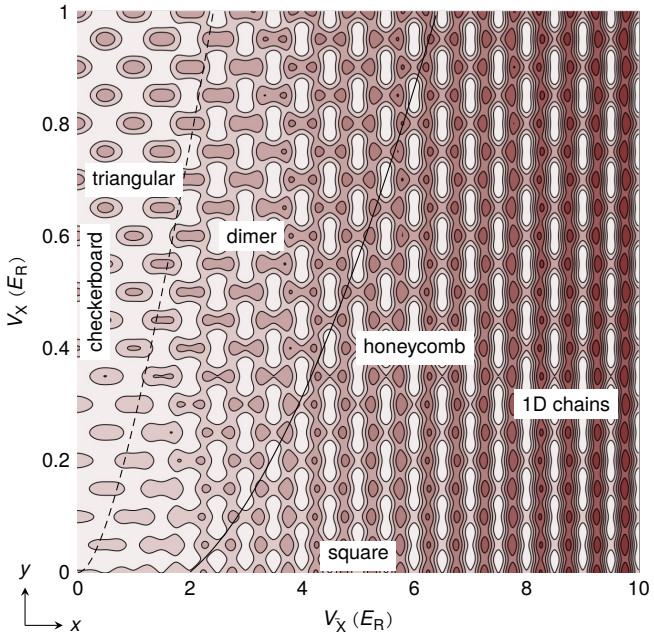

Figure 3.21: *Lattice geometries.* Diagram of the lattice geometries in the $x - y$ plane as a function of the lattice depths $V_{\bar{X}}$ and V_X. Depending on theses lattice depths, checkerboard ($V_{\bar{X}} = 0$), triangular, dimer, honeycomb, 1D chains or square geometries ($V_X = 0$) can be obtained. The dashed and solid line indicate the transition between triangular and dimer, and between dimer and honeycomb geometry, respectively. For illustration purposes, a contour plot of the lattice potential with the local lattice parameters set according to the position in the diagram is overlapped. $V_Y = 2\,E_R$ and $\alpha = 1$.

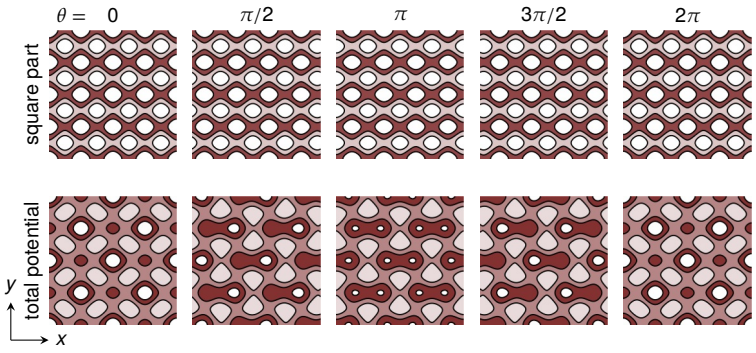

Figure 3.22: *Lattice potential for different θ.* The square part as well as the total potential are shown for different symmetry phases θ, using $V_{\bar{X},X,Y} = [1.5, 0.1, 2]\,E_R$. Symmetry phases $\theta \neq \pi$ lead to an imbalance between the left and right sites of the dimers. To obtain the total potential, the square part is summed with the checkerboard part of the potential with the same parameters and $\varphi = 0$.

on the existence of Dirac points in the band structure of the honeycomb lattice. It can only be numerically extracted based on a diagonalization of the Hamiltonian.

Keeping the lattice depths constant but changing φ and thus β leads to a shift of the square lattice with respect to the checkerboard structure along the x axis, see Fig. 3.22 on page 56. For $\theta = 0$ or 2π, the total potential, as the sum of the varying square part with the fixed checkerboard potential, is symmetric within the unit cell. In between, however, the offset between the two parts induces an asymmetry between the left and the right well of the dimers.

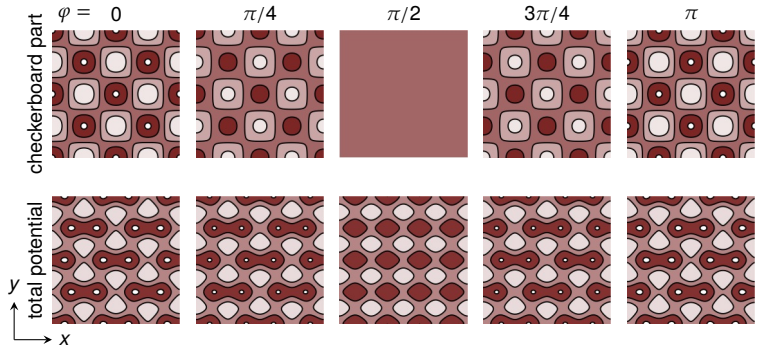

Figure 3.23: *Lattice potential for different φ.* The checkerboard part as well as the total potential are shown for different interference phases φ, for $V_{\bar{X},X,Y} = [1.5, 0.1, 2]\,E_R$. Scanning φ from zero to π switches the position of the dimerization to the next adjacent lattice site. To obtain the total potential, the checkerboard part is summed with the square part of the potential with the same parameters and $\theta = \pi$.

Scanning φ from 0 to π, while keeping the other parameters constant, changes the position at which the dimerization in the lattice takes place, see Fig. 3.23. At $\varphi = \pi/2$, the checkerboard term vanishes completely since $\cos(\pi/2) = 0$ and only a square structure remains.

The band structure of the different lattice geometries will be discussed in Section 4.1 on page 72.

TRAP FREQUENCIES

When determining the trap parameters of the harmonic confinement induced by the gaussian envelope of the lattice beams, the interference between the laser beams has to be taken into account. In the experiment, the trap frequencies in the two transversal directions of every lattice beam are measured independently with the same method as used for the FORT, see Section 3.1.4 on page 41. From this, the trap frequency contribution slopes given in Table 3.7 can be calculated.

Table 3.7: *Lattice beam trap frequency contributions.* Every lattice beam contributes to the total harmonic trap frequency along its two radial directions. These contributions are summed up according to Eq. (3.17) on the next page, which in particular takes into account the interference of the X and Y beams. The contributions per recoil energy, which are obtained from the frequency of radial dipole oscillations in the single beams, are listed in this table.

BEAM AXIS	SLOPE $\perp_1$ $(1/s^2 E_R)$	SLOPE $\perp_2$ $(1/s^2 E_R)$
x	$c_y^x = 4\pi^2 \times 30.6$	$c_z^x = 4\pi^2 \times 44.9$
y	$c_x^y = 4\pi^2 \times 100.3$	$c_z^y = 4\pi^2 \times 87.9$
z	$c_x^z = 4\pi^2 \times 89.7$	$c_y^z = 4\pi^2 \times 101.6$

Using the lattice potential and including the spatial intensity profiles of the lattice beams, the following expressions for the trap frequencies along the three spatial axes are obtained by Taylor expansion in the potential minima [Greif, 2013]:

$$\begin{aligned}
\omega_x^2 &= \left(1+\alpha^2\frac{V_\mathrm{X}}{V_{\bar{\mathrm{X}}}-V_\mathrm{X}}\right)c_x^y V_\mathrm{Y} + c_x^z V_{\bar{\mathrm{Z}}} \\
\omega_y^2 &= \left(1-\alpha^2\frac{V_\mathrm{X}V_{\bar{\mathrm{X}}}}{(V_{\bar{\mathrm{X}}}-V_\mathrm{X})^2}\right)c_y^x V_{\bar{\mathrm{X}}} + \alpha^2\frac{V_\mathrm{Y}}{V_{\bar{\mathrm{X}}}-V_\mathrm{X}}\left(1+\frac{V_\mathrm{X}}{V_{\bar{\mathrm{X}}}-V_\mathrm{X}}\right)c_y^x V_\mathrm{X} \\
&\quad + c_y^z V_{\bar{\mathrm{Z}}} \\
\omega_z^2 &= \left(1-\alpha^2\frac{V_\mathrm{X}V_\mathrm{Y}}{(V_{\bar{\mathrm{X}}}-V_\mathrm{X})^2}\right)c_z^x V_{\bar{\mathrm{X}}} + \alpha^2\frac{V_\mathrm{Y}}{V_{\bar{\mathrm{X}}}-V_\mathrm{X}}\left(1+\frac{V_\mathrm{X}}{V_{\bar{\mathrm{X}}}-V_\mathrm{X}}\right)c_z^x V_\mathrm{X} \\
&\quad + \left(1+\alpha^2\frac{V_\mathrm{X}}{V_{\bar{\mathrm{X}}}-V_\mathrm{X}}\right)c_z^y V_\mathrm{Y}\,.
\end{aligned} \tag{3.17}$$

Here, α is the visibility of the interference between X and Y. These expressions do not include the changing zero-point energy of the ground state harmonic oscillator state from the spatially varying on-site oscillator frequency. This contribution is, however, found to be at most a few percent as determined from an exact calculation of the trap frequencies.

3.3.2 LATTICE MODULATION

Apart from slow changes of the lattice geometry, a fast modulation (on the order of kHz) of the lattice beam intensity can also be a viable tool to learn more about the state of the system prepared at a certain lattice geometry and interaction [Stöferle *et al.*, 2004], see Section 8.4 on page 155.

We can modulate the set point for the intensity stabilization of one or several lattice beams using the computer controlled analog output channels. Modulation frequencies up to roughly 10 kHz can be achieved, limited by the regulation electronics. For faster modulation frequencies, the modulation can also be performed using separate frequency generators that feed directly onto the AOM rf drive signal.

3.3.3 CONTROLLING THE CONFINEMENT

In our setup, the harmonic confinement induced by the FORT and the optical lattice can be counteracted by means of two blue-detuned deconfinement beams installed on the x and z optical axes, see the schematics of the overall optical setup in Section 3.2.2 on page 46.

OPTICAL SETUP OF THE DECONFINEMENT BEAMS

Light from a dedicated *Coherent Verdi V18* with an output power of 18.5 W at a wavelength of $\lambda_\mathrm{d} = 532\,\mathrm{nm}$ is used to generate the two deconfinement beams. Combined, these two beams allow for the control of the harmonic confinement along all three spatial axes. As an alternative, we have tested a deconfinement beam propagating along the y axis, but were unable to achieve a sufficiently homogeneous intensity profile on the atomic cloud, owing to spurious reflections on the glass cell. The x and z directions, however, where found to not show these problems. In general, optical elements fabricated from the most common materials tend to be more absorptive at a wavelength of 532 nm than at 1064 nm. Especially optical fibers or AOMs are therefore more prone to thermal lensing at high powers, requiring special precautions or models fabricated from custom materials. For

Optical elements

instance, we chose to install the *Verdi* laser on the optical table on which the vacuum chamber is installed, allowing for shorter fiber lengths or optionally even free-space guiding of the laser beams to the location of the atom cloud. Moreover, only lenses and mirrors made of fused silica are used in the setup.

Beam preparation

The laser output is split into two beams by a combination of a half-wave plate and a polarization-sensitive splitter. Instead of a normal polarizing beam splitting cube, we use thin film polarizers on fused silica substrates, produced by *Precision Photonics, Inc.*. They are aligned at the Brewster angle for minimal spurious reflections. The two beams are then independently intensity stabilized by fused silica AOMs (*ASM-802B47* by *IntraAction*) operating at a modulation frequency of 80 MHz. The error signal is generated by monitoring the output power after the optical fiber. We then couple the beams into single-mode polarization maintaining photonic crystal fibers (*LMA-PM-10* by *NKT Photonics*, MFD of 8.4 µm) terminated with high-power air gapped adjustable FC connectors (by *OzOptics*, 8° angle cleaved). At 3 m, their length is kept minimal in order to avoid unnecessary losses while still providing the required mode-cleaning. Using these fibers, we achieve a maximum power of 3 W at the fiber output, with a coupling efficiency of up to 70%. At higher input powers, excessive Brillouin scattering sets in, which can cause damage to the input facet owing to the dissipated heat. We have, however, later performed tests with a photonic crystal fiber with a larger MFD (*LMA-PM-15*, MFD of 12.2 µm, angle cleaved at 5°, length 5 m). Owing to the larger MFD and the *SMA-905 High Power* connectors, we achieved stable output powers of more than 7 W for this fiber, with a coupling efficiency of 75%. For short times (< 30 s), the fiber was able to maintain output powers of up to 13 W at comparable coupling efficiencies.

On the output coupling side of the fibers, spurious polarization components are cleaned using thin-film polarizers. A small amount of the light is split off for the intensity regulation. The waist of the beams is adjusted using a telescope before they are focused down and combined with the optical lattice and FORT beams. To allow for a fully anti-confining potential, the waist of the beams at the location of the atomic cloud is set to $w = 180\,\mu\text{m}$, larger or comparable to that of the FORT and the optical lattice. However, the tests presented in the following were performed with two different beam waists. Were necessary, the stated powers have been rescaled by a factor of 2 to the equivalent power for a beam waist of $w = 180\,\mu\text{m}$.

TRAP FREQUENCY REDUCTION

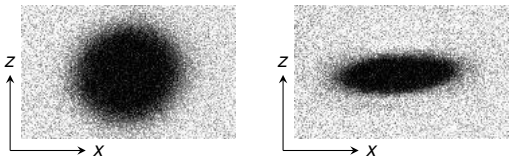

a. $P_d = 0$ W. b. $P_d = 1.8$ W.

Figure 3.24: *In-trap absorption images.* Images of ^{87}Rb BEC taken along the y axis without (a) and with a deconfinement beam along the z axis (b) are shown. The power of the two FORT beams is set to $P_{\text{FORT}} = 43\,\text{mW}$.

In order to observe the effect of the deconfinement beams, we prepare a ^{87}Rb BEC in the FORT and then increase the power in either of the two deconfinement beams up to a value P_d within 200 ms. Using a high-resolution CCD camera (*Point-Grey Flea 2G 13S2M-C*), we take absorption images of the atomic cloud in the trap (*in situ*) along the y axis. In Fig. 3.24, the measured *in situ* cloud profiles are shown for a situation without deconfinement beam (left) and with a power of 1.8 W in the z beam (right). The resulting extension of the cloud profile along the x direction is clearly visible.

Change of aspect ratio

In Fig. 3.25, we systematically investigate the aspect ratio and the atom number of the atomic cloud for varying final z deconfinement beam powers. Aspect ratios of up to 3 can be achieved without significant atom loss.

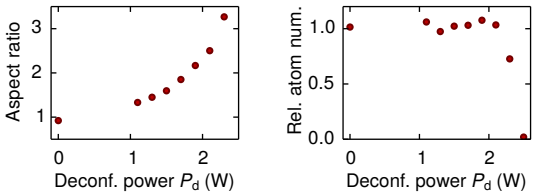

a. Aspect ratio b. Atom number

Figure 3.25: *Aspect ratio and atom number.* The *in situ* cloud profile in the $x-z$ plane is investigated for varying z deconfinement beam powers P_d.

To characterize the harmonicity of the resulting potential, we induce dipole oscillations of the BEC in the trap by abruptly switching on and off a magnetic field gradient via a short current pulse in the Ioffe coil. The frequency of the resulting dipole oscillations of the atomic cloud is measured by recording the x position of the cloud after TOF. As can be seen in Fig. 3.26, the trapping frequencies can be reduced by almost a factor of 4, from 25.2(2) to 6.8(4) Hz for a FORT power of 43 mW. Similar results are obtained for the x deconfinement beam.

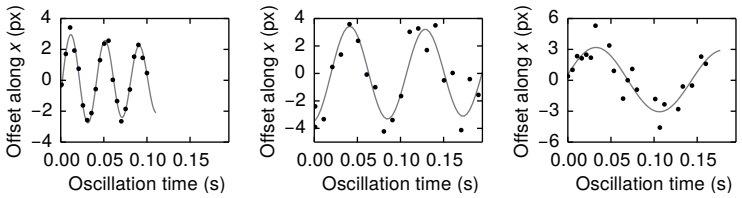

a. $P_d = 0$ W. $\omega_x/2\pi = 25.2(2)$ Hz.
b. $P_d = 1.6$ W. $\omega_x/2\pi = 11.4(2)$ Hz.
c. $P_d = 1.8$ W. $\omega_x/2\pi = 6.8(4)$ Hz.

Figure 3.26: *Reduction of the harmonic confinement.* The harmonic trapping frequencies ω along x are obtained from dipole oscillations of the atomic cloud. The measurement is performed using the z deconfinement beam with a FORT power $P_{FORT} = 43$ mW.

EVAPORATIVE COOLING

Homogeneous system

The deconfinement beams can be used to alter the harmonic confinement and thus for example to reduce the site energy offset in the optical lattice, giving rise to a more homogeneous system, which is closer to its solid state counterpart. Apart from that, the deconfinement beams could also be useful for evaporative cooling of the cloud. To test this, we stop the microwave evaporation in the QUIC trap at a point where the atomic cloud is still fully thermal. We then transfer into the FORT (with a power $P_{FORT} = 55$ mW) and then smoothly increase the power of the z deconfinement beam using an exponential ramp ($\propto 1 - \exp(-t/\tau)$) with a duration of 2.5 s and $\tau = 1$ s. The deconfinement beam therefore slowly lowers the trap depth, allowing for evaporative cooling to take place. Finally, we switch off the traps and perform TOF in order to determine the BEC condensate fraction. As can be seen in Fig. 3.27 on the next page, we have been able to produce BECs with condensate fractions of close to 50% using this cooling technique (even higher fractions can be achieved by optimizing the ramp shape).

Cooling in the lattice

We have also investigated the feasibility of performing evaporative cooling after loading into the lattice. For this, we also stop the microwave evaporation in a thermal state and load into the FORT with $P_{FORT} = 55$ mW. We then load the atoms into a lattice with $V_{Y,\tilde{Z}} = 4.5\,E_R$ within 200 ms. This results into an array of

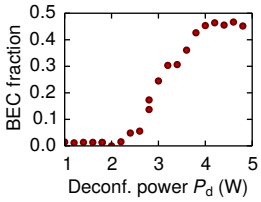

Figure 3.27: *Evaporative cooling in the FORT.* Starting from a thermal cloud loaded into the FORT with $P_{\mathrm{FORT}} = 55\,\mathrm{mW}$, the power P_d of the z deconfinement beam is slowly increased to evaporatively cool the atoms in order to obtain a BEC.

1D tubes. We now abruptly switch off the optical lattice and the trap in order to allow for 25 ms of TOF. A mostly gaussian shaped momentum distribution in the $y-z$ plane is recorded, owing to the negligible phase coherence in the thermal cloud.

Cooling perpendicular to the periodic lattice structure

Applying a similar exponential ramp of the z deconfinement beam as used above after loading into the lattice, we expect evaporative cooling to take place along the axial direction of the 1D tubes. We ramp to a final power of $P_d = 3.3\,\mathrm{W}$ and then once again record the momentum distribution after a sudden release. The momentum distribution is now characterized by a central peak with the parabolic momentum distribution of a BEC and additional well-resolved momentum components at $(\pm 2\hbar k_L, \pm 2\hbar k_L)$ as a result of the acquired phase coherence beyond the transition to a BEC.

Cooling along the lattice direction

This scheme however ceases to work when trying to evaporate along the direction of a lattice beam. For example, we loaded the atomic cloud into a 2D pancake-like arrangement created using a lattice with $V_{\tilde{X}} = 4.5\,E_R$, $V_{X,Y,\tilde{Z}} = 0\,E_R$. When performing the same ramp with the z deconfinement beam described above, no increase in the BEC fraction can be measured. Additionally, the atom number is found to be constant, indicating that the atoms fail to escape from the lattice, most likely due to the comparably slow tunneling times between the 2D layers, which are on the order of a few 100 Hz. This is confirmed when imaging the *in situ* trap profiles, see Fig. 3.28. We find that density distribution becomes increasingly bi-modal for larger P_d. However, no atoms escape at the edges. Overall, we tentatively conclude that the deconfinement beams could indeed be used to perform evaporative cooling in the lattice in order to counteract the heating occurring during the loading process (see also Section 8.5 on page 156), provided that at least along one spatial axis no lattice is present. A possible scheme to create a low-temperature state in a 3D lattice could therefore consist of first loading into the lattice generated by two of the lattice beams, then performing evaporative cooling, and finally ramping up the power of the third lattice beam.

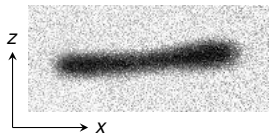

Figure 3.28: *Evaporative cooling in a lattice.* The atoms are prepared in a pancake-like lattice arrangement with $V_{\tilde{X}} = 4.5\,E_R$ and $P_{\mathrm{FORT}} = 43\,\mathrm{mW}$. When slowly increasing the z deconfinement beam power to $P_d = 2.9\,\mathrm{W}$, a bi-modal *in situ* density distribution (as obtained by absorption imaging), but no reduction in atom number is found, indicating that evaporative cooling along a lattice axis does not work.

3.3.4 MAGNETIC FIELDS

An accurate control of the spatial magnetic field distribution within the atomic cloud is essential for our experiments. To achieve this, a combination of both special-purpose magnetic coils (the Feshbach and the gradient coil) as well as coils which are also used for other purposes in the experiment (quadrupole, Ioffe and transport coils) mounted close to the glass cell are used, see Fig. 3.29 on the following page. The DC power supplies and MOSFET switches of these coils are

wired such that the coils can be driven both independently and combined in anti- or Helmholtz configuration and partly even in both current directions.

As their name indicates, the transport coils, quadrupole coils and the Ioffe coil are used in the preparation of the atomic cloud for the magnetic transport and the QUIC trap, respectively. For the actual experiment, they are then also used for other tasks. The main purposes of the coils relevant for the actual experiments are listed below:

Feshbach coils Generation of a homogeneous offset field up to about 250 G to access Feshbach resonances. For technical reasons, the atoms are not fully centered with respect to the two coils along the x axis. Therefore some residual magnetic field gradients are present, which must be compensated by other coils.

Gradient coil Gradient compensation (mainly) along the x axis. Gradients for Bloch oscillations in the optical lattice.

Lower quadrupole coil in normal current direction This coil is used for gradient compensation (mainly) along the y axis. It is also used to produce gradients for levitation of ^{87}Rb in $|F = 2, m_F > 0\rangle$.

Upper quadrupole coil in reverse current direction Large gradients for Stern-Gerlach spin separation along the y axis as for example used in double occupancy measurements. Gradients for levitation of ^{40}K in $|F = 9/2, m_F < 0\rangle$ and for Bloch oscillations in the optical lattice. Could be potentially used in combination with the lower quadrupole coil in normal direction to generate an offset field along the y axis.

Last transport coil pair Gradient compensation mainly along the z axis.

Ioffe coil Large gradients for Stern-Gerlach spin separation along the x axis.

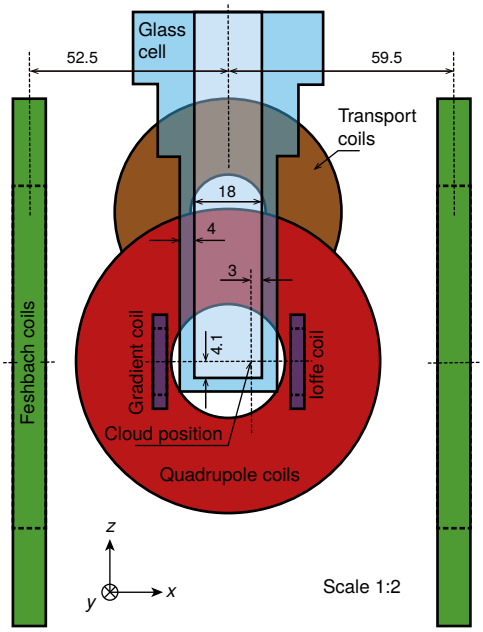

Figure 3.29: *Drawing of the magnetic coil positions.* The relevant coils for producing homogeneous magnetic fields as well as gradients at the position of the atomic cloud are shown. The upper gradient and transport coils, which are positioned symmetrically to their lower counterparts with respect to the glass cell center, are not visible in the drawing. Gravity points along y.

For an accurate compensation of residual gradients within the magnetic field of the Feshbach coils, we have recorded the *in situ* displacement of the atomic cloud as a result of gradients induced by different currents in the gradient, lower quadrupole and the transport coil pair, in order to determine the covariance matrix of the magnetic field gradient components with the coil currents. Using this matrix, the optimal currents for a net zero field gradient can be found.

3.4 DETECTION

Absorption imaging

From the detection techniques outlined in Section 2.4 on page 30 actually only absorption imaging is used regularly in our experiment. We are able to image the atomic cloud independently along all three spatial axes. For this, imaging beams with a $1/e^2$ diameter of about 1 mm and powers of a few 10 µW are shone onto the atoms, with the plane of the atoms being imaged onto CCD cameras using Keplerian telescopes (i. e. consisting of two convex achromatic lenses) with magnifications of roughly 4, see Table 3.8 on the following page. We use imaging light pulses with a duration of 40 µs created by an AOM. With these parameters, every atom scatters on the order of 100 photons during the imaging process.

Low- and high-field absorption imaging

We differentiate between low- and high-field absorption imaging. The term *low-field* refers here to the regime where the degeneracy of the m_F states is not lifted. When addressing the electronic $|F = 9/2\rangle$ to $|F' = 11/2\rangle$ transition of the D_2 line on resonance, all Zeeman states are imaged in a single shot. At low field the polarization of the laser light as seen by the light can be assumed to be isotropic and the scattering cross-section is then $\sigma_0^{\text{isotropic}} = 1.123 \times 10^{-13}\,\text{m}^2$. In the high-field regime, however, the m_F states can be independently imaged by using the respective laser detuning to drive the imaging transition. The polarization-dependent cross-sections are $\sigma_0^{\pi} = 1.871 \times 10^{-13}\,\text{m}^2$ and $\sigma_0^{\sigma+} = 2.807 \times 10^{-13}\,\text{m}^2$, respectively.

The imaging procedure then goes as follows:

1. Traps and magnetic fields are switched off if required.
2. The image acquisition of the CCD camera is triggered (image $\mathscr{I}_{\text{atoms}}(\mathbf{x})$).
3. The imaging light is switched on for a duration of 40 µs and the light which is not absorbed by the atoms is recorded on the CCD camera in the line of sight of the beam.
4. Image acquisition is stopped and the image is read out.
5. The sequence is paused for a few milliseconds until the atoms have disappeared from the field of view. To speed up this process, they can be accelerated with resonant light or magnetic fields.
6. An image of just the imaging beam is acquired on the camera in the same conditions as above, but without atoms in the field of view (image $\mathscr{I}_{\text{bright}}(\mathbf{x})$).
7. For background correction, an image without imaging light is taken ($\mathscr{I}_{\text{dark}}(\mathbf{x})$).

The fractional transmission of the probe beam per pixel is then

$$\mathscr{T}(\mathbf{x}) = \frac{\mathscr{I}_{\text{atoms}}(\mathbf{x}) - \mathscr{I}_{\text{dark}}(\mathbf{x})}{\mathscr{I}_{\text{bright}}(\mathbf{x}) - \mathscr{I}_{\text{dark}}(\mathbf{x})}\,. \tag{3.18}$$

Column-integrated optical density

In the approximation that the imaging transition is far from saturated and that no re-scattering events take place, the column integrated density of the atomic cloud can then calculated to be $n(\mathbf{x}) = -\ln \mathscr{T}(\mathbf{x})/\sigma_0$.

Fluctuations and interference effects

The quality of the obtained density distribution depends crucially on the fact that $\mathscr{I}_{\text{atoms}}(\mathbf{x})$ and $\mathscr{I}_{\text{bright}}(\mathbf{x})$ only differ in the former seeing the "shadow" cast by the atoms and the latter not. Temporal intensity or frequency fluctuations in the imaging beam, often in combination with interference effects within the optical elements in the imaging path, deteriorate the quality of the obtained data. As image quality and repeatability is a crucial basis for any experiment, and especially for low signal-to-noise applications such as noise correlations (see Chapter 10), every possible measure has to be taken to reduce imaging artifacts. One important source of interference effects is the CCD chip of the camera itself, which – when

Table 3.8: *Imaging setup parameters.* Although the two *Andor* cameras feature electron multiplying charge coupled device (EMCCD) readout, the conventional readout circuitry is used as it offers lower noise for the high photon counts available in the system. For comparison, a camera manufactured by *PointGrey*, which we use for diagnostic and supplemental imaging applications, is shown.

	X	Y	Z	SUPPLEMENTAL
magnification M	3.84	3.92	3.8	–
camera model	*Andor iXon+ 887*	*Apogee AP1E*	*Andor iXon Ultra*	*Flea 2G 13S2M-C*
chip	*e2v CCD97*	*Kodak KAF_0401E*	*e2v CCD97*	*Sony ICX445 CCD, 1/3"*
chip type	frame transfer	full frame	frame transfer	interline transfer
pixel size	16 µm	9 µm	16 µm	3.75 µm
resolution (pixel)	512 × 512	768 × 512	512 × 512	1288 × 964
window	0.5° wedged, NIR AR	removed	0.5° wedged, NIR AR	AR
illumination	back[1]	front	back	front
quantum efficiency at 767 nm	77%	40%	83%	27%
full well depth ($\times 10^3$)	220	122	160	20
horizontal shift speed (MHz)	1	n/a	1	n/a
vertical shift speed (µs)	3.4	n/a	3.3	n/a
ADC resolution (bit)	16	14	16	12
electronic gain setting	2.5	n/a	3.0	1.0
resulting e^-/ADU	≈ 1.53	7.3	1.41	n/a
readout noise (e^-)	7	11.7	5.33	12 – 20

1 This camera features as special AR coating and roughened sensor backside to suppress etaloning effects otherwise present in back-illuminated CCD cameras.

back-illuminated as is the case in our *Andor* cameras – acts as an etalon. This effect has been mitigated in the *Andor iXon Ultra* by an optimized AR coating and a slightly roughened sensor back surface, see Fig. 3.30.

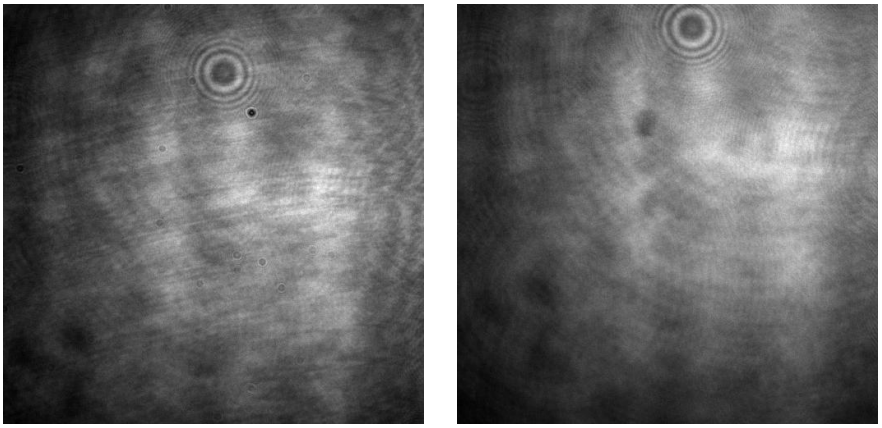

a. *Andor iXon+ 887* b. *Andor iXon Ultra*

Figure 3.30: *Etaloning on back-illuminated CCD cameras.* Brush-stroke like etaloning fringes are visible in a. On an optimized back-illuminated CCD chip (b) these features are not visible. Interference features caused by other optical elements, however, are still present.

Interference effects can also be further suppressed by taking the two images $\mathscr{I}_{\text{atoms}}(\mathbf{x})$ and $\mathscr{I}_{\text{bright}}(\mathbf{x})$ temporarily as close as possible together to minimize the effects of slow drifts in frequency or intensity of the imaging laser. At a horizontal shift speed of 1 MHz readout of the 512 × 512 pixel resolution chip takes about 250 ms, leading to a lower bound for the distance of the two images on full frame cameras. Frame transfer cameras, however, offer a so called *fast kinetics* mode, where one image can be buffered in a light-shielded part of the sensor while a second image is taken, see Fig. 3.31. After taking the first image, it is quickly (i. e. within vertical resolution × vertical shift time) shifted to the shielded area of the sensor, before acquisition of the second image can start. The two images can afterwards be readout in a non time-critical part of the experimental sequence. The timing of a *fast kinetics* imaging sequence is detailed in Fig. 3.32 on the next page.

Figure 3.31: *Fast kinetics mode.* The *fast kinetics* mode of the *Andor iXon* cameras makes use of the shielded frame transfer area on the CCD chip, which has the same area as the actual imaging area. This allows for taking two images within as little as a few ms. After the first image has been acquired ① it is vertically shifted to the shielded area ②. Then the second image is taken ③ and readout at the bottom of the chip starts ④.

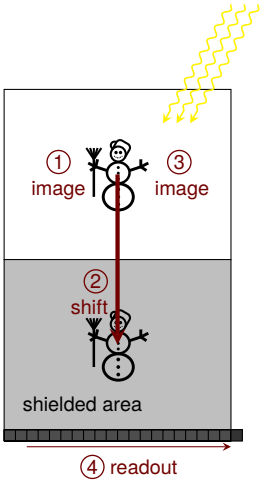

Determination of the atom number and temperature

A very typical measurement using the TOF method is the determination of the atom number and temperature of the degenerate Fermi gas by fitting the obtained

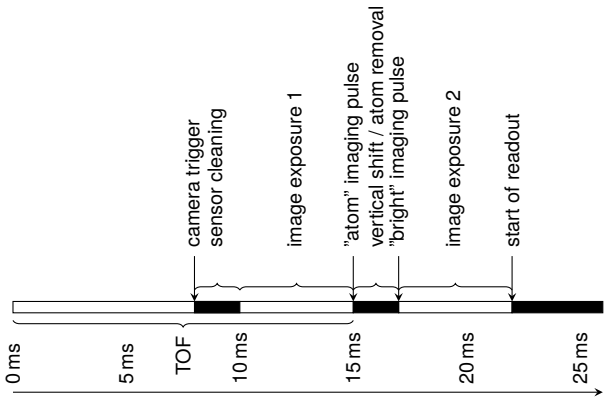

Figure 3.32: *Typical fast kinetics mode sequence timing.* The goal of using the *fast kinetics* mode of the camera is to be able to immediately shift the first image after having recorded the *atom* imaging pulse. Therefore, the camera must already be triggered before the desired TOF time is reached. The camera then first cleans the sensor, which requires about 2 ms. Then the image is exposed during typically 5 ms, with the actual imaging pulse being fired just before exposure ends. The image is then shifted down within 2 ms. This time can be used to remove the atom from the field of view by for example applying a strong magnetic field gradient using the gradient coil. Then the exposure of the second image starts, immediately followed by the *bright* imaging pulse. After the exposure of the second image is done, the readout of the whole sensor area starts at the bottom of the chip, sequentially reading out both images.

momentum distribution after TOF with the theoretically expected momentum distribution. This method of determining the temperature from the momentum distribution assumes a non-interacting Fermi gas, which can only be achieved for the $(^{-9}/_2, ^{-7}/_2)$ spin mixture (by tuning the scattering length to zero). When scanning the scattering length in the range from 0 to 130 a_0 the fitted temperature was found to increase by less than $0.03 T_\mathrm{F}$ [Strohmaier, 2010]. An alternative method to determine the temperature is a measurement of the adiabatic molecule formation efficiency when sweeping across the Feshbach resonance [Hodby *et al.*, 2005; Strohmaier, 2010].

Fitted density profiles

We typically use two different types of fits to the momentum distribution of Fermi gases [DeMarco, 2001; Ketterle *et al.*, 2008]:

$$\begin{aligned} n_\mathrm{mix}(p_x, p_y) &= o + m_x p_x + m_y p_y \\ &\quad + \begin{cases} n_0 \left(1 - 4r^2/L\right)^2 & \text{if } 1 - 4r^2/L \leq L \\ n_0 L^2 \exp\left(\frac{2}{L} - 2\right) \exp\left(-r^2/2\right) & \text{otherwise} \end{cases} \end{aligned} \tag{3.19}$$

$$\begin{aligned} n_\mathrm{Fermi}(p_x, p_y) &= o + m_x p_x + m_y p_y \\ &\quad + n_0 \frac{\mathrm{Li}_2\left(-\zeta \exp\left(-r^2/2\right)\right)}{\mathrm{Li}_2(-\zeta)}, \end{aligned} \tag{3.20}$$

where

$$\mathrm{Li}_2(x) = -\Re \int_0^x \mathrm{d}s \, \log(1-s)/s \tag{3.21}$$

is the dilogarithm. Note that in general the polylogarithm is related to the complete Fermi-Dirac integral by $\mathrm{F}_s(a) = -\mathrm{Li}_{s+1}(-e^a)$. The momentum profile has a central density n_0, radii $R_{x,y}$, a fugacity $\zeta = \exp(\beta\mu)$ (where $\beta = (k_\mathrm{B} T)^{-1}$, and μ is the chemical potential), atom number N, overall offset o and residual linear slopes $m_{x,y}$. The radius of the cloud is defined as $r = \sqrt{p_x^2/R_x^2 + p_y^2/R_y^2}$.

The *mixture* fit $n_{\mathrm{mix}}(p_x, p_y)$ patches a quartic (the $T = 0$ result for the momentum distribution) with a gaussian (the result in the classical limit) at a certain cloud radius and therefore does not rely on Fermi-Dirac statistics. From the fit parameters, the quantities of interest can then be deduced:

$$T_{\mathrm{gauss}} = \frac{m}{k_{\mathrm{B}}} \frac{(\omega R)^2}{1 + (t\omega)^2}\,, \tag{3.22}$$

$$E_{\mathrm{F}} = k_{\mathrm{B}} T_{\mathrm{F}} = \hbar \bar{\omega}_{x,y,z} (6N)^{1/3}\,. \tag{3.23}$$

Here, $\omega_{x,y,z}$ is the relevant spatial trap frequency, $\bar{\omega} = (\omega_x \omega_y \omega_z)^{1/3}$ the geometric mean trap frequency, m is the mass of ^{40}K and t is the TOF time. The atom number N is obtained via integration over the density distribution assuming a gaussian cloud shape. Combining these two:

Obtaining the degeneracy

$$\left(\frac{T}{T_{\mathrm{F}}}\right)_{\mathrm{gauss}} = \frac{T_{\mathrm{gauss}}}{T_{\mathrm{F}}}\,. \tag{3.24}$$

Alternatively, for the *fugacity* fit, T/T_{F} can be directly determined from the fugacity:

$$\left(\frac{T}{T_{\mathrm{F}}}\right)_{\mathrm{fugacity}} = \left(-6\,\mathrm{Li}_3(-\zeta)\right)^{-1/3}\,. \tag{3.25}$$

Here, $\mathrm{Li}_3(x)$ is the trilogarithmic function. Figure 3.33 shows a typical TOF image of a $(-9/2, -7/2)$ ^{40}K spin mixture.

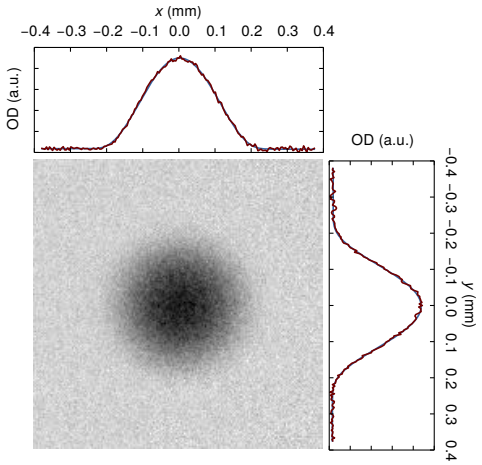

Figure 3.33: *Imaged momentum distribution of a degenerate Fermi gas.* The image shows the optical density calculated from an absorption image of a $(-9/2, -7/2)$ spin mixture after 25 ms TOF. From a Fermi fit to the density profile we obtain $N = 185 \times 10^3$ and $T/T_{\mathrm{F}} = 8.5\%$. The plots are line sums along the respective axis of the measured density distribution (red) and the fit function (blue).

The chemical potential can be obtained by numerically solving Eq. (3.25) for the fugacity ζ. The entropy of the gas can then be calculated from the expression for the entropy per particle in an ideal trapped Fermi gas ($\zeta = \exp(\beta\mu)$):

Entropy per particle

$$s = \frac{S}{N} = -\beta\mu + 4\frac{\mathrm{Li}_4\left(-e^{\beta\mu}\right)}{\mathrm{Li}_3\left(-e^{\beta\mu}\right)}\,. \tag{3.26}$$

Up to about $T/T_{\mathrm{F}} \approx 0.1$, s is found to agree within a few percent with the linear term in the Sommerfeld expansion of Eq. (3.26),

$$s = \pi^2 \frac{T}{T_{\mathrm{F}}}\,. \tag{3.27}$$

More advanced characterization techniques combine standard absorption imaging techniques for example with lattice intensity ramps for a measurement

of the quasimomentum distribution. By additionally employing rf pulses and gradients, measurements of the double occupancy or of spin correlations in the system can be performed. Details on these techniques can be found in the chapters where the respective experiments are explained. See Section 5.2.4 on page 106, Section 8.1.2 on page 149 or Section 9.3 on page 166, respectively.

Part I

PROBING THE BAND STRUCTURE

THE HONEYCOMB BAND STRUCTURE

4

In this chapter I will first discuss the methods employed in this thesis to obtain exact band structures. In a second part, the tight-binding model describing our honeycomb lattice is introduced. This is followed by a third part, where I discuss the peculiarities of the honeycomb band structure, namely the Dirac points with their associated linear dispersion relation, both from a relativistic physics viewpoint as well as from the perspective on topology.

CHAPTER CONTENTS

The notion of a band structure refers to the allowed solutions of the Schrödinger equation for a single particle in a (quasi-) periodic potential,

$$E\psi = \hat{H}\psi, \quad \text{where} \tag{4.1}$$

$$\hat{H} = -\frac{\hbar^2}{2m}\nabla^2 + V(\mathbf{r}). \tag{4.2}$$

Bloch's theorem

Here, $V(\mathbf{r})$ is a potential which is periodic in space. Bloch's theorem [1929] states that, given V fulfills $V(\mathbf{r}+\mathbf{R}) = V(\mathbf{r})$ for the lattice vectors $\mathbf{R}$ that are part of the underlying Bravais lattice, the eigenstates ψ of $\hat{H}$ can be written as the product of a plain wave and a function $u_{\nu,\mathbf{k}}$ that has the same periodicity,

$$\psi_{\nu,\mathbf{k}}(\mathbf{r}) = e^{i\mathbf{k}\cdot\mathbf{r}} u_{\nu,\mathbf{k}}(\mathbf{r}), \tag{4.3}$$

with

$$u_{\nu,\mathbf{k}}(\mathbf{r}+\mathbf{R}) = u_{\nu,\mathbf{k}}(\mathbf{r}). \tag{4.4}$$

In this thesis, also the following, equivalent notation for the eigenstates will be used:

$$|\nu,\mathbf{k}\rangle = e^{i\mathbf{k}\cdot\mathbf{r}}\,|u_{\nu,\mathbf{k}}\rangle. \tag{4.5}$$

Bloch wave vector $\mathbf{k}$

These functions are indexed by the number of the band ν and the Bloch wave vector $\mathbf{k} \in [-\pi/a, +\pi/a]$ (a is the lattice spacing) within the Brillouin zone (B.Z.). When substituting this ansatz back into the Schrödinger equation, the resulting Bloch equation reads

$$\left(\frac{\hbar^2}{2m}\left(\frac{1}{i}\nabla + \mathbf{k}\right)^2 + V(\mathbf{r})\right) u_{\nu,\mathbf{k}}(\mathbf{r}) = E_{\nu,\mathbf{k}} u_{\nu,\mathbf{k}}(\mathbf{r}). \tag{4.6}$$

This equation is best solved in momentum space since both V and u assume simple forms in their momentum representation due to their periodicity. The Fourier transform of these two functions reads

$$V(\mathbf{r}) = \sum_{\mathbf{K}} V^{\mathbf{K}} e^{i\mathbf{K}\cdot\mathbf{r}} \qquad \text{and} \qquad u_{\nu,\mathbf{k}}(\mathbf{r}) = \sum_{\mathbf{K}} c^{\mathbf{K}}_{\nu,\mathbf{k}} e^{i\mathbf{K}\cdot\mathbf{r}}. \tag{4.7}$$

The summation is taken over all reciprocal lattice vectors $\mathbf{K}$. The Fourier coefficients $V^{\mathbf{K}}$ are

$$V^{\mathbf{K}} = \frac{1}{v}\int_{\text{u.c.}} \mathrm{d}\mathbf{r}\, e^{-i\mathbf{K}\cdot\mathbf{r}} V(\mathbf{r}), \tag{4.8}$$

Equation for the Fourier coefficients

with the integration taken over the unit cell with volume v. The equation for the Fourier coefficients of $u_{\nu,\mathbf{k}}(\mathbf{r})$ becomes

$$\left(\frac{\hbar^2}{2m}(\mathbf{K}+\mathbf{k})^2 - E_{\nu,\mathbf{k}}\right) c^{\mathbf{K}}_{\nu,\mathbf{k}} + \sum_{\mathbf{K}'} V^{\mathbf{K}-\mathbf{K}'} c^{\mathbf{K}'}_{\nu,\mathbf{k}} = 0. \tag{4.9}$$

This form of Eq. (4.1) on page 71, where $\mathbf{p}/\hbar = \mathbf{K}+\mathbf{k}$, simplifies the task of finding the eigenvalues from a continuous problem to solving a system of linear equations coupling only momenta separated by reciprocal lattice vectors $\mathbf{K}$.

The eigenvalue spectrum of the Bloch equation will then exhibit certain ranges of forbidden energies. The free-space dispersion relation $E = \mathbf{p}^2/(2m)$ is therefore split into several allowed energy bands separated by band gaps.

4.1 CALCULATING THE BAND STRUCTURE

To obtain the band structure of our lattice potential (see Section 3.2 on page 44)

$$\begin{aligned} V(x,y,z) = &- V_{\bar{\mathrm{X}}} \cos^2(k_{\mathrm{L}}x + \theta/2) \\ &- V_{\mathrm{X}} \cos^2(k_{\mathrm{L}}x) - V_{\mathrm{Y}} \cos^2(k_{\mathrm{L}}y) \\ &- 2\sqrt{V_{\mathrm{X}} V_{\mathrm{Y}}} \cos(k_{\mathrm{L}}x)\cos(k_{\mathrm{L}}y)\alpha\cos\varphi \\ &- V_{\bar{\mathrm{Z}}} \cos^2(k_{\mathrm{L}}z) \end{aligned} \tag{4.10}$$

we first note that the potential along the z direction separates from the rest. Therefore this part of the eigenvalue problem can be solved independently. This will be done in Section 4.1.2 on page 76. For the remaining part of the potential first some considerations about the unit cell and the Brillouin zone (B.Z.) are helpful.

As can be seen in Fig. 4.1 on the next page, the potential minima in our lattice do not form a Bravais lattice, i. e. one cannot find a primitive unit cell that only contains one lattice site. Instead, the primitive unit cell contains two sites (as long as neither $V_{\bar{\mathrm{X}}} = 0$, $V_{\mathrm{X}} = 0$ nor $\varphi = \pi/2$), as for the regular hexagonal structure of real graphene. The two-site unit cells form a Bravais lattice, i. e. two unit vectors can be found such that the whole lattice is spanned by copies of the primitive unit cell placed at the locations defined by all possible linear combinations of integer multiples of the unit vectors. In the figure, one specific primitive cell, the Wigner-Seitz cell, is drawn (solid lines). This primitive unit cell is uniquely defined as the Voronoi cell of the primitive object of the lattice (in our case the dimer consisting of the two closest lying lattice sites is chosen). It has a size of $\lambda/\sqrt{2}$ and the unit vectors of the Bravais lattice are perpendicular to each other but rotated by 45° with respect to the axes of the lattice beams. The primitive unit cell defined by the Voronoi (or Wigner-Seitz) algorithm in the reciprocal lattice is called the Brillouin zone (B.Z.). It contains all Bloch wave vectors $\mathbf{k}$ as obtained from Bloch's

Primitive unit cell

Wigner-Seitz cell

Brillouin zone

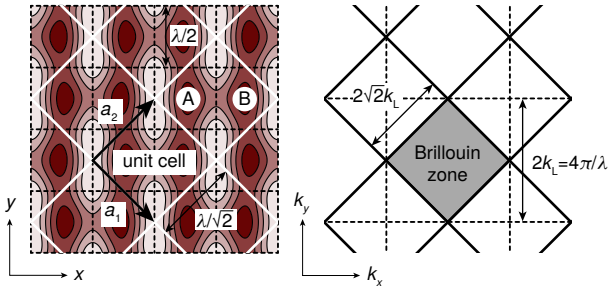

Figure 4.1: *Unit cell and Brillouin zone.* A typical real-space potential with honeycomb geometry is shown on the left, with the potential minima drawn in dark red. The lattice has a square two-site unit cell with the two sites denoted by A and B. The unit vectors of the lattice are rotated by 45° with respect to the lattice beam axes, leading to a B.Z. that is also at 45° with respect to that coordinate system. Its extent is smaller by a factor of $\sqrt{2}$ with respect to the B.Z. of the unit cell of the underlying square lattice (dashed lines).

theorem. The B.Z. is actually the Fourier transform of the Wigner-Seitz cell and has therefore for our lattice a square shape and a size $2\pi/(\lambda/\sqrt{2}) = 2\sqrt{2}k_L$, with $2k_L = 4\pi/\lambda$ being the extent of the first B.Z. along x and y. In the figure, additionally the Wigner-Seitz cell and the B.Z. of the underlying square structure are shown as dashed lines.

The two-site unit cell gives rise to a so called miniband structure, as in solid state systems subjected to a superlattice [Esaki *et al.*, 1970]. The two lowest bands are associated to the two sites in the unit cell and are energetically very close while being well separated from the next higher bands, see Fig. 4.3 on page 75.

The superlattice structure can be attributed to the breaking of the exact symmetry between two neighboring wells, which then gives rise to the two distinct sites A and B within an enlarged unit cell. Therefore, the appearance of two minibands can be seen as the result of the back-folding of the original band structure as the B.Z. is halved in size when considering a two-site unit cell, see Fig. 4.2.

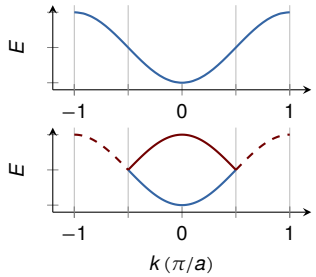

Figure 4.2: *Brillouin zone folding in 1D.* When going from a one-site to a two-site unit cell, the size of the Brillouin zone is halved and the first band is folded back, giving rise to two minibands. The lattice spacing is denoted by a.

4.1.1 EXACT DIAGONALIZATION IN THE HONEYCOMB PLANE

In order to calculate the band structure in the $x-y$ plane, we proceed as follows: Starting from the potential $V(x,y)$, following the derivations in Ref. [Jördens, 2010], we first rotate the coordinate system by 45° and enlarge it by $\sqrt{2}$ via the transformation

$$x' = x + y \qquad \text{and} \qquad y' = y - x, \tag{4.11}$$

$$k'_L = k_L/\sqrt{2}\,. \tag{4.12}$$

By applying the trigonometric identities $\cos^2(a/2) = (1 + \cos a)/2$ for all $\cos^2$ terms and $2\cos(a + b)\cos(a - b) = \cos(2a) + \cos(2b)$ for the interference term and dropping constant energy offsets, we arrive at

$$\begin{aligned} V(x', y') = &- \frac{V_{\bar{\mathrm{X}}}}{2}\cos(k'_{\mathrm{L}}x' - k'_{\mathrm{L}}y' + \theta) \\ &- \frac{V_{\mathrm{X}}}{2}\cos(k'_{\mathrm{L}}x' - k'_{\mathrm{L}}y') - \frac{V_{\mathrm{Y}}}{2}\cos(k'_{\mathrm{L}}x' + k'_{\mathrm{L}}y') \\ &- \alpha\cos\varphi\sqrt{V_{\mathrm{X}}V_{\mathrm{Y}}}\left[\cos(k'_{\mathrm{L}}x') + \cos(k'_{\mathrm{L}}y')\right]. \end{aligned} \tag{4.13}$$

For the Fourier transformation of the potential with respect to x' and y' one finds

$$\begin{aligned} \widetilde{V}(p'_x, p'_y) = &\left(-\frac{V_{\mathrm{X}}}{4} - \frac{V_{\bar{\mathrm{X}}}}{4}e^{\pm i\theta}\right)\delta_{\pm k'_{\mathrm{L}}, \mp k'_{\mathrm{L}}} \\ &- \frac{V_{\mathrm{Y}}}{4}\delta_{\pm k'_{\mathrm{L}}, \pm k'_{\mathrm{L}}} \\ &- \frac{\sqrt{V_{\mathrm{X}}V_{\mathrm{Y}}}}{4}\alpha\cos\varphi\,(\delta_{\pm k'_{\mathrm{L}}, 0} + \delta_{0, \pm k'_{\mathrm{L}}}), \end{aligned} \tag{4.14}$$

using the 2D Dirac delta function $\delta_{a,b} = \delta(p'_x - a)\delta(p'_y - b)$.

For an immediate simplification of the Schrödinger equation of the problem we now apply Bloch's theorem, which allows to represent the momentum $\mathbf{p}'/\hbar = \mathbf{K}' + \mathbf{k}'$ as the combination of a reciprocal lattice vector $\mathbf{K}'$ and a Bloch wave vector $\mathbf{k}'$, with

$$\mathbf{K}' = k'_{\mathrm{L}}\begin{pmatrix}\tilde{K}'_x \\ \tilde{K}'_y\end{pmatrix}, \qquad \tilde{K}'_x, \tilde{K}'_y \in \mathbb{Z} \tag{4.15}$$

$$\mathbf{k}' = k'_{\mathrm{L}}\begin{pmatrix}\tilde{k}'_x \\ \tilde{k}'_y\end{pmatrix}, \qquad \tilde{k}'_x, \tilde{k}'_y \in [-1, +1]\,. \tag{4.16}$$

Final eigenvalue problem in matrix form

Inserting into Eq. (4.9) on page 72 and using $E_{\mathrm{R}} = \hbar^2 k_{\mathrm{L}}^2/2m$, the eigenvalue equation for the plane wave coefficients $c^{\tilde{K}'_x, \tilde{K}'_y}$ is (note $k'_{\mathrm{L}} = k_{\mathrm{L}}/\sqrt{2}$):

$$\begin{aligned} \left(\frac{E}{E_{\mathrm{R}}}\right)c^{\tilde{K}'_x, \tilde{K}'_y} = &\, c^{\tilde{K}'_x, \tilde{K}'_y}\left(2(\tilde{K}'_x + \tilde{k}'_x)^2 + 2(\tilde{K}'_y + \tilde{k}'_y)^2\right) \\ &+ c^{\tilde{K}'_x \pm 1, \tilde{K}'_y \mp 1}\left(-\frac{V_{\mathrm{X}}}{4E_{\mathrm{R}}} - \frac{V_{\bar{\mathrm{X}}}}{4E_{\mathrm{R}}}e^{\pm i\varphi}\right) \\ &+ c^{\tilde{K}'_x \pm 1, \tilde{K}'_y \pm 1}\left(-\frac{V_{\mathrm{Y}}}{4E_{\mathrm{R}}}\right) \\ &+ \left(c^{\tilde{K}'_x \pm 1, \tilde{K}'_y} + c^{\tilde{K}'_x, \tilde{K}'_y \pm 1}\right)\left(-\frac{\sqrt{V_{\mathrm{X}}V_{\mathrm{Y}}}}{2E_{\mathrm{R}}}\alpha\cos\varphi\right). \end{aligned} \tag{4.17}$$

This matrix equation can now be solved numerically for fixed $(\tilde{k}'_x, \tilde{k}'_y)$ by diagonalization, limiting the number of higher momenta $\tilde{K}'_x, \tilde{K}'_y$ to typically ±5. By performing this step repeatedly for different $\tilde{k}'_x, \tilde{k}'_y$, the full band structure can be obtained. The result of such calculation is shown in Fig. 4.3 on the next page for typical parameters used in the experiment.

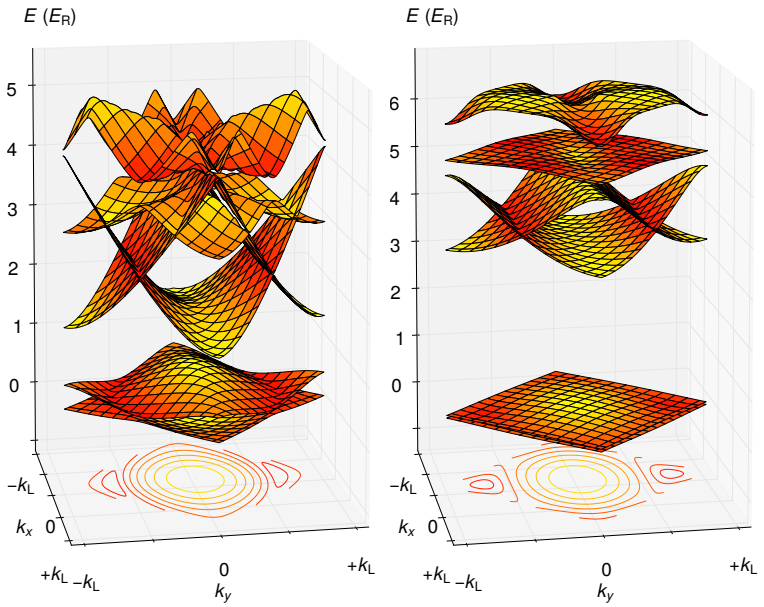

a. $V_{\tilde{X},X,Y} = [6.0, 0.1, 1.8]\,E_R$ b. $V_{\tilde{X},X,Y} = [14.0, 0.79, 6.45]\,E_R$

Figure 4.3: *Band structures.* 2D band structures are plotted for typical parameters in the experiment versus the Bloch wave vectors k_x and k_y. Contour plots of the lowest band are shown below the band structure. Both band structures contain as their lowest energy states two minibands connected by two Dirac points. The two minibands are well separated from the other bands.

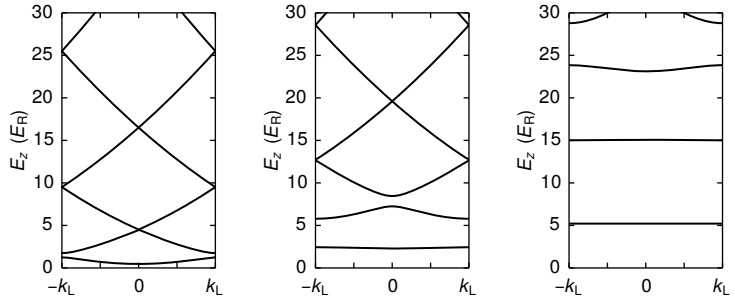

a. $V_{\tilde{Z}} = 1\,E_R$ b. $V_{\tilde{Z}} = 7\,E_R$ c. $V_{\tilde{Z}} = 30\,E_R$

Figure 4.4: *Band structures of the Mathieu lattice.* The energies associated with the allowed solutions of the Mathieu equation are given for different lattice depths. A band gap between the first and second band opens for any finite lattice depth. Here, $2k_L = 4\pi/\lambda$ is the extent of the first B.Z. along z and λ is the laser wavelength.

4.1.2 THE LATTICE ALONG THE PERPENDICULAR DIRECTION

To obtain the band structure of the lattice potential along the z direction, we start by writing down the Schrödinger equation for a particle with mass m in a 1D homogeneous lattice with the depth $V_{\tilde{Z}}$,

$$E\psi = \left(-\frac{\hbar^2}{2m}\nabla^2 + V\right)\psi, \quad \text{where} \tag{4.18}$$

$$V = V_{\tilde{Z}}\cos^2(k_L z)\,. \tag{4.19}$$

This differential equation can be brought into the form of the Mathieu equation which is found in various problems in physics and mathematics [Letokhov *et al.*, 1978; Blanch, 1972]:

$$\frac{\mathrm{d}^2\psi}{\mathrm{d}\tilde{z}^2} + \left(a - 2q\cos(2\tilde{z})\right)\psi = 0\,, \tag{4.20}$$

using the following substitutions:

$$\tilde{z} = k_L z \tag{4.21}$$

$$q = V_{\tilde{Z}}/4E_R \tag{4.22}$$

$$a = \left(E - \frac{1}{2}V_{\tilde{Z}}\right)/E_R \tag{4.23}$$

$$E_R = \frac{\hbar^2 k_L^2}{2m}\,. \tag{4.24}$$

The recoil energy E_R is the characteristic energy scale of the problem. The solutions of the Mathieu equation are shown for three typical lattice depths in Fig. 4.4 on page 75. In fact, in 1D the Mathieu equation has for any $q \neq 0$ only periodic solutions for certain values of a, i. e. the band structure has energy gaps for any $V_{\tilde{Z}} \neq 0$. The locations of the allowed bands versus lattice depth are shown as the shaded areas in Fig. 4.5.

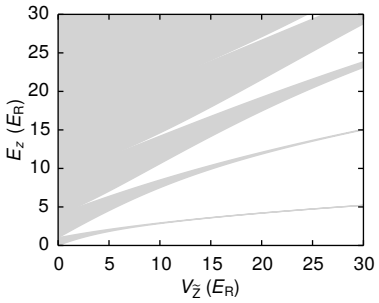

Figure 4.5: *Energy bands of the Mathieu lattice.* The 1D lattice potential of Eq. (4.19) has real-valued solutions within the shaded areas. While in the 1D case a band gap exists for every finite $V_{\tilde{Z}}$, the situation is more complicated if one considers the full 3D potential: the total energy of a particle is then the sum of the obtained solution along the separable directions $E_{\mathrm{tot}} = E_{x,y} + E_z$. In a 3D Mathieu lattice for example, the first band gap opens for $V_{\tilde{Z}} > 2.24\,E_R$. Adapted from [Jördens, 2010].

4.2 THE TIGHT-BINDING MODEL

While the method described in Section 4.1.1 on page 73 successfully describes the exact motion of a single particle in the homogeneous lattice potential, it is often desirable to simplify the complex emerging dispersion relation. One such simplification is offered by the tight-binding approximation, a model used in solid state physics when describing a crystal in which the wave functions of the electrons are best treated as superpositions of the wave functions of the electrons tightly bound to single atoms [Ashcroft *et al.*, 1976], hence the name. This is in contrast to other approaches such as e. g. the nearly free electron approximation, where the

electrons are considered as being able to move almost freely through the crystal structure. While the tight-binding model by itself is a single-particle model, it is also the basis for solid state models that involve interactions, e. g. the Hubbard Hamiltonian, which is discussed in Chapter 7. The derivations in this section follow loosely those presented in [Ibañez-Azpiroz *et al.*, 2013b], where more details on the tight-binding model tailored to our lattice structure can be found.

We start with the Hamiltonian in second quantization,

$$\hat{\mathscr{H}} = \int \mathrm{d}\mathbf{r}\, \hat{\psi}^\dagger(\mathbf{r}) \hat{H} \hat{\psi}(\mathbf{r}) \qquad \text{with} \tag{4.25}$$

$$\hat{H} = -\frac{\hbar^2}{2m}\nabla^2 + V(\mathbf{r}). \tag{4.26}$$

Wannier functions

As an ansatz, we construct the field operator as a linear combination of orthogonal Wannier functions $w_{\nu,\mathbf{j}}(\mathbf{r})$ in the band ν, which are closely localized around the unit cell located at $\mathbf{R}_\mathbf{j}$ [Wannier, 1937; Marzari *et al.*, 2012]:

$$\hat{\psi}(\mathrm{r}) = \sum_{\nu,\mathbf{j}} \hat{c}_{\nu,\mathrm{j}} w_{\nu,\mathrm{j}}(\mathrm{r}). \tag{4.27}$$

Generalized maximally localized Wannier functions

Here, $\hat{c}^\dagger_{\nu,\mathbf{j}}$ ($\hat{c}_{\nu,\mathbf{j}}$) represent the creation (annihilation) operators of a single particle at the respective unit cell $\mathbf{j}$. The maximally localized Wannier functions are then obtained by a Fourier transform of the Bloch functions $\psi_{\mu,\mathbf{k}}(\mathbf{r})$ under the application of a unitary transformation $U_{\nu,\mu}(\mathbf{k}) \in U(N)$ preserving their periodicity[1] [Marzari *et al.*, 1997]. The number of involved bands to construct the Wannier function is called N. It is equal to the number of sites in the unit cell if the Wannier functions are supposed to be independently localized at the well minima within the unit cell. With this, the Wannier function becomes

$$w_{\nu,\mathbf{j}}(\mathbf{r}) = \frac{1}{\sqrt{V_B}} \int_B \mathrm{d}\mathbf{k}\, e^{-i\mathbf{k}\cdot\mathbf{R}_\mathrm{j}} \sum_{\mu=1}^{N} U_{\nu,\mu}(\mathbf{k}) \psi_{\mu,\mathbf{k}}(\mathbf{r}). \tag{4.28}$$

The volume of the first B.Z. is denoted by V_B. The transformations $U_{\nu,\mu}(\mathbf{k})$ must be chosen such that the spatial extent of the resulting Wannier functions is minimized. Note that this is a more general definition than the one normally used for systems with one-site unit cells, where $N = 1$. Using $N = 1$ to define the Wannier functions would result in the Wannier functions being localized simultaneously on both sites of the unit cell. Wannier functions localized independently on the A or B site are either directly obtained by setting $N = 2$ or can be derived from the $N = 1$ states by symmetric and anti-symmetric combinations of the Wannier functions of adjacent bands 2ν and $2\nu + 1$, thereby halving the number of bands [Fölling, 2008]:

$$\begin{aligned} w^A_{\nu,\mathbf{j}}(\mathbf{r}) &= \frac{w_{2\nu,\mathbf{j}}(\mathbf{r}) - w_{2\nu+1,\mathbf{j}}(\mathbf{r})}{\sqrt{2}} \\ w^B_{\nu,\mathbf{j}}(\mathbf{r}) &= \frac{w_{2\nu,\mathbf{j}}(\mathbf{r}) + w_{2\nu+1,\mathbf{j}}(\mathbf{r})}{\sqrt{2}}. \end{aligned} \tag{4.29}$$

Tight-binding expansion of the Hamiltonian

When inserting the ansatz given in Eq. (4.27) into the Hamiltonian (Eq. (4.25)) one obtains

$$\hat{\mathscr{H}} = \sum_{\nu,\nu'} \sum_{\mathbf{j},\mathbf{j}'} \hat{c}^\dagger_{\nu,\mathbf{j}} \hat{c}_{\nu',\mathbf{j}'} \langle w_{\nu,\mathbf{j}} | \hat{H} | w_{\nu',\mathbf{j}'} \rangle = \sum_{\nu,\nu'} \sum_{\mathbf{j},\mathbf{j}'} \hat{c}^\dagger_{\nu,\mathbf{j}} \hat{c}_{\nu',\mathbf{j}'} t_{\nu,\nu',\mathbf{j},\mathbf{j}'}. \tag{4.30}$$

1 In the single band case ($N = 1$) U takes the form $U_{\nu,\mu}(\mathbf{k}) = e^{i\phi_\nu(\mathbf{k})}\delta_{\nu,\mu}$, i. e. it is a phase shift of the Bloch functions.

This is called the tight-binding expansion of the Hamiltonian. We note that the matrix elements $\langle w_{\nu,\mathbf{j}}|\hat{H}|w_{\nu',\mathbf{j}'}\rangle$ depend only on $\mathbf{i} = \mathbf{j}' - \mathbf{j}$ owing to the periodicity of the lattice. They correspond to tunneling amplitudes between different lattice sites (with the exception $\mathbf{i} = \mathbf{0}$, $\nu = \nu'$, which corresponds to the on-site energy),

$$t_{\nu,\nu',\mathbf{i}} = \langle w_{\nu,\mathbf{0}}|\hat{H}|w_{\nu',\mathbf{i}}\rangle\,. \tag{4.31}$$

Tunneling matrix elements as the Fourier transform of the band structure

Inserting the definition of the Wannier states as the Fourier transform of the Bloch states and using the orthogonality of the Bloch functions, we obtain:

$$t_{\nu,\nu',\mathbf{i}} = \frac{1}{V_B}\int_B \mathrm{d}\mathbf{k}\, e^{-i\mathbf{k}\cdot\mathbf{R}_\mathbf{i}} \sum_{\mu=1}^{N} U^*_{\nu,\mu}(\mathbf{k})U_{\nu',\mu}(\mathbf{k})E_{\mu,\mathbf{k}}\,, \tag{4.32}$$

which simplifies in the case $N = 1$ to

$$t_{\nu,\nu',\mathbf{i}} = \delta_{\nu,\nu'}\frac{1}{V_B}\int_B \mathrm{d}\mathbf{k}\, e^{-i\mathbf{k}\cdot\mathbf{R}_\mathbf{i}} E_{\nu,\mathbf{k}}\,, \tag{4.33}$$

where it becomes clear that the tunneling matrix elements are in fact obtained by a Fourier transform of the band structure. The reverse obviously also holds: given the tunneling coefficients, the band structure of the tight-binding Hamiltonian can be obtained by the inverse Fourier transform, e. g. for $N = 1$,

$$E_{\nu,\mathbf{k}} = \int_{\mathbf{R}_\mathbf{i}} \mathrm{d}\mathbf{R}_\mathbf{i}\, e^{i\mathbf{R}_\mathbf{i}\mathbf{k}} t_{\nu,\mathbf{i}}\,. \tag{4.34}$$

We note that the $A \leftrightarrow B$ tunnelings only depend on the difference of the two band energies, while the $A \leftrightarrow A$ or $B \leftrightarrow B$ tunnelings depend only on the sum. For a lattice with a two-site unit cell, we can therefore define the tunneling matrix elements on the basis of the maximally localized Wannier functions on the A and B sites (as given in Eq. (4.29) on page 77):

$$t^{A,B}_{\nu,\mathbf{i}} = \frac{1}{2V_B}\int_B \mathrm{d}\mathbf{k}\, e^{-i\mathbf{k}\cdot\mathbf{R}_\mathbf{i}}(E_{2\nu,\mathbf{k}} - E_{2\nu+1,\mathbf{k}}) \tag{4.35}$$

$$t^{A,A}_{\nu,\mathbf{i}} = \frac{1}{2V_B}\int_B \mathrm{d}\mathbf{k}\, e^{-i\mathbf{k}\cdot\mathbf{R}_\mathbf{i}}(E_{2\nu,\mathbf{k}} + E_{2\nu+1,\mathbf{k}})\,. \tag{4.36}$$

As for the exact solution of the single particle problem by direct diagonalization, the eigenvalues for the tight-binding Hamiltonian are easiest found in momentum space using the Fourier transformed Hamiltonian,

$$\hat{H} = \sum_{\nu,\nu'}\int_B \mathrm{d}^2\mathbf{k}\, h_{\nu,\nu'}(\mathbf{k})\hat{c}^\dagger_{\nu,\mathbf{k}}\hat{c}_{\nu',\mathbf{k}} \qquad \text{with the coefficients} \tag{4.37}$$

$$h_{\nu,\nu'}(\mathbf{k}) = \sum_{\mathbf{j}} e^{i\mathbf{k}\cdot\mathbf{R}_\mathbf{j}}\langle w_{\nu,\mathbf{0}}|\hat{H}|w_{\nu',\mathbf{j}}\rangle\,, \tag{4.38}$$

where the creation operator in momentum space is defined by

$$\hat{c}^\dagger_{\nu,\mathbf{k}} = \frac{1}{\sqrt{V_B}}\sum_{\mathbf{i}} e^{-i\mathbf{k}\cdot\mathbf{R}_\mathbf{i}}\hat{c}^\dagger_{\nu,\mathbf{i}} \tag{4.39}$$

(analogous for the annihilation operator). For a practical solution of the problem, the sum defining the expansion coefficients (Eq. (4.39)) must be truncated at a certain $|\mathbf{i}|$. This is justified, since the overlap of two separate maximally localized Wannier functions decays exponentially with their distance $\mathbf{i}$.

4.2.1 THE TIGHT-BINDING MODEL FOR THE HONEYCOMB LATTICE

To obtain the tight-binding model in our honeycomb lattice, we will restrict ourselves to the two lowest bands, with the associated Wannier functions localized on the two sites of the unit cell denoted by $\kappa \in \{A, B\}$. The Hamiltonian given in Eq. (4.37) on page 78 can then be written in a spinor representation

$$h(\mathbf{k}) = \begin{pmatrix} \varepsilon^A(\mathbf{k}) & z(\mathbf{k}) \\ z^*(\mathbf{k}) & \varepsilon^B(\mathbf{k}) \end{pmatrix} \quad \text{with} \tag{4.40}$$

$$\varepsilon_\kappa(\mathbf{k}) = + \sum_{m,n} t^{\kappa,\kappa}_{(m,n)} e^{-i\mathbf{k}\cdot\mathbf{R}_{(m,n)}} \tag{4.41}$$

$$z(\mathbf{k}) = - \sum_{m,n} t^{B,A}_{(m,n)} e^{-i\mathbf{k}\cdot\mathbf{R}_{(m,n)}}, \tag{4.42}$$

where $\mathbf{R}_{(m,n)} = m\mathbf{a_1} + n\mathbf{a_2}$ ($m, n \in \mathbb{Z}$) is a parametrized vector of the Bravais lattice, see Fig. 4.6. The tunneling matrix elements are as defined above,

$$\begin{aligned} t^{\kappa,\kappa}_{(m,n)} &= +\langle w^\kappa_{\mathbf{0}} | \hat{H} | w^\kappa_{\mathbf{R}_{(m,n)}} \rangle \\ t^{B,A}_{(m,n)} &= -\langle w^A_{\mathbf{0}} | \hat{H} | w^B_{\mathbf{R}_{(m,n)}} \rangle . \end{aligned} \tag{4.43}$$

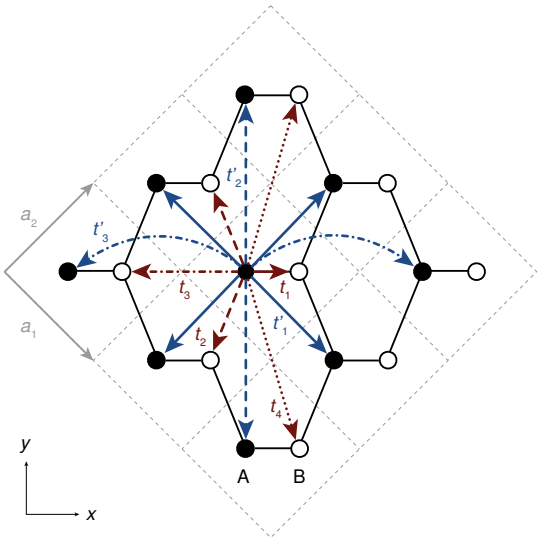

Figure 4.6: *Tight binding model.* Each unit cell (dashed gray lines) contains two sites (A and B). The nearest-neighbor hopping terms from the A to the B sublattice $t_{1,2,3,4}$ are drawn in red. The hopping processes on the same sublattice $t'_{1,2,3}$ are shown in blue. Adapted from [Ibañez-Azpiroz *et al.*, 2013b].

The eigenvalues of Eq. (4.40) give then rise to the two lowest energy bands: *Eigenvalues*

$$E_\pm(\mathbf{k}) = \varepsilon_+(\mathbf{k}) \pm \sqrt{\varepsilon^2_-(\mathbf{k}) + |z(\mathbf{k})|^2}, \tag{4.44}$$

with $\varepsilon_\pm(\mathbf{k}) = (\varepsilon^A(\mathbf{k}) \pm \varepsilon^B(\mathbf{k}))/2$. We will now restrict ourselves to the on-site energies and tunneling between nearest-neighbor sites of either the same or the other sublattice, $m, n = 0, \pm 1$. For convenience, we define the following abbreviations, see also Fig. 4.6: The $\kappa \leftrightarrow \kappa$ tunneling terms (where $\kappa \in \{A, B\}$) are called

$$\begin{aligned} t'_{\kappa,1} &\doteq t^{\kappa,\kappa}_{(1,0)} = t^{\kappa,\kappa}_{(0,1)} = t^{\kappa,\kappa}_{(0,-1)} = t^{\kappa,\kappa}_{(-1,0)} \\ t'_{\kappa,2} &\doteq t^{\kappa,\kappa}_{(1,-1)} = t^{\kappa,\kappa}_{(-1,1)} \\ t'_{\kappa,3} &\doteq t^{\kappa,\kappa}_{(1,1)} = t^{\kappa,\kappa}_{(-1,-1)}, \end{aligned} \tag{4.45}$$

and the $A \leftrightarrow B$ terms

$$\begin{aligned} t_1 &\doteq t^{B,A}_{(0,0)} \\ t_2 &\doteq t^{B,A}_{(1,0)} = t^{B,A}_{(0,1)} \\ t_3 &\doteq t^{B,A}_{(-1,-1)} \\ t_4 &\doteq t^{B,A}_{(1,-1)} = t^{B,A}_{(-1,1)} \,. \end{aligned} \tag{4.46}$$

Diagonal terms

We first discuss the diagonal terms of Eq. (4.40) on page 79. We set the energy offset such that the energies are symmetric around zero,

$$\begin{aligned} \varepsilon^A(\mathbf{k}) &= +\Delta/2 + \tilde{\varepsilon}^A(\mathbf{k}) \\ \varepsilon^B(\mathbf{k}) &= -\Delta/2 + \tilde{\varepsilon}^B(\mathbf{k}) \,, \end{aligned} \tag{4.47}$$

A-B site energy offset Δ

where we have defined the A-B site offset energy as

$$\Delta = t^{A,A}_{(0,0)} - t^{B,B}_{(0,0)} \,. \tag{4.48}$$

The correction terms $\tilde{\varepsilon}^\kappa(\mathbf{k})$ [Ibañez-Azpiroz *et al.*, 2013b] are (note that the κ-κ nearest neighbor tunneling terms are usually small as compared to the A-B tunnelings; $k_\mathrm{L} = 2\pi/\lambda$):

$$\begin{aligned} \tilde{\varepsilon}^\kappa(\mathbf{k}) &= t'_{\kappa,1}\left(e^{-2i\frac{\pi}{k_\mathrm{L}}k_y} + e^{+2i\frac{\pi}{k_\mathrm{L}}k_y}\right) \\ &\quad + t'_{\kappa,2}\left(e^{-i\frac{\pi}{k_\mathrm{L}}(k_x+k_y)} + e^{-i\frac{\pi}{k_\mathrm{L}}(k_x-k_y)} + e^{-i\frac{\pi}{k_\mathrm{L}}(-k_x+k_y)} + e^{-i\frac{\pi}{k_\mathrm{L}}(-k_x-k_y)}\right) \\ &\quad + 2t'_{\kappa,3}\left(e^{-2i\frac{\pi}{k_\mathrm{L}}k_x} + e^{+2i\frac{\pi}{k_\mathrm{L}}k_x}\right) \\ &= 2t'_{\kappa,1}\cos\left(2\frac{\pi}{k_\mathrm{L}}k_y\right) + 4t'_{\kappa,2}\cos\left(\frac{\pi}{k_\mathrm{L}}k_y\right)\cos\left(\frac{\pi}{k_\mathrm{L}}k_x\right) \\ &\quad + 2t'_{\kappa,3}\cos\left(2\frac{\pi}{k_\mathrm{L}}k_x\right) \,. \end{aligned} \tag{4.49}$$

When $\theta = \pi$, the A and B wells have the same on-site energy and therefore $\Delta = 0$. It follows $t'_{A,i} = t'_{B,i} = t'_i$, so that $\tilde{\varepsilon}^A(\mathbf{k}) = \tilde{\varepsilon}^B(\mathbf{k}) = \tilde{\varepsilon}(\mathbf{k})$. This simplifies the expression for the eigenenergies given in Eq. (4.44) on page 79 to

$$E_\pm(\mathbf{k}) = \tilde{\varepsilon}(\mathbf{k}) \pm |z(\mathbf{k})| \,. \tag{4.50}$$

Off-diagonal terms

The off-diagonal matrix elements $z(\mathbf{k})$ of Eq. (4.40) on page 79 are calculated to be

$$\begin{aligned} z(\mathbf{k}) &= -\left[t_1 + t_2\left(e^{-i\frac{\pi}{k_\mathrm{L}}(k_x+k_y)} + e^{+i\frac{\pi}{k_\mathrm{L}}(k_x-k_y)}\right) + t_3 e^{-2i\frac{\pi}{k_\mathrm{L}}k_x}\right. \\ &\quad \left. + t_4\left(e^{-2i\frac{\pi}{k_\mathrm{L}}k_y} + e^{+2i\frac{\pi}{k_\mathrm{L}}k_y}\right)\right] \\ &= -\left[t_1 + 2t_2\cos\left(\frac{\pi}{k_\mathrm{L}}k_y\right)e^{-i\frac{\pi}{k_\mathrm{L}}k_x} + t_3 e^{-2i\frac{\pi}{k_\mathrm{L}}k_x}\right. \\ &\quad \left. + 2t_4\cos\left(2\frac{\pi}{k_\mathrm{L}}k_y\right)\right] \,. \end{aligned} \tag{4.51}$$

In the case $\Delta = 0$, it is evident from the form of Eq. (4.50) that the two emerging minibands touch or cross at $z(\mathbf{k}) = 0$. These crossing points are called the Dirac points due to the linearity of the band structure close to the points, as discussed in Section 4.3 on page 86. Their position $\mathbf{k}^\mathrm{D} = (k_x, k_y)$ is obtained by solving $z(\mathbf{k}) = 0$

Position of the Dirac points

for k_x and k_y. By independently solving for the imaginary and real part we find

$$k_x = 0 \qquad \text{and} \tag{4.52}$$

$$k_y = \pm\frac{k_\mathrm{L}}{\pi}\cos^{-1}\left(\frac{-t_2+\sqrt{t_2^2+4t_4\left(2t_4-t_1-t_3\right)}}{4t_4}\right). \tag{4.53}$$

As the tunneling t_4 can usually be neglected when compared to $t_{1,2,3}$ (this is for example obvious from the potential shown in Fig. 4.1 on page 73), the expression for k_y can be simplified further to:

$$k_y \simeq \pm\frac{k_\mathrm{L}}{\pi}\cos^{-1}\left(-\frac{t_1+t_3}{2t_2}\right). \tag{4.54}$$

From this expression it is immediately clear that a real solution only exists if [Montambaux *et al.*, 2009b] *Merging point*

$$t_1 + t_3 \leq 2t_2\,. \tag{4.55}$$

For $t_1 + t_3 > 2t_2$ the two minibands do not cross anymore and the Dirac points vanish.

4.2.2 OBTAINING THE TUNNELING

In this section, we discuss two different methods to obtain the tunneling matrix elements necessary for a description by a tight-binding model.

WANNIER FUNCTIONS

This subsection is based on parts of the preprint of the following publication:

> T. Uehlinger, G. Jotzu, M. Messer, D. Greif, W. Hofstetter, U. Bissbort, and T. Esslinger, *Artificial graphene with tunable interactions*, Phys. Rev. Lett. **111**, 185307 (2013), DOI : 10 . 1103 / PhysRevLett . 111 . 185307, preprint available on ArXiv e-prints, arXiv:1308.4401.

One approach for the calculation of the maximally localized Wannier functions is to start at Eq. (4.28) on page 77 with the goal of finding unitary transforms $U_{\nu,\mu}(\mathbf{k})$ by numerical optimization such that the spatial extent of that function becomes minimal. This is what is known as the Marzari-Vanderbilt scheme [Marzari *et al.*, 1997; Souza *et al.*, 2001], which is heavily used for electronic structure calculations for complex crystals in solid state physics. The algorithm has been implemented into a open source numerical package, `wannier90` [Mostofi *et al.*, 2008], which includes algorithms to efficiently cope with the problem at hand, by for example making use of symmetries. *Marzari-Vanderbilt scheme*

The Marzari-Vanderbilt approach has also been successfully applied to optical lattice systems in order to derive *ab initio* Hubbard models for hexagonal lattice geometries [Walters *et al.*, 2013; Ibañez-Azpiroz *et al.*, 2013a,b]. However, care has to be taken to avoid local minima when directly optimizing the spread of the Wannier functions, and lattice-specific modifications may be required [Walters *et al.*, 2013]. For complex lattice structures, this algorithm entails a minimization in a d-dimensional parameter space with the spatial spread function featuring local minima, where d scales with the number of involved bands squared times the desired resolution in quasimomentum space.

In this thesis, a novel numerical method based on the alternative definition of Wannier states as eigenstates of band-projection operators [Kivelson, 1982] is

used. The alternative approach has ben worked out by Ulf Bissbort and has been generously shared with us. The details on this approach can be found in his thesis [Bissbort, 2012]. Instead of the numerical optimization, the essential step of the algorithm is the solution of an eigenvalue problem, i. e. a diagonalization of a $d \times d$ matrix. This intrinsically avoids the problem of local minima and is numerically highly efficient, scaling better with respect to a direct optimization for increasing d.

Wannier states as eigenstates of band-projection operators

For clarity, the procedure is first worked out for a 1D lattice system with a single potential minimum per lattice unit cell. We start by assuming that a set of Bloch states is given, each in the form

$$|\nu, k\rangle = \sum_n c^n_{\nu,k} \, |p/\hbar = k + 2\pi n/a\rangle \,, \tag{4.56}$$

with the normalization condition $\sum_n |c^n_{\nu,k}|^2 = 1$, $|p\rangle$ being a pure momentum state and a the lattice spacing. This corresponds to each real-space Bloch function being normalized in the unit cell. In terms of the Bloch functions, the projection operator onto a band ν can be written as

$$\mathscr{P}_\nu = \sum_k |\nu, k\rangle \langle \nu, k| \,. \tag{4.57}$$

Phase of the Bloch functions

Note that $\mathscr{P}_\nu$ does not depend on the complex phase of the Bloch functions (which is arbitrary, since it is not fixed by via their definition).

The central idea developed by Kivelson [1982] is to consider the Wannier states as eigenstates of the operator $\hat{x}_\nu$,

$$\hat{x}_\nu = \mathscr{P}_\nu \hat{x} \mathscr{P}_\nu \,. \tag{4.58}$$

Relation to the standard definition using Fourier transforms

In many standard cases, this definition of the Wannier states coincides with the usual definition via the Fourier transform of the Bloch states, with the additional requirement of minimizing the spatial variance. This definition can however be used for an efficient calculation of the Wannier states by a numerical diagonalization of $\hat{x}_\nu$. Within each band ν, the natural basis for the explicit representation of $\hat{x}_\nu$ is the Bloch basis. In this basis its matrix elements $X^\nu_{k,k'}$ can be expressed as the real-space integrals of terms involving the Bloch functions $\psi_{\nu,k}(x) = \langle x | \nu, k\rangle$ over the entire spatial region of the lattice consisting of L sites

$$X^\nu_{k,k'} = \int_{-\frac{a}{2}}^{(L-\frac{1}{2})a} \psi^*_{\nu,k}(x) \, \psi_{\nu,k'}(x) \, x \, \mathrm{d}x \,. \tag{4.59}$$

This integration can be performed analytically and we obtain

$$\begin{aligned} X^\nu_{k,k'} = {} & \delta_{k,k'} \frac{a(L-1)}{2} + a \, e^{i\frac{a}{2}(k-k')} \\ & \times \sum_{n,n'=-\infty}^{\infty} \left(1 - \delta_{k,k'} \, \delta_{n,n'}\right) \frac{(-1)^{n-n'} \, c^{n\,*}_{\nu,k} c^{n'}_{\nu,k'}}{2\pi i (n-n') + ia(k-k')} , \end{aligned} \tag{4.60}$$

reducing the calculation of each matrix element to a summation. Here, δ is the Kronecker delta function. Diagonalizing the resulting matrix X directly leads to the Wannier states (up to a complex phase) without any ambiguity.

Both the eigenvalues (corresponding to the position of the respective Wannier state) and the eigenstates at the edge of a finite system contain finite size effects. However, these decay exponentially towards the center. In fact, it is sufficient to

determine one Wannier function per sublattice (i. e. two Wannier states for our bipartite honeycomb lattice) to obtain the entire basis set of orthogonal Wannier states. All other Wannier states are related and can directly be obtained from simple phase rotations of the eigenvector elements, as follows from the Wannier states being related to the Bloch states by a discrete Fourier transformation. It is thus useful to determine a Wannier state at the center of the lattice to minimize finite size effects.

Two-dimensional honeycomb lattice

In the 2D case of our tunable-geometry optical lattice, the Bloch state with Bloch wave vector $\mathbf{k}$ in band ν is of the form

$$|\nu, \mathbf{k}\rangle = \sum_{n_1,n_2} c_{\nu,\mathbf{k}}^{n_1,n_2} \, |\mathbf{p}/\hbar = \mathbf{k} + n_1\mathbf{b}_1 + n_2\mathbf{b}_2\rangle \tag{4.61}$$

as obtained from the band structure calculations detailed in Section 4.1.1 on page 73. For lattice geometries such as the honeycomb lattice with two or more potential minima per lattice unit cell, one has to allow for maximally localized Wannier states to be composed of Bloch states from multiple energy bands. We therefore define the projection operator onto a suitable subset of bands $\mathscr{A}$ as

Localization on single sites of complex lattice geometries

$$\mathscr{P}_{\mathscr{A}} = \sum_{\nu\in\mathscr{A},\,\mathbf{k}} |\nu, \mathbf{k}\rangle \langle \nu, \mathbf{k}| \tag{4.62}$$

and consider the Wannier states to be eigenstates of suitable position operators projected onto $\mathscr{A}$. Generally, in the higher-dimensional case, the Wannier states are maximally localized along the directions of the reciprocal lattice vectors, which are

$$\mathbf{b}_1 = k_\mathrm{L}(\mathbf{e}_x + \mathbf{e}_y) \qquad \mathbf{b}_2 = k_\mathrm{L}(\mathbf{e}_x - \mathbf{e}_y) \tag{4.63}$$

for our honeycomb lattice. We therefore define the real-space coordinate operators along these directions,

$$\hat{a}_1 = \mathbf{b}_1 \cdot \begin{pmatrix}\hat{x}\\ \hat{y}\end{pmatrix} = k_\mathrm{L}(\hat{x} + \hat{y}) \qquad \hat{a}_2 = \mathbf{b}_2 \cdot \begin{pmatrix}\hat{x}\\ \hat{y}\end{pmatrix} = k_\mathrm{L}(\hat{x} - \hat{y})\,, \tag{4.64}$$

and the 2D Wannier states are simultaneous eigenstates of both band-projected operators $R_1 = \mathscr{P}_{\mathscr{A}}\,\hat{a}_1\,\mathscr{P}_{\mathscr{A}}$ and $R_2 = \mathscr{P}_{\mathscr{A}}\,\hat{a}_2\,\mathscr{P}_{\mathscr{A}}$. Note that, although $[R_1, R_2] \neq 0$, the Wannier states in the bulk are asymptotic eigenstates of both R_1 and R_2 for large systems. We parametrize the Bloch wave vector by $\mathbf{k} = \frac{m_1}{L}\mathbf{b}_1 + \frac{m_2}{L}\mathbf{b}_2$ with integer m_1 and m_2 for a 2D lattice with L lattice sites along each dimension and define the collective index function $I(\nu, m_1, m_2)$, which maps every Bloch state onto a unique integer value. Additionally, we note that $\mathscr{P}_{\mathscr{A}}\,|\nu, \mathbf{k}\rangle = |\nu, \mathbf{k}\rangle$ if $\nu \in \mathscr{A}$. With this, the matrix elements of the band-projected position operators determined from the real-space integration are

$$\begin{aligned} R_{1,2}^{I(\nu,m_1,m_2),I(\nu',m_1',m_2')} &= \langle \nu, \mathbf{k}|\, k_\mathrm{L}(\hat{x} \pm \hat{y})\, |\nu', \mathbf{k}'\rangle \\ &= k_\mathrm{L} \int_{\text{r.s.l.}} \mathrm{d}^2 r \sum_{\substack{n_1,n_2\\ n_1',n_2'}} c_{\nu,\mathbf{k}}^{n_1,n_2\,*}\, c_{\nu',\mathbf{k}'}^{n_1',n_2'}\, e^{-i(n_1\mathbf{b}_1 + n_2\mathbf{b}_2 + \mathbf{k})\cdot\mathbf{r}}\, e^{i(n_1'\mathbf{b}_1 + n_2'\mathbf{b}_2 + \mathbf{k}')\cdot\mathbf{r}}\, (x \pm y)\,, \end{aligned} \tag{4.65}$$

where the integration is to be performed over the entire real-space lattice (r.s.l.). The explicit real-space integration can be performed analytically in full analogy to the 1D case, leading to a similar expression involving only the summation over n_1 and n_2.

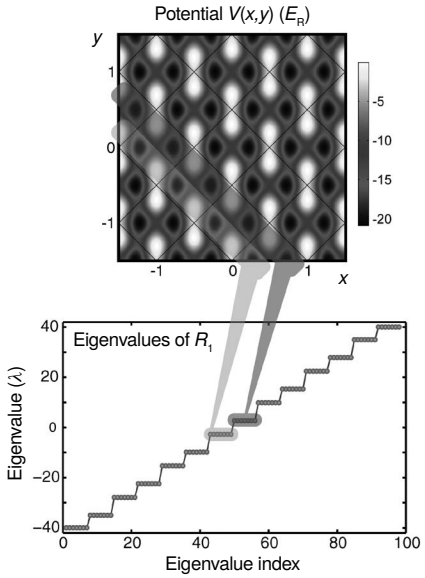

Figure 4.7: *Eigenvalues of* R_1. The plot displays the spectrum of the operator R_1 for a lattice consisting of $L = 7$ units cells per dimension, corresponding to 98 physical sites. Each degenerate set of eigenvalues corresponds to a subset of states maximally localized along the direction $\mathbf{b}_1$, but not necessarily localized along $\mathbf{b}_2$, as indicated by the respective shaded regions.

To determine the Wannier states as the simultaneous eigenstates, one can first diagonalize R_1. The spectrum of R_1 is composed of degenerate plateaux of eigenvalues[2], each corresponding to a subspace of states maximally localized along $\mathbf{b}_1$, but with arbitrary localization properties along $\mathbf{b}_2$, see Fig. 4.7. To obtain the final Wannier states, the operator R_2 is diagonalized within one such degenerate subspace. A typical Wannier state obtained in this manner for the honeycomb lattice considered in this work is shown in Fig. 4.8.

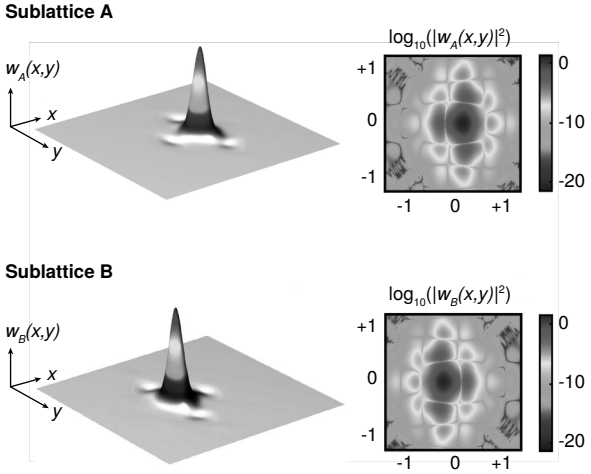

Figure 4.8: *Calculated Wannier functions.* The plots show the 2D maximally localized Wannier functions obtained from our numerical procedure for both sublattices of a honeycomb lattice. The parameters are those used in the experiments presented in Chapter 8, $V_{\tilde{X},X,Y} = [14, 0.8, 6.45]\, E_R$ and $\theta = \pi$. The Wannier function length scale is normalized to λ.

Realness of Wannier functions

A property which has been much discussed but not resolved is why the real-space representation of the Wannier functions obtained from the Marzari-Vanderbilt minimization approach is real (up to an arbitrary constant complex phase factor) if the spatial variance is minimal. This property follows naturally within our approach for lattice Hamiltonians, which are invariant under time reversal. In this case, the real-space wave functions of all energy eigenstates can be chosen purely real. This seems to contradict the complex form of the Bloch functions for a system which is infinitely large or has periodic boundary conditions, but is easily resolved by noting that the Bloch states $|\nu, \mathbf{k}\rangle$ and $|\nu, -\mathbf{k}\rangle$ are pairwise degenerate. By performing a unitary transformation within each such two-dimensional subspace to an equivalent basis $(|\nu, \mathbf{k}\rangle + |\nu, -\mathbf{k}\rangle)/\sqrt{2}$ and $(|\nu, \mathbf{k}\rangle - |\nu, -\mathbf{k}\rangle)/\sqrt{2}$ for some

2 Up to deviations from finite size effects, which decay rapidly and are exponentially suppressed for states in the bulk of the lattice.

suitable choice of initial phases, states with purely real-space wave functions can be formed. Clearly, the definition via eigenstates is basis-independent and can equally well be performed in this alternative purely real basis without altering the resulting Wannier states. However, it is directly evident that the matrix elements of the operator $\hat{x}_{\mathscr{A}}$ are purely real in this basis, since they can be expressed as integrals of a product of three real functions (two real energy eigenfunctions and the position x). Hence, the representation of $\hat{x}_{\mathscr{A}}$ in this basis is a real, symmetric matrix. Since the eigenvector elements of a symmetric matrix can be chosen to be purely real and the Wannier states can be written as superpositions of these elements and the corresponding real basis functions, the Wannier functions are purely real.

Implementation into the data analysis framework

Despite its numerical efficiency, an accurate calculation of the Wannier functions, which are the basis for many of the theoretical descriptions of our system used in this thesis, requires several minutes on a desktop computer. To speed up repeated data evaluations, the results of the calculations are stored in a central `MySQL` database, set up specifically for that purpose. The code to obtain the tight-binding parameters transparently either calculates the parameters or obtains them from the database, with the option of interpolating from previously calculated results. The obtained tight-binding parameters as a function of the lattice depths $V_{\bar{\mathrm{X}}}$ and V_{X} in the relevant regimes used in this thesis are shown in Section 7.1.1 on page 133.

BAND STRUCTURE FITS

Obtaining the tunneling matrix elements by fitting a tight-binding model to the calculated band structure

Another approach to obtain the tight-binding parameters is to fit the expression for the band structure within the tight-binding model (Eq. (4.44) on page 79) to the results obtained by exact diagonalization (see Section 4.1.1 on page 73) [Lebrat, 2012]. By doing so, the large number of parameters (overall energy offset, site energy offset and the tunnel couplings) can lead to instabilities of the fit. The number of parameters can, however, be reduced by using the fact that $E_+ - E_-$ only depends on Δ and the $A \leftrightarrow B$ tunneling terms while $E_+ + E_-$ depends only on the overall energy offset and the κ-κ tunnelings [Lebrat, 2012]. Even though these tunnelings are usually small compared to the A-B tunneling terms, they need to be included in order to account for the asymmetry of the two minibands. Additionally, good initial fit parameters have to be chosen to ensure that the fit does not get stuck in local minima.

Figure 4.9 shows a cut through a fitted band structure along $k_x = 0$ for typical parameters used in the experiment. Good agreement for the specific parameters is obtained when including the κ-κ tunnel couplings. In general, reasonable agreement is found for all regimes with honeycomb structure explored in this thesis, with the largest deviations (about 20% in the tunneling amplitude) found close to the point where a gap between the two minibands appears. In the limit of deep lattices with a single-beam depth on the order of $\gtrsim 10\,E_{\mathrm{R}}$, the tight-binding model is even able to perfectly reproduce the full band structure.

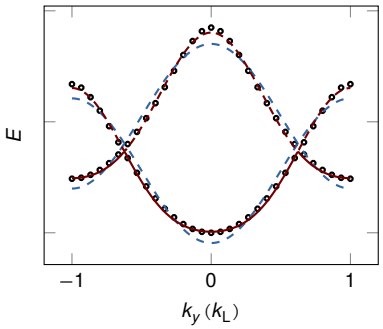

Figure 4.9: *Fitting the tight binding model to the exact band structure.* The black points are the result of the exact band structure calculation for a lattice with $V_{\bar{\mathrm{X}},\mathrm{X},\mathrm{Y}} = [6.0, 0.1, 1.8]\,E_{\mathrm{R}}$. The blue dashed line is a fit using only nearest-neighbor tunnelings between different sublattices, while the red solid line also includes hoppings between the same sublattices.

4.3 PROPERTIES OF THE HONEYCOMB BAND STRUCTURE

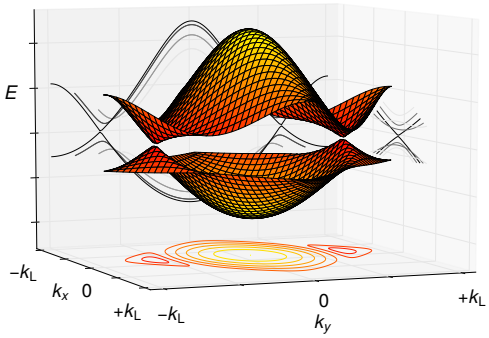

Figure 4.10: *Dirac points.* Typical band structure obtained by numerical diagonalization of the lattice potential with parameters $V_{\bar{X},X,Y} = [7.0, 0.5, 1.8]\,E_R$. The band structure contains two isotropic Dirac points located inside the first B.Z. on the $k_x = 0$ line. Cuts through the dispersion relation in the vicinity of one of the Dirac points are shown behind the 3D plot, with the linear dispersion relation at the points clearly visible. Equipotential energy lines of the lower band are shown below the band structure.

Dirac points / accidental band crossings / diabolical points

Since the honeycomb lattice consists of two sublattices A and B, the wave functions are two-component spinors. Tunneling between the two states attributed to the two sublattices leads to the formation of two energy bands, which are well separated from the higher bands and have a conical intersection at two quasimomentum points in the B.Z. – the Dirac points, see Fig. 4.10. Such conical intersections where first described by Hamilton when studying the refraction from optical crystals [Hamilton, 1837]. Accidental crossings of energy levels where later theoretically studied by Berry and Wilkinson, who termed them *diabolical points* [Berry *et al.*, 1984], after their double-cone structure reminiscent of a diabolo. The Dirac points are thus nothing else than diabolical points in quasimomentum space.

Dirac points always occur in pairs.

The Dirac points always occur in pairs due to time inversion symmetry, i. e. the inversion symmetry of the quasimomentum space, from which follows that, if a Dirac point is found at $\mathbf{k}^D$, there must be second point at $-\mathbf{k}^D$. In a broader sense, the occurrence of the Dirac points in pairs is a consequence of the fermion doubling theorem [Nielsen *et al.*, 1983], which states that given a certain set of symmetries the contact points between two bands in 2D lattice models must appear in pairs with opposite chirality. These points are topological defects in the band structure, with an associated geometric phase of $\pm\pi$, called Berry's phase [Berry, 1984] (see Section 4.3.2 on page 92). This topological protection warrants their stability with respect to lattice perturbations, so that over a large range of lattice anisotropies only the position of the Dirac points varies inside the B.Z.. In contrast, breaking the inversion symmetry of the potential by introducing an energy offset Δ between sublattices opens an energy gap at the Dirac points, proportional to the offset. In our implementation, the energy offset Δ between the A and B sites only depends on the phase θ, which can be precisely controlled by adjusting the frequency offset between the $\bar{X}$ and X beam, see Section 3.2.5 on page 53.

As already discussed in Section 4.1 on page 72, the B.Z. has a square shape, see Fig. 4.11a on the next page. The two Dirac points are located at non-symmetry points within the first B.Z., as evident from the band structure calculations obtained by numerical diagonalization of the Hamiltonian as well as the tight-binding model, Section 4.1.1 on page 73 and Section 4.2 on page 76, respectively. Their position is pinned to $k_x = 0$, owing to the reflection symmetries of the system [Salger *et al.*, 2007]. It is interesting to note that whenever a band structure exhibits a minimal energy gap located away from any symmetry point of the B.Z., as is the case for our lattice structure, it follows mathematically that it must be a Dirac point [Wunsch *et al.*, 2008].

Any minimal energy gap away from symmetry points of the B.Z. is a Dirac point.

The situation is different to the case of real graphene, which has a B.Z. of hexagonal shape, see Fig. 4.11b on the facing page. There, the six vertices of the B.Z. belong to two different symmetry points identified by Bragg reflections in quasimomentum space, the K and K' points. These two symmetry points each include the vertices of one of the regular triangles that can be formed by the vertices of

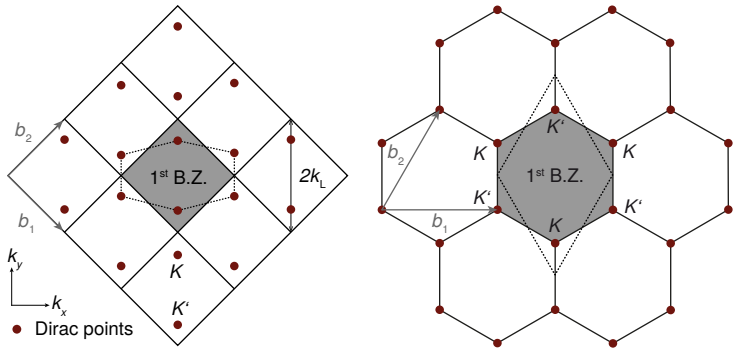

a. Our lattice b. Real graphene

Figure 4.11: *Location of the Dirac points.* a. For our lattice geometry, the two Dirac points, denoted by K and K', are located within the first B.Z., while in the case of real graphene (b.) (which has a regular hexagonal structure), they are located at the corners of the B.Z.. The B.Z. vertices denoted by K (and K' respectively) are identified by Bragg reflections and therefore belong to one and the same Dirac point. Deformed unit cells (dotted lines) can be drawn in both reciprocal lattices such that they are equivalent to the B.Z. of the respective other lattice geometry (up to a rescaling of one axis).

the hexagon. Even though the shape of the B.Z. of real graphene is different, its band structure also contains two Dirac points owing to the two-site unit cell. For unstrained graphene, i. e. a perfectly regular hexagonal lattice, they are located exactly at the vertices of the B.Z., with one at the K and the other at the K' point, see Fig. 4.12.

In terms of the underlying geometric structure, our lattice corresponds to linearly strained graphene, i. e. one of the real space axes and the corresponding quasimomentum axis is stretched, leading to an irregular hexagon. This interpretation is confirmed by comparing our tight-binding Hamiltonian Eq. (4.40) on page 79 with that of graphene [Castro Neto *et al.*, 2009]: when rescaling the x axis by $\tilde{x} = x\sqrt{3}$ they are actually the same. In our system the effect of this deformation can however be compensated by adjusting the height of the potential hills between the sites, such that the tunneling matrix elements along the different spatial axis are the same. Therefore our lattice potential can be used to realize effectively the same physics as found in regular hexagonal lattice structures. The analogy of the two structures can also be seen in the fact that for both geometries primitive unit cells in quasimomentum space of either hexagonal or rhombic shape can be found. For example for our lattice, a unit cell with hexagonal shape with the Dirac points located at the vertices can be drawn, see Fig. 4.11a, dotted lines.

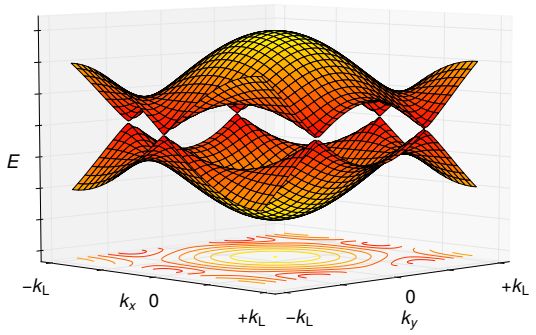

Figure 4.12: *Band structure of real graphene.* The band structure contains two isotropic Dirac points located at the six corners of the hexagonal B.Z.. The six corners correspond to two symmetry points in quasimomentum space. Equipotential lines of the lower band are shown below the band structure.

4.3.1 THE LINEAR BAND CROSSINGS

In this section I will discuss two aspects of the conical band crossings at the Dirac points: on one hand this is the analogy of the behavior of the particles in the vicinity of the Dirac points with that of relativistic particles, which is due to the linear dispersion relation. On the other hand, the density of states and the classification of the band structure with respect to conducting or insulating behavior is reviewed.

Analogy to relativistic physics

In order to analyze the linear band crossings and the analogy to relativistic physics, we will first consider the tight-binding model of our band structure. For simplicity, we will neglect nearest-neighbor tunneling to the same sublattice, $t'_{1,2,3} = 0$ and assume for the diagonal A-B tunneling $t_4 = 0$. Both are fair approximations within most of our experimental regimes. As has been deduced in Section 4.2 on page 76, the location of the Dirac points is then given by

Location of the Dirac points

$$k_x^{\mathrm{D}} = 0 \tag{4.66}$$

$$k_y^{\mathrm{D}} \simeq \pm \frac{k_{\mathrm{L}}}{\pi} \cos^{-1}\left(-\frac{t_1 + t_3}{2t_2}\right). \tag{4.67}$$

We are interested in the approximate form of the Hamiltonian and its dispersion relation close to the Dirac point. To this end, we perform a Taylor series expansion of the expression $z(\mathbf{k})$ (see Eq. (4.51) on page 80) around

Taylor expansion of the dispersion relation in the vicinity of a Dirac points

$$\tilde{\mathbf{k}} = \mathbf{k} - \begin{pmatrix} k_x^{\mathrm{D}} \\ k_y^{\mathrm{D}} \end{pmatrix}. \tag{4.68}$$

We will choose the Dirac point with $k_y > 0$, without loss of generality, as the two points are symmetric. When expanding separately along the two directions up to second order, one obtains the following expressions:

$$\begin{aligned} z(\tilde{k}_x, \tilde{k}_y = 0) &\simeq -i\frac{\pi}{k_{\mathrm{L}}}(t_1 - t_3)\tilde{k}_x - \frac{1}{2}\frac{\pi^2}{k_{\mathrm{L}}^2}(t_1 - 3t_3)\tilde{k}_x^2 \\ z(\tilde{k}_x = 0, \tilde{k}_y) &\simeq 2\frac{\pi}{k_{\mathrm{L}}}t_2\sqrt{1 - \left(\frac{t_1 + t_3}{2t_2}\right)^2}\tilde{k}_y - \frac{1}{2}\frac{\pi^2}{k_{\mathrm{L}}^2}(t_1 + t_3)\tilde{k}_y^2 . \end{aligned} \tag{4.69}$$

Both expressions are actually dominated by linear terms, leading per Eq. (4.44) on page 79 to a linear dispersion relation close to the Dirac points (note that $\varepsilon'_\nu(\mathbf{k}) = 0$ in our approximation). It is interesting to note that at the merging point of the two Dirac points, i. e. where the two minibands split, the behavior is different. When applying the merging condition $t_1 + t_3 = 2t_2$, we obtain

$$\begin{aligned} z^{\mathrm{m}}(\tilde{k}_x, \tilde{k}_y = 0) &\simeq -i\frac{\pi}{k_{\mathrm{L}}}(t_1 - t_3)\tilde{k}_x - \frac{1}{2}\frac{\pi^2}{k_{\mathrm{L}}^2}(t_1 - 3t_3)\tilde{k}_x^2 \\ z^{\mathrm{m}}(\tilde{k}_x = 0, \tilde{k}_y) &\simeq -\frac{1}{2}\frac{\pi^2}{k_{\mathrm{L}}^2}(t_1 + t_3)\tilde{k}_y^2 , \end{aligned} \tag{4.70}$$

i. e. the dispersion relation has become quadratic along the y direction while it remains linear along x. One also notes that the merging occurs at the B.Z. vertices, i. e. the Dirac points are moving outwards in the B.Z. when approaching the merging transition.

Slopes of the dispersion relation close to the Dirac points

From Eq. (4.69) the slopes of the dispersion relation close to the Dirac points

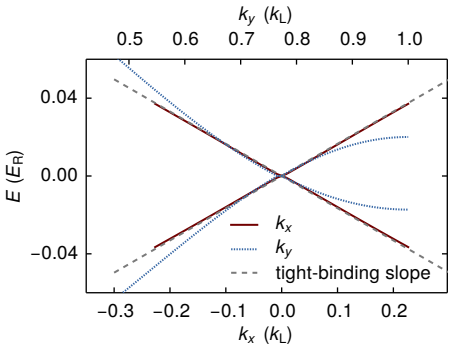

Figure 4.13: *Linear dispersion relation in the vicinity of isotropic Dirac points.* Cuts through the exact dispersion relation in the vicinity of a Dirac point (red solid and blue dotted lines) are drawn for a band structure containing isotropic Dirac points ($V_{\tilde{X},X,Y} = [12.8, 0.79, 6.45]\,E_R$, $\alpha = 0.9$). The slopes obtained from the tight-binding model (Eq. (4.71)) using $t_{1,2,3} = [242, 168, 9]$ Hz are drawn as dotted lines.

can be extracted,

$$\begin{aligned} c_x &\doteq \frac{\partial E}{\partial \hbar \tilde{k}_x} \simeq \frac{\pi}{\hbar k_L}(t_1 - t_3) \\ c_y &\doteq \frac{\partial E}{\partial \hbar \tilde{k}_y} \simeq 2\frac{\pi}{\hbar k_L} t_2 \sqrt{1 - \left(\frac{t_1 + t_3}{2t_2}\right)^2}\,. \end{aligned} \tag{4.71}$$

Therefore, the low energy spectrum close to the Dirac points can be written as follows:

$$E(\tilde{\mathbf{k}}) = \hbar\sqrt{c_x^2 \tilde{k}_x^2 + c_y^2 \tilde{k}_y^2}\,. \tag{4.72}$$

Isotropic Dirac points

By equating the two expressions of Eq. (4.71), the condition for isotropic Dirac points is found to be

$$t_1^2 + t_3^2 = 2t_2^2\,. \tag{4.73}$$

In Fig. 4.13, cuts through the band structure calculated by exact diagonalization along k_x and k_y are shown for a lattice with parameters chosen to give rise to isotropic Dirac points. Note that the isotropy in our system is not perfect, even under this condition, and the Dirac cones are therefore not exactly round, even though the slopes along k_x and k_y are the same. This is a result of the underlying square geometry. The slopes at the Dirac points are indeed found to be the same along the two directions and also match with the slope calculated from the tight-binding expressions. In the limit $t_3 = 0$, the isotropic Dirac points are located at $\mathbf{k}^D = (0, \pm 3/4)k_L$.

CONNECTION TO RELATIVISTIC PHYSICS

In the following, we will loosely follow the derivations in [Castro Neto *et al.*, 2009; Lee, Grémaud, *et al.*, 2009; Lee, 2010]. Close to an isotropic Dirac point, the linearized Hamiltonian discussed above can be written in the following form [Wallace, 1947]:

$$h(\tilde{\mathbf{k}}) = \begin{pmatrix} \varepsilon^A(\tilde{\mathbf{k}}) & z(\tilde{\mathbf{k}}) \\ z^*(\tilde{\mathbf{k}}) & \varepsilon^B(\tilde{\mathbf{k}}) \end{pmatrix} \simeq m_* c_*^2 \sigma_z + \hbar c_* (\tilde{k}_x \sigma_y \pm \tilde{k}_y \sigma_x)\,, \tag{4.74}$$

where

$$c_* = \frac{\pi}{\hbar k_L}(t_1 - t_3) \tag{4.75}$$

$$m_* = \frac{\Delta}{2}\frac{1}{c_*^2}\,, \tag{4.76}$$

and ± accounts for the two Dirac points, and $\sigma_{x,y,z}$ are the Pauli matrices,

$$\sigma_x = \begin{pmatrix} 0 & 1 \\ 1 & 0 \end{pmatrix}, \quad \sigma_y = \begin{pmatrix} 0 & -i \\ i & 0 \end{pmatrix}, \quad \sigma_z = \begin{pmatrix} 1 & 0 \\ 0 & -1 \end{pmatrix}. \tag{4.77}$$

Definition of a Dirac algebra

We now define the Dirac matrices for a (2+1)-dimensional Dirac algebra[3] by $\gamma^\mu = (\gamma^0, \gamma^1, \gamma^2) = (\sigma_z, -i\sigma_x, -\sigma_y)$, which satisfies the commutation relations $\left\{\gamma^\mu, \gamma^\nu\right\} = 2g^{\mu\nu}$ and $\left[\gamma^\mu, \gamma^\nu\right] = -2i\epsilon^{\mu\nu\lambda}\gamma_\lambda$, where $g^{\mu\nu} = (1, -1, -1)$ and $\epsilon^{\mu\nu\lambda}$ is the Levi-Civita symbol. We additionally set

$$\psi = \begin{pmatrix} \psi_K \\ \psi_{K'} \end{pmatrix}, \quad \psi_K(\mathbf{k}) = \begin{pmatrix} c_{A,\tilde{\mathbf{k}}_K} \\ c_{B,\tilde{\mathbf{k}}_K} \end{pmatrix}, \quad \psi_{K'}(\mathbf{k}) = \sigma_x \begin{pmatrix} c_{A,\tilde{\mathbf{k}}_{K'}} \\ c_{B,\tilde{\mathbf{k}}_{K'}} \end{pmatrix}, \tag{4.78}$$

where $\tilde{\mathbf{k}}_{K,K'}$ refer to Bloch wave vectors close to one of the two Dirac points denoted by K, K'. When transforming back to real space using $\tilde{\mathbf{k}} \to -i\hbar\boldsymbol{\nabla}$, we obtain

$$\hat{\mathscr{H}} = c_* \int \mathrm{d}\mathbf{r}\, \hat{\psi}^+(\mathbf{r}) \begin{pmatrix} -i\hbar\boldsymbol{\gamma}\cdot\boldsymbol{\nabla} + m_* c_* & 0 \\ 0 & -i\hbar\boldsymbol{\gamma}\cdot\boldsymbol{\nabla} - m_* c_* \end{pmatrix} \hat{\psi}(\mathbf{r}), \tag{4.79}$$

where we have defined $\hat{\psi}_i^+ = \psi_i^\dagger \gamma^0$.

Modified speed of light c_* and mass m_*

This is the 2D Weyl-Dirac equation with a modified speed of light c_* and mass m_*. In real graphene, this modified speed of light is on the order of 1/300 of the real speed of light [Li *et al.*, 2007], while for typical parameters of our lattice it is even on the order of only a few mm/s. This analogy is the reason for calling the two linear crossing points in the band structure *Dirac points*. Note that by deforming the lattice geometry different effective "velocities of light" can be realized and that at the merging point the particles behave as massless particles along one spatial direction and as massive along the other. For the case where $m_* = 0$, the particles are called *massless Dirac fermions* and the band crossing a *massless Dirac point*. If on the other hand $m_* \neq 0$, they are named *massive Dirac particles* or *massive Dirac points*, since even though the band crossing itself is quadratic in this case, the dispersion relation is still linear in the vicinity of the crossing.

Klein tunneling

The relativistic behavior of the particles close to the Dirac points leads for example to the effect of Klein tunneling [1929], where the particle is found to be able to overcome a potential barrier that is larger than the energy of the particle with high transmission probability for certain angles of incidence [Castro Neto *et al.*, 2009]. As the height of the potential barrier approaches infinity, the barrier becomes even fully transparent, in contrast with the classical behavior, where the transmission probability decays exponentially with the potential height. While Klein tunneling has so far not been observed for free relativistic particles due to the extremely fast timescales involved [Zhang *et al.*, 2012], it has been tested in systems exhibiting a Dirac-like dispersion relations, as for example in real graphene [Katsnelson *et al.*, 2006; Young *et al.*, 2009] as well as in cold atom systems [Salger *et al.*, 2011].

Zitterbewegung

Another phenomenon is *Zitterbewegung*, a trembling motion of free relativistic particles [Schrödinger, 1930], which is the result of interference between positive and negative energy states that result in a fluctuation of the position of the particle. As for Klein tunneling, direct experimental observation for free particles is challenging. However, quantum simulations of the phenomenon where performed with, among others, trapped ions [Gerritsma *et al.*, 2010] and recently ultracold bosonic atoms [LeBlanc *et al.*, 2013; Qu *et al.*, 2013].

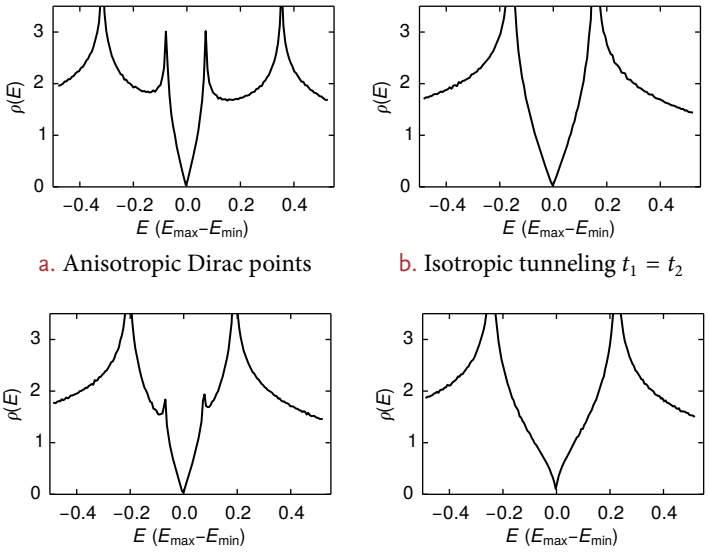

a. Anisotropic Dirac points b. Isotropic tunneling $t_1 = t_2$

c. Isotropic Dirac points d. Merging point

Figure 4.14: *Density of states.* Density of states of the two lowest minibands obtained from a numerical band structure calculation of the optical lattice potential. The energy units are chosen such that the bandwidth is one, i. e. $E_{\max} - E_{\min} \equiv 1$. The states are counted per unit cell; therefore the integral of $\rho(E)$ will be equal to the number of particles per unit cell when both bands are filled, i. e. 2. Parameters: a. $V_{\bar{X},X,Y} = [18.0, 0.79, 6.45]\, E_R$, b. $V_{\bar{X},X,Y} = [14.08, 0.79, 6.45]\, E_R$, c. $V_{\bar{X},X,Y} = [12.8, 0.79, 6.45]\, E_R$, d. $V_{\bar{X},X,Y} = [11.79, 0.79, 6.45]\, E_R$, all with $\alpha = 0.9$.

SEMIMETALLIC BEHAVIOR

In a solid, the Fermi energy of a lattice system with a graphene-like geometry would lie exactly between the two minibands, i. e. at the Dirac points. Therefore, at zero temperature, the first band is completely filled and there are no free (conducting) charge carriers. The Fermi surface then reduces to only the two Dirac points. But at any non-zero temperature, free carriers can be created by gapless excitations to the second miniband, which is continuously connected to the first by the Dirac points. The system can therefore be considered as a zero-gap semiconductor, also called a semimetal [Wallace, 1947; Castro Neto *et al.*, 2009]. *Semimetal*

As a result of the linear dispersion relation close to the Dirac points, the system shows nodal low-energy excitations in the form of massless quasiparticles, the Dirac fermions. These kinds of excitations are also expected to emerge in the low-energy sector in the pseudogap phase of *d*-wave superconductors like for example the high-T_c cuprates [Hussey, 2002], which makes the two systems analogous in that respect.

The density of states is defined as *Density of states*

$$\rho(E) = \frac{1}{\mathscr{V}_{\text{u.c.}}} \sum_{\mathbf{k}} \delta\left(E - E(\mathbf{k})\right). \tag{4.80}$$

Here $\mathscr{V}_{\text{u.c.}}$ is the size of the unit cell and the sum is taken over all Bloch wave vectors $\mathbf{k}$. The result of an integration in energy,

$$n = \frac{N}{\mathscr{V}_{\text{u.c.}}} = \int_{E_1}^{E_2} \rho(E)\, \mathrm{d}E, \tag{4.81}$$

3 Note that we consider spinless particles here.

is then the number of particles per unit cell for filled energy bands between E_1 and E_2. For real graphene, the density of states can be calculated analytically within the tight-binding regime [Castro Neto *et al.*, 2009], whereas for our lattice, we have to rely on the numerical band structure calculation from which $\rho(E)$ can be obtained by computing a histogram of the energy distribution. The result of such a calculation is shown in Fig. 4.14 on page 91. In the plot, the energy units are chosen such that the combined bandwidth of the two lowest minibands is 1.

Density of states at the Dirac point

van Hove singularity

In general, one observes a vanishing density of states at the Dirac points ($E = 0$) and two or more logarithmic van Hove singularities located inside the minibands. Close to the Dirac points, by using the low-energy spectrum of Eq. (4.72) on page 89, we find that the density of states is linear with the slope given by the inverse of the effective velocity of the particles [Wunsch *et al.*, 2008],

$$\rho(E) \propto \frac{|E|}{c_x c_y} \,. \tag{4.82}$$

At the merging point ($t_1 + t_3 = 2t_2$), the density of states assumes a square root behavior close the Dirac point, see Fig. 4.14d on page 91. In the insulating regime, i. e. after the Dirac points have merged and annihilated, the density of states is approximately linear up to the band gap, where it goes to zero.

4.3.2 TOPOLOGY OF THE BAND STRUCTURE

In the previous section, we have discussed the shape of the band structure, i. e. the eigenvalues of the Schrödinger equation in momentum space, and the resulting phenomena. The touching of the two minibands at the Dirac points genuinely alters the topology of the bands as compared to a trivial gapped band structure: for example, a loop in momentum space enclosing one of the Dirac points cannot be continuously deformed to not contain the point. This observation is reflected in the fact that the eigenstates acquire a non-trivial phase (i. e. which is not a multiple of 2π) when they are adiabatically moved around such a topological defect. The derivations in this section loosely follow those in [Fuchs *et al.*, 2012].

GENERAL BLOCH STATES

Consider a closed loop in quasimomentum space $\mathscr{C} : \mathbf{k}(0) \to \mathbf{k}(\tau) = \mathbf{k}(0)$: the evolution of an eigenstate $|u_{\nu,\mathbf{k}}(t)\rangle$ is then written as

$$|u_{\nu,\mathbf{k}}(t)\rangle = \underbrace{\exp\left\{\frac{i}{\hbar}\int_0^t E(\mathbf{k}(\tau))\,\mathrm{d}\tau\right\}}_{\text{trivial phase}} \underbrace{\exp\left\{i\gamma_\nu(\mathscr{C})\right\}}_{\text{geometric phase}} |u_{\nu,\mathbf{k}}(0)\rangle \,. \tag{4.83}$$

The state acquires two different phases, namely a trivial phase (also called *band phase* in the context of solid state systems), caused by the temporal evolution of the eigenenergy, and a geometric phase due to the adiabatic evolution of the state itself. This second phase was first described by Berry [1984] in an abstract context and by Zak [1989] for Bloch states.

Berry's phase

Berry's phase can be obtained from the Bloch states by a loop integral over the path $\mathscr{C}$,

$$\gamma_\nu(\mathscr{C}) = \oint_{\mathscr{C}} \mathscr{A}_\nu(\mathbf{k}) \cdot \mathrm{d}\mathbf{k} \quad \text{with} \tag{4.84}$$

$$\mathscr{A}_\nu(\mathbf{k}) = \langle u_{\nu,\mathbf{k}} | \nabla_{\mathbf{k}} u_{\nu,\mathbf{k}} \rangle \,. \tag{4.85}$$

Berry curvature

Here we have defined the vector potential, called Berry connection, $\mathscr{A}_\nu(\mathbf{k})$, such that the analogy to the Aharonov-Bohm phase, which is defined for real space loops, becomes obvious. Following this analogy, the Berry curvature – which corresponds to a "magnetic field" in momentum space – can be defined as follows

$$\mathbf{\Omega}_\nu(\mathbf{k}) = \nabla_\mathbf{k} \times \mathscr{A}_\nu = \Omega_\nu \mathbf{e}_z\,, \tag{4.86}$$

with

$$\Omega_\nu(\mathbf{k}) = \partial_{k_x}\mathscr{A}_y - \partial_{k_y}\mathscr{A}_x = i\left[\langle\partial_{k_x}u_{\nu,\mathbf{k}}|\partial_{k_y}u_{\nu,\mathbf{k}}\rangle - \langle\partial_{k_y}u_{\nu,\mathbf{k}}|\partial_{k_x}u_{\nu,\mathbf{k}}\rangle\right]. \tag{4.87}$$

In terms of the Berry curvature, the Berry phase can be calculated as the integral over the surface $\mathscr{S}$ enclosed by the loop $\mathscr{C}$,

$$\gamma_\nu(\mathscr{C}) = \int_\mathscr{S} \mathbf{\Omega}_\nu(\mathbf{k})\,\mathrm{d}^2\mathbf{k}\,. \tag{4.88}$$

The expression can be rewritten in a gauge-invariant form (i. e. independent of the phase of the Bloch wave functions) [Xiao *et al.*, 2010]:

$$\mathbf{\Omega}_\nu(\mathbf{k}) = i\sum_{\nu'\neq\nu} \frac{\langle u_{\nu,\mathbf{k}}|\partial_{k_x}h(\mathbf{k})|u_{\nu',\mathbf{k}}\rangle\langle u_{\nu',\mathbf{k}}|\partial_{k_y}h(\mathbf{k})|u_{\nu,\mathbf{k}}\rangle}{\left(E_\nu(\mathbf{k}) - E_{\nu'}(\mathbf{k})\right)^2} + \text{c.c.} \tag{4.89}$$

This also gives more insight about the origin of the Berry curvature: it is due to the restriction of momentum space to a single band and the resulting virtual transitions to the other bands, with decreasing contributions for bands with a large energy separation. From this representation one also sees that the Berry curvature becomes singular at closed Dirac points and therefore only has a finite spread for a band structure containing massive Dirac points.

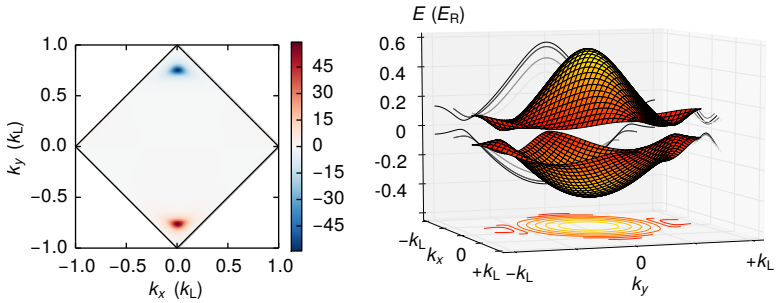

a. Berry curvature b. Band structure

Figure 4.15: *Berry curvature.* a. The Berry curvature obtained from the eigenenergies and eigenvectors of the single-particle time-independent Schrödinger equation is shown for the lowest band. b. The corresponding band structure, containing a band gap at the Dirac points owing to an *A*-*B* site imbalance, is shown. Parameters: $V_{\bar{\mathrm{X}},\mathrm{X},\mathrm{Y}} = [4.5, 0.28, 1.8]\,E_\mathrm{R}$, $\alpha = 0.9$, $\theta = 0.975\pi$.

In Fig. 4.15 we plot the numerically calculated Berry curvature in the first band for a band structure containing massive Dirac points. The calculation uses the eigenvalues and eigenvectors obtained from the numerical diagonalization of the Hamiltonian containing the exact optical potential. The Berry curvature is positive close to one of the Dirac points and negative in the vicinity of the other.

Chern number

One can define the Chern number as the integral of the Berry curvature over

the whole B.Z., divided by 2π:

$$\Gamma_\nu = \frac{1}{2\pi} \int_{\mathbf{k}\in \text{B.Z.}} \mathbf{\Omega}_\nu(\mathbf{k})\, \mathrm{d}^2\mathbf{k}\,. \tag{4.90}$$

For the above example, the Chern number is zero since the Berry curvatures of the two Dirac points exactly compensate each other.

Experimental observation

While evidence for Berry's phase has been seen in real graphene [Novoselov *et al.*, 2005; Zhang *et al.*, 2005], it has so far not been directly observed in cold-atom based implementations of hexagonal lattices, although several proposal to do so exist [Xiao *et al.*, 2010; Alba *et al.*, 2011; Price *et al.*, 2012; Goldman, Anisimovas, *et al.*, 2013; Abanin *et al.*, 2013]. The recent measurement of the related Zak phase in the band structure of a 1D dimer lattice [Atala *et al.*, 2013] however serves as proof of concept for further experiments.

SPINOR REPRESENTATION OF THE TWO MINIBANDS

Within the tight binding model describing the two lowest bands discussed before, the Hamiltonian in momentum space Eq. (4.40) on page 79 (in the case $\tilde{\varepsilon}^A(\mathbf{k}) = \tilde{\varepsilon}^B(\mathbf{k}) = 0$) can be rewritten as [Fuchs *et al.*, 2010]

$$h(\mathbf{k}) = |E| \begin{pmatrix} \cos\beta & \sin\beta\, e^{-i\theta} \\ \sin\beta\, e^{i\theta} & -\cos\beta \end{pmatrix}, \tag{4.91}$$

with

$$\begin{aligned} \cos\beta &= \Delta/(2|E|) \\ \sin\beta &= |z|/|E| \quad \text{and} \\ \theta &= -\operatorname{Arg} z\,. \end{aligned} \tag{4.92}$$

The eigenenergies of the Hamiltonian are $\pm|E|$ and its eigenvalues can be written in a spinor representation with the azimutal and polar angles of the eigenvectors on the Bloch sphere $\beta(\mathbf{k})$ and $\theta(\mathbf{k})$, respectively.:

$$\psi_+(\mathbf{k}) = \begin{pmatrix} +e^{-i\theta/2}\cos(\beta/2) \\ +e^{+i\theta/2}\sin(\beta/2) \end{pmatrix} \quad \text{and} \quad \psi_-(\mathbf{k}) = \begin{pmatrix} -e^{-i\theta/2}\sin(\beta/2) \\ +e^{+i\theta/2}\cos(\beta/2) \end{pmatrix}. \tag{4.93}$$

The Berry curvature is then

$$\mathbf{\Omega} = \frac{\nu}{2} \boldsymbol{\nabla}_\mathbf{k} \cos\beta \times \boldsymbol{\nabla}_\mathbf{k}\theta\,, \tag{4.94}$$

with $\nu = \pm 1$ indexing the two bands. If $\mathscr{C}$ is a cyclotron orbit, i. e. it travels through the band structure at constant energy, a simple expression for the Berry phase can be found:

$$\gamma(\mathscr{C}) = \pi W_\mathscr{C} \left(1 - \cos\beta\right) = \pi W_\mathscr{C} \left(1 - \frac{\Delta}{2|E|}\right), \tag{4.95}$$

Topologically invariant winding number

where

$$W_\mathscr{C} \doteq -\nu \oint_\mathscr{C} \mathbf{d}\theta/2\pi \tag{4.96}$$

is the topologically invariant winding number. It counts the total "charge" of the vortices of θ enclosed by the loop $\mathscr{C}$. Based on this definition, the Berry phase will generally assume fractional values for gapped Dirac points, while the winding number remains an integer topological invariant.

LOW ENERGY APPROXIMATION

In the linear low-energy expansion of the Hamiltonian around a momentum $\tilde{\mathbf{k}}$ close to the two Dirac points K, K', as in Eq. (4.74) on page 89, the eigenvalues can, in analogy to Eq. (4.92) on page 94, be represented on the Bloch sphere using the following identifications:

$$\begin{aligned} \cos\beta &= \Delta/(2|E|) \\ \sin\beta &= \hbar c|\tilde{\mathbf{k}}|/|E| \\ \theta &= -\operatorname{Arg}(\tilde{k}_x + i\tilde{k}_y)\,. \end{aligned} \tag{4.97}$$

The Berry phase for a circular cyclotron orbit $\mathscr{C}$ with radius $\tilde{k}$ around one of the Dirac points is:

$$\gamma(\tilde{k}) = -\nu\xi\pi\left(1 - \frac{\Delta}{2|E|}\right). \tag{4.98}$$

Here, $\xi = \pm 1$ indexes the expansion around either of the two Dirac points K, K'. The winding number is

$$W_{\mathscr{C}} = -\nu\xi, \tag{4.99}$$

and the Berry curvature becomes

$$\Omega = \frac{1}{2\pi\tilde{k}}\frac{\mathrm{d}\gamma}{\mathrm{d}\tilde{k}} = -\nu\xi(c\hbar)^2\frac{\Delta}{4|E|^3}\,. \tag{4.100}$$

If the energy E of the orbit travelled is large compared to the gap at the Dirac points Δ – which is equivalent to a large radius $|\mathbf{k}|$ – or if the gap is zero, the Berry phase acquired by encircling one of the Dirac points is therefore $\pm\pi$, depending on the direction and on which point is enclosed. This topological phase of π is the origin of the half-integer quantum Hall effect (also called the unconventional or anomalous quantum Hall effect) of graphene and the phenomenon of weak antilocalization [Castro Neto *et al.*, 2009], see below. In the other limit, if the loop has a small radius, the Berry phase is close to zero for a massive Dirac point. This can also be seen in the Berry curvature: For massive Dirac points it is spread in the vicinity of the points, while in the limit of a vanishing gap it goes to infinity at the point and is zero elsewhere. We also note that the Berry phases of the two Dirac points cancel each other due to time reversal symmetry.

Topological Berry phase of π

Recalling the representation of the Hilbert space of a spin-½ system as a bispinor, we can draw an analogy to our system discussed above: the involved wave functions can actually be seen as sublattice pseudo-spins. And, as is evident from Eq. (4.93) on page 94, the Berry phase of $\pm\pi$ is nothing else than the phase $\exp(i\pi) = -1$ acquired by the wave functions as a result of a rotation of 2π in quasimomentum space (which is equivalent to a 2π change of θ).

Sublattice pseudo-spins

CONDUCTIVITY The fact that the wave functions of the particles in the lattice are spinors and are therefore chiral leads to a strongly reduced backscattering at impurities, as long as the size of the impurities is larger than the lattice constant [Castro Neto *et al.*, 2009]. This is due to the additional geometric phase that is acquired on the incoming and outgoing scattering path, which leads to a destructive interference of the two paths and therefore suppresses backscattering. The effect can also be understood in terms of Klein tunneling, which counteracts Anderson localization and leads to weak antilocalization as long as the disorder is smooth on the atomic length scale [Katsnelson *et al.*, 2006]. This effect is suspected to play a role for explaining the experimental observation that the conductivity of graphene never falls below one conductance quantum e^2/h, even when the carrier density goes to zero [Novoselov *et al.*, 2005].

STABILITY OF THE DIRAC POINTS

Space and time inversion symmetry guarantee the individual stability of the Dirac points.

The Berry phase remains invariant under all perturbations that preserve space and time inversion symmetry, guaranteeing the stability of the two Dirac points [Mañes *et al.*, 2007]. By breaking the translational symmetry of the lattice structure (which is in solid state systems achieved by placing the material on a substrate resulting in a superlattice structure) or by deforming all the unit cells uniformly (by e. g. straining the material) the distance of the two Dirac points can, however, be reduced, leading to a hybridization of the two orbitals. This can be done up to the point where they merge and annihilate each other, followed by a gap opening. This is possible since space and time inversion symmetry only ensure the individual stability of the Dirac points but do not prevent merging.

Inversion symmetry can be broken by the introduction of an A-B site energy offset, as can be achieved by tuning the frequency difference between the X and $\bar{\text{X}}$ laser beams in our experiment or by substrate interactions in real graphene [Zhou *et al.*, 2007; Hunt *et al.*, 2013]. A site offset also exists naturally in ionic materials with hexagonal lattice geometry, such as boron nitride [Taylor *et al.*, 1952; Robertson, 1984; Watanabe *et al.*, 2004]. A gap opening caused by a sublattice energy offset induces a transition from a semimetallic to an insulating state (which is called a Semenoff insulator [1984]). See Section 6.1 on page 117 for an experimental investigation of this transition.

Semenoff insulator

Time reversal symmetry can be broken by either applying a real or effective magnetic field. Using real magnetic fields, a gap opening could so far not be directly observed, owing to the large magnetic fields required. However, by applying strain along several coupled directions, the Dirac points can be affected in a similar way as a uniform perpendicular magnetic field would do [Guinea *et al.*, 2010]. The generated pseudo-magnetic field is only present in the reference frame of the Dirac fermions, and not in the laboratory frame, and therefore, – in the strict sense – does not violate time-reversal symmetry of the crystal as a whole. The proposed type of strain has amongst others been engineered in molecular graphene (an artificial graphene system), allowing to enter the relativistic magnetic quantum limit, which so far could not be accessed in natural graphene [Gomes *et al.*, 2012]. Our system cannot be strained geometrically, but effective (staggered) magnetic fields can be created by modulating the tunnel couplings or the whole lattice position in a circular fashion (see Chapter 11 on page 196).

DETECTING DIRAC POINTS THROUGH BLOCH-ZENER OSCILLATIONS

5

The quintessential features in the band structure a honeycomb lattice are the two Dirac points with the associated linear dispersion relation in their vicinity. Detecting the existence and probing the properties of these features has however turned out to be challenging in our artificial graphene system. This is mainly since the density of states vanishes at the Dirac points and therefore – in equilibrium – no or very few atoms are affected by the band structure close to the Dirac points.

Probing the Dirac points dynamically through Bloch-Zener oscillations

Instead, we chose to probe the Dirac points dynamically. We prepare a spin-polarized Fermi gas in the tunable-geometry optical lattice set to the honeycomb geometry, with no lattice along the perpendicular (i. e. z) direction. We therefore create a structure containing atoms confined to "tubes" arranged in a honeycomb geometry. Since the particles are non-interacting and their motion will not be altered along the z direction, we can in the following restrict our discussion to the $x - y$ plane. We then drive Bloch oscillations [Zener, 1934; Bloch, 1929] either along x or y and use the thereby induced Landau-Zener transitions to higher bands [Zener, 1932; Holthaus, 2000] to detect the existence of a linear crossing in the band structure. We furthermore use the characteristic sequence of Bloch oscillations and Landau-Zener transitions, called Bloch-Zener oscillations [Breid *et al.*, 2006], to obtain information about the location of the Dirac points inside the B.Z..

CHAPTER CONTENTS

In this chapter, I will first describe how we prepare the spin-polarized gas in the optical lattice. This is followed by a section discussing the theory and numerical simulation of Bloch oscillations in 2D lattices under the influence of an external confining potential. Details of the experimental sequence and of the detection method are reviewed as well. In the next section, I present the experimental evidence for Dirac points obtained from a single or a double transfer through the band crossing. The chapter is closed by a discussion of how the transfer efficiency through the Dirac points can be modeled by use of the Landau-Zener formula describing a non-adiabatic transition between two states. In the next chapter, the techniques developed in this chapter, combined with the tunability of the optical

lattice, will be used to observe the transition to massive Dirac fermions as well as the movement and merging of the Dirac points.

Bloch oscillations

Bloch oscillations are a purely quantum mechanical phenomenon, occurring when a potential gradient is applied to particles in a periodic structure. They are as such a direct consequence of the quantum theory of electrical conductivity for solids developed by Bloch and Zener [Bloch, 1929; Zener, 1934]. The emerging oscillatory motion of the particles both in real and momentum space is notoriously hard to detect in real solids, due to the fact that in most solids the mean free path is much shorter than that required to perform even one full Bloch oscillation cycle [Ashcroft *et al.*, 1976][1].

Bloch oscillations in real solids

They have, however, been observed in various systems, where either the Bloch oscillation period has been altered by an increased lattice constant or which contain less defects. Among these are semiconductor superlattices, where for example the emitted high-frequency radiation due to the undulating motion of the electrons could be observed as a signature of the Bloch oscillations [Feldmann *et al.*, 1992; Leo *et al.*, 1992; Waschke *et al.*, 1993]. This was followed by a demonstration of the effect using cold atoms in a 1D optical lattice [Ben Dahan *et al.*, 1996] and related experiments observing the Wannier-Stark ladder [Wilkinson *et al.*, 1996]. Bloch oscillations have also been observed in other periodic systems, such as in periodically arranged arrays of optical waveguides [Pertsch *et al.*, 1999; Morandotti *et al.*, 1999] and using sound waves propagating in a superlattice of water cavities [Sanchis-Alepuz *et al.*, 2007].

Bloch oscillations in multiband systems

Theoretical studies soon reached out to consider Bloch oscillations not only in a single band, but in multiband systems and particularly in systems containing two minibands [Fukuyama *et al.*, 1973]. In such systems one expects Bloch oscillations in combination with periodic Landau-Zener transitions between the two minibands occurring at the band gap minimum. This phenomenon, studied in detail in Refs. [Breid *et al.*, 2006, 2007], is called Bloch-Zener oscillation. Again, first experimental observations were made in semiconductor superlattices [Shimada *et al.*, 2004], followed by studies using optical waveguide arrays [Dreisow *et al.*, 2009]. For cold atom systems, atoms under the influence of gravity were found to periodically escape from the optical lattice by Landau-Zener tunneling [Anderson *et al.*, 1998]. Subsequent studies were conducted on actual Bloch-Zener oscillations using a BEC loaded into a Fourier-synthesized optical lattice [Salger *et al.*, 2007, 2009; Kling *et al.*, 2010] and accelerated lattices [Zenesini *et al.*, 2009, 2010]. Bloch-Zener oscillations should also be detectable in graphene nanoribbons [Krueckl *et al.*, 2012], with the work presented in the following being the first experimental demonstration for a graphene-like system.

Bloch oscillations in cold atom systems

Ultracold atoms loaded into optical lattices, as compared to other periodic systems, allow for a direct observation of the oscillatory motion, both in real and momentum space, and also allow for a both time- and momentum-resolved investigation of the Landau-Zener transfers. For this reason they have found diverse applications in the field. In addition to the experiments already mentioned, the influence of interactions on the Landau-Zener rate [Morsch *et al.*, 2001; Cristiani *et al.*, 2002] and on the dephasing of Bloch oscillations [Gustavsson *et al.*, 2008] was studied, with several measurements using fermions [Roati *et al.*, 2004] and bosons [Ferrari *et al.*, 2006; Fattori *et al.*, 2008] performed in view of future applications for ultra-precise measurements of gravity. Furthermore, Bloch oscillations using ultracold atoms have also been used to determine fundamental constants [Battesti *et al.*, 2004; Cladé *et al.*, 2006]. For a review see [Morsch *et al.*, 2006]. In this thesis, we will use a combination of these techniques, detailed below, to study the properties of the linear band crossings in the band structure of our lattice.

1 For typical electric field strengths and relaxation times in a solid, the mean free path within the B.Z. is on the order of 10^{-1} cm^{-1}, while a typical B.Z. has a size of 10^{8} cm^{-1} [Ashcroft *et al.*, 1976].

5.1 2D BLOCH-ZENER OSCILLATIONS

5.1.1 THEORY

Semiclassical equation of motion

An intuitive picture of the origin of Bloch oscillations is obtained by considering the semiclassical equation of motion of a particle in a 1D band structure under the influence of an external force,

$$\hbar \frac{\mathrm{d}k}{\mathrm{d}t} = F \tag{5.1}$$

$$\frac{\mathrm{d}x}{\mathrm{d}t} = \frac{1}{\hbar}\frac{\partial E(k)}{\partial k}. \tag{5.2}$$

Here, k is the Bloch wave vector and x the real space position of the particle and F the external force. The solution for the quasimomentum trajectory is

$$k(t) = k(0) + \frac{F}{\hbar}t, \tag{5.3}$$

Linear increase of quasimomentum up to the B.Z. edge

i. e. the particle linearly gains momentum. Since the Bloch wave vector k is bounded to the Brillouin zone size $|k| < k_\mathrm{L}$, the quasimomentum effectively only increases up to the Brillouin zone edge, where a Bragg reflection $k \to -k$ occurs and the process starts anew. The particle therefore performs a periodic motion in momentum space. The period of this motion and the associated angular frequency are

$$T_\mathrm{B} = \frac{2\hbar k_\mathrm{L}}{|F|} = \frac{h}{d|F|} \qquad \omega_\mathrm{B} = \frac{2\pi}{T_\mathrm{B}}, \tag{5.4}$$

where d is the lattice spacing. Information about the corresponding real-space motion can be gained by considering the group velocity and effective mass of the particle, defined as

$$v_g(k) = \frac{1}{\hbar}\frac{\partial E(k)}{\partial k} \qquad m_*(k) = \hbar^2 \left(\frac{\partial^2 E(k)}{\partial k^2}\right)^{-1}. \tag{5.5}$$

Real space extent

Owing to the continuity of the dispersion relation at the B.Z. edge and time-reversal symmetry, the group velocity must change its sign at the B.Z. edge, which also gives rise to an oscillatory motion in real space with a total extent s given by the energy width W of the band and the force:

$$s = \frac{W}{F}. \tag{5.6}$$

The dynamics in a lattice under the influence of an external force is counter-intuitive.

This holds exactly if the wave function of the particle is fully localized in quasimomentum space. For a finite spread, the extent of the oscillation reduces, see the discussion below. The dynamics in a lattice under the influence of an external field is therefore rather counter-intuitive with respect to several aspects:

- In contrast to a free particle, the motion is not accelerated towards infinity, but is bounded in all observables.
- In the extreme case of an infinite force (neglecting Landau-Zener transfers), the particle even becomes fully localized, $s = 0$, a phenomenon known as Wannier-Stark localization.
- During certain parts of an oscillation period, the group velocity actually decreases with increasing Bloch wave vector k, with the consequence, that the particle is accelerated in the direction opposite to the force.

- Following the above arguments, even for weak forces no net particle transport can be obtained. In real materials, conduction is only observed because the particles never perform full Bloch oscillations owing to their comparably small mean free path, which is limited by scattering events. These scattering events allow a particle to subsequently start new Bloch oscillations at the position attained during the previous oscillation, but with a different momentum as a result of the scattering event. However, this mechanism can only take place if the band is partially filled and other quasimomenta to scatter to are available. Filled bands are always stable and do not allow for particle conduction, as a consequence of the semiclassical version of Liouville's theorem [Ashcroft *et al.*, 1976].

Note that the band structure can be reconstructed from the spatial motion during the Bloch oscillation. Integrating Eq. (5.2) on page 99, we obtain

$$\int_0^t \frac{\mathrm{d}x}{\mathrm{d}t}\,\mathrm{d}t = \frac{1}{\hbar}\int_0^t \frac{\partial E(k)}{\partial k}\,\mathrm{d}t \quad \Rightarrow \tag{5.7}$$

$$x(t) - x(0) = \frac{1}{F}\left[E(k(t)) - E(k(0))\right], \tag{5.8}$$

where we have substituted Eq. (5.3) on page 99 on the right side of the expression. Therefore a time-resolved measurement of the spatial position during a full Bloch oscillation contains information about the full band structure of the respective band. Alternatively, the band structure can also be reconstructed using Stückelberg oscillations, which occur in the context of Landau-Zener oscillations, see [Kling *et al.*, 2010].

QUANTUM MECHANICAL TREATMENT

More insight can be gained by considering a 1D tight-binding model in the first band:

$$\hat{\mathscr{H}} = -\frac{W}{4}\sum_{j=-\infty}^{\infty}\left(\hat{c}_j^\dagger \hat{c}_{j+1} + \hat{c}_{j+1}^\dagger \hat{c}_j\right) + dF\sum_{j=-\infty}^{\infty} j\hat{c}_j^\dagger \hat{c}_j\,, \tag{5.9}$$

with its diagonal representation in momentum space ($\langle k'|\hat{\mathscr{H}}|k\rangle = d\delta(k'-k)h(k)$),

$$h(k) = -\frac{W}{2}\cos(kd) + iF\frac{\mathrm{d}}{\mathrm{d}k}\,. \tag{5.10}$$

Along the lines of the derivation given in [Hartmann *et al.*, 2004], the solutions of the time-independent Schrödinger equation $h(k)\psi(k) = E\psi(k)$ are the Wannier-Stark functions

$$\psi_n(k) = \sqrt{\frac{d}{2\pi}}\exp\left[-inkd + i\zeta\sin(kd)\right], \tag{5.11}$$

where $\zeta = W/(2dF)$ is the characteristic parameter of the Bloch oscillation and $n \in \mathbb{N}$. The corresponding eigenenergies form the Wannier-Stark ladder:

$$E_n = ndF. \tag{5.12}$$

The time evolution in quasimomentum space reads

$$\begin{aligned} U_{k',k}(t) &= \sum_n \psi_n^*(k')e^{-iE_nt/\hbar}\psi_n(k) \\ &= \exp\left[-i\zeta(\sin(k'd) - sin(kd))\right]\delta(k' - k + Ft\hbar)\,, \end{aligned} \tag{5.13}$$

from which the periodicity $kd \mod 2\pi$ of the momentum space movement becomes obvious again. For a discussion of the real space behavior, it is helpful to calculate the Wannier-Stark states in the Wannier basis using a Fourier transform:

$$\begin{aligned} \psi_n(j) &= \sqrt{\frac{d}{2\pi}} \int_{-k_\mathrm{L}}^{k_\mathrm{L}} e^{ijkd} \psi_n(k)\,\mathrm{d}k = J_{j-n}(\zeta) \\ \Rightarrow \quad \hat{\psi}_n &= \sum_j J_{j-n}(\zeta)\hat{c}_j \ , \end{aligned} \tag{5.14}$$

where $J_{j-n}(\zeta)$ is the Bessel function of the first kind. The Bessel function is predominantly localized within $|j-n| < \zeta$, once again allowing to deduce the extent of the real space oscillation,

$$s = 2\zeta d = W/F. \tag{5.15}$$

The propagator in the Wannier basis becomes

$$\begin{aligned} U_{j',j}(t) &= \sum_n \psi_n^*(j') e^{-iE_n t/\hbar} \psi_n(j) \\ &= J_{j'-j}\left(2\zeta \sin\frac{\omega_\mathrm{B} t}{2}\right) \exp\left[i(j'-j)(\pi-\omega_\mathrm{B}t)/2 - ij\omega_\mathrm{B}t\right]. \end{aligned} \tag{5.16}$$

Time evolution of a gaussian wave packet

More insight into the wave packet dynamics can be gained by replacing the quantum mechanical position and momentum operators by real variables and solving the classical equations of motion for the tight-binding Hamiltonian using a gaussian distribution in phase space as the initial condition:

$$\rho(x,k,t=0) = \frac{1}{2\pi\Delta x(0)\Delta k(0)} \exp\left[-\frac{(x-x_0(0))^2}{2\Delta x^2(0)} - \frac{(k-k_0(0))^2}{2\Delta k^2(0)}\right]. \tag{5.17}$$

Here, $x_0(0)$ and $k_0(0)$ are the initial centers of the x and k distribution and $\Delta x(0)$, $\Delta k(0)$ the respective initial spreads. The time evolution of the parameters of the gaussian is calculated to be:

$$\begin{aligned} k_0(t) &= k_0(0) + \frac{F}{\hbar}t \\ \Delta k^2(t) &= \Delta k^2(0) \end{aligned} \tag{5.18}$$

and

$$\begin{aligned} x_0(t) &= x_0(0) + \frac{W}{F}\exp\left[-\Delta k^2(0)d^2/2\right]\sin\frac{\omega_\mathrm{B}t}{2}\sin\left(\frac{\omega_\mathrm{B}t}{2} - k_0(0)d\right) \\ \Delta x^2(t) &= \Delta x^2(0) + \frac{W^2}{2F^2}\left(1-\exp\left[-\Delta k^2(0)d^2\right]\right)\sin^2\frac{\omega_\mathrm{B}t}{2}. \end{aligned} \tag{5.19}$$

From the real-space evolution two regimes can be identified: if

$$\exp\left[-\Delta k^2(0)d^2\right] \approx 1\,, \tag{5.20}$$

Criterion for Bloch oscillations: the particles need to be considerably delocalized over the real space lattice.

i. e. if the quasimomentum spread $\Delta k(0)$ of the initial distribution is small with respect to the size of the B.Z. – which, for a quantum mechanical system, necessarily corresponds to a spread over several lattice sites in real space –, the classical "wave packet" performs a sinusoidal oscillation with angular frequency ω_B and constant width $\Delta x(t)$. In the case of large quasimomentum spread, i. e. strong real-space

localization, the real space position stays constant, but the width of the distribution oscillates sinusoidally instead. In this case the wave packet does not perform a Bloch oscillation, but is subject to a breathing motion. Therefore, Bloch oscillations are only observed when the particles are delocalized over the real space lattice, a criterion which can also be proved rigorously within the full quantum mechanical description.

BLOCH-ZENER OSCILLATIONS

Inclusion of Landau-Zener transitions between different bands

Concerning the quantum mechanical treatment, a natural extension is the inclusion of higher bands, which is relevant for our lattice structure. Here, the problem of two closely-spaced minibands, with Landau-Zener transfers occurring between them in the vicinity of the B.Z. edges, has been studied intensively [Breid *et al.*, 2006]. For the two-band system, a second time scale is introduced by the transmission probability to the second miniband. This timescale governs the oscillations between the populations of the lower and higher band, which occur in addition to the normal Bloch oscillations. The emerging dynamics of these Bloch-Zener oscillations are rather complex. For example, a full reconstruction of the initial state only takes place if the two oscillation periods are commensurate.

In the limit of very strong forces in the presence of higher bands, the problem is best treated in the formalism of *metastable* (also called *resonance*) Wannier-Stark states, which include a decay to higher bands, from where the particles are lost from the system, as observed by a pulsed output of a certain fraction of atoms at the Bloch oscillation frequency.

2D SYSTEMS

A second extension of the formalism considers 2D systems. In such a system, both for separable and non-separable lattice potentials, the real space position of the particles traces complex Lissajous figures if the driving force is not aligned with the lattice axes [Witthaut *et al.*, 2004]. Additionally, for non-separable potentials, Landau-Zener events leading to an escape to higher bands via tunneling along diagonal directions as well as a large spread in real space are observed [Witthaut *et al.*, 2004].

In the 2D case the semiclassical equation of motion becomes [Price *et al.*, 2012]:

$$\hbar \frac{\mathrm{d}\mathbf{k}}{\mathrm{d}t} = \mathbf{F} \tag{5.21}$$

$$\frac{\mathrm{d}\mathbf{x}}{\mathrm{d}t} = \frac{1}{\hbar}\frac{\partial E(\mathbf{k})}{\partial \mathbf{k}} - \left(\frac{\mathrm{d}\mathbf{k}}{\mathrm{d}t} \times \mathbf{e}_\perp\right)\Omega(\mathbf{k})\,, \tag{5.22}$$

where $\Omega(\mathbf{k})$ is the Berry curvature as discussed in Section 4.3.2 on page 92 and $\mathbf{e}_\perp$ is the unit vector along the direction perpendicular to the plane of the lattice.

EXTERNAL CONFINEMENT

The presence of an external confinement in addition to the lattice potential leads to a modification of the Bloch oscillations. In particular, a dephasing and subsequent rephasing has been predicted [Ponomarev *et al.*, 2006] and observed in an experiment using ultracold atoms [Gustavsson *et al.*, 2008]. We will here discuss the situation where the applied force does not remove the trap barrier, i. e. the potential still has a (local) minimum at a finite position. In this regime, the sudden switch-on of an external force essentially corresponds to a sudden displacement of the trap minimum by a certain distance l, a situation which is discussed in [Ponomarev *et al.*, 2006]. The evolution of the system is then given by that of the particles in the *absence* of a force, but with an initial displacement from the trap center of l.

The 1D tight-binding Hamiltonian of this system takes the form

$$\hat{\mathscr{H}} = -t \sum_{j=-\infty}^{\infty} \left(\hat{c}_j^\dagger \hat{c}_{j+1} + \hat{c}_{j+1}^\dagger \hat{c}_j \right) + \frac{\gamma}{2} \sum_{j=-\infty}^{\infty} j^2 \hat{c}_j^\dagger \hat{c}_j \,, \tag{5.23}$$

where $\gamma = m\omega^2 d^2$ is the characteristic trap energy and ω the angular trapping frequency. In momentum space, this Hamiltonian actually assumes the form of that of a quantum pendulum,

$$h(k) = \frac{\gamma}{2} L^2 - 2t \cos\theta \,, \quad \text{with} \quad L = -i \frac{\partial}{\partial \theta} \,, \; \theta = kd \,. \tag{5.24}$$

Quantum pendulum model

The eigenmodes of the pendulum can be categorized into those giving rise to librational (rotating slightly back and forth) or rotational motion (where full periods of rotation are performed). The separatrix is located at a normalized shift

$$\chi^* = 2 \left(\frac{2t}{\gamma} \right)^{1/2} . \tag{5.25}$$

If the normalized initial shift of the trap minimum $\chi = l/d$ is smaller than this value, $\chi < \chi^*$, the system shows librational motion, i. e. the particle perform dipole oscillations in the shifted trap. In the opposite case $\chi > \chi^*$, the system performs a rotational motion in the form of Bloch oscillations with an effective force

Effective force in a trap

$$F' = \frac{\gamma \chi}{d} . \tag{5.26}$$

However, the external confinement actually leads to position-dependent force, with the consequence that different parts of the spatial wave function of a particle actually perform Bloch oscillations with different frequencies. This leads to a dephasing. Due to the discreteness of the energy spectrum, this is followed by a complete rephasing when the relative phases of the eigenstates of the initial distribution are all multiples of 2π. The dephasing and rephasing times (called τ and T) far in the Bloch oscillation (BO) or dipole oscillation (DO) regime are found to be:

Dephasing in a trap

$$\tau^{\mathrm{BO}} = \frac{\hbar}{\sigma\gamma} \qquad \tau^{\mathrm{DO}} = \frac{8\hbar}{\sigma\gamma} \tag{5.27}$$

$$T^{\mathrm{BO}} = \frac{2\pi\hbar}{\gamma} \qquad T^{\mathrm{DO}} = \frac{16\pi\hbar}{\gamma} , \tag{5.28}$$

where σ is the spatial extent of the initial wave function normalized to the lattice spacing, $\sigma = \Delta x/d$.

Estimate for the parameters of the experiment

Finally, let us perform some estimates for the regime of the Bloch oscillations used in the measurements presented in the following sections. We assume the following typical parameters: trap frequency $\omega/2\pi = 30\,\mathrm{Hz}$, applied force $Fd/h = 89\,\mathrm{Hz}$, tunneling $t/h = 700\,\mathrm{Hz}$. This leads to a shift of the trap minimum of approximately 90 sites, with the separatrix located at 75 sites. We are therefore just in the regime where one would, according to the simple model, still expect Bloch oscillations. Assuming that the spatial wave function is delocalized over some tens of lattice sites, the dephasing time is found to be on the order of some 10 ms, consistent with the experimental observation. The rephasing time is one second, which is beyond the accessible regime in our experiments.

BLOCH OSCILLATIONS AND INTERACTIONS

The effect of inter-particle interactions on Bloch oscillations has been studied both for bosons [Kolovsky, 2007] as well as two-component fermions [Ponomarev,

2008] within the Hubbard model. Weak and strong interaction regimes have been identified, in which, depending on the magnitude of the force either regular Bloch oscillations, decaying or amplitude modulated oscillations were observed. In the presence of an external confinement, moderate interactions were found to stabilize the Bloch oscillations against dephasing [Ponomarev *et al.*, 2006].

5.1.2 SIMULATION BY FULL DIAGONALIZATION

In collaboration with Lei Wang from ETH Zurich we have performed numerical simulations of the time evolution of the many-body trapped system based on an exact diagonalization of the Hamiltonian. For the simulations, the optical lattice potential is described by the following tight-binding Hamiltonian [Lim *et al.*, 2012],

Tight-binding Hamiltonian

$$\begin{aligned}\hat{H}_{\text{lattice}} = & -t_1 \sum_{\langle ij\rangle\in L_x} \hat{c}_i^\dagger \hat{c}_j - t_2 \sum_{\langle ij\rangle\in L_y} \hat{c}_i^\dagger \hat{c}_j - t_3 \sum_{\langle ij\rangle\in L_x^d} \hat{c}_i^\dagger \hat{c}_j \\ & + \frac{\Delta}{2}\sum_{i\in A}\hat{n}_i - \frac{\Delta}{2}\sum_{i\in B}\hat{n}_i\,,\end{aligned} \tag{5.29}$$

where the hopping amplitudes of the dimerized bond along the x, the y bond, as well as the diagonal bond along x are t_1, t_2 and t_3, respectively, see Fig. 4.6 on page 79. The lattice consists of two sites per unit cell. Δ is the staggered on-site energy on the A and B sublattices. The tight-binding parameters t_1, t_2, t_3 and Δ are extracted from the Wannier function calculation of the homogeneous optical potential. The real-space Hamiltonian (Eq. (5.29)) is Fourier transformed to momentum space to get a two-by-two matrix $\hat{H}_{\mathbf{k}}$. It is diagonalized by $\hat{U}_{\mathbf{k}}^\dagger \hat{H}_{\mathbf{k}} \hat{U}_{\mathbf{k}} = E_{\mathbf{k}}$. When $\Delta = 0$ and $t_1 + t_3 < 2t_2$, the tight-binding model features Dirac points [Hasegawa *et al.*, 2012].

Harmonic trapping potential

In the experiment there is an additional harmonic trapping potential

$$\hat{H}_{\text{trap}} = \sum_i (\gamma_x x_i^2 + \gamma_y y_i^2)\hat{n}_i\,, \tag{5.30}$$

where x_i, y_i are the spatial coordinates of the i-th site. They are measured in units of $\lambda/2$. $\gamma_{x(y)} = \frac{1}{2}m\omega_{x(y)}^2(\lambda/2)^2$ are the strengths of the harmonic confinement along the x (y) direction. To simulate the Bloch-Zener oscillation experiment, we first solve the ground state $|\Psi\rangle$ of $N = 256$ spinless fermions of $\hat{H}_{\text{lattice}} + \hat{H}_{\text{trap}}$, then apply a linear gradient field $\hat{H}_{\text{field}}^x = F_x(\lambda/2)\sum_i x_i\hat{n}_i$ or $\hat{H}_{\text{field}}^y = F_y(\lambda/2)\sum_i y_i\hat{n}_i$ to the system and evolve the wave function

$$|\hat{\Psi}(t)\rangle = e^{-i(\hat{H}_{\text{lattice}}+\hat{H}_{\text{trap}}+\hat{H}_{\text{field}})\frac{t}{\hbar}}|\Psi\rangle\,. \tag{5.31}$$

The time evolution is performed with the Lanczos algorithm [Park *et al.*, 1986] with 200 Lanczos vectors. The number of lattice sites (2×200^2) is chosen such that the cloud does not touch the boundary during the Bloch oscillation. The time step is $0.05T_B$. At each time step, we measure the density matrix $\hat{\rho}_{ij} = \langle\hat{\Psi}(t)|\hat{c}_j^\dagger\hat{c}_i|\hat{\Psi}(t)\rangle$ of the system.

To extract momentum distributions, we reshape $\hat{\rho}_{ij}$ into $\hat{\rho}_{IJ}^{ab}$, where I, J are indices for the unit cell, and a, b are sublattice indices. A Fourier transform with respect to I, J gives $\hat{\rho}_{\mathbf{k}}^{ab} = \hat{\rho}_{\mathbf{k}}$. Applying the unitary transformation $\hat{U}_{\mathbf{k}}^\dagger\hat{\rho}_{\mathbf{k}}\hat{U}_{\mathbf{k}}$, the two diagonal elements become the band filling $\hat{n}_{\mathbf{k},\text{lower}}$ and $\hat{n}_{\mathbf{k},\text{upper}}$.

5.2 EXPERIMENTAL SEQUENCE

The Bloch oscillation experiments are performed with a low temperature spin-polarized ^{40}K gas prepared in the $|F = 9/2, m_F = -9/2\rangle$ Zeeman sublevel loaded into the lowest band of the tunable-geometry optical lattice set to the honeycomb geometry. A non-interacting spin-polarized gas is chosen in order to avoid damping of the Bloch oscillations and washing out of the recorded momentum distributions. We typically perform one Bloch oscillation cycle along either the x or y direction, followed by a band mapping procedure which allows for a measurement of the quasimomentum distribution of the gas in the lattice by means of a TOF experiment.

5.2.1 PREPARING A SPIN-POLARIZED FERMI GAS

To obtain the spin-polarized gas, we first adhere to the usual procedure to create a $(-9/2, -7/2)$ spin mixture on the low-field side of the respective Feshbach resonance in the optical dipole trap, described in detail in Section 3.1.4 on page 43. During evaporation, the FORT power is ramped from 200 mW to 45 mW within 2.5 s using an exponential ramp with a time constant of 450 ms. Using this procedure, we prepare a spin mixture of about 150×10^3 atoms at 20% of the Fermi temperature.

The FORT is then re-compressed within 200 ms to a power of 100 mW, followed by a ramp of the magnetic bias field to about 10 G within another 200 ms. Using the upper quadrupole coil in reverse current direction and the gradient coil, we then apply a magnetic field gradient along the y direction within 100 ms in order to compensate gravity for the $m_F = -9/2$ Zeeman state. The power of the optical trap is then lowered thereafter to 6 mW within 500 ms, during which the not levitated $m_F = -7/2$ spin component is accelerated out of the now very weak trap by gravity. In this way, about 50×10^3 spin-polarized fermions are obtained.

5.2.2 LATTICE POTENTIAL

We then load the atoms into the optical lattice by simultaneously ramping up the $V_{\bar{\mathrm{X}}}$, V_{X} and V_{Y} beams within 200 ms to their final depths as given in the following sections. Throughout, no lattice is present along the third spatial direction z, which decouples from the other directions owing to the absence of interactions. Since no forces will be applied along z, the momenta p_z of the particles along that direction will remain unaffected and can be neglected. The FORT is then completely switched off within 100 ms, as the required confinement to counteract an unlimited expansion of the cloud is now provided by the optical lattice beams.

Experiments are performed in hexagonally arranged tubes

The resulting potential for the atoms becomes

$$\begin{aligned} V(x,y) = &- V_{\bar{\mathrm{X}}} \cos^2(k_{\mathrm{L}} x + \theta/2) - V_{\mathrm{X}} \cos^2(k_{\mathrm{L}} x) \\ &- V_{\mathrm{Y}} \cos^2(k_{\mathrm{L}} y) - 2\alpha\sqrt{V_{\mathrm{X}} V_{\mathrm{Y}}} \cos(k_{\mathrm{L}} x) \cos(k_{\mathrm{L}} y) \cos\varphi\,. \end{aligned} \tag{5.32}$$

We stabilize the phase φ between the X and Y beams at the position of the atoms to $0.00(3)\pi$. The symmetry phase θ is set to close to π. We infer the precise value $\theta/\delta = [\pi/384.7(6)]\,\mathrm{MHz}^{-1}$ (where δ is the detuning of the $\bar{\mathrm{X}}$ and X beams) from the peak position in Fig. 6.1 on page 118. This is in good agreement with the independent calibration obtained using Raman-Nath diffraction on a ^{87}Rb BEC, which yields $\theta/\delta = [\pi/388(4)]\,\mathrm{MHz}^{-1}$ (see Section 3.2.5 on page 53). At the edges of the cloud the phase differs by approximately $\pm 10^{-4}\pi$. The visibility $\alpha = 0.90(5)$ and the lattice depths $V_{\bar{\mathrm{X}},\mathrm{X},\mathrm{Y}}$ are calibrated by Raman-Nath diffraction. The method has a systematic uncertainty of 10% for the lattice depths, whereas the statistical uncertainties are given in the text. The trap frequencies are

determined using approximate expressions of Eq. (3.17) on page 58. For example, for the measurements in Fig. 5.8 on page 110, we find

$$\omega_{x,y,z}/2\pi = [17.6(1), 31.8(5), 32.7(5)]\,\text{Hz},$$

as calibrated from dipole oscillations of the cloud.

5.2.3 BLOCH OSCILLATIONS

We then abruptly switch the magnetic field gradients using the upper quadrupole and the gradient coils such that the atoms feel a net force F either directed along the x or the y direction, while they continue to be levitated. This is equivalent to applying an electric field in solid state systems, and therefore leads to Bloch oscillations along the respective direction. After a certain time t, the magnetic field gradients are abruptly switched back to their original configuration in which the atoms are levitated.

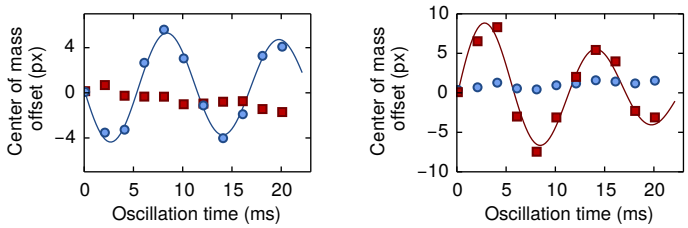

a. x oscillations b. y oscillations

Figure 5.1: *Bloch oscillation gradient calibration.* The center of mass of the momentum space distribution of the clouds is shown after applying the Bloch oscillation gradient for a varying amount of time. The blue circles and the red squares are the center of mass position along x and y, respectively. We fit damped harmonic oscillator functions to the position and obtain oscillation frequencies of 88(1) Hz (x osc.) and 95(1) Hz (y osc.). Lattice parameters: $V_{\bar{X},X,Y} = [3.6(2), 0, 1.8(1)]\,E_R$.

Calibration of the oscillation direction and frequency

We have calibrated the exact oscillation direction and frequency by recording the center of mass of the atoms in absorption images displaying the quasimomentum space distribution of the atoms during several oscillation periods in a square lattice, see Fig. 5.1. The oscillations are found to be only slightly damped and can be observed over several periods, with the largest contributions to the damping coming from the variation of the net force due to the external confinement which corresponds to a position dependent force towards the trap center.

We have determined the required currents to perform Bloch oscillations along the x and y directions with different frequencies, see Fig. 5.2 on the next page, as well as for diagonal oscillations along $\pm(x + y)$ and $\pm(x - y)$, see Table 5.1 on the facing page.

For the experiments presented in the following, we chose gradients giving rise to Bloch oscillations with a period of $T_B = 11.3(1)$ ms and $T_B = 10.5(1)$ ms along the x and y directions, respectively, with a minimal force component along the respective perpendicular directions. The magnitude of the main component of these forces corresponds to about 1/6 of gravity.

5.2.4 MEASURING THE QUASIMOMENTUM DISTRIBUTION

We record the position of the atoms using absorption imaging onto a CCD camera after slowly ramping down the optical lattice using an S-shaped ramp with a duration of 500 µs. This is followed by a free expansion during 2 ms (with the

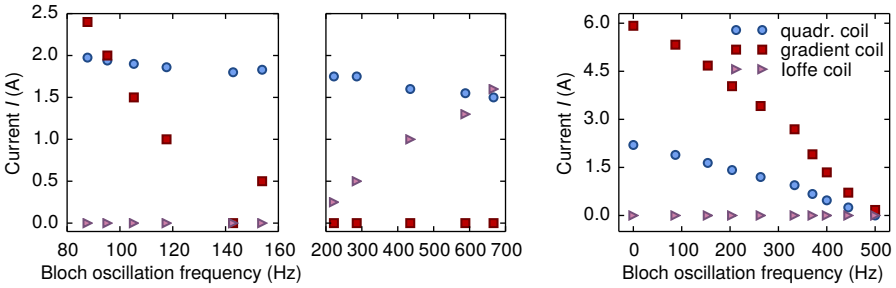

a. x oscillations b. y oscillations

Figure 5.2: *Bloch oscillation gradients.* The experimentally optimized currents in the upper quadrupole, gradient and Ioffe coils required to obtain a Bloch oscillation with a given frequency along x or y are plotted.

Table 5.1: *Bloch oscillation gradients.* The required currents in the upper quadrupole (in reverse direction), gradient and Ioffe coil (see Fig. 3.29 on page 62) as well as the measured Bloch oscillation frequencies are given for the gradients used to perform the Bloch oscillations presented in this chapter. Additionally, diagonal gradients were determined in order to explore the full B.Z. in future experiments. Throughout, a current of 2.2 A is run through the Feshbach coils to create a small bias field on the order of about 10 Gauss.

	DIR.	ν_B (Hz)	I_{uqp} (A)	$I_{grad.}$ (A)	I_{loffe} (A)
levitation of $m_F = -9/2$	·	0	2.2	5.92	0
x Bloch osc.	←	88(1)	1.975	2.4	0
y Bloch osc.	↓	95(1)	1.89	5.33	0
	→	91	2.45	9.6	0
	↙	233	1.55	1.05	0
	↗	239	2.915	11.5	0
	↖	233	2.25	1.85	0
	↘	235	2.08	9.45	0

Band mapping procedure

levitating magnetic fields still on). The magnetic fields are then abruptly switched off and we allow for 13 ms of free expansion under the influence of gravity. Using this band mapping procedure, the quasimomentum distribution can be obtained [Köhl, Moritz, Stöferle, Günter, *et al.*, 2005; Esslinger, 2010]. To ensure a faithful mapping of the lattice quasimomenta to the free space momentum acquired in TOF, the lattice intensity ramp must be fast enough such the tunneling during the ramp can be neglected but slow enough such that the atoms can follow the change in on-site trap frequency. Within this regime, the atoms stay adiabatically in their band while quasimomentum is approximately conserved.

Experimental images of the quasimomentum distribution obtained for different lattice geometries and lattice fillings are shown in Fig. 5.3 on the next page. The momentum distributions appear as in the extended zone scheme, see Fig. 5.4 on the following page. From these images, the actual quasimomentum distribution in the higher bands can therefore be reconstructed by folding the higher B.Z. back into the first one as indicated in the figure. When loading the atoms into the lattice using a smooth ramp, the energy levels within the band structure are populated according to the Fermi distribution, i. e. beginning from the lowest energy states, which are in our case located at the center of the first B.Z.. When increasing the atom number, higher B.Z. are gradually populated.

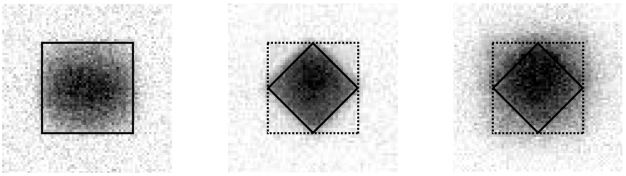

a. Square lattice b. Checkerboard lattice c. Checkerboard lattice, 2nd B.Z. partially filled

Figure 5.3: *Exemplary measured quasimomentum distributions.* An exemplary selection of detected quasimomentum distributions is shown for a square lattice ($V = 30\,E_R$) and a checkerboard lattice ($V_{X,Y} = 5\,E_R$, $V_{\bar{Z}} = 3\,E_R$, $\varphi = 0.4\pi$), where either only the first B.Z. or also the second B.Z. is partially filled. Different fillings of the B.Z. are achieved by varying the number of atoms loaded into the lattice. The first (solid lines) and second B.Z. (dotted) are drawn as a guide to the eye.

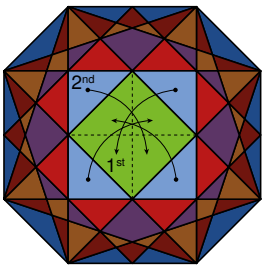

Figure 5.4: *Brillouin zone folding.* The first seven B.Z.s of our lattice are shown in the extended zone scheme. As an example, the folding of the second B.Z. back onto the first is indicated by the arrows and the dotted lines.

For example by modulating the intensity or the phase of the lattice, atoms can be excited to higher bands in order to obtain non-equilibrium situations where the population is inverted and higher B.Z.s are preferentially populated. Alternatively, population inversion can also be created by an abrupt change of the band structure, which can be induced by quickly switching to a different lattice depth. Two quasimomentum distributions obtained using the latter technique are shown in Fig. 5.5.

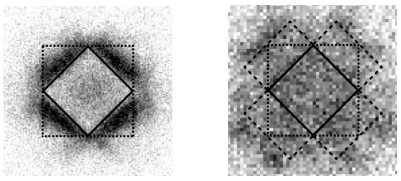

a. $V_X = 0.7\,E_R$ b. $V_X = 1.35\,E_R$

Figure 5.5: *Populating higher bands.* The plots show measured quasimomentum distributions obtained by loading into honeycomb lattices with $V_{\bar{X},Y,\bar{Z}} = [15, 6, 20]\,E_R$ (variable V_X) and abruptly switching off $\bar{X}$ in order to populate higher bands. The first (solid lines) and higher B.Z. (dotted and dashed) are drawn as a guide to the eye.

5.3 DETECTING THE DIRAC POINTS

This and the following sections of this chapter are partly based on the preprints of the following publications:

> L. Tarruell, D. Greif, T. Uehlinger, G. Jotzu, and T. Esslinger, *Creating, moving and merging Dirac points with a Fermi gas in a tunable honeycomb lattice*, Nature (London) **483**, 302 (2012), DOI:10.1038/nature10871, preprint on ArXiv e-prints, arXiv:1111.5020,

and

T. Uehlinger, D. Greif, G. Jotzu, L. Tarruell, T. Esslinger, L. Wang, and M. Troyer, *Double transfer through Dirac points in a tunable honeycomb optical lattice*, Eur. Phys. J. Special Topics **217**, 121 (2013), DOI:10.1140/epjst/e2013-01761-y, preprint on ArXiv e-prints, arXiv:1210.0904.

5.3.1 SINGLE TRANSFER

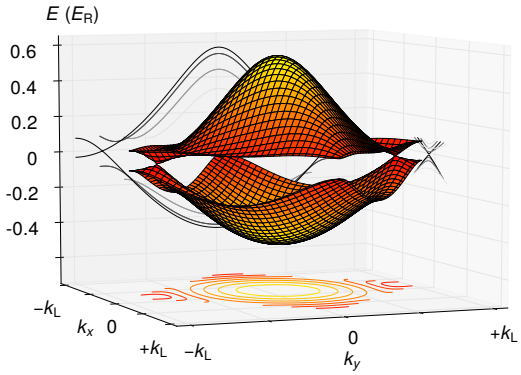

Figure 5.6: *Band structure.* The plot shows the band structure calculated by exact diagonalization of the single-particle Hamiltonian. Cuts in the vicinity of the two Dirac points are shown in the background. A contour plot of the lowest band is shown at the bottom.

In order to characterize the Dirac points using Bloch oscillations, we prepare the atoms as described above in the lowest energy band of a honeycomb lattice with

$$V_{\bar{X},X,Y} = [4.0(2), 0.28(1), 1.8(1)]\, E_R.$$

The calculated band structure for this lattice is shown in Fig. 5.6 and the resulting tunneling matrix elements are $t_{1,2,3}/h = [809, 610, 196]$ Hz. We then induce a Bloch oscillation along the x direction. The atoms are hence accelerated such that their Bloch wave vector k_x increases linearly up to the edge of the Brillouin zone, where a Bragg reflection occurs. The cloud eventually returns to the center of the band, performing one full Bloch oscillation [Ben Dahan *et al.*, 1996]. We then measure the quasimomentum distribution of the atoms in the different bands as described above.

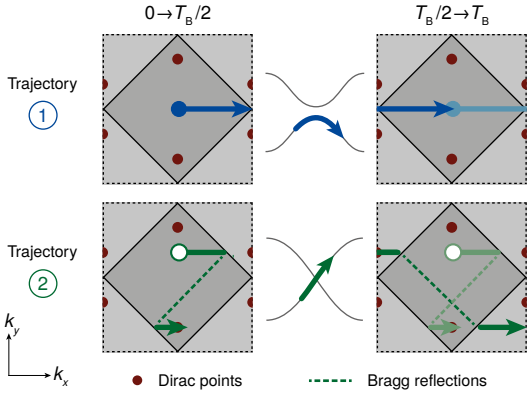

Figure 5.7: *Quasimomentum trajectories.* The cloud explores several trajectories in quasimomentum space simultaneously. For trajectory ① (blue solid circle) the atoms remain in the first energy band. In contrast, trajectory ② (green open circle) passes through a Dirac point at $t = T_B/2$. There, the energy splitting between the bands vanishes and the atoms are transferred to the second band. In the quasimomentum distribution at $t = T_B$, these atoms are missing in the first B.Z. and appear in the second one.

Owing to the finite momentum width of the cloud, trajectories with different Bloch wave vectors k_y are simultaneously explored during the Bloch cycle, as illustrated in Fig. 5.7. Neglecting the harmonic trap, one can treat trajectories for different k_y as independent. For a trajectory far from the Dirac points, the atoms remain in the lowest energy band (trajectory ①). In contrast, when passing through

Different quasimomentum trajectories are probed simultaneously by the cloud.

a Dirac point (trajectory ②), the atoms are transferred from the first to the second band because of the vanishing energy splitting at the linear band crossing. When measuring the quasimomentum distribution, these atoms are missing in the first B.Z. and appear in the second band, as can be seen in Fig. 5.8.

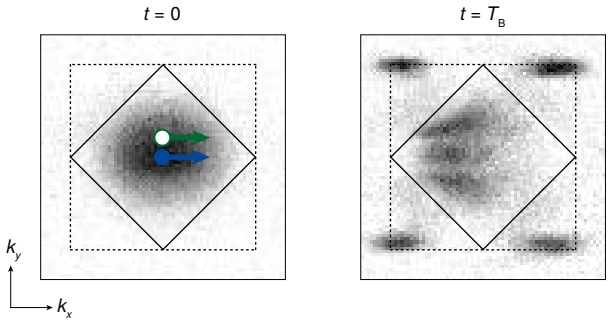

Figure 5.8: *Probing the Dirac points.* Quasimomentum distribution of the atoms before and after one Bloch oscillation of period T_B. In the first B.Z., stripes appear at the quasimomenta where atoms have been transferred to the second band. These atoms then appear at the corresponding four positions in the second B.Z., which are pair-wise identified by Bragg reflections.

Points of maximum transfer are identified with the Dirac points.

We identify the points of maximum transfer with the location of a minimal band gap. As can be seen from the experimental momentum distributions (*cf.* also the experiments where the Dirac points are moved, Section 6.2 on page 119), these minimal band gaps are located within the B.Z. at non-symmetry points and therefore cannot be mere band touchings, but must be linear crossings, as for example argued in [Wunsch *et al.*, 2008]. The energy resolution of the method is set by the characteristic energy of the applied force [Ben Dahan *et al.*, 1996] $E_B/h = F\lambda/2h = 88.6(7)$ Hz, which is small compared to the full bandwidth $W/h = 4.6$ kHz and the minimum band gap at the edges of the Brillouin zone $E_G/h = 475$ Hz.

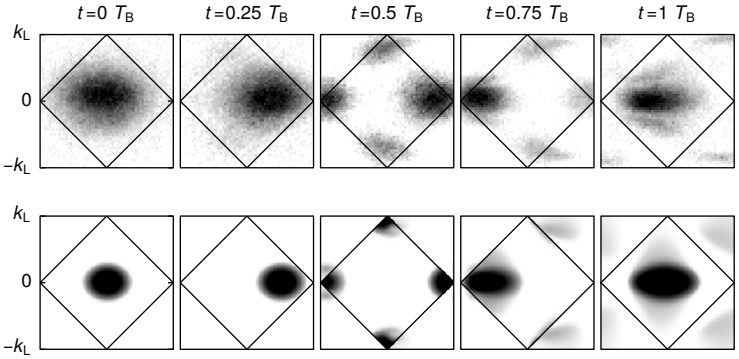

Figure 5.9: *Time-resolved Bloch oscillations along x.* A comparison of the quasimomentum distribution for Bloch oscillations resulting from a force pointing along x in the experiment (top) and in the numerical simulation of a 2D trapped system for $N = 256$ atoms (bottom) is shown. Parameters: $V_{\tilde{X},X,Y} = [4.3(2), 0.28(1), 1.8(1)]\, E_R$, $\theta = 1.013(1)\pi$, corresponding to $t_{1,2,3}/h = [789, 602, 166]$ Hz, $\gamma_{x,y}/h = [0.15, 0.59]$ Hz, $\Delta/h = 266$ Hz. $F\lambda/2h = 89$ Hz.

By repeatedly creating new samples and imaging them after a certain oscillation time, we obtain time resolved images during a Bloch cycle, which can be compared to the simulation of the trapped system, see Fig. 5.9. This allows for following the path of the atoms in more detail (see also Fig. 5.7): The atoms initially centered around $\mathbf{k} = 0$ in the lowest energy band move towards the right (corresponding to higher k_x) as they are accelerated by the force. For simplicity, in the following we will only discuss the trajectory of the upper part of the atomic cloud. As the

cloud touches the edge of the 1st B.Z. at $t = 0.25T_B$, the atoms are diagonally Bragg-reflected from the right upper edge to the left lower edge (dotted arrow in Fig. 5.7). This gives rise to the additionally populated momenta at the lower corner of the 1st B.Z.. The momenta appearing in the left corner get populated by consequent Bragg reflections of this additional momentum population as it reaches the right lower edge of the 1st B.Z..

At $t = T_B/2$, the lower momentum population starts to touch the Dirac point, where, due to Landau-Zener tunneling, a certain fraction of atoms transfers to the 2nd band. In Fig. 5.7, the two upper red half-circles denoting the Dirac point in the 2nd B.Z. correspond to the lower Dirac point in the 1st B.Z. and vice versa. Therefore, transferred atoms appear at the left outer edge of the 2nd B.Z. and are thereafter Bragg-reflected at the outer edge of the 1st B.Z. (dotted arrow) as they move right in the 2nd B.Z.. They appear as small stripes forking off from the lower momentum component in the 1st B.Z. at $t = 0.75T_B$. Due to the two consecutive Bragg-reflections, this stripe in the 2nd B.Z. appears at the k_y position of the Dirac point.

The fraction and position of the transferred atoms can be used to characterize the system.

After one full Bloch cycle ($t = T_B$), the main cloud has returned to the center of the 1st B.Z.. It exhibits two dips in the atomic distribution close to the upper and lower edge, which correspond to the missing atoms now appearing as four stripes in the 2nd B.Z. (the two lower and the two upper can be identified by Bragg reflections). Slight distortions and asymmetries as well as extensions into the 3rd B.Z. can be attributed to limitations and imperfections of our band-mapping procedure, namely that the quasimomentum resolution is limited to the *in situ* size of the atomic cloud and the fact that the method relies on finite band gaps.

Measuring the fraction of transferred atoms and the position of maximum transfer along k_y allows to characterize the system when tuning various parameters of the lattice, such as the sublattice energy offset and the tunneling timescales along different directions, *cf.* Chapter 6.

Dependence of the transferred fraction on the total atom number

The fraction of atoms ξ transferred to the 2nd B.Z. depends on the number of atoms at quasimomenta that pass in the vicinity of the Dirac points during the Bloch oscillation. It should therefore depend on the initial filling of the 1st B.Z., and thus on the atom number. We have investigated this dependence, with the according results shown in Fig. 5.10.

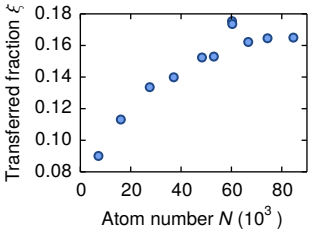

Figure 5.10: *Changing the atom number.* When the initial atom number loaded into the lattice is changed, the population of higher quasimomenta increases, which leads to a larger fraction of atoms ξ. Lattice parameters: $V_{\bar{X},X,Y} = [3.4(2), 0.12(1), 1.8(1)]\, E_R$.

5.3.2 DOUBLE TRANSFER

Bloch oscillations along y

Alternatively, the Dirac points can be probed by Bloch oscillations along the y direction[2]. For this measurement, we apply a force with a characteristic energy $E_B/h = F\lambda/2h = 95(1)$ Hz to the atoms along the y direction using another magnetic field gradient. After 11.5 ms (corresponding to roughly one Bloch oscillation cycle) we again measure the quasimomentum distribution of the gas.

The result of a typical measurement is shown in Fig. 5.11 on the following page. Again, for $t \approx T_B$ atoms appear in the 2nd B.Z. and are missing at the correspond-

2 We also performed Bloch oscillations along other directions, but the results are hard to interpret due to the inherent coupling of the two axes and of the real- and momentum-space movements owing to the presence of the external confinement.

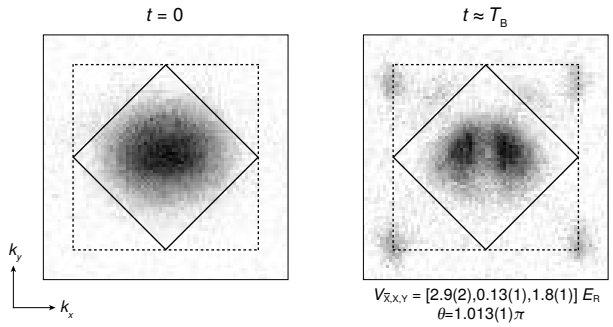

Figure 5.11: *Probing the Dirac points.* Absorption images of the quasimomentum distribution of the atomic cloud after preparation ($t = 0$) and after performing one Bloch oscillation cycle along the y direction ($t \approx T_B$). Color scale: black indicates a high density of atoms, white indicates no atoms.

ing quasimomenta in the 1st B.Z.. A qualitative difference between the situation for x and y oscillations however exists: in the latter case, since the Dirac points are located at $k_x \equiv 0$, they are always probed by the central trajectory, where one would therefore expect the maximum transfer efficiency. This is confirmed by comparison with the numerical simulation, see Fig. 5.12.

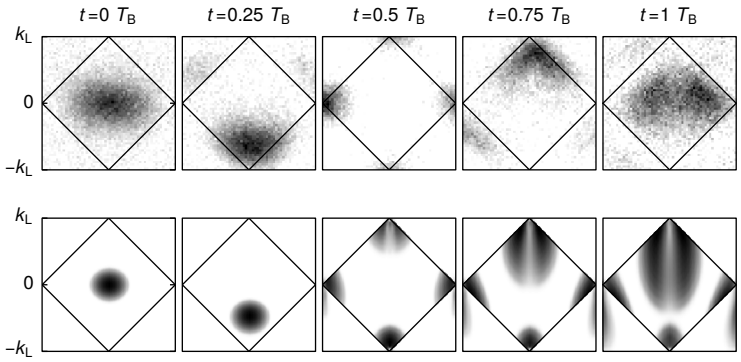

Figure 5.12: *Time-resolved Bloch oscillations along y.* Comparison of the quasimomentum distribution for Bloch oscillations resulting from a force pointing along y in the experiment (top) and in the numerical simulation of a 2D trapped system for $N = 256$ atoms (bottom). Parameters: $V_{\bar{X},X,Y} = [3.6(2), 0.28(1), 1.8(1)]\, E_R$, $\theta = 1.000(1)\pi$, corresponding to $t_{1,2,3}/h = [970, 589, 185]$ Hz, $\gamma_{x,y}/h = [0.18, 0.57]$ Hz, $\Delta/h = 21$ Hz. $F\lambda/2h = 89$ Hz. $T_B = 15$ ms for this measurement.

Sequential transfer through the two Dirac points

Another crucial difference is the fact that this central trajectory actually passes through the two Dirac points sequentially. To understand the consequences of this double passing of the Dirac points, we attribute a transfer probability ξ_S to a single band crossing along a k_x-trajectory, see Fig. 5.13 on the facing page. The double transfer must in principle be treated as a coherent admixture of second band states acquired in the vicinity of the first band crossing, followed by a phase evolution, which is different for the first and second band due to the different shape of the bands, and an alteration of the admixture at the second crossing. The outcome then not only depends on the evolution of the states in the vicinity of the points, but also on the phase acquired in between, which can lead to constructive or destructive interference at the second Landau-Zener transition.

Stückelberg interferometer

This system therefore effectively realizes a Stückelberg interferometer [Shevchenko *et al.*, 2010]. The phenomenon of Stückelberg interferometry has been realized in various two-level systems, for example in atomic physics [Stückelberg, 1932], recently in superconducting qubits [Oliver *et al.*, 2005], as well as

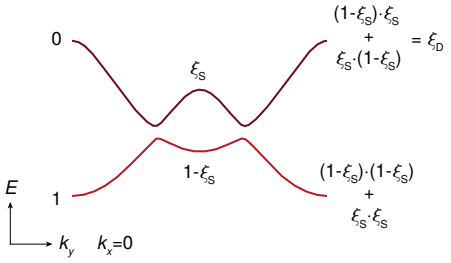

Figure 5.13: *Double Landau-Zener transfer.* Cut through the band structure at $k_x \neq 0$. During one Bloch cycle, the atoms pass through two band crossings. Neglecting the phase evolution (see Section 6.2.3 on page 122), each band crossing has a transfer probability ξ_S. For $k_x = 0$, the band crossings would coincide with the two Dirac points and $\xi_S = 1$, but for $k_x \neq 0$, a gap is present in the respective cut through the band structure, and $\xi_S < 1$.

in ultracold atom systems [Zenesini *et al.*, 2010; Kling *et al.*, 2010]. For reasons which will be justified in Section 6.2.3 on page 122, we will however for the moment neglect the phase evolution and resulting interference of the two bands between the crossings.

Total transfer probability

The probability for ending up in the higher band after passing the second crossing can then be obtained by simply multiplying the probabilities for transfer at the two crossings and summing up the two possible paths:

$$\xi_D = \left(1 - \xi_S\right)\xi_S + \xi_S\left(1 - \xi_S\right) = 2\xi_S\left(1 - \xi_S\right). \tag{5.33}$$

The total transfer probability ξ_D is plotted as a function of the single transfer probability ξ_S in Fig. 5.14. The function has a maximum value of 1/2 for a Landau-Zener transition probability of $\xi_S = 1/2$, which leads to interesting consequences when ξ_S is varied, see below.

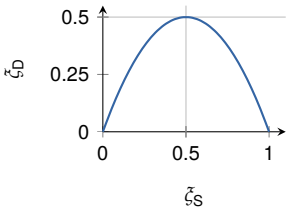

Figure 5.14: *Total probability of transfer for the sequential transition at two Dirac points.* The probability ξ_D of ending up in the second band after the sequential transfer through two Dirac points is shown as a function of the single transfer probability ξ_S.

5.4 MODELING THROUGH LANDAU-ZENER TRANSITIONS

5.4.1 GENERAL TREATMENT

Landau-Zener formula

In the following, we will develop a simple model which allows for calculating the transfer probability ξ_S in the vicinity of a single Dirac point. The basic assumption of the model is that a transfer at a Dirac point can be treated as a non-adiabatic Landau-Zener transfer with a finite velocity and a driving force F given by the applied magnetic field gradient. The transfer probability is then given by the famous Landau-Zener formula [Landau, 1932a,b; Zener, 1932]:

$$\xi = \exp\left(-2\pi\delta\right), \qquad \delta = \frac{\varepsilon^2}{4\hbar|\beta|} \tag{5.34}$$

where δ is the adiabaticity parameter of the transition, ε the (full) energy gap at the position of the crossing and β is the product of the asymptotic slope of the energy difference of the two states $\Delta E(\lambda)$ and the rate of change of the parameter describing the transition λ,

$$\varepsilon = \Delta E(\lambda_0), \qquad \beta = \left.\frac{\mathrm{d}\Delta E(\lambda)}{\mathrm{d}\lambda}\right|_{\lambda_0} \frac{\mathrm{d}\lambda}{\mathrm{d}t}, \tag{5.35}$$

where λ_0 is the position of the crossing.

Expression for the single transfer probability

In our specific case, the band gap at the position where the respective trajectory is closest to the Dirac point is taken as the spacing of the two energy levels. The asymptotic slope of the dispersion relation is taken from the expansion coefficients of the band structure in the vicinity of the Dirac point, $c_{x,y}$, and the rate of change of the driving parameter $\lambda = k_{x,y}$ is given by the applied force multiplied with the lattice spacing d:

$$\xi_S = \exp\left(-\frac{\pi(E_+(\mathbf{k}^\perp) - E_-(\mathbf{k}^\perp))^2}{4\hbar(\hbar c^{\parallel}_{x,y})(F_{x,y}/\hbar)}\right). \tag{5.36}$$

The slopes $c_{x,y}$ are obtained from the linear expansion of the energy spectrum of the tight-binding model in the vicinity of the Dirac points, as detailed in Section 4.3.1 on page 88:

$$\begin{aligned} c_x &= \frac{\pi}{\hbar k_L}(t_1 - t_3) \\ c_y &= 2\frac{\pi}{\hbar k_L} t_2 \sqrt{1 - \left(\frac{t_1 + t_3}{2t_2}\right)^2}. \end{aligned} \tag{5.37}$$

They are assumed to be independent on whether the trajectory passes exactly through the Dirac point or only at a certain distance to it. Additionally, we also make use of the tight-binding expansion to calculate the gap, where we denote $k^\perp_{x,y}$ as the point of least distance to the Dirac point on the respective trajectory. With $z(\mathbf{k})$ denoting the off-diagonal term of the tight-binding Hamiltonian and Δ the gap at the Dirac points due to a A-B site offset, the expression becomes:

$$\xi_S = \exp\left(-\pi^2 \frac{|z(\mathbf{k}^\perp)|^2 + \Delta^2/4}{\hbar c^{\parallel}_{x,y} k_L F_{x,y} d}\right). \tag{5.38}$$

MOMENTUM-SPACE INTEGRATION OF TRANSFER FRACTIONS

In the following, we describe how the total transfer ξ for the entire atomic cloud in 3D is calculated from the momentum-dependent transfer $\xi_D(k_{x,y})$ following the procedure presented in [Lim *et al.*, 2012]. We assume a semi-classical expression for the energy of the particles

$$\varepsilon(\mathbf{k}, \mathbf{r}) = \frac{\hbar^2 k_x^2}{2m_x} + \frac{\hbar^2 k_y^2}{2m_y} + \frac{\hbar^2 k_z^2}{2m_z} + \frac{1}{2}\left(m_x\omega_x^2 x^2 + m_y\omega_y^2 y^2 + m_z\omega_z^2 z^2\right), \tag{5.39}$$

where the effective masses $m_{x,y,z}$ are obtained by expanding the dispersion relation around the Bloch wave vector $\mathbf{k} = 0$ in the tight-binding regime and $\omega_{x,y,z}$ are the trapping frequencies in the three different directions. At zero temperature the expression for the integrated transfer fraction is then given by

$$\xi = \frac{\int_{\varepsilon(\mathbf{k},\mathbf{r})<\mu} \xi_D(k_{x,y})\mathrm{d}\mathbf{k}\mathrm{d}\mathbf{r}}{\int_{\varepsilon(\mathbf{k},\mathbf{r})<\mu} \mathrm{d}\mathbf{k}\mathrm{d}\mathbf{r}} = \frac{96}{15\pi k_F}\int_0^{k_F} \xi_D(k_{x,y})\left(1 - \frac{k_{x,y}^2}{k_F^2}\right)^{5/2} \mathrm{d}k_{x,y}. \tag{5.40}$$

Here we used the fact that the transfer only depends on $k_{x,y}$, and denote the Fermi wave vector $k_F = \sqrt{2m_{x,y}\mu}/\hbar$ and the chemical potential μ. For the semi-classical expression of the energy of the particles, the total atom number N is related via $\mu = \hbar\bar{\omega}(6N)^{1/3}$, where $\bar{\omega}$ is the geometric mean of the trapping frequencies.

Using this momentum-space integration and the tight-binding parameters as obtained from the Wannier function calculation, the calculated transfer fractions

for Bloch oscillations along x are found to be in good agreement with the experimental data, see Fig. 6.8 on page 125. For oscillations along y, the transfer fraction agrees well if the two Dirac points are separated from each other. The theory overestimates the transfer efficiency close to the point where the Dirac points merge.

5.4.2 TRANSFER EFFICIENCIES FOR DIFFERENT TRAJECTORIES

For oscillations along y, upon closer evaluation of the measured quasimomentum trajectories for different lattice parameters, we surprisingly observe a single or a double slit of missing atoms in the lowest B.Z. after one full Bloch cycle, see Fig. 5.15. The appearance of a double-peak feature in the transfer fraction $\xi_D(k_x)$ is a direct consequence of the double transition through the two band crossings. The single transfer probability ξ_S generally decreases for quasimomenta away from the center due to the increased gap at the crossing. The transfer probability ξ_S is close to 1 at the two linear band crossings. Therefore, the maximum total transfer (i.e. $\xi_D = 1/2 \Leftrightarrow \xi_S = 1/2$) is always reached at a finite value of k_x. For the lattice parameters used in the left panel of Fig. 5.15, the trajectories where $\xi_S = 1/2$ are located close to the central $k_x = 0$ line, such that due to limited momentum resolution only a single central slit of missing atoms is visible. For the parameters used in the right panel, however, two distinct transfer maxima appear, since here the points of maximum transfer are located further away as a result of the altered band structure.

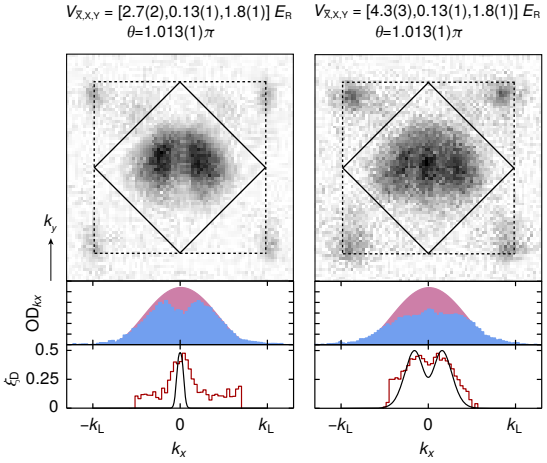

Figure 5.15: *Transfer for different quasimomentum trajectories.* Transfer for two sets of lattice parameters. Left. Maximum transfer is observed for a central trajectory. Right. Maximum transfer happens to the left and right of the central trajectory. The plots depict the line sums along k_y of the measured optical densities as a function of k_x (blue area) and the expected line sums without transfer (purple area). From this the transfer $\xi_D(k_x)$ is calculated and compared to the prediction of the analytical model (red and black curve, for the model see below).

For a quantitative treatment, we perform a line sum of the optical density (OD) in the 1st B.Z. (blue area in the figure). The initial cloud profile obtained from a fit to the quasimomentum distribution after a Bloch cycle for a set of lattice parameters not giving rise to Dirac points is shown in purple. From these two profiles, the experimental transfer fraction $\xi_D(k_x)$ (red curve below) can be obtained. As can be seen in the figure, the transfer is peaked at $k_x = 0$ for the left situation, whilst we observe a double-peak (with a dip at $k_x = 0$) for the situation on the right.

A UNIVERSAL HAMILTONIAN DESCRIBING THE TOPOLOGICAL TRANSITION

The transfer efficiencies per trajectory can be compared to theory. To evaluate the transfer probability ξ_S we use, instead of the general Landau-Zener model outlined above, a simplified effective Hamiltonian well suited for describing the dispersion relation close to the two Dirac points as well as the merging transition.

This approach has been worked out in detail in Refs. [Montambaux *et al.*, 2009a; Lim *et al.*, 2012]. The following Hamiltonian is used:

$$H = \begin{pmatrix} 0 & \Delta_* + \frac{\hbar^2 k_y^2}{2m_*} - ic_x k_x \\ \Delta_* + \frac{\hbar^2 k_y^2}{2m_*} + ic_x k_x & 0 \end{pmatrix}. \tag{5.41}$$

Here, $\Delta_* = -c_y^2 m_* / \left(2\hbar^2\right)$ defines the *merging gap*, m_* the effective mass along k_y at the saddle point between the two Dirac points and c_x and c_y the slopes of the dispersion relation along the different directions at the Dirac point. Their values are directly obtained from the lattice parameters using approximate expressions extracted from a fit to the exact band structure [Lim *et al.*, 2012]. Denoting the gap at the Dirac points with Δ, the transfer probability for oscillations along y is then

$$\xi_S = \exp\left(-\pi \frac{c_x^2 k_x^2 + \Delta^2/4}{\hbar c_y F}\right). \tag{5.42}$$

This expression differs from Eq. (5.38) on page 114 by the use of the simpler linear dispersion model to calculate the gap at a finite distance of the trajectory with respect to the Dirac point ($c_x^2 k_x^2$ in this case). In Eq. (5.38), the full off-diagonal element of the tight-binding Hamiltonian is used ($|z(\mathbf{k}^\perp)|^2$). The theoretical prediction of this simple analytical model is shown as the black curve in the bottom panel of Fig. 5.15 on page 115. The main features of the experimental momentum-resolved transfer fractions obtained from the atomic distribution in the lowest band are captured by theory. Deviations are possibly due to the finite resolution of the band-mapping technique as well as the uncertainties in the calibration of $V_{\bar{X}}$.

Numerical simulation of the time evolution

The simple picture of two independent Landau-Zener transitions is confirmed when performing the numerical time evolution of a trapped 2D lattice system in a tight binding limit, see Fig. 5.16. The transfer fraction at $k_x = 0$ increases with time on the left panel as the atoms pass the two Dirac points. On the right, however, after having passed through the first crossing, the transferred fraction decreases again. In contrast, the transferred fraction increases monotonously in both cases for quasimomenta away from the center.

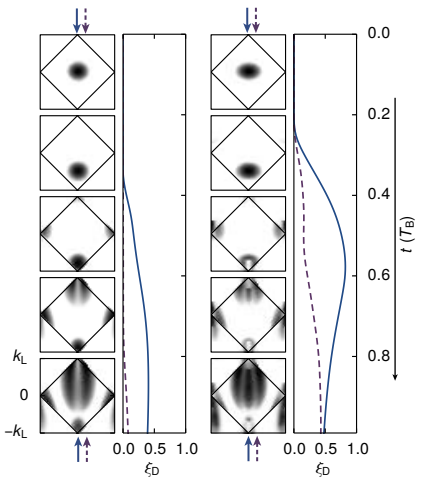

Figure 5.16: *Transfer for different quasimomentum trajectories in the numerical simulation.* Numerical simulation of a trapped 2D system with $N = 256$ atoms: quasimomentum distribution during one Bloch cycle for two exemplary situations. The population of the 2nd B.Z. is plotted for two different k_x-trajectories (position indicated by the colored arrows). Simulation parameters for the left simulation: $t_{1,2,3}/h = [969, 589, 184]$ Hz, $\gamma_{x,y}/h = [0.09, 0.28]$ Hz, $\Delta/h = 20$ Hz, $F\lambda/2h = 63$ Hz; right: $t_{1,2,3}/h = [525, 620, 131]$ Hz, $\gamma_{x,y}/h = [0.09, 0.28]$ Hz, $\Delta/h = 17$ Hz, $F\lambda/2h = 63$ Hz.

MANIPULATING THE DIRAC POINTS

6

In this chapter, using the methods developed in the previous chapter, the changes occurring in the band structure when introducing an energy offset between the *A* and *B* sublattices are studied. Moreover, the movement of the Dirac points when deforming the lattice geometry is detected from the quasimomentum distributions, allowing for the study of the transition to a dimerized lattice geometry. Finally, the transition from a honeycomb lattice to a square lattice and the dependence of the transfer efficiency on the magnitude of the Bloch oscillation gradient is investigated.

CHAPTER CONTENTS

This chapter is partly based on the preprints of the following publications:

> L. Tarruell, D. Greif, T. Uehlinger, G. Jotzu, and T. Esslinger, *Creating, moving and merging Dirac points with a Fermi gas in a tunable honeycomb lattice*, Nature (London) **483**, 302 (2012), DOI:10.1038/nature10871, preprint on ArXiv e-prints, arXiv:1111.5020,

and

> T. Uehlinger, D. Greif, G. Jotzu, L. Tarruell, T. Esslinger, L. Wang, and M. Troyer, *Double transfer through Dirac points in a tunable honeycomb optical lattice*, Eur. Phys. J. Special Topics **217**, 121 (2013), DOI:10.1140/epjst/e2013-01761-y, preprint on ArXiv e-prints, arXiv:1210.0904.

6.1 FROM MASSLESS TO MASSIVE DIRAC POINTS

By changing the frequency detuning between the $\bar{\text{X}}$ and X lattice beams, we can change the phase θ in the resulting optical potential, leading to an energy offset between the sites on the *A* and *B* sublattices, as discussed in Section 3.3.1 on page 54. Breaking the inversion symmetry of the lattice leads to a gap opening at the Dirac points, which effectively corresponds to the transition from a system containing massless to one containing massive Dirac fermions in the vicinity of the (avoided) band crossing. In this section, the corresponding transition is studied both for single transfers through the Dirac points (oscillations along x) as well as double transfers (oscillations along y).

6.1.1 SINGLE TRANSFER

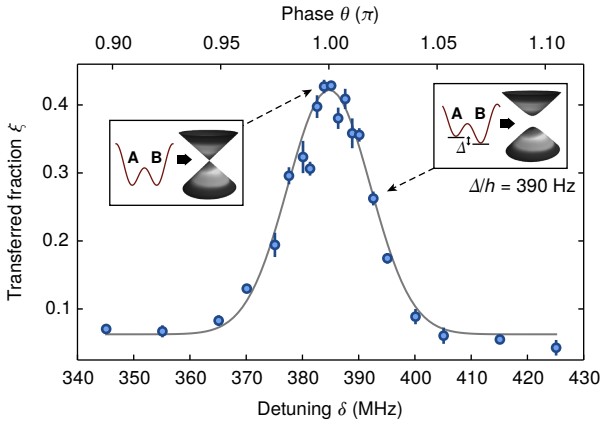

Figure 6.1: *Gap opening.* The plot shows the dependence of the total fraction of atoms transferred to the second band ξ on the detuning of the lattice beams δ, which controls the sublattice energy offset Δ. The maximum indicates the point of inversion symmetry, where $\Delta = 0$ ($\Leftrightarrow\ \theta = \pi$ in Eq. (5.32) on page 105) and the gap at the Dirac point vanishes. Away from the peak, the atoms behave as Dirac fermions with a tunable mass (see insets). Values and error bars denote the mean and standard deviation of five consecutive measurements, whereas the solid line is a gaussian fit to the data.

Inversion symmetry is broken by varying the sublattice offset Δ

To investigate how breaking the inversion symmetry of the lattice affects the Dirac points, we vary the sublattice offset Δ as described above and measure the total fraction of atoms transferred to the second band ξ. The results obtained for a honeycomb lattice with

$$V_{\bar{\mathrm{X}},\mathrm{X},\mathrm{Y}} = [3.6(2), 0.28(1), 1.8(1)]\, E_{\mathrm{R}}$$

are displayed in Fig. 6.1. The plot shows a sharp maximum in the transferred fraction. We identify this situation as the point of inversion symmetry $\Delta = 0$ ($\Leftrightarrow\ \theta = \pi$), in good agreement with the independent calibration using Raman-Nath diffraction on a ^{87}Rb BEC (see Section 3.2.5 on page 53). We use the point of inversion symmetry as determined using this method as the calibration for further measurements. At this point, the band gap at the Dirac points vanishes for an infinite system in the absence of an external confinement. However, in our system, trap and finite size effects lead to a small gap opening, even at the point of perfect inversion symmetry. This gap opening is nonetheless found to be below the experimental resolution. When breaking the inversion symmetry, a gap opens up, and the population in the second band decreases symmetrically on both sides of the peak, indicating the transition from massless to massive Dirac fermions.

6.1.2 DOUBLE TRANSFER

Dip in the transfer fraction for y oscillations

At first sight, for Bloch oscillations along the y direction, one would expect a similar behavior of the transferred fraction of atoms as a function of the gap at the Dirac point. However, the double transfer through the two Dirac points leads to unexpected additional features, see Fig. 6.2 on the facing page. In the figure, the transferred fraction of atoms ξ as a function of the symmetry phase is plotted for three different sets of lattice parameters. For parameters deep in the honeycomb regime, we observe a pronounced dip in ξ at the point where naively the maximum transfer would be expected.

This feature is a direct consequence of the dependence of the total transfer efficiency ξ_{D} for a transfer through both points on the transfer efficiency for a single

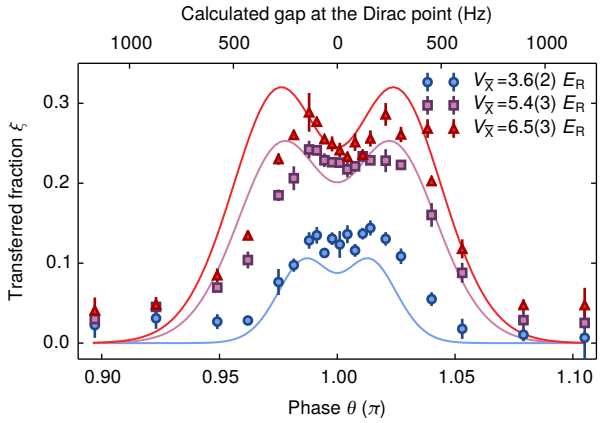

Figure 6.2: *Scanning the gap at the Dirac point.* The total transfer fraction ξ is measured for three different lattice depths $V_{\bar{X}}$ versus the phase θ, which directly controls the energy offset between neighboring sites. The gap at the Dirac point is obtained from the band structure calculation. Values and error bars denote the mean and standard deviation of five consecutive measurements. The solid lines show the theoretical predictions from the simple analytical model without fitting parameters including the integration over k_x.

point ξ_S. Deep within the honeycomb regime, ξ_S is well above 1/2 in the vicinity of the Dirac points for $\theta = \pi$, leading to a total transfer efficiency that is actually lower than that obtained for $\theta \approx 0.98\pi$. Already at this point, a non-negligible gap is present at the Dirac points, lowering ξ_S to $\approx$ 1/2, such that the maximum total transfer efficiency is reached.

The double-peak structure reduces for smaller values of $V_{\bar{X}}$. This is caused by the decreased slope c_y and increased slope c_x of the dispersion relation close to where the two Dirac points merge and annihilate, leading to an overall reduction of ξ_S and thus to a less pronounced double-peak feature. The main features of the experimental results agree with the predictions of the simple analytical model without fitting parameters, using an integration over the entire cloud. The point of inversion symmetry has been calibrated using Bloch oscillations along x. The slight shift of the symmetry axis for the data presented here is smaller than an estimate for a possible systematic error[1].

Estimate for a residual gap at the Dirac points

The comparison to theory allows for obtaining an upper estimate for a possible small residual gap at the Dirac points. For the dataset where $V_{\bar{X}} = 3.6\,E_R$, a gap of 140 Hz would already lead to a vanishing of the double-peak structure. From this we conclude that the residual small gap at the Dirac points caused by the finite size of the system and the trap is considerably smaller than 140 Hz. This is about a factor of 30 smaller than the bandwidth.

6.2 MOVING THE DIRAC POINTS

The relative strength of the tunnel couplings between the different sites of the lattice fixes the position of the Dirac points inside the B.Z., as well as the slope of the associated linear dispersion relation [Hasegawa *et al.*, 2006; Zhu *et al.*, 2007; Wunsch *et al.*, 2008; Montambaux *et al.*, 2009b; Lee, Grémaud, *et al.*, 2009]. However, the tunability of our optical lattice structure allows for an independent adjustment of the tunneling parameters along the x and y directions simply by controlling the intensity of the laser beams. Under the condition $t_1^2 + t_3^2 = 2t_2^2$ for the tunnel couplings, the slope of the Dirac cones is the same in all directions (see Section 4.3.1 on page 88), while being anisotropic otherwise. The distance of the Dirac points

1 The estimate is based on an comparison the independent calibration of the $\theta = \pi$ point using Raman-Nath diffraction on a ^{87}Rb BEC [Tarruell *et al.*, 2012].

to the corners of the B.Z. along k_y can be varied between 0 and $k_L/2$, whilst $k_x = 0$ due to reflection symmetry [Asano *et al.*, 2011]. Here $2k_L = 4\pi/\lambda$ is the extent of the first B.Z..

6.2.1 SINGLE TRANSFER

We exploit the momentum resolution of the interband transitions to directly observe the movement of the Dirac points. Starting from a honeycomb lattice with

$$V_{\bar{X},X,Y} = [5.4(3), 0.28(1), 1.8(1)]\, E_R,$$

we gradually increase the tunneling along the x direction by decreasing the intensity of the $\bar{X}$ beam. As displayed in Fig. 6.3, the position of the Dirac points continuously approaches the corners of the Brillouin zone, as expected from the *ab initio* 2D band structure calculation (gray line).

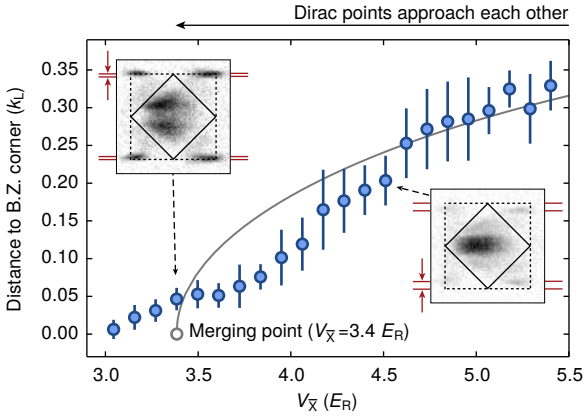

Figure 6.3: *Movement of the Dirac points.* The plot shows the distance of the Dirac points to the corners of the B.Z., as measured through momentum-resolved interband transitions. The tunneling along the x direction increases when decreasing the lattice depth $V_{\bar{X}}$. The distance is extracted from the second band quasimomentum distribution after one Bloch cycle (see insets). The merging of the two Dirac points at the corners of the B.Z. is signaled by a single line of missing atoms in the first band. Values and error bars are the mean and standard deviation of three to nine measurements. The solid line is the prediction of a 2D band structure calculation without any fitting parameters.

When changing the lattice depth $V_{\bar{X}}$, not only the position of the Dirac points along k_y changes. As can be seen when drawing the energy splitting between the two minibands as obtained from the exact band structure calculation for different lattice parameters in Fig. 6.4 on the next page, the Dirac cones assume an anisotropic shape as they move towards the center of the B.Z.. The decreasing slope of the dispersion relation along k_x close to the Dirac points heavily influences the transferred fraction of atoms as $V_{\bar{X}}$ is varied, a feature that will be studied in Section 6.3 on page 123.

6.2.2 DOUBLE TRANSFER

Similar to the measurement presented in Fig. 5.15 on page 115, we investigate the momentum-dependent transfer fraction for oscillations along y as function of the position of the Dirac points. Figure 6.5a on the facing page shows the results of such a scan versus $V_{\bar{X}}$ along with the theoretical expectation based on the simple analytical model. For $V_{\bar{X}} < 3.4\,E_R$ there are no Dirac points in the band structure and thus no significant transfer is observed (no missing atoms). For $V_{\bar{X}} > 3.4\,E_R$ two Dirac points are present in the band structure, leading to the

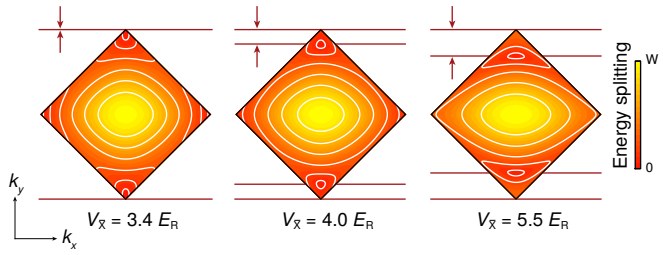

Figure 6.4: *Position of the Dirac points.* The contour plots display the energy splitting between the two lowest bands. It shows the displacement of the Dirac cones inside the Brillouin zone, as well as their deformation depending on the lattice depth $V_{\bar{X}}$.

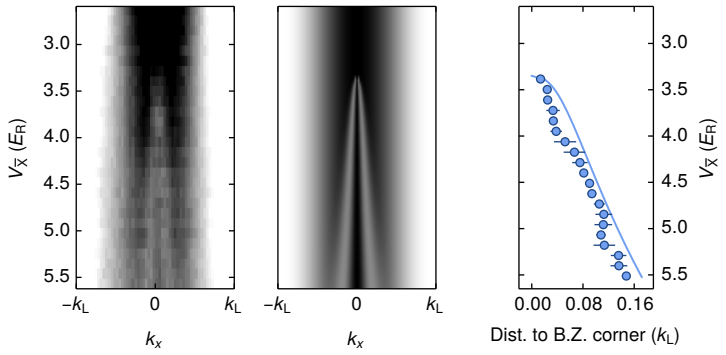

a. Momentum-dependent transfer fractions

b. Position of the transfer peak

Figure 6.5: *Transfer for different lattice parameters.* a. The plots show the experimental (left) and theoretical (right) quasimomentum distribution $\xi_D(k_x)$ in the 1st B.Z. after one full Bloch cycle integrated along the k_y direction for different values of $V_{\bar{X}}$. The experimental data is the average of three consecutive measurements. The theoretical quasimomentum distributions are calculated under the assumption of a fixed k_x distribution for the initial atomic cloud, which is obtained from a fit to the density profile at $V_{\bar{X}} = 2.5\,E_R$ in the left panel. At this point the band structure does not contain Dirac points. A dark color indicates a high atomic density. b. The extracted position of maximum transfer along k_x using the distribution in the 2nd band is plotted. Values and error bars denote the mean and standard deviation of three measurements. The solid line shows the theoretical expectation of the maximum transfer position using the simple analytical model without free parameters. The experimental data was taken with θ set to $1.000(1)\pi$.

formation of a progressively more pronounced double-peak feature as $V_{\bar{X}}$ gets larger. This double-peak feature is caused by the same effect as in the measurements versus the site energy offset: it is a consequence of the overall increased single transfer probability ξ_S for larger $V_{\bar{X}}$ due to the deformation of the Dirac cones, shifting the points of maximum transfer ξ_D (where $\xi_S = 1/2$) further apart. The position along k_x in quasimomentum space for maximum transfer can in fact be obtained by extracting the peak position of the atomic distribution in the 2nd B.Z. after taking a line sum along k_y. The results of this procedure are shown in Fig. 6.5b, which are in good agreement with the calculated position obtained from the simple analytical model.

The presence of a transition regime from a single- to a double-peak feature in the momentum-resolved transfer $\xi_D(k_x)$ depends on the gap at the Dirac points, which is controlled by the energy offset between neighboring sites. For a vanishing gap only double-peak features appear, as the single transfer in the center is always close to 1. This is the case for the data presented in Fig. 6.5, as $\theta \approx \pi$ for this dataset. In contrast, an overly large gap merely leads to single-peak profiles with a

very low overall transfer fraction, as the transfer in the center is already far below 1/2. Only if the gap is set to an intermediate value, a transition from a single- to a double-peak profile occurs for increasing $V_{\bar{X}}$, which is the case for the parameters of the measurements in Fig. 5.15 on page 115.

6.2.3 STÜCKELBERG INTERFERENCE

Correction factor accounting for coherences

As already mentioned, a full description of the system studied here would necessarily take coherence into account. The two sequential band crossings along one k_x trajectory would therefore effectively realize a Stückelberg interferometer [Stückelberg, 1932; Shevchenko *et al.*, 2010] with an associated dynamical phase φ. This phase depends both on the energy difference between the upper and the lower path (see Fig. 5.13 on page 113) and the time spent in between the two crossings, and therefore on the lattice geometry and the applied force. In the simple analytical model used so far this phase has been neglected. In fact, it can be taken into account by multiplying the transfer fraction with a correction factor:

$$\xi_D' = 2\xi_S(1-\xi_S) \times 2\cos^2(\varphi_d + \varphi_S + \varphi_g), \tag{6.1}$$

where the dynamical phase φ_d, transfer phase φ_S (Stokes phase) and the geometric phase φ_g are defined as [Lim *et al.*, 2012, 2014]:

$$\varphi_d = \frac{1}{2}\int_{\tau_K}^{\tau_{K'}} \mathrm{d}\tau\ (E_+(\tau) - E_-(\tau)) = 2\int_0^{k_D} \mathrm{d}k_y \sqrt{\left(\Delta_* + k_y^2/(2m_*)\right)^2 + c_x^2 k_x^2}/F \tag{6.2}$$

$$\varphi_S = -\frac{\pi}{4} + \delta(\log\delta - 1) + \mathrm{Arg}\,\Gamma(1 - i\delta) \tag{6.3}$$

$$\varphi_g = \frac{1}{2}\int_{\tau_K}^{\tau_{K'}} \mathrm{d}\tau \left(\langle\psi_+|i\partial_\tau|\psi_+\rangle - \langle\psi_-|i\partial_\tau|\psi_-\rangle\right). \tag{6.4}$$

Here, Γ is the gamma function and $\delta = c_x^2 k_x^2/(2c_y F)$ the adiabaticity parameter of the Landau-Zener transfer (see Section 5.4.1 on page 113). The Stokes or transfer phase accounts for the phase skip at the transition and is similar to the phase skip at an optical beam splitter. The dynamical phase on the other hand is due to the temporal evolution of the eigenenergies of the two states in between the two points. Finally, the geometric phase takes into account the adiabatic evolution of the eigenstates between the two points and therefore includes the topological structure of the band structure [Lim *et al.*, 2014; Gasparinetti *et al.*, 2011]. It is equal to the difference in Berry phase pickup between the lower and the upper band on the path between the two points (τ_K and $\tau_{K'}$ are the times at which the respective Dirac point is crossed). As the two Dirac points have opposite chirality in our system, the two Berry phase pickups cancel and $\varphi_g = 0$.

Coherences in the experiment

Figure 6.6 on the facing page shows a comparison of the total 3D averaged transfer ξ versus $V_{\bar{X}}$ for the simple incoherent model (blue line) and the extended coherent model including this correction factor (purple dotted line). The experimental data agrees very well with the incoherent model, whereas the oscillatory behavior as predicted by the extended model cannot be observed.

For a correct treatment of the Stückelberg interference, the variation of the effective force F due to the harmonic confinement over the cloud size has to be taken into account. Using an estimate for the cloud size of approximately 30 µm based on the trapping frequencies, one calculates a variation of the effective force over the cloud on the order of 60 Hz. We include this effect by assuming a gaussian distribution of forces over the entire sample, leading to different Stückelberg oscillation frequencies and thus to a reduced visibility of the oscillations. The result

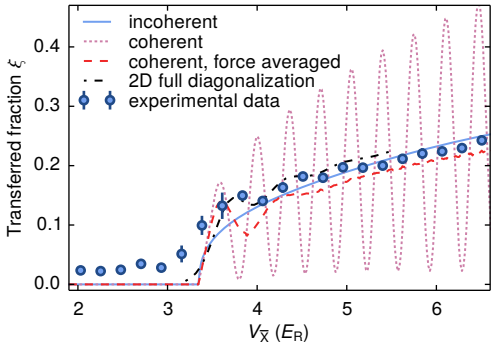

Figure 6.6: *Visibility of the Stückelberg interference.* The total transfer fraction ξ versus $V_{\bar{X}}$ for $\theta = 1.000(1)\pi$ is shown. Values and error bars denote the mean and standard deviation of three consecutive measurements. The lines show the theoretical prediction for the fully integrated transfer fraction using the simple incoherent analytical model (blue solid line) and the extended model including the Stückelberg correction factor (purple dotted line). The red dashed line includes a gaussian distribution of forces with a width of 60 Hz resulting from the harmonic trapping potential. The result from the numerical time evolution of the trapped 2D system for $N = 256$ atoms is shown as the black dash-dotted line. Simulation parameters: $t_{1,2,3}$ as obtained from a fit to the calculated band structure for the given lattice parameters, $\gamma_{x,y}$ as deduced from the lattice parameters. $\Delta/h \approx 20$ Hz, $F\lambda/2h = 89$ Hz.

is shown in Fig. 6.6, where the force averaged curve (red dashed line) is in close agreement with the experimental data. This picture is confirmed by the results of the numerical simulation of the trapped lattice system (black dash-dotted line), which already shows a comparable reduction in visibility of the oscillations for a purely 2D system. While additional effects, such as the variation of the lattice depths along the third spatial axis z, are smaller than the effect identified above, they probably cause the remaining loss of visibility leading to no visible oscillations in the experimental data. Therefore it can be safely assumed that the simple incoherent version of the analytical model is sufficient for comparison with the experiment.

6.3 MERGING DIRAC POINTS

As $V_{\bar{X}}$ is lowered, the two Dirac points move towards the corner of the B.Z.. When reaching the corners, they merge, annihilating each other. There, the dispersion relation becomes quadratic along the k_y axis, while remaining linear along k_x. Beyond this critical point, a finite band gap appears for all quasimomenta of the B.Z.. This situation signals the transition between band structures of two different topologies, one containing two Dirac points and the other none. We here observe this transition for the first time in a system with hexagonal lattice geometry. The observation has subsequently been reproduced in a hexagonal array of microwave cavities [Bellec *et al.*, 2013]. For purely 2D honeycomb lattices at half filling, it corresponds to a Lifshitz phase transition (i.e. a transition in the topological structure of the Fermi surface) from a semimetallic to a band insulating phase [Zhu *et al.*, 2007; Wunsch *et al.*, 2008], *cf.* Section 8.6.2 on page 160.

Mapping out the transition line to a dimerized system

We experimentally map out the transition line by recording the fraction of atoms transferred to the second band ξ as a function of the lattice depths $V_{\bar{X}}$ and V_X, while keeping $V_Y = 1.8(1)\,E_R$. The results are displayed in Fig. 6.7 on the following page, left panel. There, the onset of population transfer to the second band signals the appearance of Dirac points in the band structure of the lattice. The transferred fraction ξ decreases for large values of $V_{\bar{X}}$, as the Dirac points move beyond the momentum width of the cloud.

Finite extent of the atomic cloud

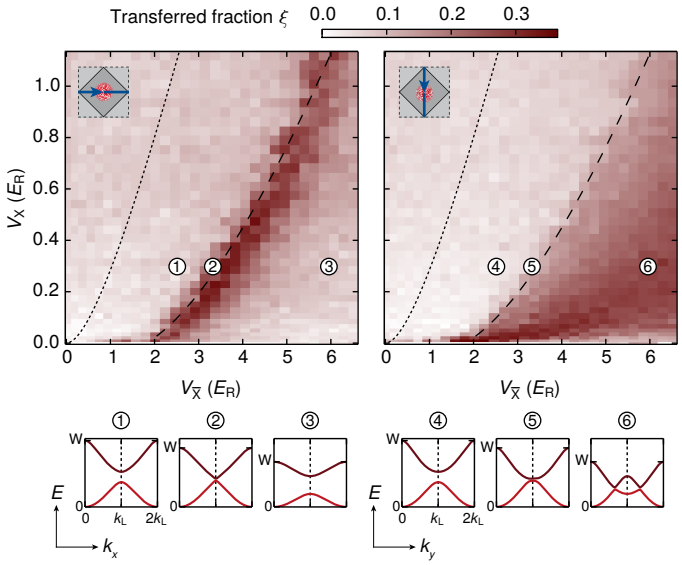

Figure 6.7: *Transition to the dimerized geometry.* The plots show the fraction of atoms transferred to the second band ξ as a function of lattice depths $V_{\bar{X}}$ and V_X, with $V_Y = 1.8(1)\,E_R$. We consider trajectories in quasimomentum space along the k_x and k_y directions (left and right panel, resp.). To maximize the transfer for the k_y trajectories, where the cloud successively passes the two Dirac points, we set $\theta = 1.013(1)\pi$ for both plots. In both cases, the onset of population transfer to the second band signals the topological transition where the Dirac points appear. The dotted and the dashed lines are the theoretical predictions for the transition line between the triangular and dimerized and between the dimerized and the honeycomb geometry, respectively, calculated without any fitting parameters. The insets show cuts of the band structure along the k_x and k_y axes (with $k_y = k_y^D$ and $k_x = 0$, respectively), illustrating the behavior of the Dirac points when increasing $V_{\bar{X}}$.

The Bloch oscillations along y allow for the investigation of very anisotropic Dirac cones, which become almost flat along the k_x direction as we approach the crossover to a 1D lattice structure ($V_{\bar{X}} \gg V_X$). As displayed in Fig. 6.7, right panel, we again identify the transition through the onset of population transfer to the second band. The results for the transition line obtained for both measurement series are in excellent agreement with *ab initio* band structure calculations.

Numerical calculation of the transfer efficiencies for the different lattice geometries

In Fig. 6.8 on the facing page, the calculated integrated transfer efficiency is shown, as obtained from the general Landau-Zener model using the same lattice parameters as in the experiment. The experimental results are qualitatively reproduced, with an excellent agreement of the quantitative transfer efficiencies for oscillations along y. Deviations for the oscillations along x appear close to the merging transition, possibly due to experimental imperfections that limit the maximum achievable transfer efficiency at the Dirac points.

6.4 SCANNING THE INTERFERENCE PHASE

Scanning φ corresponds to a decrease in V_X

By scanning the interference phase φ, the transition from a honeycomb lattice structure to a square geometry can be observed, as a reduction of the interference term in the potential essentially corresponds to a decrease in the lattice depth V_X. Additionally, such a scan can be used as a calibration for the interference phase stabilization mechanism allowing to find the phase setting at which the interference of X and Y is maximized. Figure 6.9 on the next page shows the result of such a measurement using Bloch oscillations both along x and y. The lattice parameters are set such that the geometry is close to the merging line of the two Dirac points for $\varphi = 0$. For oscillations along x, the transferred fraction decreases as the

Calibration of the point of maximum interference

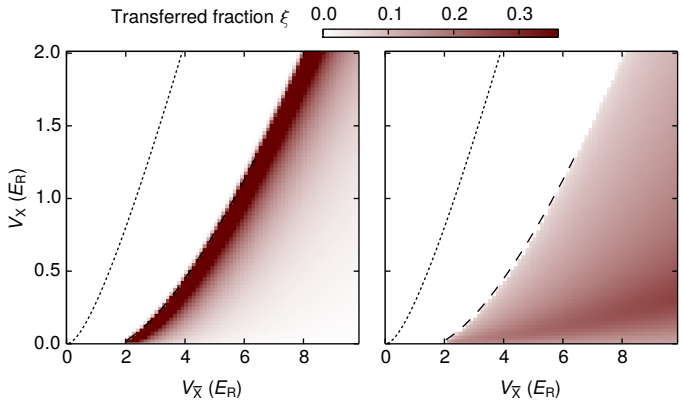

Figure 6.8: *Transition to the dimerized geometry: numerically calculated transfer efficiencies.* The integrated transferred fraction for oscillations along x (left panel) and y (right panel) is calculated using the general Landau-Zener model detailed in Section 8.6.2 on page 160. For comparability, the color scale is set to the same range as in Fig. 6.7 on page 124. For the Bloch oscillations along x the numerically calculated maximum transfer efficiencies close to the merging line however exceed this scale and reach values of more than 80%.

interference term becomes smaller, owing to the fact that the Dirac points move out of the highly populated quasimomenta in the middle of the cloud, and the additionally decreasing slope c_x of the dispersion relation close to the Dirac points. For y oscillations, the transferred fraction first increases as the slope c_y gets larger, until it reaches its maximum, which is located close to where $\varphi \approx 180°$ or equivalently $V_X \approx 0$. The transfer efficiency should then drop to zero as the interference is completely removed and the two minibands become one band in the larger square B.Z.. Since the interference phase is most sensitive to imperfections in the phase stabilization scheme at the point where $\varphi = 180°$, the interference is never fully removed during the course of a Bloch oscillation, leading to a considerable amount of atoms that are detected in the 2nd B.Z..

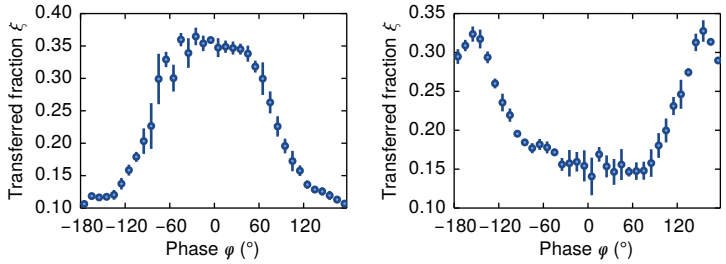

a. x oscillations b. y oscillations

Figure 6.9: *Scanning the interference phase.* For a system with a geometry close to the merging line ($V_{\bar{X},X,Y} = [3.6(1), 0.28(1), 1.8(1)]\,E_R$), the transferred fraction ξ for Bloch oscillations along the x and y directions is recorded as a function of the interference phase φ as set by the interference stabilization electronics. An increase of φ with respect to the point of maximum interference at $\varphi = 0$ corresponds effectively to a reduction of the lattice depth V_X, which in turn leads to a reduction of the transfer efficiency for x oscillations, and an increase for y oscillations. The method can be used to calibrate the point of maximum interference.

6.5 VARYING THE FORCE

Finally, we study the dependence of the transfer efficiency on the applied force. We perform a scan from a dimerized lattice to a honeycomb geometry, once using the normal Bloch oscillation gradient giving rise to oscillations of a period of approximately 11 ms and another larger gradient resulting in a period of 2 ms, see Fig. 6.10. Both for oscillations along x and y, the transfer efficiency is enhanced when using the larger gradient, in agreement with the expectation from the Landau-Zener formula. For y oscillations, we compare the measured efficiencies with the theoretical expectation from the momentum-integrated model based on the universal Hamiltonian and find good agreement for the normal gradient and qualitative agreement for the larger force. The deviations for large $V_{\bar{X}}$ are most likely due to the blurred distribution of the transferred atoms reaching into the 1st B.Z.. This is possibly due to the increased dephasing during the Bloch oscillation. As already observed in Fig. 6.8 on page 125, the theory fails to reproduce the exact total transfer efficiencies for oscillations along x and therefore was not applied here.

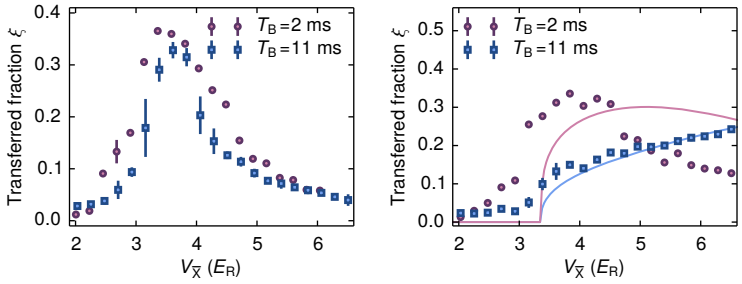

a. x oscillations b. y oscillations

Figure 6.10: *Varying the force.* The plots show the transfer efficiencies for a scan from a dimerized to a honeycomb lattice using Bloch oscillation gradients of different magnitude. Along both oscillation directions, the transferred fraction increases for larger forces, in agreement with the expectations from the Landau-Zener model. For the y oscillations, there is qualitative agreement with the theory taking into account the finite extent of the atom cloud in momentum space. Lattice parameters for the scan and the calculation: $V_{X,Y} = [0.28(1), 1.8(1)]\, E_R$.

6.6 CONCLUSION

In this work we have realized Dirac points with highly tunable properties using ultracold fermionic atoms in a honeycomb optical lattice. Bloch-Zener oscillations have proved to be a versatile tool in probing the linear dispersion relation close to the Dirac points. Both the existence and the position of the Dirac points can be deduced from the quasimomentum distribution of the atoms after one Bloch oscillation. By deforming the honeycomb lattice such that the two Dirac points approach each other and finally merge, we have observed the transition into a gapped phase, a phenomenon that could so far not be observed in real graphene. On a more quantitative level, the amount of atoms transferred to the higher band was found to contain information about the slope of the band structure close to the Dirac points and the residual gap. Results from measurements of this quantity agree well with those obtained from *ab initio* band structure calculations, using a theory without free parameters, based on a universal Hamiltonian describing the band structure in the vicinity of the Dirac points [Montambaux *et al.*, 2009a; Lim *et al.*, 2012], as well as with an *ab initio* numerical simulation of the time

evolution of the trapped system. Subsequent transfer through both Dirac points leads to the appearance of a distinct feature: double peaks in the probability of finding atoms in the higher band after one Bloch oscillation, both as a function of sublattice energy offset as well as of the Bloch wave vector k_x. The absence of Stückelberg interference was successfully explained by large differences in the acquired Stückelberg phases due to the inhomogeneity of the force applied to the atoms – an effect of the harmonic trapping potential.

A new class of physical phenomena is now within the domain of quantum gas experiments. Furthermore, the flexibility and novel observables of these systems will provide new insights. For example, the unique coherence properties of quantum gases offers the possibility of directly measuring the Berry phase [Atala *et al.*, 2013] or Berry curvature [Price *et al.*, 2012] associated to the Dirac points by interferometric methods or by measurements of the real-space trajectory. Topological order could be obtained by introducing artificial gauge fields, either via Raman transitions [Lin *et al.*, 2009] or time-dependent lattice modulation [Kitagawa *et al.*, 2010]. Moreover, the exceptionally tunable lattice potential opens up a wealth of new avenues for optical lattice experiments. For spin mixtures with repulsive interactions, the dynamic transition between dimer and square lattices should facilitate the adiabatic preparation of an antiferromagnetic state [Lubasch *et al.*, 2011] and enable the study of quantum criticality [Sachdev, 2008]. Additionally, the triangular and honeycomb lattices provide the possibility to explore magnetic frustration and spin liquid phases [Balents, 2010; Meng *et al.*, 2010; Sorella *et al.*, 2012; Assaad *et al.*, 2013].

Part II

PROBING INTERACTION EFFECTS

IMPLEMENTING THE FERMI-HUBBARD MODEL

7

In this chapter I will discuss the construction, the phase diagram and a possible approach for a theoretical treatment of the Hubbard model. Proposed by the British physicist J. Hubbard [1963], the Hubbard Hamiltonian is one of the most simple models for fermions[1] in a lattice system that incorporates the interplay between kinetic and interaction energy.

CHAPTER CONTENTS

In the simplest form that has been implemented using cold atoms, the Fermi-Hubbard Hamiltonian has the following form:

Fermi-Hubbard Hamiltonian

$$\begin{aligned}\hat{H} &= \hat{H}_t + \hat{H}_U + \hat{H}_\varepsilon \\ &= \underbrace{-t \sum_{\langle \mathbf{i},\mathbf{j}\rangle,\sigma} \hat{c}^\dagger_{\mathbf{i},\sigma}\hat{c}_{\mathbf{j},\sigma}}_{\text{kinetic energy}} + \underbrace{U \sum_{\mathbf{i}} \hat{n}_{\mathbf{i},\uparrow}\hat{n}_{\mathbf{i},\downarrow}}_{\text{on-site interaction}} + \underbrace{\sum_{\mathbf{i},\sigma} \varepsilon_{\mathbf{i}}\hat{n}_{\mathbf{i},\sigma}}_{\text{external confinement}},\end{aligned} \tag{7.1}$$

where $\hat{c}^\dagger_{\mathbf{i},\sigma}$ and $\hat{c}_{\mathbf{i},\sigma}$ denote the creation and annihilation operators for two (pseudo-) spin states $\sigma \in \{\uparrow, \downarrow\}$ at a lattice site $\mathbf{i}$. In the summation, $\langle \mathbf{i}, \mathbf{j}\rangle$ denotes nearest neighbors on the lattice (including double-counting[2]) and $\hat{n}_{\mathbf{i},\sigma} = \hat{c}^\dagger_{\mathbf{i},\sigma}\hat{c}_{\mathbf{i},\sigma}$ is the density operator on site $\mathbf{i}$. The operators $\hat{c}^\dagger_{\mathbf{i},\sigma}$ and $\hat{c}_{\mathbf{i},\sigma}$ obey the fermionic commutation rules, $\{\hat{c}^\dagger_{\mathbf{i},\sigma}, \hat{c}_{\mathbf{j},\sigma'}\} = \delta_{\mathbf{ij}}\delta_{\sigma\sigma'}$ and $\{\hat{c}^\dagger_{\mathbf{i},\sigma}, \hat{c}^\dagger_{\mathbf{j},\sigma'}\} = \{\hat{c}_{\mathbf{i},\sigma}, \hat{c}_{\mathbf{j},\sigma'}\} = 0$.

As illustrated in Fig. 7.1 on the following page, the model allows every lattice site only to be occupied by none, one or two fermions of different spin. Two or more of the same spins are not allowed to occupy the same site (in the lowest band, to which the simplest Hubbard model is restricted to) due to Pauli blocking. The spins can hop from one site to one of its nearest neighbors with an associated matrix element t. The energy of two opposite spins residing on the same lattice site is U. The energy of the external confining potential is $\varepsilon_{\mathbf{i}}$. This varying site energy is a unique feature of the Hubbard model implementations using optical

1 Note that since the original model was proposed for electrons, the term *Hubbard model* usually relates to the version of the model for fermionic particles, while the one for bosonic particles is called *Bose-Hubbard model*.

2 I.e. it accounts for both the process $\mathbf{i} \to \mathbf{j}$ as well as $\mathbf{i} \leftarrow \mathbf{j}$. If these processes are counted only as one, another sum of the hermitian conjugates has to be added.

lattices, and is due to the trapping potential required to hold the atoms in place, see Fig. 2.5 on page 25.

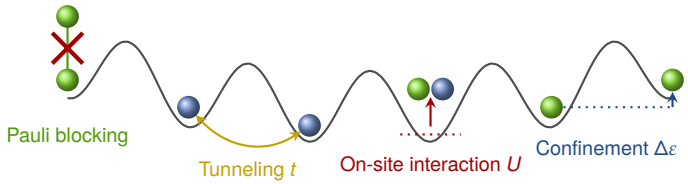

Figure 7.1: *The Fermi-Hubbard model in an optical lattice.* A spin-up and a spin-down (pseudo-) spin (blue and green spheres) obeying fermionic commutation relations can hop between neighboring sites with a matrix element t. Two opposite spins residing on the same lattice site feel a repulsive or attractive interaction U. In optical lattice implementations the on-site energy usually spatially varies by a certain energy $\Delta\varepsilon$ owing to the trap required to hold the particles. Adapted from [Jördens, 2010].

Competition between kinetic and interaction energy

In most simple terms, the kinetic energy favors delocalization of the wave function of the particles over the lattice, which is counteracted by the on-site repulsion (for $U > 0$). Therefore, in the limit of no interactions or very large tunneling, the particles will be delocalized over essentially the whole system (for an infinite system and no external confinement). In the limit of no tunneling (the so-called *atomic limit*) or very large on-site interactions, the particles are fully localized and form an unusual insulator, which does not emerge because of a filled band but is due to interactions. This insulating state was proposed by the British physicist N.F. Mott [1949], hence the name *Mott insulator*. In his seminal paper, Mott successfully explained the insulating behavior of certain transition metal oxides by an electron model including Coulomb interactions.

Mott insulator

Quantum Heisenberg model

For the case of large on-site interactions, the model simplifies to the quantum Heisenberg model. While U was assumed to be positive in the original context of electrons under the influence of Coulomb repulsion, using cold atoms also negative U, i. e. attractive interactions, can be realized. The external confinement $\varepsilon_\mathbf{i}$ leads to a spatially varying chemical potential, which gives rise to a coexistence of different phases in the same realization of the system at different locations in the potential.

Note that for simplicity, we assumed here that the nearest neighbor tunneling matrix elements t are the same on all bonds and that the interaction energy is the same on all sites. Additionally, we have assumed that at any point in time only the first band is populated, that the interactions are on-site only and that tunneling to other sites apart from nearest neighbors can be neglected. By including these terms and/or allowing for two or more different tunnelings or interactions, more sophisticated Hubbard models can be defined. For example, for square lattices the extension to unequal nearest neighbor tunnelings is called an anisotropic Hubbard model. Periodic alternation between two on-site interactions U_A and U_B – a special case of unequal on-site interactions – on the other hand is treated within ionic Hubbard models [Egami *et al.*, 1993].

Extended Hubbard models

Experimental implementations using cold atoms

The implementation of Hubbard models using cold atoms was originally proposed by Jaksch *et al.* [1998]. First, number squeezed states in 1D systems were observed [Orzel *et al.*, 2001], followed by the breakthrough observation of the superfluid to Mott insulator transition in a bosonic gas loaded into an optical lattice by Greiner *et al.* [2002]. The bosonic Mott insulator transition was subsequently also studied in depth for 1D and 2D systems [Stöferle *et al.*, 2004; Spielman *et al.*, 2007]. In 2010, two groups reported the *in situ* observation of the 2D bosonic Mott insulator shells with single-site resolution [Bakr *et al.*, 2010; Sherson *et al.*, 2010]. Using fermionic atoms, Mott-insulating states of repulsively interacting atoms were realized for the first time in 2008 in our and the group of I. Bloch [Jördens *et al.*,

2008; Schneider *et al.*, 2008]. Within the attractive Fermi-Hubbard model, so far the thermodynamic properties were investigated experimentally [Hackermüller *et al.*, 2010].

7.1 CONSTRUCTION

In this section the derivation of the Fermi-Hubbard model from the original Hamiltonian of the atoms in the optical lattice potential is discussed. This derivation is summarized in [Jaksch *et al.*, 2005]. Moreover, a derivation of the Hubbard model specific to honeycomb optical lattices can be found in [Walters *et al.*, 2013; Ibañez-Azpiroz *et al.*, 2013a,b], with a focus on obtaining the tunneling matrix elements.

We start with the Hamiltonian in second quantization,

$$\begin{aligned}\hat{H} = &\sum_{\sigma} \int \mathrm{d}^3\mathbf{x}\, \hat{\psi}^\dagger_\sigma(\mathbf{x}) H_0(\mathbf{x}) \hat{\psi}_\sigma(\mathbf{x}) \\ &+ \frac{1}{2} \sum_{\sigma,\sigma'} \int \mathrm{d}^3\mathbf{x}\, \mathrm{d}^3\mathbf{x}'\, \hat{\psi}^\dagger_{\sigma'}(\mathbf{x}') \hat{\psi}^\dagger_\sigma(\mathbf{x}) H_{\mathrm{int}}(\mathbf{x}-\mathbf{x}') \hat{\psi}_\sigma(\mathbf{x}) \hat{\psi}_{\sigma'}(\mathbf{x}'),\end{aligned} \tag{7.2}$$

with

$$\begin{aligned}H_0(\mathbf{x}) &= \left(-\frac{\hbar^2}{2m}\boldsymbol{\nabla}^2 + V_{\mathrm{lattice}}(\mathbf{x}) + V_{\mathrm{trap}}(\mathbf{x})\right), \\ H_{\mathrm{int}}(\mathbf{x}-\mathbf{x}') &= V_{\mathrm{int}}(\mathbf{x}-\mathbf{x}').\end{aligned} \tag{7.3}$$

In a next step, we will replace the field operators by their expansion in terms of Wannier functions of the band ν, see Eq. (4.27) on page 77. In order to obtain the simplest form of the Hubbard model introduced above, this expansion is truncated after the first band contribution:

Wannier functions

$$\hat{\psi}_\sigma(\mathrm{r}) = \sum_\nu \sum_{\mathbf{j}} \hat{c}_{\nu,\mathbf{j},\sigma} w_{\nu,\mathbf{j}}(\mathbf{x}) \xrightarrow{\text{single-band approx.}} \sum_{\mathbf{j}} \hat{c}_{0,\mathbf{j},\sigma} w_{0,\mathbf{j}}(\mathbf{x}). \tag{7.4}$$

This corresponds to the first major approximation which the single-band Hubbard model given in Eq. (7.1) on page 131 introduces: any higher band physics are completely neglected. The approximation obviously breaks down as soon as higher bands are populated, be it because the Fermi energy lies in the higher bands, due to thermal excitations of higher bands as a result of $k_\mathrm{B}T$ being larger than the band gap or if the interaction energy U exceeds the band gap. See [Georges, 2007] for a detailed discussion of the applicability of the Hubbard model. The limitations can be overcome by applying multi-band Hubbard models [Diener *et al.*, 2006].

Truncation to a set of bands

The second approximation will be the truncation of the tight-binding expansion of the non-interacting part of the Hamiltonian to merely include nearest-neighbor tunneling. The third is the reduction of the interaction range to on-site interactions only. These will be discussed in more detail in the following sections.

7.1.1 TUNNELING

The non-interacting part of the Hubbard Hamiltonian is in fact equivalent to the tight-binding Hamiltonian which was derived in Section 4.2 on page 76, with an added term accounting for the external confinement.

In this context is is helpful to remember that the tunneling matrix elements can be obtained from a Fourier transform of the band energies, see Eq. (4.32) on

page 78, and equivalently the band structure of the resulting tight-binding model can be calculated from the tunnel matrix elements by the inverse Fourier transform. To obtain the Hubbard Hamiltonian, the tight-binding expansion is truncated already after the nearest-neighbor terms, leading in the case of a square or simple cubic lattice to only one tunneling matrix element $t \equiv t_{0,\mathrm{n.n.}}$ that is kept.

As discussed in Section 4.2, the lattice must be deep enough for the tight-binding approximation to be valid. For a $\mathscr{D}$ dimensional lattice composed of overlapping 1D lattices with spacing d along all spatial directions, the non-interacting band structure of the Hubbard Hamiltonian is just a cosine along each direction:

$$E_k = -2t\mathscr{D}\cos(kd)\,. \tag{7.5}$$

Bandwidth

The total bandwidth is then $W = 2zt$, with $z = 2\mathscr{D}$ the number of nearest neighbors. For such a lattice, a reasonable bound for the validity of the Hubbard model is set at a single-beam lattice depth $V_0 \geq 5\,E_\mathrm{R}$, where the next nearest neighbor tunneling is a factor of 10 smaller than the nearest neighbor tunneling. For large lattice depths, the tunneling can be approximately calculated from the width of the lowest band in the solutions of the 1D Mathieu equations [Zwerger, 2003] (see also Section 4.1.2 on page 76),

$$t = \frac{4}{\sqrt{\pi}} E_\mathrm{R} \left(\frac{V_0}{E_\mathrm{R}}\right)^{3/4} \exp\left(-2\sqrt{\frac{V_0}{E_\mathrm{R}}}\right), \tag{7.6}$$

from which the exponential suppression of the tunneling with increasing lattice depth becomes apparent.

Tunneling matrix elements for the tunable-geometry optical lattice

The calculation of the tunneling matrix elements is more involved for the tunable-geometry optical lattice, which is not separable in the $x - y$ plane. As discussed in Section 4.2 on page 76, the tight-binding parameters can either be obtained from a numerical calculation of the Wannier functions or from band structure fits. Results of the former method as a function of the lattice depths $V_{\bar{\mathrm{X}}}$ and V_X are shown in the following figures for typical regimes used in this thesis. In Fig. 7.3 and Fig. 7.4 on the facing page, V_Y is set to $1.8\,E_\mathrm{R}$ as is the case for the results presented in Part I. The same plots but with $V_\mathrm{Y} = 6.45\,E_\mathrm{R}$ are shown in Fig. 7.5 and Fig. 7.6 on page 136, corresponding to the regime used in Chapter 8. The notation used for the different tunneling links in these figures is illustrated in Fig. 7.2.

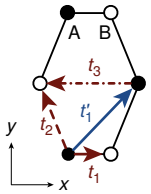

Figure 7.2: *Notation for the tunneling links.* The schematics shows the relevant tunneling links in the honeycomb lattice structure as used in the following figures.

7.1.2 INTERACTION

For the following construction of the interaction term, we use the assumption that the effective range of the van der Waals interaction between the atoms is much smaller than the inter-particle spacing, allowing us to treat the scattering problem in its asymptotic limit, see Section 2.3.1 on page 25. Additionally we replace the real scattering potential by the pseudopotential introduced in Eq. (2.26) on page 27,

$$V_\mathrm{int}(\mathbf{r}) = V_\mathrm{pseudo}(r) \doteq g\delta(r)\frac{\partial}{\partial r}r, \tag{7.7}$$

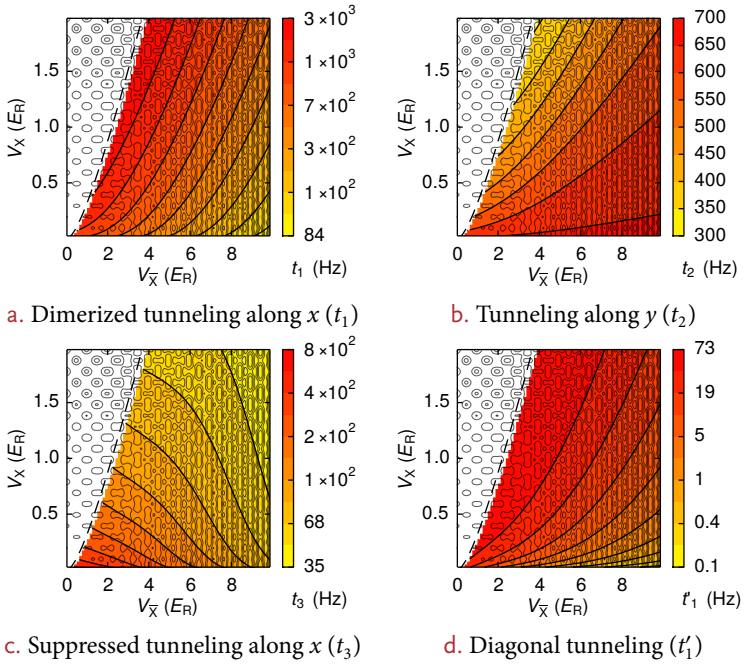

a. Dimerized tunneling along x (t_1)

b. Tunneling along y (t_2)

c. Suppressed tunneling along x (t_3)

d. Diagonal tunneling (t'_1)

Figure 7.3: *Tunnelings for* $V_Y = 1.8\,E_R$. The tunneling matrix elements $t_{1,2,3}$ and t'_1 (see Fig. 7.2 on page 134) for the honeycomb and dimerized lattice geometries as obtained from the Wannier function calculation (Section 4.2.2 on page 81) are shown as a function of $V_{\bar{X}}$ and V_X. The transition line to the triangular geometry is plotted as a dashed line. For illustration purposes, the lattice potential for the given lattice parameters is shown in the background. The contour plots are clipped before they reach the transition line to remove plotting artifacts. The visibility of the interference pattern is set to $\alpha = 0.9$.

Figure 7.4: *Ratio of tunnelings for* $V_Y = 1.8\,E_R$. The ratio t_1/t_2 is shown as a function of the lattice depths $V_{\bar{X}}$ and V_X for the same parameters as used in Fig. 7.3. The locations where the two Dirac points merge ($t_1/t_2 \approx 2$) and where the tunnelings are the same ($t_1/t_2 = 1$) are drawn as red dashed lines.

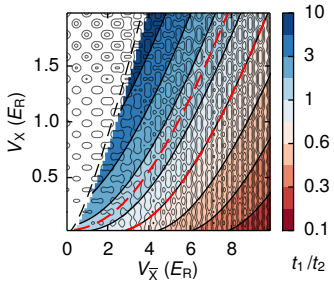

with the interaction parameter g, which is proportional to the scattering length a,

$$g = \frac{4\pi\hbar^2}{m} a\,. \tag{7.8}$$

Inserting the pseudopotential, the interacting part of the Hamiltonian given in Eq. (7.2) on page 133 reads:

$$\begin{aligned}\hat{H}_{\text{int}} &= \frac{g}{2} \sum_{\sigma,\sigma'} \int \hat{\psi}^\dagger_{\sigma'}(\mathbf{x}) \hat{\psi}^\dagger_{\sigma}(\mathbf{x}) \hat{\psi}_{\sigma}(\mathbf{x}) \hat{\psi}_{\sigma'}(\mathbf{x})\, \mathrm{d}\mathbf{x} \\ &= \frac{g}{2} \sum_{\sigma,\sigma'} \sum_{\substack{q,r,s,t \\ \mathbf{i},\mathbf{j},\mathbf{k},\mathbf{l}}} \hat{c}^\dagger_{q,\mathbf{i},\sigma'} \hat{c}^\dagger_{r,\mathbf{j},\sigma} \hat{c}_{s,\mathbf{k},\sigma} \hat{c}_{t,\mathbf{l},\sigma'} \int w^*_{q,\mathbf{i}}(\mathbf{x}) w^*_{r,\mathbf{j}}(\mathbf{x}) w_{s,\mathbf{k}}(\mathbf{x}) w_{t,\mathbf{l}}(\mathbf{x})\, \mathrm{d}\mathbf{x}\,,\end{aligned} \tag{7.9}$$

where the second line was obtained by inserting the multiband expansion of the field operators in Wannier functions, Eq. (7.4) on page 133, left side. Here, q, r, s, t

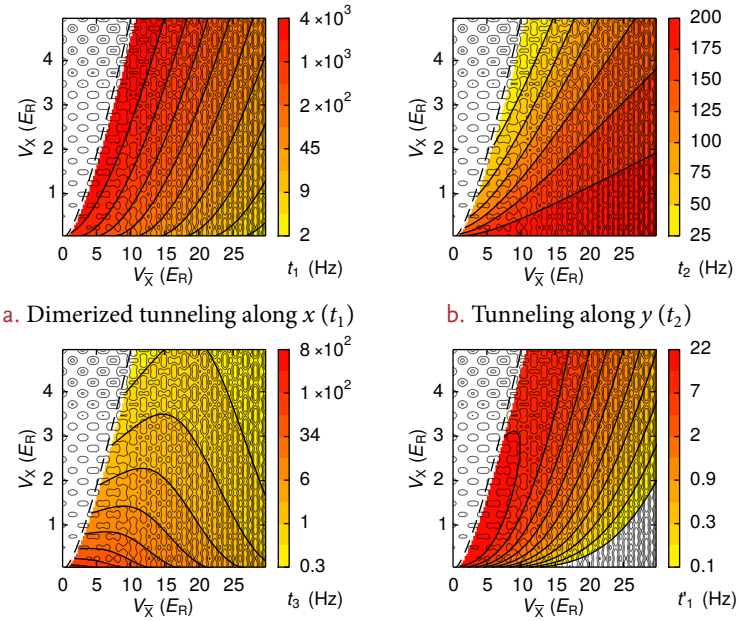

a. Dimerized tunneling along x (t_1)

b. Tunneling along y (t_2)

c. Suppressed tunneling along x (t_3)

d. Diagonal tunneling (t'_1)

Figure 7.5: *Tunnelings for $V_Y = 6.45\,E_R$.* The tunneling matrix elements $t_{1,2,3}$ and t'_1 (see Fig. 7.2 on page 134) for the honeycomb and dimerized lattice geometries as obtained from the Wannier function calculation (Section 4.2.2 on page 81) are shown as a function of $V_{\bar{X}}$ and V_X. The transition line to the triangular geometry is plotted as a dashed line. For illustration purposes, the lattice potential for the given lattice parameters is shown in the background. The contour plots are clipped before they reach the transition line to remove plotting artifacts. The visibility of the interference pattern is set to $\alpha = 0.9$.

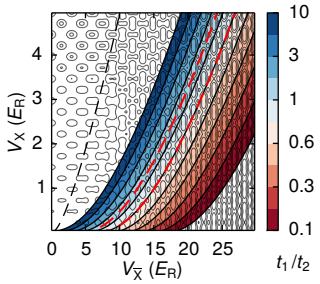

Figure 7.6: *Ratio of tunnelings for $V_Y = 6.45\,E_R$.* The ratio t_1/t_2 is shown as a function of the lattice depths $V_{\bar{X}}$ and V_X for the same parameters as used in Fig. 7.5. The locations where the two Dirac points merge ($t_1/t_2 \approx 2$) and where the tunnelings are the same ($t_1/t_2 = 1$) are drawn as red dashed lines.

are the band indices and $\mathbf{i}, \mathbf{j}, \mathbf{k}, \mathbf{l}$ the site locations of the Wannier functions. Next, we will neglect the overlap of the Wannier function of a site with those of neighboring sites, limiting the interactions to on-site only,

$$\hat{H}_{\text{int,on-site}} = \frac{1}{2} \sum_{\sigma,\sigma'} \sum_{\substack{q,r,s,t \\ \mathbf{i}}} U_{q,r,s,t} \hat{c}^\dagger_{q,\mathbf{i},\sigma'} \hat{c}^\dagger_{r,\mathbf{i},\sigma} \hat{c}_{s,\mathbf{i},\sigma} \hat{c}_{t,\mathbf{i},\sigma'} \tag{7.10}$$

$$U_{q,r,s,t} = g \int w^*_{q,\mathbf{0}}(\mathbf{x}) w^*_{r,\mathbf{0}}(\mathbf{x}) w_{s,\mathbf{0}}(\mathbf{x}) w_{t,\mathbf{0}}(\mathbf{x})\, \mathrm{d}\mathbf{x}\,. \tag{7.11}$$

Single-band approximation

In the single-band approximation ($q = r = s = t \equiv 0$) the expression finally

simplifies to

$$\hat{H}_U = U \sum_{\mathbf{i}} \hat{n}_{\mathbf{i},\uparrow} \hat{n}_{\mathbf{i},\downarrow} \tag{7.12}$$

$$U = U_{0,0,0,0} = g \int |w_{0,\mathbf{0}}(\mathbf{x})|^4 \, \mathrm{d}\mathbf{x} \,. \tag{7.13}$$

Again, for a simple cubic lattice, an approximate analytic expression in the limit of large lattice depths can be found [Zwerger, 2003]:

$$U = \sqrt{\frac{8}{\pi}} k_{\mathrm{L}} a E_{\mathrm{R}} \left(\frac{V}{E_{\mathrm{R}}} \right)^{3/4} . \tag{7.14}$$

Once again, the situation is more involved for the case of our lattice in the $x-y$ plane, where the Wannier functions have a complicated anisotropic shape, see for example Fig. 4.8 on page 84. To obtain U, the Wannier functions therefore have to be calculated numerically and the on-site energy determined via integration. In Fig. 7.7 and Fig. 7.8 the obtained on-site interaction U and interaction parameter $U/(t_1 + 2t_2 + t_3 + 2t_z)$ as a function of the lattice depths $V_{\tilde{\mathrm{X}}}$ and V_{X} are shown for typical regimes used in this thesis.

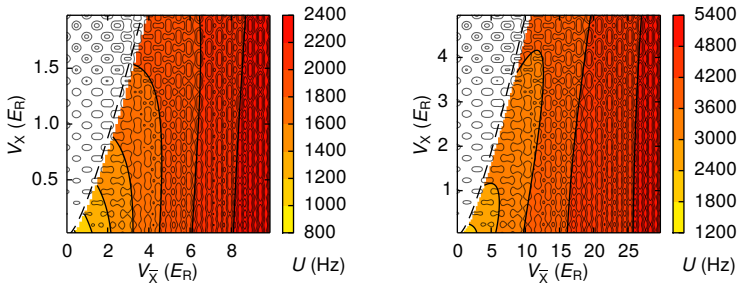

a. $V_{\mathrm{Y}} = 1.8\, E_{\mathrm{R}}$ b. $V_{\mathrm{Y}} = 6.45\, E_{\mathrm{R}}$

Figure 7.7: *Interaction energy U calculated from Wannier functions.* The values have been obtained from the numerical Wannier function calculation discussed in Section 4.2.2 on page 81. The scattering length is fixed at $a = 500 a_0$ and the lattice depth along the perpendicular direction is set to $V_{\tilde{\mathrm{Z}}} = 7\, E_{\mathrm{R}}$. The visibility of the interference pattern is set to $\alpha = 0.9$.

7.1.3 EXTERNAL CONFINEMENT

The slowly varying external confinement present in cold atom based implementations of Hubbard models is usually caused by the combination of the light intensity gradients within the lattice laser beams and the FORT, or is due to a magnetic trap or residual magnetic field gradients.

For the term accounting for the external confinement, we also insert the Wannier function expansion of the field operators in the single-band approximation and use their orthonormality,

$$\hat{H}_{\mathrm{trap}} = \sum_{\mathbf{i},\sigma} \varepsilon_{\mathbf{i}} \hat{n}_{\mathbf{i},\sigma} \tag{7.15}$$

$$\varepsilon_{\mathbf{i}} = \int |w_{0,\mathbf{i}}(\mathbf{x})|^2 \, V_{\mathrm{trap}}(\mathbf{x}) \, \mathrm{d}\mathbf{x} \,. \tag{7.16}$$

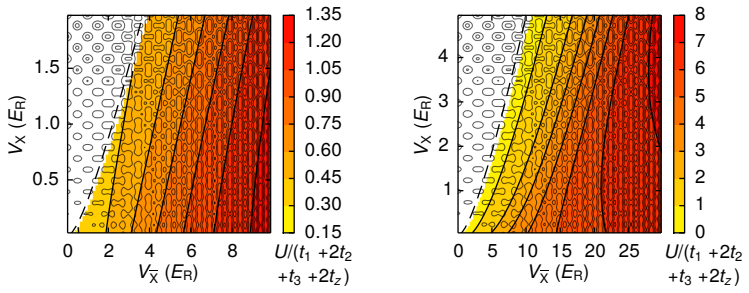

a. $V_Y = 1.8\,E_R$ b. $V_Y = 6.45\,E_R$

Figure 7.8: *Interaction parameter $U/(t_1+2t_2+t_3+2t_z)$ calculated from Wannier functions.* The values have been obtained from the numerical Wannier function calculation discussed in Section 4.2.2 on page 81. The scattering length is fixed at $a = 500a_0$ and the lattice depth along the perpendicular direction is set to $V_{\bar{Z}} = 7\,E_R$. The visibility of the interference pattern is set to $\alpha = 0.9$.

Since the external confinement varies only slowly over the extent of the Wannier functions, the potential at the site center can be used:

$$\varepsilon_{\mathbf{i}} = V_{\text{trap}}(\mathbf{R}_{\mathbf{i}})\,. \tag{7.17}$$

7.1.4 LIMITING CASES

For $U = 0$, the Hubbard model corresponds to just a tight-binding model. In the strongly interacting limit on the other hand, double occupancy is suppressed and the on-site interaction energy gives rise to a superexchange coupling between the spins, $J_{\text{ex}} = 4t^2/U$. This limiting case is described by the $t-J$ model [Auerbach, 1994]:

$t-J$ model

$$\hat{H}_{t\text{–}J} = -t \sum_{\langle \mathbf{i},\mathbf{j}\rangle,\sigma} (1-\hat{n}_{\mathbf{i},\bar{\sigma}})\hat{c}^{\dagger}_{\mathbf{i},\sigma}\hat{c}_{\mathbf{j},\sigma}(1-\hat{n}_{\mathbf{j},\bar{\sigma}}) + \frac{1}{2}J_{\text{ex}} \sum_{\langle \mathbf{i},\mathbf{j}\rangle} \left(\hat{S}_{\mathbf{i}}\cdot\hat{S}_{\mathbf{j}} - \frac{\hat{n}_{\mathbf{i}}\hat{n}_{\mathbf{j}}}{4}\right), \tag{7.18}$$

where $\hat{n}_{\mathbf{i}} = \hat{n}_{\mathbf{i},\uparrow} + \hat{n}_{\mathbf{i},\downarrow}$ and $\bar{\sigma}$ refers to the opposite spin of σ, i. e. $\bar{\sigma} = -\sigma$. The spin-1/2 operator on site $\mathbf{i}$ is denoted by $\hat{S}_{\mathbf{i}}$. The $(1-\hat{n}_{\mathbf{i},\bar{\sigma}})$ terms ensure that a particle can only hop to an empty site, i. e. that no double occupancies can be created. The $\frac{\hat{n}_{\mathbf{i}}\hat{n}_{\mathbf{j}}}{4}$ term can be neglected if the system is close to half-filling. Exactly at half-filling ($n_{\mathbf{i}} = 1$), hopping is completely forbidden and the $t-J$ Hamiltonian reduces to the quantum Heisenberg model,

Quantum Heisenberg model

$$\hat{H}_{\text{QH}} = \frac{1}{2}J_{\text{ex}} \sum_{\langle \mathbf{i},\mathbf{j}\rangle} \left(\hat{S}_{\mathbf{i}}\cdot\hat{S}_{\mathbf{j}} - \frac{\hat{n}_{\mathbf{i}}\hat{n}_{\mathbf{j}}}{4}\right), \tag{7.19}$$

which describes interacting quantum mechanical spins, localized on a lattice.

7.2 THE PHASE DIAGRAM

7.2.1 SQUARE LATTICE

First investigations on the presence of a Mott transition in the phase diagram of the homogeneous half-filled 1D repulsive Hubbard model at $T = 0$ were performed by Lieb and Wu in 1968 [Lieb *et al.*, 1968]. They concluded that the system was conducting for $U = 0$, but insulating for any $U \neq 0$. The regime for $U > 0$ was

found to be characterized both by a Mott-insulating behavior as well as antiferromagnetic spin ordering. The Mott-insulating behavior is due to the cost of energy for building double occupancies in the system. The tendency towards ordering at any finite interaction, which is also observed in square and cubic lattices, is a consequence of the Fermi surface nesting and the van Hove singularity coinciding at half-filling [Hirsch, 1985]. The occurrence of antiferromagnetism is best understood in the large U/t limit, where the Hubbard model at half-filling becomes equivalent to the quantum Heisenberg model (see Section 7.1.4 on page 138),

Tendency towards ordering as a consequence of Fermi surface nesting and the van Hove singularity

Antiferromagnetic ordering

$$\hat{H} = \frac{1}{2} J_{\mathrm{ex}} \sum_{\langle \mathbf{i},\mathbf{j} \rangle} \hat{\mathbf{S}}_{\mathbf{i}} \cdot \hat{\mathbf{S}}_{\mathbf{j}} \,. \tag{7.20}$$

At repulsive interactions, the positive superexchange energy J_{ex} favors the antiferromagnetic ground state owing to the competition between kinetic and interaction energy. Note that the transitions from metallic to a Mott-insulating and a spin-ordered (antiferromagnetic) state do not necessarily need to coincide. To distinguish the effects of insulating behavior and magnetic ordering, however, magnetic ordering at $T = 0$ needs to be excluded, which is for example the case for triangular geometries, where magnetic frustration occurs. Later, the 3D Hubbard model was studied at finite temperature, with an overview of the results shown in Fig. 7.9. For repulsive interactions, the system is in a metallic state, while the antiferromagnetic state occurring at larger interactions persists up to the Néel temperature, with the maximum transition temperature found to be roughly at $U/t \approx 8$ [Staudt *et al.*, 2000]. Intuitively speaking, spin exchange effects play a role as long as the temperature is lower than the superexchange energy J_{ex}. Already above the Néel temperature, a smooth crossover from the metallic Fermi liquid to a Mott-insulating state is found, driven by the increasing interactions. The repulsive interactions disfavor double occupancies in the system, leading to a Mott-insulating state.

Distinguishing Mott-insulating behavior and antiferromagnetic ordering

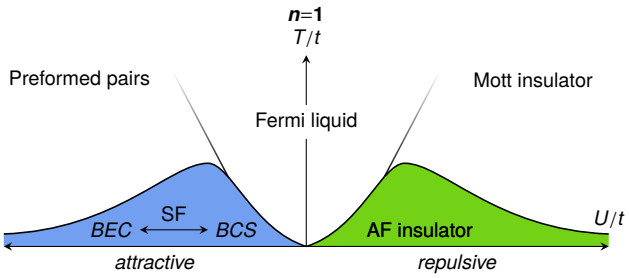

Figure 7.9: *Schematic phase diagram of the Hubbard model at half-filling in a simple cubic lattice.* At low temperature, the Hubbard model contains a spin-ordered Mott-insulating state. At higher temperatures, a smooth crossover from a normal metal to a Mott insulator is found when increasing the interactions. On the attractive side, related by a particle-hole transformation, superfluidity (SF) occurs at low temperature, containing a crossover from a BCS to a BEC state.

The Hubbard model exhibits discrete symmetries under particle-hole transformations. At half-filling (i. e. at one particle per site), for example, these allow for a mapping of the repulsive ($U > 0$) to the attractive ($U < 0$) Hubbard model: antiferromagnetic order in the z plane on the repulsive side becomes charge density wave (CDW) order for attractive interactions, and antiferromagnetic order in the $x-y$ plane results in pairing. This explains the obvious symmetry of the phase diagram. For attractive interactions, the system is in an s-wave superfluid (SF) state, with a BCS to a BEC crossover occurring for increasing interactions. During this transition the initially weakly bound and distant Cooper pairs become increasingly tighter bound, leading eventually to the formation of bosonic molecules,

built from two fermions. These can establish long-range phase coherence and thus Bose condense. For ultracold fermions in optical lattices, quantum simulation of the respective phases has been proposed to be easier to perform using attractive interactions [Ho, Cazalilla, *et al.*, 2009].

When shifting the Fermi level away from half-filling (i. e. when the system is *doped*), a quasi-2D system is expected to cross into a *d*-wave symmetric superfluid state [Lee *et al.*, 2006], see Fig. 7.10. However, the location of the phase boundary and possible intermediate phases remain unclear so far.

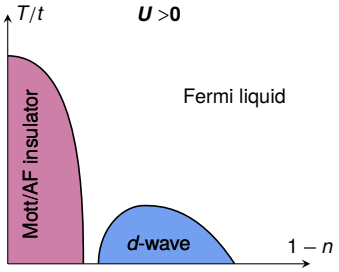

Figure 7.10: *Schematic phase diagram of the doped repulsive quasi-2D Hubbard model on the square lattice.* When shifting the Fermi level away from half-filling ($n = 1$), a *d*-wave symmetric superfluid state is expected close to the antiferromagnetic state at low temperatures. Long-range order, absent in 1D and 2D systems at $T > 0$, is stabilized by the presence of a small coupling between the 2D layers.

7.2.2 HONEYCOMB LATTICE

In contrast to the Hubbard model on the square lattice, the 2D Hubbard model on the honeycomb lattice was found to contain a quantum phase transition at $T = 0$ from a semimetallic state at weak interactions to an antiferromagnetic state at large interactions, with the quantum critical point located at $U/t = 4.5 \pm 0.5$ [Sorella *et al.*, 1992; Paiva *et al.*, 2005], see Fig. 7.11 on the facing page. The critical U_c for the transition is shifted away from zero owing to the vanishing density of states at the Fermi level, counteracting the tendency for CDW or spin density wave (SDW) order as a result of the partial nesting of the Fermi surface [Makogon *et al.*, 2011]. Meng *et al.* [2010] predicted the occurrence of a spin liquid phase located between the semimetallic and antiferromagnetic (AF) phases, with the lower and upper boundaries located at $U/t = 3.5$ and $U/t = 4.3$, respectively. In a spin liquid [Balents, 2010], the disorder of the spin system present at non-zero temperature is retained in the ground state at $T = 0$. The lower boundary would then correspond to the opening of a single particle gap and therefore the emergence of Mott-insulating behavior, while the upper boundary would be located where the staggered magnetization becomes non-zero, i. e. where antiferromagnetic ordering appears. However, the existence of a spin liquid is questioned by simulations with larger cluster sizes and a more accurate way to detect (small) magnetic order [Sorella *et al.*, 2012; Assaad *et al.*, 2013]. These later works allow for the conclusion that this specific type of spin liquid phase would most likely only occur in the presence of magnetic frustration [Balents, 2010].

Putative spin liquid phase

Away from half-filling, the system generally tends either towards a metallic or antiferromagnetic state, depending on the interactions [Peres *et al.*, 2004]. At the filling corresponding to the van Hove singularity (see Section 4.3.1 on page 91), perfect nesting of the Fermi surface is restored, leading to a strong tendency towards ordering or pairing. At or close to the van Hove singularity, chiral or other uncommon spin density waves, chiral superconductivity with $d + id$ pairing, or possibly a ferromagnetic state have been debated [Peres *et al.*, 2004; Pathak *et al.*, 2010; Makogon *et al.*, 2011; Wang, Xiang, *et al.*, 2012; Nandkishore, Levitov, *et al.*, 2012; Nandkishore, Chern, *et al.*, 2012; Kiesel *et al.*, 2012].

For weak attractive interactions, the system is semimetallic at and possibly also close to half-filling [Lee, Bouadim, *et al.*, 2009]. When increasing the interactions, a phase transition into the putative pseudo-spin liquid occurs, with a degenerate

superfluid and density-wave phase appearing for even larger interactions. Away from half-filling, the system becomes superfluid, containing a crossover from a BCS to a BEC state [Zhao *et al.*, 2006].

Anisotropic tunneling or non-local interaction terms lead to an even richer phase diagram, possibly containing other spin liquid phases [Wang *et al.*, 2011] or competition between SDW, ferromagnetic [Peres *et al.*, 2005], and CDW [Herbut, 2006] ordering, respectively, which might even lead to intrinsic pairing and superconductivity [Honerkamp, 2008] emerging from a CDW.

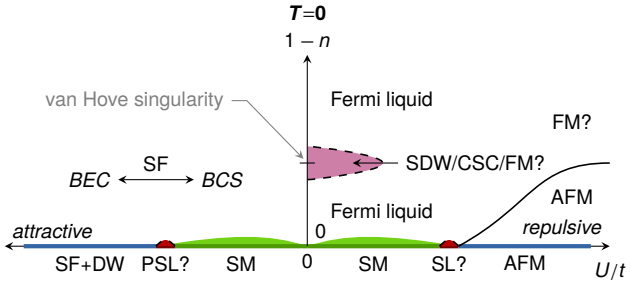

Figure 7.11: *Schematic phase diagram of the 2D Hubbard model on the honeycomb lattice.* At half-filling ($n = 1$), the system is semimetallic for weak interactions and becomes antiferromagnetic or superfluid for larger repulsive or attractive interactions, respectively. The phases between strong and weak interactions are separated by a debated spin liquid phase. Away from half-filling, additional metallic and ferromagnetic phases are found. Abbreviations: SM: semimetal, SL: spin liquid, AFM: antiferromagnetic Mott insulator, SDW: spin density wave, CSC: chiral superconductor, FM: ferromagnetism, PSL: pseudo-spin liquid, SF: superfluid, DW: density wave.

Extended Hubbard models

For the case of real graphene, the long-range Coulomb interactions are mostly unscreened in the semimetallic phase at half-filling [Castro Neto *et al.*, 2009], requiring for a mapping to an extended Hubbard model which includes interactions with particles on neighboring sites,

$$\hat{H} = \hat{H}_{\text{Hubbard}} + \frac{1}{2} \sum_{\substack{i \neq j \\ \sigma,\sigma'}} V_{i,j} \hat{n}_{i,\sigma} \hat{n}_{j,\sigma'} \,. \tag{7.21}$$

Hubbard parameters of real graphene

The nearest-neighbor hopping term for graphene is $t = 2.8\,\text{eV}$, and the effective Hubbard parameters for distances of up to 4 sites were found to be $U/t = 3.63$, as confirmed by measurements on polyacethylene [Castro Neto *et al.*, 2009], and $V_{0,[1,2,3,4]}/t = [2.03, 1.45, 1.32, 1.14]$ [Schüler *et al.*, 2013]. The nearest-neighbor interactions were found to effectively decrease the on-site interactions. Therefore, when mapping to a Hubbard model only including on-site interactions, a renormalized on-site interaction $U^*/t = 1.6$ should be used, reflecting the tendency of the non-local interactions to stabilize the semimetallic phase [Schüler *et al.*, 2013].

7.3 NUMERICAL TREATMENT

Since the fermionic Hubbard model cannot be solved analytically, numerical simulation or quantum simulations as discussed before in this thesis have to be used to learn about its ground and excited state properties. By numerically diagonalizing the Hamiltonian or by quantum Monte Carlo (QMC) methods exact solutions for the ground state can in principle be found. However, due to the exponentially growing number of states in the Hilbert space, exact diagonalization is not feasible for systems larger than a few times ten sites. At least some of the quantum

Monte Carlo (QMC) models on the other hand suffer form the so-called fermion sign problem and converge slowly at low temperatures [Duchon *et al.*, 2013].

Approximate treatments are possible using dynamical mean field theory (DMFT), which maps the problem to a single impurity problem, or 1D density-matrix renormalization group (DMRG) methods and their extensions to higher dimensions, projected entangled pair states (PEPS), which are both variational approaches on matrix product states (MPS). Both methods can, in an extension (tDMRG), also be used to simulate dynamics [White *et al.*, 2004; Daley *et al.*, 2004]. In Chapter 9 on page 163 results for the spin correlator in an anisotropic Hubbard model obtained from dynamical cluster approximation (DCA) calculations are presented. This method is an extension of dynamical mean field theory (DMFT) that can incorporate spatially nonlocal correlations.

In the regime where the temperature is larger than the associated energy η of a certain part of the Hamiltonian, a so called high-temperature series expansion (HTSE) of the grand canonical potential of the system [Oitmaa *et al.*, 2006; Haaf *et al.*, 1992; Henderson *et al.*, 1992] in the parameter $\beta\eta$ can be performed. Here, $\beta = 1/(k_B T)$. The most commonly used expansion is the one in the tunneling t, i. e. $\eta = t$. Such an expansion up to second order in the perturbation βt will be used in Chapter 8 on page 147 to compare the measured double occupancy in the system with theoretical predictions. A sketch of the method will be given in the following section.

7.3.1 HIGH-TEMPERATURE SERIES EXPANSION

As discussed above, a requirement for performing a HTSE is that the temperature of the system is larger than the associated energy of a certain part of the Hamiltonian. This part can therefore be treated as a perturbation $\hat{H}_1$,

$$\hat{H} = \hat{H}_0 + \hat{H}_1. \tag{7.22}$$

Therefore, in order to expand in powers of βt, we will choose

$$\hat{H}_0 = U \sum_{\mathbf{i}} \hat{n}_{\mathbf{i},\uparrow}\hat{n}_{\mathbf{i},\downarrow} + \sum_{\mathbf{i},\sigma} \varepsilon_{\mathbf{i}} \hat{n}_{\mathbf{i},\sigma} \qquad \hat{H}_1 = -t \sum_{\langle \mathbf{ij}\rangle,\sigma} \hat{c}^\dagger_{\mathbf{i},\sigma}\hat{c}_{\mathbf{j},\sigma}\,. \tag{7.23}$$

We then switch to the interaction (Dirac) picture,

$$\hat{H}_0'(\tau) = e^{\tau\hat{H}_0}\hat{H}_0 e^{-\tau\hat{H}_0} = \hat{H}_0 \qquad \hat{H}_1'(\tau) = e^{\tau\hat{H}_0}\hat{H}_1 e^{-\tau\hat{H}_0}\,, \tag{7.24}$$

Grand partition function

and use the fact that the grand partition function of the full Hamiltonian can be expressed as a product of the partition function of the unperturbed Hamiltonian and a series in β,

$$\begin{aligned}\mathcal{Z} &= \mathrm{Tr}\left\{e^{-\beta\hat{H}}\right\} \\ &= \mathcal{Z}_0\left\{1 + \sum_{r=1}^{\infty}(-1)^r \int_0^\beta \mathrm{d}\tau_1 \int_0^{\tau_1} \mathrm{d}\tau_2 \ldots \int_0^{\tau_{r-1}} \mathrm{d}\tau_r \langle \hat{H}_1'(\tau_1)\hat{H}_1'(\tau_2)\ldots\hat{H}_1'(\tau_r)\rangle_0\right\},\end{aligned} \tag{7.25}$$

where $\mathcal{Z}_0$ is the partition function of the unperturbed Hamiltonian. For a system of S sites, $\mathcal{Z}_0$ decomposes into a product of the unperturbed single-site partition functions z_0,

$$\mathcal{Z}_0 = \mathrm{Tr}\left\{e^{-\beta\hat{H}_0}\right\} = z_0^S. \tag{7.26}$$

The symbol $\langle ... \rangle_0$ denotes the expectation value of the respective quantity in the unperturbed Hamiltonian,

$$\langle ... \rangle_0 = \mathrm{Tr}\left\{ e^{-\beta \hat{H}_0} ... \right\} / \mathscr{Z}_0 \,. \tag{7.27}$$

Grand canonical potential

The single-site partition function z_0 is the trace over a matrix containing the Boltzmann factors of the four states of the single-site Hubbard model, $|0\rangle$, $|\uparrow\rangle$, $|\downarrow\rangle$, and $|\uparrow\downarrow\rangle$,

$$z_0 = 1 + 2\zeta + \zeta^2 w, \tag{7.28}$$

where we have defined the unitless interaction parameter $w = \exp(-\beta U)$ and the fugacity $\zeta = \exp(\beta\mu)$. Next, we calculate the grand canonical potential from the partition function using $-\beta\Omega = \log \mathscr{Z}$:

$$-\beta\Omega = S \log z_0 + \sum_{r=1}^{\infty} (-1)^r \int_0^{\beta} \mathrm{d}\tau_1 \int_0^{\tau_1} \mathrm{d}\tau_2 \ldots \int_0^{\tau_{r-1}} \mathrm{d}\tau_r \, \langle \hat{H}_1'(\tau_1) \hat{H}_1'(\tau_2) \ldots \hat{H}_1'(\tau_r) \rangle_0 \,. \tag{7.29}$$

Tunneling graphs

The series terms can be expressed using graphs, were each application of $\hat{H}_1'$ corresponds to the movement along a bond of the graph, i. e. in our specific expansion to a hopping from one to a next site (note that we now evaluate the grand potential per site),

$$-\beta\Omega/S = \log z_0 + \sum_{r=1}^{\infty} (-1)^r \underbrace{\sum_{g(m,l \le r)} z_0^{-m} c_{r,g} \mathrm{X}_{r,g}(\zeta, \beta, w) (\beta t)^l}_{\text{graph contribution}} \,, \tag{7.30}$$

Weak lattice contant

where m and l are the number of sites and bonds in the graph g, respectively. The graphs are weighted by the so-called weak lattice constant $c_{r,g}$, which is for example for the second order ($r = 2$) $c_{2,g} = [1, 2, 3]$ for a linear chain, square lattice or cubic lattice, respectively. This weak lattice constant originates from the reduction of the evaluation of $\langle ... \rangle_0$ over the entire lattice to just the graphs originating from a single site (which is valid since we assume all sites to be equal at this point, i. e. $\varepsilon_{\mathbf{i}} \equiv \varepsilon$). For the second order graphs on bipartite lattices, $c_{2,g}$ is half the coordination number z, since if for every site z and not $z/2$ graphs would be counted, every bond in the whole lattice would be counted twice. From this argument the extension to an anisotropic Hubbard model with tunneling matrix elements $t_{1 \ldots z}$ along the nearest-neighbor links numbered $1, ..., z$ becomes clear, e. g. for the second-order term of bipartite lattices,

Extension to the anisotropic Hubbard model on bipartite (e. g. square or cubic) lattices

$$c_{2,g} t^2 = \frac{1}{2} \sum_{l=1 \ldots z} t_l^2 \,. \tag{7.31}$$

Using this, also lattices of other than square or cubic geometry can be treated within a HTSE that uses the graphs for bipartite lattices, as long as the order of the HTSE is lower than that required to explore graphs which are either forbidden or additionally present in the new geometry. Therefore, to treat a 2D honeycomb lattice (which is equivalent to a brick lattice) within a HTSE up to second order, we set $c_{2,g} = 2$ and

2D honeycomb lattice

$$t_{1,2,3,4} = [t_{\text{horizontal}}, 0, t_{\text{vertical}}, t_{\text{vertical}}] \,, \tag{7.32}$$

where $t_2 = 0$ accounts for the missing horizontal link that differentiates the brick lattice from a square lattice. In Fig. 7.12 on the following page the influence of the tunneling corrections for 2D systems on the local density and the trap-averaged

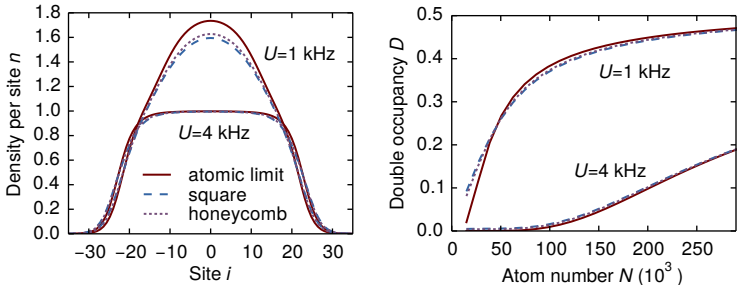

a. Density profiles b. Trap-averaged double occupancy

Figure 7.12: *Tunneling corrections in 2D systems.* Density profiles (for $N = 50 \times 10^3$) and trap-averaged double occupancies obtained from a HTSE of different 2D systems are compared for weak and strong interactions. The data is calculated for $t = 0$ (atomic limit), and, using second order corrections, for a square lattice with $t = 173$ Hz and for a honeycomb lattice with $t_{\text{horizontal}} = t_{\text{vertical}} = 173$ Hz. The tunneling corrections play only a role in the regime of low atom numbers and weak interactions, otherwise they are negligible. The entropy and averaged trap frequency are set to experimentally realistic values of $s = 1.5k_B$ and $\bar{\omega}/2\pi = 84$ Hz.

Size of the second order contributions

double occupancy (see Section 7.3.2) is shown. Corrections to the atomic limit ($t = 0$, i. e. HTSE in zeroth order) are relatively small and most pronounced in the regime of low atom numbers and weak interactions.

Note that strictly speaking Eq. (7.30) on page 143 is not an expansion in βt, since there is not only a term $(\beta t)^l$ but the expansion coefficients $\mathrm{X}_{r,g}(\zeta, \beta, w)$ also depend on β. Also note that in the case of bipartite lattices such as those of square or simple cubic geometry, all odd contributions vanish since there are no cycles with odd length in any graph. The first non-vanishing contribution will therefore be proportional to $(\beta t)^2$.

In general, the graph weight $\mathrm{X}_{r,g}$ is determined by taking the trace of a matrix containing the expectation values $\langle ... \rangle_0$ for all eigenstates of the unperturbed Hamiltonian $|\Psi_i\rangle$ in the reduced graph Hilbert space containing only s sites:

$$\mathrm{X}_{r,g} = \sum_{|\Psi_i\rangle} \int_0^\beta \mathrm{d}\tau_1 \int_0^{\tau_1} \mathrm{d}\tau_2 \ldots \int_0^{\tau_{r-1}} \mathrm{d}\tau_r \, \langle \Psi_i | e^{-\beta \hat{H}_0} \hat{H}_1'(\tau_1) \hat{H}_1'(\tau_2) \ldots \hat{H}_1'(\tau_r) | \Psi_i \rangle_{0,l} \,. \quad (7.33)$$

Here, $\langle ... \rangle_{0,l}$ is now only evaluated on the l tunneling links of the corresponding graph. In second order on bipartite lattices, there is only one contributing graph, namely that which corresponds to a tunneling process to a second site and back. The calculated expectation values of the $4 \times 4 = 16$ possible states of the two-site Hubbard model which contribute to the graph weight $\mathrm{X}_{2,1}$ are shown in Table 7.1 on the facing page.

Summing up these contributions, the total graph weight is obtained,

$$\mathrm{X}_{2,1} = 2\zeta(1 + \zeta^2 w) + \frac{4\zeta^2}{\beta U}(1 - w) \,, \quad (7.34)$$

resulting in the following expression for the grand potential up to second order for bipartite lattices:

$$-\beta \Omega / S = \log z_0 + z_0^2 c_{2,g} \mathrm{X}_{2,1} (\beta t)^2 \,. \quad (7.35)$$

Observables

For simple lattice structures, such as those described by HTSEs for a square or cubic lattice, quantities such as density, entropy and double occupancy (in this

Table 7.1: *Graph weight contributions.* The weight contributions of the 16 states of the two-site Fermi-Hubbard model for the second order graph in the HTSE are listed. Every contribution is the product of the number of associated states times the number of involved tunneling processes times the Boltzmann factor. The total graph weight $X_{2,1}$ is given by the sum of these contributions.

$\lvert\psi_{A,B}\rangle = \lvert n_{A\uparrow} n_{A\downarrow}, n_{B\uparrow} n_{B\downarrow}\rangle$	$\langle\psi_{A,B}\rvert \hat{H}_1'(\tau_1)\hat{H}_1'(\tau_2) \lvert\psi_{A,B}\rangle_0$
$\lvert 0,0\rangle$	$1 \times 0 \times \zeta^0 w^0$
$\lvert\uparrow\downarrow,\uparrow\downarrow\rangle$	$1 \times 0 \times \zeta^4 w^2$
$\lvert\uparrow,\uparrow\rangle, \lvert\downarrow,\downarrow\rangle$	$2 \times 0 \times \zeta^2 w^0$
$\lvert\uparrow,0\rangle, \lvert\downarrow,0\rangle, \lvert 0,\uparrow\rangle, \lvert 0,\downarrow\rangle$	$4 \times 1 \times \zeta^1 w^0$
$\lvert\uparrow\downarrow,\uparrow\rangle, \lvert\uparrow\downarrow,\downarrow\rangle, \lvert\uparrow,\uparrow\downarrow\rangle, \lvert\downarrow,\uparrow\downarrow\rangle$	$4 \times 1 \times \zeta^3 w^1$
$\lvert\uparrow,\downarrow\rangle, \lvert\downarrow,\uparrow\rangle$	$2 \times 2 \times \zeta^2 w^0 \exp(-U(\tau_2 - \tau_1))$
$\lvert\uparrow\downarrow,0\rangle, \lvert 0,\uparrow\downarrow\rangle$	$2 \times 2 \times \zeta^2 w^1 \exp(U(\tau_2 - \tau_1))$

case defined as the fraction of doubly occupied sites) can be obtained based on the above expression via the usual rules,

$$n = -\frac{1}{S}\frac{\partial\Omega}{\partial\mu} \qquad s = -\frac{1}{S}\frac{\partial\Omega}{\partial T} \qquad d = \frac{1}{S}\frac{\partial\Omega}{\partial U}. \tag{7.36}$$

In general, however, the evaluation of arbitrary observables is not straightforward and requires special techniques [Greif, 2013].

Range of validity

The obtained expansion will be valid as long as $t \ll k_B T \ll U$ [Oitmaa *et al.*, 2006]. Since a truncated series expansion is just a polynomial in the expansion parameter, it is obvious that a HTSE cannot describe any real phase transitions since all thermodynamic quantities will always be continuous due to the fact that they are derived from a continuous thermodynamic potential. Therefore, when for example approaching the phase transition to an antiferromagnetic state in the repulsive Fermi-Hubbard model starting from a large temperature, the series must break down at a certain point before entering the phase. However, when comparing the results obtained for a simple cubic lattice from HTSE with those from more advanced techniques such as QMC or DMFT, which reach beyond the phase transition, one finds that they agree down to about $k_B T/t \approx 2$ for a HTSE of sufficiently high order [Kozik *et al.*, 2010] (which is 10 in the given reference).

No phase transitions

Details on how observables, for example the nearest-neighbor density or spin correlator, are obtained in bipartite or dimerized lattices can be found in the thesis of Daniel Greif [2013].

7.3.2 LOCAL DENSITY APPROXIMATION

The results of the HTSE are valid for a homogeneous system in thermal equilibrium at a certain fixed temperature T and a fixed chemical potential μ. In reality, however, optical lattice systems are not homogeneous since the energy of every site varies slightly with respect to the neighboring ones due to the external confinement. To obtain thermodynamic quantities of this trapped system, the method known as local density approximation (LDA)[3] in the context of cold atom systems comes into play. The basic assumption is that the external potential is only slowly varying, or more precisely that the energy difference between two neighboring sites $\Delta\epsilon$ does not exceed any other energy scale in the problem. The thermodynamics at each site is then approximately obtained by calculating the quantities

3 Note that LDA has a slightly different meaning in the context of solid state theory.

Position dependent chemical potential

for the homogeneous system using a global temperature T and a chemical potential which is shifted by the local trapping potential,

$$\mu_{\mathbf{i}} = \mu_0 - \varepsilon_{\mathbf{i}} \,. \tag{7.37}$$

The value of a global observable $\mathscr{O}^{\text{trap}}$ of the trapped system can then be obtained by summing over the contributions from every site,

$$\mathscr{O}^{\text{trap}}(\mu_0, T) = \sum_i \mathscr{O}_{\mathbf{i}}^{\text{hom}}(\mu_{\mathbf{i}}, T) \,. \tag{7.38}$$

Trap integration

If $\varepsilon_{\mathbf{i}}$ is a continuous function of the space coordinate (i. e. $\varepsilon(\mathbf{r})$), this summation can be rewritten in terms of an integral. In our experiment the external confinement is given by the gaussian intensity envelope of the lattice and the FORT beams, which can close to its minimum be approximated by a harmonic function. The curvatures of this external harmonic potential along the three spatial directions are given by the harmonic trapping frequencies $\omega_{x,y,z}$. This trapping potential can be made radially symmetric by replacing the separate trapping frequencies by their geometric mean, $\bar{\omega} = (\omega_x \omega_y \omega_z)^{1/3}$, resulting in

$$\mu(r) = \mu_0 - \frac{1}{2} m \bar{\omega}^2 \left(\frac{\lambda}{2}\right)^2 r^2, \tag{7.39}$$

where we have set – without loss of generality – μ_0 as the chemical potential in the trap center and r is in units of the site distance. The integral to obtain a global observable $\mathscr{O}^{\text{trap}}$ then becomes:

$$\mathscr{O}^{\text{trap}}(\mu_0, T) = \int_0^\infty 4\pi r^2 \mathscr{O}^{\text{hom}}(\mu(r), T)\, \mathrm{d}r. \tag{7.40}$$

Application to the experiment: obtaining the chemical potential and the temperature

In the experiment, typically only global extensive thermodynamic quantities such as the total atom number N_{exp} or the total entropy S_{exp} of the gas can be measured, for example by fitting the density profiles of the gas released from the FORT in TOF. In order to obtain the essential intensive quantities such as temperature and chemical potential, the following system of equations ($\mathscr{O}^{\text{hom}} = n, s$) has to be solved numerically:

$$\begin{aligned} N^{\text{trap}}(\mu_0, T) &= N_{\text{exp}} \\ S^{\text{trap}}(\mu_0, T) &= S_{\text{exp}} \,. \end{aligned} \tag{7.41}$$

Using the obtained μ_0 and T, other observables can then be calculated via the integration over the trap using Eq. (7.40).

Coexistence of phases

The locally varying chemical potential leads to the unique feature that in cold atom based implementations of solids several phases coexist at different trap radii in the same realization. This feature is for example nicely illustrated by single-site resolved *in situ* density profiles of bosonic atoms loaded into 2D optical lattices [Bakr *et al.*, 2010; Sherson *et al.*, 2010]. In these experiments, the so-called wedding cake structure of the bosonic Mott insulator as a function of distance from the trap center, with small superfluid regions at the interface between the plateaux of pinned density, is directly visible in the measured density profiles.

THE MOTT INSULATOR TRANSITION

8

In this chapter we study the effects of interactions in the artificial graphene system. We load an interacting balanced mixture of two magnetic spin states into the tunable-geometry optical lattice while inhibiting the motion of the atoms along the third spatial direction by a deep perpendicular lattice. In this way, we realize decoupled layers of artificial graphene sheets very much akin to real graphene, see Fig. 8.1. The state of the system is characterized by a spectroscopic measurement of the double occupancy.

CHAPTER CONTENTS

Exploring interaction regimes beyond that of real graphene

Our system, however, enables us to explore interaction regimes beyond those accessible in real graphene. By performing state dependent rf spectroscopy in order to measure the double occupancy of the system, i. e. the fraction of atoms on doubly occupied sites, we observe the crossover from the metallic regime to a 2D Mott-insulating state at strong repulsive interactions.

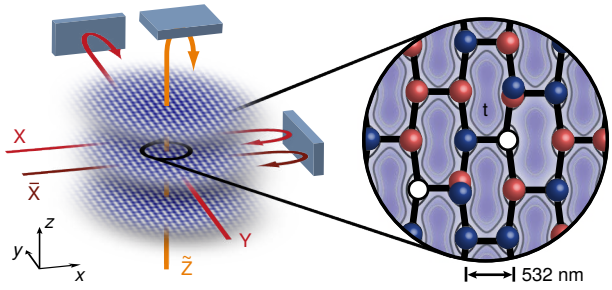

Figure 8.1: *Experimental setup used to create the artificial graphene system.* Independent 2D layers of honeycomb geometry are realized using the tunable-geometry optical lattice. A sketch of the tunneling structure within the layers is shown on the right. A repulsively interacting two-component spin mixture of fermionic ^{40}K atoms (red and blue spheres) is loaded into the lattice. Gravity points along *y*.

Theoretical description: Fermi-Hubbard Hamiltonian

The system can be described using the Fermi-Hubbard Hamiltonian, which allows for comparison of the data with theory predictions obtained from a high-temperature series expansion (HTSE) of the grand partition function. Moreover, we characterize the Mott-insulating state by measuring its excitation spectra. The equilibration properties of the 2D systems are of utter importance when preparing such samples. In particular, we study the dynamics of the double occupancy while loading the lattice to determine the equilibration times. Finally, we extend our measurements to coupled layer systems whose static and dynamic properties

are studied. Additionally, the behavior of the double occupancy when crossing the transition to a dimerized lattice geometry is explored.

This chapter is partly based on the preprint of the following publication:

> T. Uehlinger, G. Jotzu, M. Messer, D. Greif, W. Hofstetter, U. Bissbort, and T. Esslinger, *Artificial graphene with tunable interactions*, Phys. Rev. Lett. **111**, 185307 (2013), DOI : 10 . 1103 / PhysRevLett . 111 . 185307, preprint available on ArXiv e-prints, arXiv:1308.4401.

8.1 EXPERIMENTAL TECHNIQUES

8.1.1 PREPARATION

To obtain a quantum degenerate Fermi gas we adhere to the procedure used in previous work [Jördens *et al.*, 2008] described in detail in Section 3.1.4 on page 41. A balanced (ratio 0.50(5)) spin mixture of ^{40}K atoms in the $m_F = {}^{-9}/_{2}$ and $^{-7}/_{2}$ magnetic sublevels of the $F = {}^{9}/_{2}$ hyperfine manifold is evaporatively cooled in the crossed beam optical dipole trap to 15(2)% of the Fermi temperature. We prepare Fermi gases with total atom numbers between $N = 25 \times 10^3$ and 300×10^3, with 10% systematic uncertainty [Jördens *et al.*, 2010]. We either set the scattering length to $86(2)a_0$ using a Feshbach resonance or transfer to an $m_F = ({}^{-9}/_{2}, {}^{-5}/_{2})$ mixture, where we access larger repulsive interactions in the range of $a = 242(1)a_0$ to $632(12)a_0$.

We then load the atoms into the tunable-geometry optical lattice [Tarruell *et al.*, 2012; Lim *et al.*, 2012; Uehlinger, Greif, Jotzu, Tarruell, Esslinger, *et al.*, 2013] using all four beams $\bar{\mathrm{X}}$, X , Y and $\tilde{\mathrm{Z}}$, see Section 3.2 on page 44. This gives rise to the potential

$$\begin{aligned} V(x,y,z) = & -V_{\bar{\mathrm{X}}}\cos^2(k_{\mathrm{L}}x+\theta/2) - V_{\mathrm{X}}\cos^2(k_{\mathrm{L}}x) \\ & - V_{\mathrm{Y}}\cos^2(k_{\mathrm{L}}y) - V_{\tilde{\mathrm{Z}}}\cos^2(k_{\mathrm{L}}z) \\ & - 2\alpha\sqrt{V_{\mathrm{X}}V_{\mathrm{Y}}}\cos(k_{\mathrm{L}}x)\cos(k_{\mathrm{L}}y)\cos\varphi\,, \end{aligned} \tag{8.1}$$

Lattice depths used for the experiments

with $k_{\mathrm{L}} = 2\pi/\lambda$, visibility $\alpha = 0.90(5)$, $\varphi = 0.00(3)\pi$, and θ set to $1.000(1)\pi$, i. e. zero A-B site offset. The final lattice depths in units of the recoil energy E_{R} are

$$V_{\bar{\mathrm{X}},\mathrm{X},\mathrm{Y},\tilde{\mathrm{Z}}} = [14.0(4), 0.79(2), 6.45(20), 30(1)]\,E_{\mathrm{R}},$$

unless explicitly stated otherwise. All beams are ramped up simultaneously to their final intensities within 200 ms. The resulting potential contains several independent 2D honeycomb layers with an inter-layer tunneling rate below 2 Hz. For the combined external confining potential of the dipole trap and the lattice laser beams we measure harmonic trapping frequencies of

$$\omega_{x,y,z}/2\pi = [86(2), 122(1), 57(1)]\,\mathrm{Hz}.$$

We have calculated the band structure for the given lattice parameters by numerically diagonalizing the single-particle Hamiltonian containing the true optical potential (see Section 4.1.1 on page 73). The band structure is found to contain two nearly isotropic Dirac points, located at $k_y^{\mathrm{D}} \approx {}^{3}/_{4}\,k_{\mathrm{L}}$, see Fig. 8.2 on the facing page.

Using the maximally localized Wannier functions within the two minibands (calculated as described in Section 4.2.2 on page 81) we obtain the following tight-binding parameters in the $x-y$ plane:

Tight-binding parameters

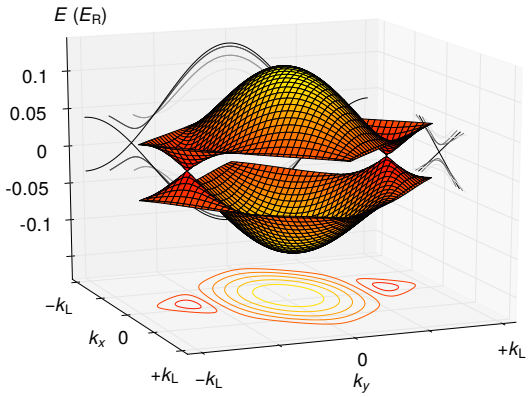

Figure 8.2: *Band structure.* The band structure contains two nearly isotropic Dirac points, with the other bands well separated from the two minibands. Cuts through the band structure in the vicinity of the Dirac points are shown in the background. A contour plot of the lower band is shown at the bottom.

$$t = t_1/h = 172(20)\,\text{Hz} \qquad t = t_2/h = 172(20)\,\text{Hz} \qquad t_3/h = 8(2)\,\text{Hz} \tag{8.2}$$

$$t_1'/h < 2\,\text{Hz} \qquad t_{\text{others}} < t_1'\,. \tag{8.3}$$

8.1.2 DOUBLE OCCUPANCY MEASUREMENT

We characterize the state of our system by measuring the fraction of atoms on doubly occupied sites D [Jördens *et al.*, 2008; Jördens *et al.*, 2010]. To determine D, all tunnelings processes are suppressed by switching off V_X in roughly 5 µs and ramping up V_X and V_Y linearly to a depth of 30 E_R within 500 µs. We then perform interaction dependent rf spectroscopy to obtain D [Jördens *et al.*, 2008].

This detection technique can be used for both $(-9/2, -7/2)$ as well as $(-9/2, -5/2)$ spin mixtures. In detail, we proceed for the $(-9/2, -7/2)$ spin mixture prepared on the left side of the Feshbach resonance located at 224 G as follows, see also Fig. 8.3:

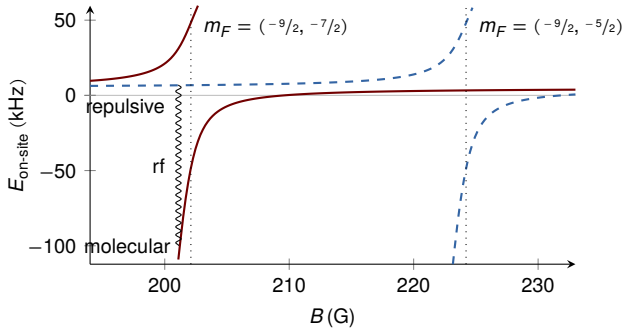

Figure 8.3: *On-site energy in the optical lattice and rf spectroscopy.* The energy of two atoms of opposite spin in the lattice is drawn as a function of magnetic field for the two used spin mixtures. The energy difference between the bound state on the low-field side of the $(-9/2, -7/2)$ resonance position (solid red) and the unbound state above originating from the $(-9/2, -5/2)$ resonance (dashed blue) allows selectively addressing double occupancies with rf pulses (coiled) with a frequency which is shifted by ∼ 100 kHz. Adapted from [Jördens, 2010].

Freezing the atomic motion

1. The lattice is deformed to a simple square (when starting with a 2D system) or cubic lattice to ensure a consistent and reproducible starting point for the following detection steps. In order not to change the density distribution, the lattice ramp needs to be on a faster time scale than the corresponding tunneling process. On the other hand the rate in the change of the on-site harmonic oscillator frequency must be smaller compared to the frequency itself to avoid higher band population. The deformation is achieved

by switching off V_X, which restores the (anisotropic) square geometry in the $x-y$ plane of the lattice by removing the dimerization. As the resulting change in the on-site trap frequency during this ramp is relatively small, the switch-off can be performed within only a few µs.

2. The lattice depths $V_{\tilde{X}}$, V_Y, and, if necessary, $V_{\tilde{Z}}$ are ramped to a depth of $30\,E_R$ within 500 µs to fully suppress any further tunneling. The ramp time is defined by the same criteria as for the deformation to a square lattice.
3. The magnetic bias field is then ramped within 10 ms from its initial setting to 202.8 G, which is just a bit above the Feshbach resonance position.

Association of molecules

4. The bias field is then further decreased to 201.3 G within 5 ms, thereby crossing the Feshbach resonance. This causes the association of weakly bound molecules on sites that are occupied by two atoms in different spin states.

rf transition

5. These molecules can then be dissociated by addressing the rf transition from the $m_F = -7/2$ to the $m_F = -5/2$ Zeeman state using a π pulse, without affecting the atoms on singly occupied sites. The selectiveness of the transition is due to the binding energy of the molecule, which increases the required rf frequency with respect to an unbound atom. As a result, the $m_F = -5/2$ spin state is populated with a fraction of atoms that is proportional to the amount of doubly occupied lattice sites.
6. The bias field is swept back over the Feshbach resonance to 208 G within 10 ms in order to dissociate any (possibly remaining) molecules.
7. The intensity of the optical lattice beams is then ramped to 0 within 50 ms using an S-shaped ramp. This lowers the external confinement in order to counteract excessive expansion of the cloud during the following TOF. We have checked that the population of the spin states is not altered during this step.
8. The FORT beams are abruptly switched off to start the TOF expansion.

Stern-Gerlach experiment

9. After 1 ms of TOF, the magnetic bias fields is switched off and a current pulse of $I = 18$ A with a duration of 3 ms is run through the upper quadrupole coil. This induces a strong magnetic field gradient along the y direction leading both to a spatial separation of the Zeeman spin populations similar as in a Stern-Gerlach experiment as well as a total acceleration against gravity.
10. After a total TOF time of 8 ms, absorption images of the three spin populations are taken, see Fig. 8.4a on the next page.
11. The density profiles of the spin populations are fitted by gaussians with position, distance and width locked to each other. From the fits, the atom number per spin state is extracted.
12. The double occupancy D, defined as the fraction of atoms residing on double occupied sites, is then calculated as

$$D = 2\frac{N_{-5/2}}{N_{-9/2} + N_{-7/2} + N_{-5/2}}. \tag{8.4}$$

The method works in a similar way when starting with a $(-9/2, -5/2)$ spin mixture. In this case the π pulse selectively associates molecules which after the pulse consist of one atom with $m_F = -9/2$ and one with $m_F = -7/2$. These molecules are then dissociated by a following upward sweep over the Feshbach resonance and then imaged in the same way.

In fact, with the rf pulse either the Zeeman state of atoms sitting on doubly occupied states can be changed, as described above, or the transition of atoms on singly occupied sites is addressed, at a frequency that is lower by the molecular binding energy, see Fig. 8.4b on the facing page. Rabi oscillations between the weakly repulsively interacting unbound state and the molecular state obtained

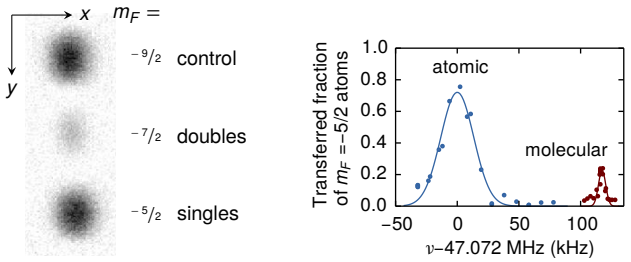

a. Stern-Gerlach separation

b. rf spectrum

Figure 8.4: *Double occupancy measurement.* a. A typical absorption image after performing Stern-Gerlach separation of the three spin states obtained from the $(-9/2, -5/2)$ spin mixture by performing the state-dependent rf spectroscopy is shown. b. The rf spectrum in the vicinity of the $m_F = -7/2 \leftrightarrow -5/2$ transition shows two peaks, one corresponding to the association of molecules on doubly occupied sites (*molecular peak*), the other to changing the Zeeman state of an atom on a singly occupied site (*atomic peak*). Different π pulse times of 130 µs and 35 µs, respectively, where used, owing to the different Franck-Condon overlaps.

when varying the pulse time are shown in Fig. 8.5. Several cycles of oscillations are visible, demonstrating the coherence of the transition.

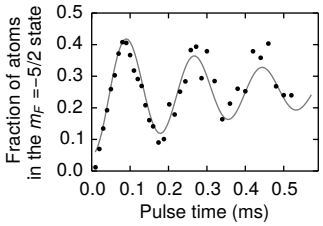

Figure 8.5: *Rabi oscillations.* The fraction of atoms in the $m_F = -5/2$ spin state is measured as a function of the rf pulse time for a sample initially prepared in the $(-9/2, -7/2)$ spin mixture at attractive interactions. Several periods of Rabi oscillations with a damping mainly caused by magnetic field fluctuations are visible. The lattice depth used for freezing the atomic motion is 30 E_R.

DETECTION EFFICIENCY OF THE ZEEMAN STATES

After the gradient pulse all currents in the magnetic field coils are set to zero in order to perform absorption imaging at zero magnetic field. Owing to eddy currents and residual magnetization in the *Mu-metal* shielding, the magnetic fields are however found to have not completely decayed at the time of absorption imaging. As a result, the imaging transitions for the three Zeeman states are slightly detuned from the zero-field energy as well as from each other, owing to the Zeeman shift. This would lead to a wrong atom number determination and therefore possibly an under- or overestimation of the double occupancy.

Correcting for the spin-dependent detuning

To correct for the detuning, we acquire separate resonance curves for the three spin states and fit them with lorentzian functions, see Fig. 8.6 on the following page. We then divide the atom numbers measured in the actual experiments by the relative height of the respective Lorentz function at the actual imaging detuning δ, which we choose to lie at roughly the mean of the three peak positions.

CALIBRATING THE DOUBLE OCCUPANCY DETECTION EFFICIENCY

The double occupancy detection efficiency of the presented method is mainly determined by the transfer efficiency of the rf π pulse, which we find to be less than unity. This is most probably caused by temporal and spatial fluctuations of the magnetic bias field, which leads to shifts of the transition frequency. The temporal fluctuations are caused by noise in the current stabilization, while the spatial

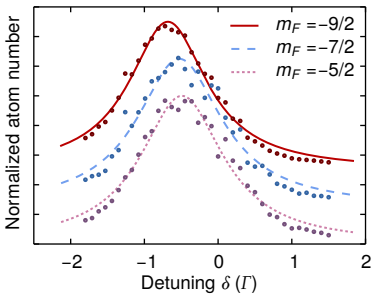

Figure 8.6: *Detection efficiency of the Zeeman states.* The resonance curves of the three Zeeman states obtained for correcting the measured atom numbers are shown. They are rescaled to the same height and subsequently fitted by lorentzians. The corrections, obtained from the peak height at the detuning δ actually used for the following measurements, are on the order of not more than 10%.

fluctuations are due to the fact that the atoms are not positioned exactly in the center of the Helmholtz coils used to create the bias field, see Fig. 3.29 on page 62.

Calibration using a spin-polarized gas

We have determined the double occupancy detection efficiency using two independent methods: the single occupancy detection efficiency can be measured using a spin-polarized cloud, where the rf pulse should theoretically transfer 100% of the atoms. In an rf spectrum for a spin mixture as shown in Fig. 8.4b on page 151, the sum of the atomic peak height corrected by the single occupancy transfer efficiency plus the molecular peak height corrected by the double occupancy detection efficiency should be one. Knowing the single occupancy detection efficiency, the double occupancy detection efficiency can therefore be extracted from the spectrum.

Calibration using molecule formation

Alternatively, after associating molecules using the magnetic field sweep over the Feshbach resonance, TOF expansion followed by absorption imaging can be performed directly by instantaneously switching off the lattice and the FORT as well as all magnetic fields. The bound molecules are invisible in the absorption image as their imaging transition is shifted, leading to an apparent reduction in the detected atom number. The difference in measured atom number with and without associating molecules is then given by the number of atoms on doubly occupied sites. This alternative way of detecting double occupancies has a close to unity detection efficiency and can – by comparison with the normal detection method – be used to calibrate the efficiency of the latter. This alternative way of detecting the occupancy might seem preferable at first sight as the general detection method. However, it has the disadvantage that it requires two identical experimental runs to obtain the double occupancy, making it prone to atom number fluctuations.

Both methods lead to a double occupancy detection efficiency of 89(2)%. This efficiency is taken into account when analyzing the obtained data. Additionally, an independently measured offset of $\Delta D = 2.2(3)\%$, caused by a residual population of the third spin state after preparation of the spin mixture is subtracted from the obtained double occupancies D.

8.2 OBSERVING THE METAL TO MOTT INSULATOR TRANSITION

In the experiment we tune interactions from weakly ($U/3t = 1.8(3)$) to strongly repulsive ($U/3t = 13(1)$) and measure the double occupancy D as a function of the atom number N in the lattice, see Fig. 8.7 on the next page. For weak interactions, the system is in a metallic state which is compressible, as signaled by an initial strong increase of D [Scarola *et al.*, 2009]. Here, creating more double occupancies requires less energy than placing additional atoms in the outside region of the harmonic trap where the potential energy is large. For high atom numbers D saturates as the system enters a band insulating state.

When increasing interactions, an incompressible Mott-insulating state forms in the center of the trapped system. Therefore, D is strongly suppressed and does not increase as more atoms are added to the system. Only for the highest atom

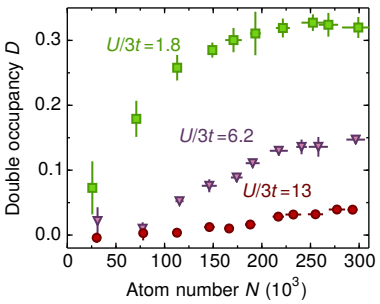

Figure 8.7: *Observing the metal to Mott insulator crossover in artificial graphene.* The measured double occupancy D versus atom number N is shown for three different interaction strengths $U/3t$. For strong interactions an incompressible Mott-insulating core forms, leading to a strong suppression of D. Error bars in D and N show the standard deviation of 5 measurements. Data for additional interactions can be found in Fig. 8.8 on the following page. Negative values of D are caused by the subtraction of an independently measured offset.

numbers the chemical potential becomes comparable to the on-site interaction, which allows for the creation of double occupancies [Jördens *et al.*, 2008].

8.3 COMPARISON TO THEORY

A quantitative comparison of our results with a microscopic theory is made possible by mapping our system to the Fermi-Hubbard Hamiltonian as discussed in detail in Chapter 7 on page 131. The nearest-neighbor tunneling t and the interaction energy U are determined from the Wannier function calculation (Section 4.2.2).

We validate the qualitative interpretation of the data shown above using a high-temperature series expansion (HTSE) up to second order of the grand canonical partition function [Oitmaa *et al.*, 2006] (*cf.* Section 7.3.1 on page 142) to determine the expected D, see Fig. 8.8 on the following page, where also additional data for intermediate interactions is shown.

Theory parameters

For the calculation we use a nearest-neighbor tunneling of $t/h = 172(20)$ Hz within the layers and the separately measured on-site interaction energies (see Section 8.4 on page 155 for the measurement procedure)

$$U/h = [0.92(12), 2.96(3), 3.18(2), 3.95(2), 4.75(2), 6.52(3)]\ \text{kHz}$$

at the chosen scattering lengths

$$a = [86(1), 242(1), 270(1), 347(3), 429(4), 632(11)]a_0.$$

The model assumes a connectivity of $z = 3$ within the 2D planes and no interlayer tunneling, as well as a globally thermalized cloud. Both finite temperature and the harmonic trap are taken into account. We obtain overall good agreement with theory when allowing for the entropy per atom in the lattice $s = S/N$ as a fit parameter [Jördens *et al.*, 2010]. For the six interactions, the fitted entropies of $s = [2.1, 2.2, 2.7, 3.4, 2.7, 1.7]k_B$ are comparable to $s_{in} = 1.5(2)\,k_B$ and $s_{out} = 2.5(1)\,k_B$ measured in the dipole trap before loading and after reversing the loading procedure.

We compute that about 50 layers contain Mott-insulating cores, each of which consists of up to 2000 atoms. Deviations from theory are likely to arise because of incomplete thermalization. The tunneling timescale is expected to be sufficiently fast for equilibration within layers (see Section 8.5 on page 156). Yet, the slow interlayer tunneling when approaching the final configuration hinders the formation of a globally thermalized state. A more detailed analysis would require a full non-equilibrium model of coupled 2D layers.

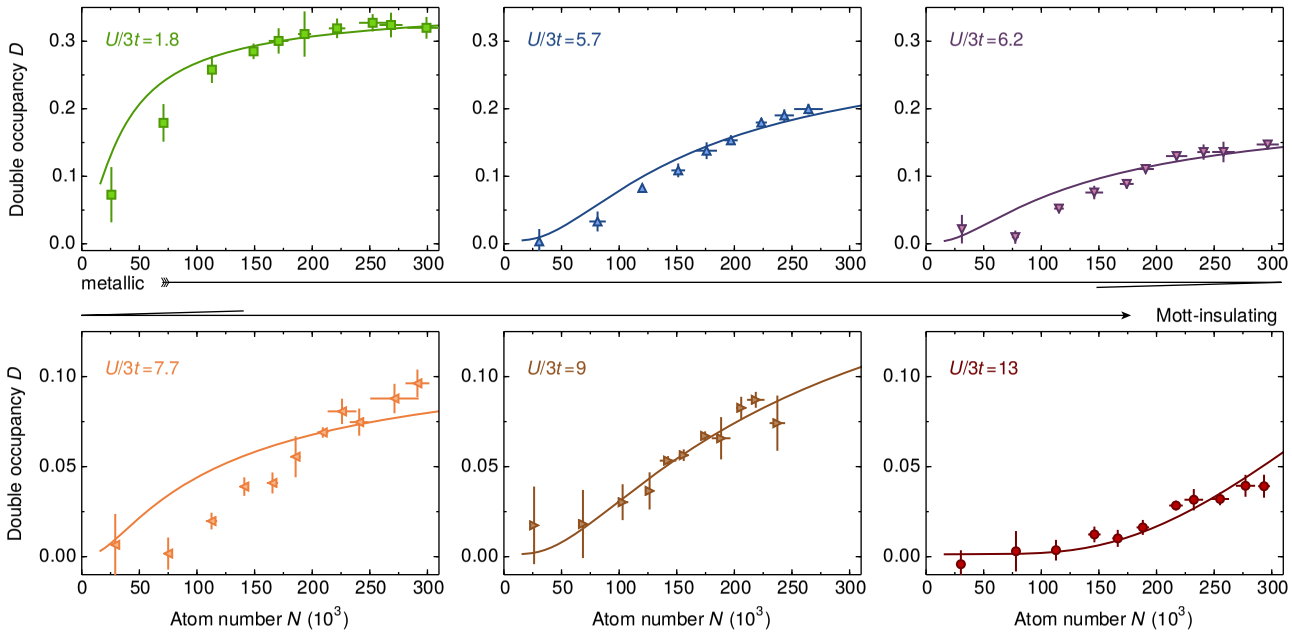

Figure 8.8: *Observing the metal to Mott insulator crossover in artificial graphene.* The measured double occupancy D versus atom number N is shown for additional interactions as compared to Fig. 8.7 on page 153, with scattering lengths $a = [86(1), 242(1), 270(1), 347(3), 429(4), 632(11)]a_0$. Solid lines are theoretical predictions from the HTSE up to second order with fitted entropies of $s = [2.1, 2.2, 2.7, 3.4, 2.7, 1.7]k_B$ for $U/3t = [1.8(3), 5.7(7), 6.2(7), 7.7(9), 9(1), 13(1)]$ respectively. Error bars in D and N show the standard deviation of 5 measurements.

8.4 PROBING THE EXCITATION SPECTRUM

A characteristic feature of a Mott insulator is a gapped excitation spectrum [Brinkman *et al.*, 1970], which we probe by recording D in response to modulating the lattice depth at different frequencies ν [Jördens *et al.*, 2008].

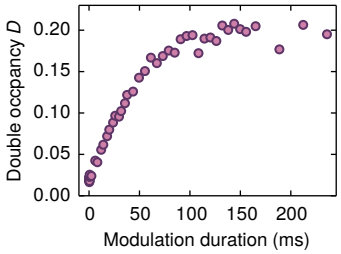

Figure 8.9: *Double occupancy buildup.* The measured double occupancy after a variable duration of lattice intensity modulation of the Y beam with an amplitude of ±10% at a frequency of $\nu = 4240$ Hz is shown. The atom number is set to $N = 270(13) \times 10^3$ and the interaction to $U/h = 4.2$ kHz. The modulation is performed in a square lattice with $V_{\tilde{X},Y,\tilde{Z}} = [7.0(2), 7.0(2), 7.0(2)]\, E_R$, resulting in a tunneling $t/h = 174$ Hz.

After loading the gas into the lattice, we sinusoidally modulate V_Y for 40 ms by ±10%. As V_Y interferes with V_X, this leads to a modulation in the tunneling t_1 (t_2) of ∼ ±7% (∓17%) as well as an additional modulation of U by ±3% caused by the changing width of the Wannier functions.

Double occupancy buildup

The typical dynamical response of the double occupancy to a modulation of varying duration is shown for the case of a square lattice in Fig. 8.9 (similar results are obtained for the honeycomb lattice). For all further measurements, we chose a modulation duration of 40 ms, such that the response of the system is within the linear regime of double occupancy creation [Greif *et al.*, 2011] for the whole parameter range. In the linear regime the creation rate is proportional to the energy absorption rate [Tokuno *et al.*, 2012]. For longer modulation durations, D saturates at a certain value. This regime will not be considered in the present work, as it contains little information about the initial state of the system.

In Fig. 8.10, we plot both the response and the measured base level without modulation (arrows) for the same interactions as used in Fig. 8.8 on page 154, with $N = 80(2) \times 10^3$. For weak interactions there is almost no detectable response. When entering the Mott-insulating regime we observe a gapped spectrum with a pronounced peak at $\nu = U/h$, corresponding to the creation of localized double occupancies.

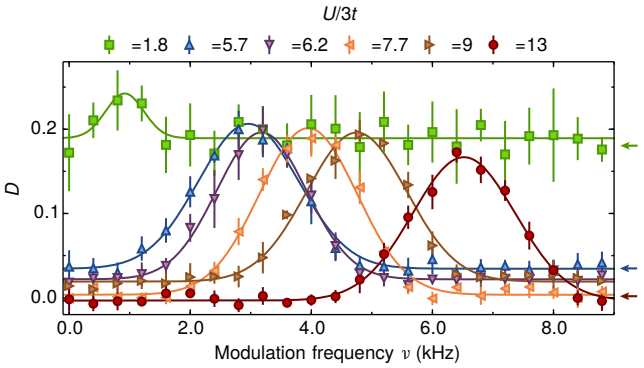

Figure 8.10: *Excitation spectra.* The spectra are obtained in the artificial graphene system by measuring D after sinusoidal modulation of the lattice depth V_Y at the interaction strengths used in Fig. 8.8. The solid lines are gaussian fits to the spectra. Arrows indicate the reference values without modulation. Error bars show the standard deviation of 5 measurements.

Comparison of the excitation energies to theory

In Fig. 8.11 on the following page, we compare the peak position at $\nu = U/h$ obtained from gaussian fits to modulation spectra (shown in Fig. 8.10) with the on-site interaction energy calculated using maximally localized Wannier functions. For weak interactions the *ab initio* calculation of the Hubbard parameter U agrees well with the measured value (see also Fig. 8.19 on page 161). Deviations are observed for the strongest interactions. We attribute these to the deep optical lattice in one direction leading to a size of the Wannier function which becomes compa-

rable to the scattering length and possibly to higher band effects. A more detailed theory would however be necessary for a quantitative comparison in this regime.

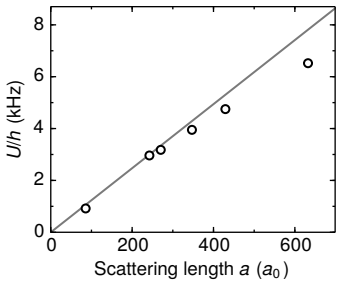

Figure 8.11: *Theory comparison.* Comparison of the Hubbard parameters U extracted from the experiments (circles) with those obtained from a calculation of the Wannier functions in the honeycomb lattice (solid line). The statistical uncertainty in a and the fit error for the peak positions are smaller than the displayed data points.

8.5 THE LATTICE LOADING PROCESS

The equilibration within the 2D honeycomb layers requires a change of the quantum many-body state during the lattice loading process. This is determined by the time necessary for the global density redistribution and the formation of correlations associated to the change in external potential. So far, equilibration dynamics have been investigated experimentally for bosonic atoms in optical lattices [Gericke *et al.*, 2007; Hung *et al.*, 2010; Bakr *et al.*, 2010], whereas for strongly correlated fermions the time evolution from the continuum to the Hubbard regime has not been studied yet.

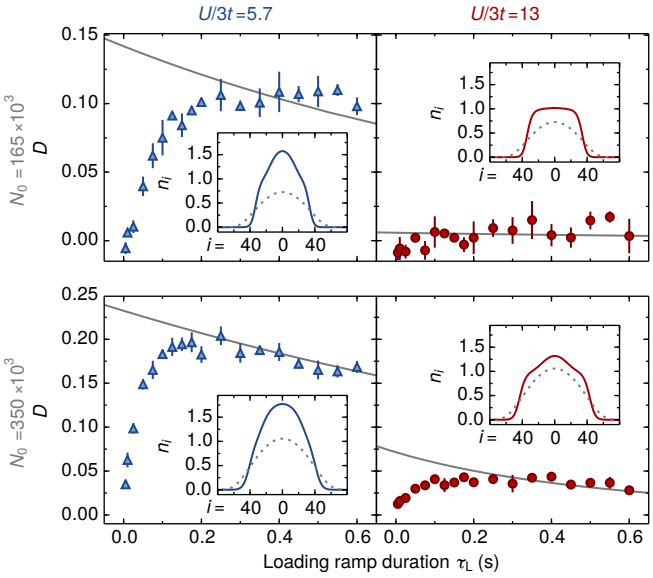

Figure 8.12: *The lattice loading process.* The panels show D after loading ramps with varying duration τ_L for two interactions and two initial atom numbers. The solid line is the expected D from the HTSE taking atom loss and heating during lattice loading into account. The insets show the calculated equilibrium density profiles for the atomic cloud in the optical dipole trap (dashed) and in the lattice (solid lines), illustrating the required density redistribution during the loading. Here the initial atom number and entropies before loading into the lattice were used. Error bars in D show the standard deviation of 3 measurements.

In Fig. 8.12 we study the lattice loading process by measuring the resulting D after the loading ramp lasting between $\tau_L = 5$ ms and $\tau_L = 600$ ms. For the load-

ing of the lattice from the dipole trap we use an S-shaped intensity ramp to the final lattice depth V_0. The full time-dependent expression of the intensity ramp is

Lattice loading intensity ramp

$$V(\tau) = 3V_0\left(\frac{\tau}{\tau_L}\right)^3 - 2V_0\left(\frac{\tau}{\tau_L}\right)^2. \tag{8.5}$$

Both for intermediate ($a = 242(1)\,a_0$, blue triangles) and strong interactions ($a = 632(12)\,a_0$, red circles) we observe a fast rise of D up to $\tau_L = 200$ ms followed by a slow decay. We additionally plot the expected D as derived from the HTSE (solid line) assuming global thermal equilibrium and taking into account atom loss and the independently determined heating rate. This heating rate is measured by reversing the loading procedure and extracting the resulting entropy in the dipole trap. For ramp durations larger than 200 ms we find a roughly linear increase in entropy with time. The theoretical predictions for the double occupancy versus loading time are then obtained using the parameters from the double occupancy measurements shown in Fig. 8.8 on page 154 and Fig. 8.10 on page 155.

Optimal lattice loading duration

For $\tau_L \gtrsim 200$ ms the measured double occupancy agrees with the theoretical model. When comparing this timescale with the nearest-neighbor tunneling time of 6 ms in the honeycomb layers, this suggests that 200 ms is sufficient for density redistribution within the 2D layers (for the case of coupled layers similar timescales are observed, see Fig. 8.20 on page 162).

The calculated density profiles for different interactions and atom numbers (insets Fig. 8.12 on page 156) indicate that the core density has to increase when loading the atoms from the dipole trap into the lattice. For very short ramp times this density redistribution cannot occur, leading to too low densities in the trap center. This is confirmed by the observed low values of D as compared to theory for short τ_L.

8.6 COUPLED HONEYCOMB LAYERS

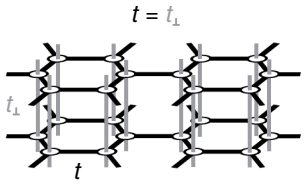

Figure 8.13: *Coupled layers of artificial graphene.* Detail of the coupled layer structure with $t = t_\perp$. The atoms populate about 80 layers. In contrast to e. g. multilayer graphene, the layers are stacked exactly on top of each other.

The coupling between 2D layers is known to alter their physical properties as compared to mono-layer systems. For the case of real graphene, this has been used to modify the dispersion relation around the Dirac points [Novoselov *et al.*, 2006]. In our experiment, coupled honeycomb layers stacked as shown in Fig. 8.13 can be produced, opening the possibility to simulate multilayer systems with tunable interactions. The tunneling between sites of adjacent layers $t_\perp$ can be controlled via the lattice depth $V_{\tilde{Z}}$.

In the following we set $V_{\tilde{Z}} = 7.0(2)\,E_R$ (corresponding to $t = t_\perp$) and investigate the dependence of the double occupancy on atom number, see Fig. 8.14 on the following page. The scattering length is set to the same values as in Fig. 8.12 on page 156 and the trapping frequencies are $\omega_{x,y,z}/2\pi = [55.7(7), 106(1), 57(1)]$ Hz.

8.6.1 OBSERVING THE METAL TO MOTT INSULATOR TRANSITION

For weak repulsive interactions ($U/5t = 2.5(3)$ with $U/h = 2.18(4)$ kHz) the system is metallic, whereas for large interactions ($U/5t = 5.6(7)$ with $U/h =$

4.82(2) kHz) the system is in the Mott-insulating regime, signaled by a strong suppression of D. We find excellent agreement with the theoretical predictions of the HTSE using a connectivity of $z = 5$, see Fig. 8.16 on the facing page, where also additional datasets for intermediate interactions are shown.

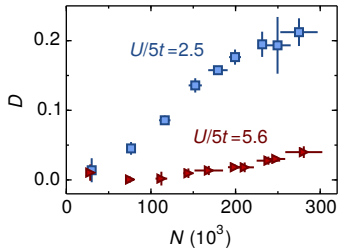

Figure 8.14: *Coupled layers of artificial graphene.* The double occupancy D versus atom number N in the metallic and Mott-insulating regime for stacked layers of artificial graphene is shown. Error bars in D and N show the standard deviation of 5 measurements.

For these measurements, we choose the interactions

$$U/5t = [2.5(3), 3.1(4), 4.0(5), 4.9(6), 5.6(7)]\,,$$

with

$$U/h = [2.19(5), 2.68(3), 3.41(3), 4.18(2), 4.83(2)]\,\text{kHz}$$

at the same scattering lengths as for the 2D measurements,

$$a = [242(1), 270(1), 347(3), 429(4), 632(11)]a_0.$$

The fitted entropies per particle are $s = [1.8, 2.5, 2.4, 1.7, 1.8]k_B$. As compared to the 2D measurements, we find only negligible deviations from the calculated double occupancy for the whole range of interactions. We attribute this to the fast tunneling time between layers leading to equilibration even between the honeycomb planes.

Differences to the case of independent honeycomb layers

Both the uncoupled- and coupled-layer systems show a crossover from the metallic to the Mott-insulating regime. However, quantitative differences are observed in the double occupancy dependence for the case of coupled layers. These differences originate from the altered lattice structure, which changes both the lattice connectivity and on-site interaction U.

The transition into an insulating regime can also be observed by keeping the atom number fixed and scanning the interaction, see Fig. 8.15. We set the atom number to $N = 177(6) \times 10^3$ and scan the scattering length in the range $a = 220a_0$ to $a = 630a_0$. The observed decrease in double occupancy for larger interactions agrees well with the prediction of the HTSE assuming a constant entropy of $s = 2.2k_B$. Deviations from the theory could be explained by previous observations that the heating during lattice loading is interaction-dependent [Jördens *et al.*, 2010].

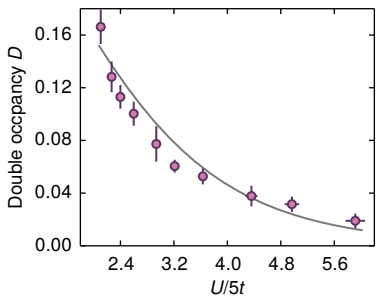

Figure 8.15: *Double occupancy as a function of interaction.* The Mott insulator transition is observed when varying the interaction at a constant atom number of $N = 177(6) \times 10^3$. Good agreement with theory is obtained for an experimentally realistic entropy of $s = 2.2k_B$.

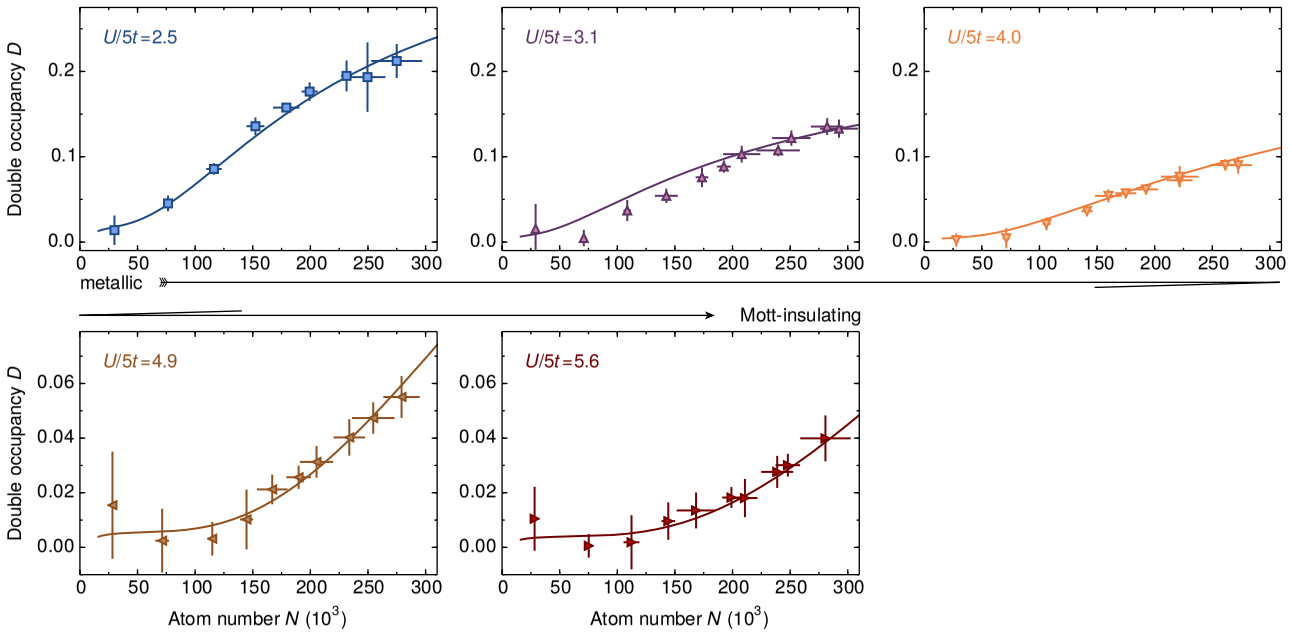

Figure 8.16: *Observing the metal to Mott insulator crossover in coupled honeycomb layers.* The measured double occupancy D versus atom number N is shown for additional interactions as compared to Fig. 8.14 on page 158. The same scattering lengths as for the 2D measurements shown in Fig. 8.8 on page 154 are used, except for the lowest scattering length. Solid lines are theoretical predictions from a HTSE up to second order, from which we obtain fitted entropies of $s = [1.8, 2.5, 2.4, 1.7, 1.8]k_B$ for $U/5t = [2.5(3), 3.1(4), 4.0(5), 4.9(6), 5.6(7)]$ respectively. Error bars in D and N show the standard deviation of 5 measurements.

8.6.2 ANISOTROPIC HONEYCOMB LATTICES

The tunability of the optical lattice allows for extending our studies of the static properties of the artificial graphene system to linearly strained honeycomb geometries and even beyond the transition where the two Dirac points merge.

In Fig. 8.17 we study the double occupancy as a function of $V_{\bar{X}}$ for weak and strong interactions at different atom numbers. The other lattice parameters are kept unchanged. In the non-interacting band structure the two Dirac points merge at $V_{\bar{X}} \approx 10\,E_R$ and the transition from the dimerized lattice structure to a triangular geometry takes place at $V_{\bar{X}} \approx 2.5\,E_R$.

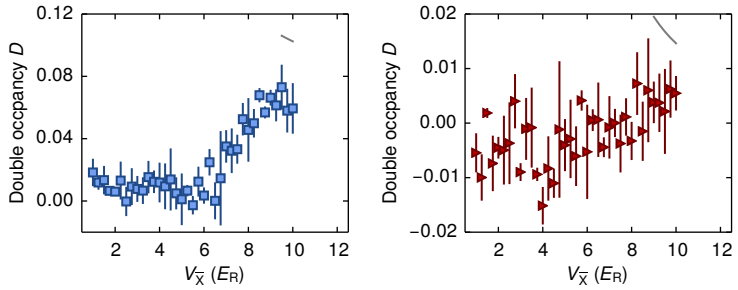

a. $a = 242.5(9)a_0$, $N = 97(3) \times 10^3$ b. $a = 630(10)a_0$, $N = 128(3) \times 10^3$

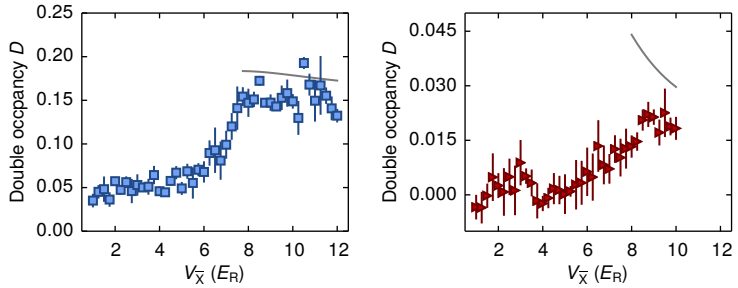

c. $a = 242.5(9)a_0$, $N = 207(8) \times 10^3$ d. $a = 630(10)a_0$, $N = 192(5) \times 10^3$

Figure 8.17: *Double occupancy for dimerized lattices.* The measured double occupancy for lattice geometries beyond the merging transition of the two Dirac points are shown for weak and strong interactions for different atom numbers. The data is compared to a HTSE for bipartite lattices, which shown up to the point where $T/t_1 = 1.5$. Lattice parameters: $V_{X,Y,\bar{Z}} = [0.65(2), 6.65(20), 7.0(2)]\,E_R$.

Transition to a dimerized system

Close to the merging point, the double occupancy still qualitatively agrees with the values predicted by the HTSE for bipartite lattices (gray lines in the figure). The disagreement however generally increases for decreasing $V_{\bar{X}}$, as is expected since a decrease of $V_{\bar{X}}$ leads to an increase in the intra-dimer tunneling t_1, which eventually becomes comparable or even larger than the temperature T. Therefore the HTSE predictions are only shown up to $T/t_1 = 1.5$. Beyond this bound, considerable disagreement was found in previous studies [Jördens *et al.*, 2010]. Interestingly, for weak interactions and large atom numbers, the agreement seems to hold up to that point, followed by a considerable decrease in double occupancy around $V_{\bar{X}} \approx 7\,E_R$. A similar behavior is observed for lower atom numbers.

For large interactions, a continuous decrease of D is observed as $V_{\bar{X}}$ is lowered, with a noticeable re-increase close to the transition line to the triangular geometry. However, for possible explanations of the observed behavior comparison to more advanced theories, such as a HTSE for dimerized lattices [Greif, 2013], as well as additional measurements would be necessary.

8.6.3 PROBING THE EXCITATION SPECTRUM

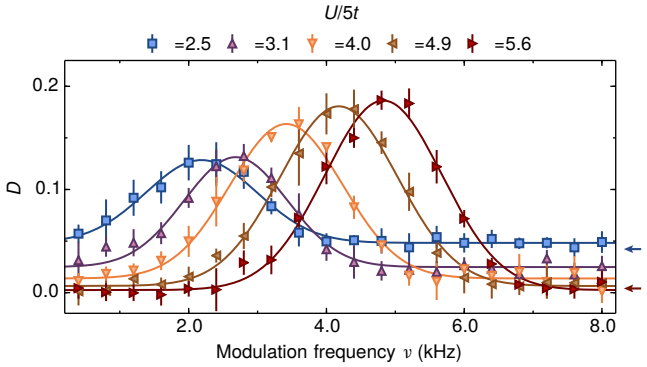

Figure 8.18: *Excitation spectra.* The spectra are obtained in coupled honeycomb layers by measuring D after sinusoidal modulation of the lattice depth V_Y at the interaction strengths used in Fig. 8.16. The solid lines are gaussian fits to the spectra. Arrows indicate the reference value without modulation. Error bars in D and N show the standard deviation of 5 measurements.

Using the same method as for the 2D data, we measure the lattice modulation spectra and find a reduction by about 25% for the value of U at the same scattering length, see Fig. 8.18. For strong interactions a gapped excitation spectrum is found, as expected for the Mott-insulating state. The experimentally determined U is shown in Fig. 8.19. In contrast to the 2D measurements, it does not deviate from the results obtained from lowest-band Wannier function overlap integrals even for the largest scattering lengths, owing to the smaller lattice depth along the coupled layer direction. The scattering lengths are the same as for the data in Fig. 8.16 on page 159.

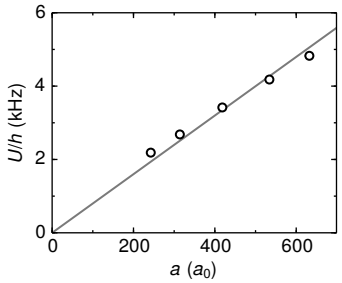

Figure 8.19: *Theory comparison.* The on-site interaction energy U measured via lattice modulation is compared to the theoretical expectation. We find good agreement over the whole range of accessible scattering lengths. Error bars in D and N show the standard deviation of 5 measurements.

8.6.4 THE LATTICE LOADING PROCESS

We have also studied the lattice loading process in coupled honeycomb layer systems, using the same method as for the independent layers. In Fig. 8.20 on the following page, we plot the measured double occupancy D versus the lattice loading ramp duration τ_L. Similar to the case of independent layers, we also find a quick rise for up to a ramp duration of 200 ms, after which heating and atom loss lead to a slow decay. From the data, we conclude that the system is thermalized for lattice loading ramps with $\tau_L \gtrsim 200$ ms, as is the case for the independent layer system.

8.7 CONCLUSION

In conclusion, we have investigated the properties of our artificial graphene system as a function of interactions. The state of the system was probed by measurements of the double occupancy and the excitation spectra obtained by lattice modulation. The measured double occupancies are in good agreement with theory predictions from a HTSE up to second order. The excitation spectra allow for an

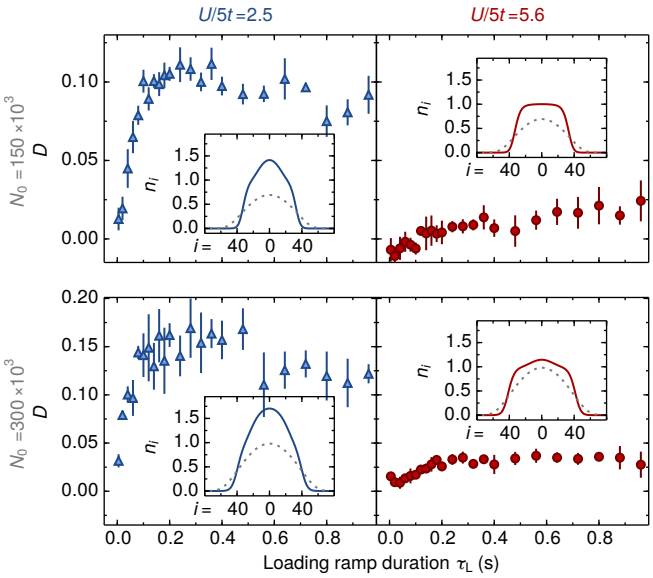

Figure 8.20: *The lattice loading process for coupled honeycomb layers.* The panels show D after loading ramps with varying duration τ_L for two interactions and two initial atom numbers. The insets show the calculated equilibrium density profiles for the atomic cloud in the FORT (dashed) and in the lattice (solid lines), illustrating the required density redistribution during the loading. Error bars in D show the standard deviation of 3 measurements.

independent calibration of the on-site interaction energy, validating a novel numerical method to obtain the Wannier functions for complex lattice geometries. We furthermore studied the equilibration during the lattice loading procedure for the 2D honeycomb layers. Extending our measurements to coupled honeycomb layers, we found a shifted Mott insulator transition owing to the altered on-site energies. At $\approx$ 200 ms, the equilibration time, however, was found to be on the same order as in the system with independent layers.

Outlook

Our results allow for studying interaction effects on Dirac points using a previously developed technique [Lim *et al.*, 2012; Uehlinger, Greif, Jotzu, Tarruell, Esslinger, *et al.*, 2013]. The realization of a 2D fermionic Mott insulator marks an important step towards investigating the origin of high-temperature superconductivity [Hofstetter *et al.*, 2002]. In combination with a recently implemented entropy redistribution scheme [Greif *et al.*, 2013], the low-temperature phase diagram of the Fermi-Hubbard model on a honeycomb lattice may be accessible. There, a spin liquid phase at half-filling has been discussed [Meng *et al.*, 2010; Sorella *et al.*, 2012; Assaad *et al.*, 2013], whereas superconducting states have been suggested for attractive and repulsive interactions beyond half-filling [Zhao *et al.*, 2006; Nandkishore, Levitov, *et al.*, 2012]. In the future, the complex interplay of interactions and topological lattices characterized by a non-zero Chern number may be investigated [Rachel *et al.*, 2010].

SHORT-RANGE MAGNETIC ORDER IN COMPLEX LATTICES

9

In this chapter, a preparation and detection method for short-range magnetic correlations in dimerized and anisotropic cubic lattices is presented. The magnitude of the magnetic correlations is studied as a function of entropy and lattice geometry. In the future, the developed preparation and detection methods could also be applied to the honeycomb lattice geometry.

CHAPTER CONTENTS

Quantum magnetism

Quantum magnetism describes quantum many-body states of spins coupled by exchange interactions and lies at the heart of many fundamental phenomena in condensed matter physics [Auerbach, 1994; Sachdev, 2008]. While spin systems often tend to show long-range order at low temperatures, the fascinating interplay of exchange interactions with geometry and quantum fluctuations can lead to quantum states characterized by short-range magnetic order. Examples include valence-bond crystals, spin liquids and possibly high-temperature superconductors [Sachdev, 2008; Anderson *et al.*, 2004; Balents, 2010; Auerbach, 1994]. Quite remarkably, the underlying many-body physics gives rise to computationally and theoretically intractable regimes even in the phase diagrams of simple models, such as the Fermi-Hubbard model. Moreover, the direct measurement of local spin correlations in solids remains a major challenge.

Previous experiments

For repulsively interacting fermions the metal to Mott insulator transition could already be explored experimentally [Jördens *et al.*, 2008; Schneider *et al.*, 2008]. Yet, progress towards entering the regime of quantum magnetism has been hindered by the ultra-low temperatures, and entropies, required to observe exchange-driven spin ordering in optical lattices. For bosonic quantum gases promising developments have been reported: by mapping the spin to other degrees of freedom the temperature limitation could be circumvented, which allowed for the exploration of 1D decoupled Ising spin chains and the simulation of classical magnetism on a triangular lattice [Simon *et al.*, 2011; Struck *et al.*, 2011]. Furthermore, exchange interactions were observed in artificially prepared arrays of isolated double-wells or plaquettes [Trotzky *et al.*, 2008; Nascimbène *et al.*, 2012].

This chapter is based on the preprints of the following publications:

D. Greif, T. Uehlinger, G. Jotzu, L. Tarruell, and T. Esslinger, *Short-range quantum magnetism of ultracold fermions in an optical lattice*, Science **340**, 1307 (2013), DOI:10.1126/science.1236362, preprint on ArXiv e-prints, arXiv:1212.2634,

and

J. Imriška, Iazzi, L. Wang, E. Gull, D. Greif, T. Uehlinger, G. Jotzu, L. Tarruell, T. Esslinger, and M. Troyer, *Thermodynamics and magnetic properties of the anisotropic 3D Hubbard model*, Phys. Rev. Lett. **112**, 115301 (2014a), DOI:10.1103/PhysRevLett.112.115301, preprint on ArXiv e-prints, arXiv:1309.7362 (erratum [Imriška *et al.*, 2014b]).

9.1 ENTROPY REDISTRIBUTION SCHEME

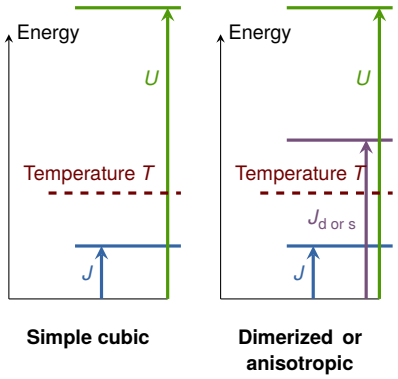

Figure 9.1: *Energy scales.* Currently, temperatures $k_B T$ below the interaction energy U can be reached. For simple cubic lattices, the exchange energy scale J however remains inaccessible. In dimerized or anisotropic lattices access to the spin sector can be gained by increasing the exchange energy on a subset of links, leading to an entropy redistribution. The increased exchange energies are called J_d for the dimerized link or J_s for the strong link direction (in the anisotropic lattice), respectively.

The temperature challenge

To overcome the prevalent temperature limitations and directly access exchange-driven physics in thermalized systems, cooling schemes based on the redistribution of entropy between different regions of the trap have been suggested [Ho and Zhou, 2009; Bernier *et al.*, 2009]. In this work, we instead propose and implement a local entropy redistribution scheme within the lattice structure to reach the regime of quantum magnetism. A sketch of the energy scales involved in our system is shown in Fig. 9.1. In simple cubic systems, the energy associated with the currently reachable temperature $k_B T$ is below the interaction energy U, allowing for the observation of a Mott-insulating state in the system. The temperature is however still above the exchange energy scale, which inhibits ordering of the spin degree of freedom. As we are considering a thermodynamically closed system, an increase of the exchange energy by interactions or lattice geometry would also increase the temperature of the system accordingly owing to entropy conservation, and therefore does not help to access low-temperature phases.

Local entropy redistribution

A possible route, however, is to prepare the atoms in either a dimerized or an anisotropic simple cubic lattice, see Fig. 9.2 on the facing page. In both geometries, a subset of links of the underlying simple cubic lattice is set to a larger exchange energy as compared to the other links. As a result, the entropy is predominantly stored in configurations involving the weak links. For fixed total entropy in the trapped system, this allows us to reach temperatures between the two exchange energy scales, see Fig. 9.1. In the dimerized lattice the resulting correlations on the strong links correspond to an excess population of the low energy singlet as compared to the triplet state – in close resemblance to an explicit valence-bond crystal in the Heisenberg model [Diep *et al.*, 2005]. In the anisotropic lattice the low temperatures lead to antiferromagnetic spin correlations along one spatial

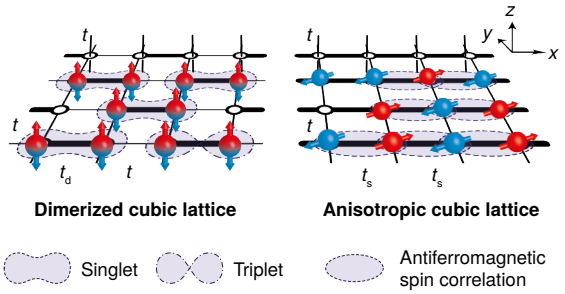

Figure 9.2: *Magnetic spin correlations.* Schematic view of the nearest-neighbor spin correlations observed in the experiment. A two-component spin mixture of fermionic atoms (red and blue) is prepared close to half-filling in a cubic lattice with two different tunnel coupling configurations. On the left, a dimerized lattice with the strong dimer links t_d and weaker links t is shown. Low temperatures lead to an excess number of singlets over triplets. The anisotropic lattice contains a strong and weak tunneling link t_s and t along different spatial axes. Antiferromagnetic spin correlations in the transverse direction are formed along the strong link direction. In both figures exemplary thermal excitations in the form of spin excitations or holes are shown.

axis, the transverse component of which is also detected via a singlet-triplet imbalance. For both systems we study the dependence of the spin correlations as a function of temperature and tunneling balance and find good agreement with theory.

9.2 PREPARATION

The experiment is performed with a harmonically confined, balanced two-component spin mixture of a quantum degenerate Fermi gas of ^{40}K. After sympathetic cooling with ^{87}Rb, 2×10^6 ^{40}K atoms are transferred into the optical dipole trap operating at a wavelength of 826 nm. A balanced incoherent mixture of atoms in the Zeeman levels $m_F = -9/2$ and $-7/2$ of the $F = 9/2$ hyperfine manifold is then prepared and evaporatively cooled to temperatures below 10% of the Fermi temperature [Jördens *et al.*, 2008]. The two Zeeman levels are denoted by $\uparrow$ and $\downarrow$. When taking data as a function of entropy, the gas is heated through inelastic losses[1] by setting the magnetic bias field to a value close to the Feshbach resonance at 202.1 G. We can measure the entropy per particle in the dipole trap s_{in} using Fermi fits to the momentum distribution of the cloud after expansion. The field is finally increased to 221.4 G resulting in a repulsive scattering length of 106(1) a_0.

The optical lattice is subsequently turned on in 200 ms using an S-shaped laser-intensity ramp. We load 50×10^3 to 100×10^3 atoms into the tunable-geometry optical lattice. The measured visibility of the interference pattern α is 0.90(5), and is included when calculating the Hubbard parameters. The phase φ is stabilized to $0.00(3)\pi$, whilst θ is set to $1.000(1)\pi$, see Eq. (3.6) on page 46. We can introduce a checkerboard dimerization in the $x - y$ plane by strengthening every second tunneling link along the x axis, see Fig. 9.2, left panel. The checkerboard pattern replicates along the z axis. Our system is well described by a 3D single-band Hubbard model with a repulsive on-site interaction energy U, unless explicitly stated. The tunneling along the weak links in both the dimerized as well as the anisotropic cubic lattice geometry is set to $t/h = 67(3)$ Hz for all measurements. For theory

Description by a Hubbard model

1 The gas is heated by the energy released as pairs of atoms form deeply bound molecules in the vicinity of the Feshbach resonance.

comparison, an accurate determination of the harmonic confinement induced by the lattice and dipole trap beams is essential. For

$$V_{\tilde{X},X,Y,\tilde{Z}} = [3.7(1), 0.13(1), 9.8(3), 11.0(3)]\, E_R,$$

as in Fig. 9.6a on page 169, the lattice contributes harmonic trapping frequencies of

$$\omega_{x,y,z}^{\text{Lattice}}/2\pi = [62.7(9), 57(1), 54.3(3)]\,\text{Hz}.$$

Additionally, the optical dipole trap contributes with the trapping frequencies

$$\omega_{x,y,z}^{\text{Dipole}}/2\pi = [30.7(2), 105.9(3), 34.6(2)]\,\text{Hz},$$

in all data sets shown, except for Fig. 9.5 and Fig. 9.12a, where

$$\omega_{x,y,z}^{\text{Dipole}}/2\pi = [28.1(2), 90.1(3), 31.6(2)]\,\text{Hz}.$$

9.3 DETECTION OF SPIN CORRELATIONS

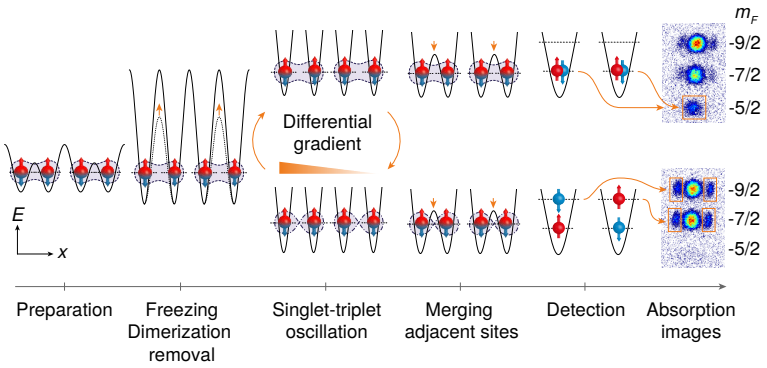

Figure 9.3: *Summary of the technique used for measuring the atomic singlet and triplet fractions p_s and p_{t_0}.* The different detection steps for the exemplary case of two singlet states in a dimerized lattice are sketched. Depending on the oscillation time, the absorption images on the right show either a large double occupancy in the lowest band corresponding to singlets (top row), or an increased higher band fraction indicating triplet states (bottom row). For the symbol legend, see Fig. 9.2.

As shown in Fig. 9.3, the fraction of atoms forming singlets and triplets on neighboring lattice sites (p_s and p_{t_0}) is detected by transforming the lattice to a checkerboard geometry (see Fig. 9.4 on the facing page), similar to a previously developed technique [Trotzky *et al.*, 2010].

In the first detection step, the atomic motion in the initial lattice is frozen by rapid conversion to a simple cubic structure with negligible tunneling.

FREEZING LATTICE RAMPS

For measurements in the dimerized lattice, the lattice is ramped up in two steps. All beam intensities are linearly increased over the course of 0.5 ms up to the point where $V_Y = 30(1)\, E_R$, $V_{\tilde{Z}} = 40(1)\, E_R$ and all other intensities in the $x-y$ plane are ramped such that the potential is not deformed. In a second linear ramp lasting 10 ms, the lattice is changed to a simple cubic geometry where $V_{\tilde{X},X,Y,\tilde{Z}} = [25(1), 0, 30(1), 40(1)]\, E_R$.

This ramp can be considered sudden for the inter-dimer links but adiabatic for the intra-dimer links. Our observable hence locally projects onto the two-site

eigenstates of individual dimers, which includes an admixture of double occupancies. We use an exact calculation of a two-site Hubbard model to estimate the adiabaticity of the ramp. The unnormalized singlet ground state of this system is given by

Singlet ground state

$$\frac{4t_\mathrm{d}}{-U+\sqrt{16t_\mathrm{d}^2+U^2}}\Big(|\uparrow,\downarrow\rangle-|\downarrow,\uparrow\rangle\Big)+\Big(|\uparrow\downarrow,0\rangle+|0,\uparrow\downarrow\rangle\Big). \tag{9.1}$$

There is hence a significant contribution of double occupancy in the regime where $U \sim t_\mathrm{d}$, as applies for the most strongly dimerized lattices investigated in this work, whilst the contribution vanishes for the deep simple cubic lattice used for detection, where $U/t \approx 600$. For the given ramp-times and including site-offsets due to the harmonic trapping potential, the probability of populating excited states on a dimer during such a ramp remains below 0.1% for all values of U and t_d explored in the dimerized systems.

Double occupancy admixture

In the anisotropic lattice, we directly ramp to $V_{\tilde{\mathrm{X}},\mathrm{Y},\tilde{\mathrm{Z}}} = [25(1), 30(1), 40(1)]\,E_\mathrm{R}$ in 0.5 ms ($V_\mathrm{X} = 0\,E_\mathrm{R}$ throughout). In contrast to the dimer lattice ramp, this process can be considered sudden for all links, as the duration of the ramp is always well below the tunneling time in the initial lattice. Our detection method then corresponds to locally projecting the wave function of the system onto $\big(|\uparrow,\downarrow\rangle - |\downarrow,\uparrow\rangle\big)/\sqrt{2}$ on pairs of sites when measuring p_s, hence excluding any contributions from double occupancies. The probability of this projection, as calculated from the two-site Hubbard model, lies above 80% for all shown data and is higher for deeper lattices. For both lattice geometries, the triplet state remains unaffected by changes in U and t.

DOUBLE OCCUPANCY REMOVAL

For both systems, once the ramp to the deep simple cubic lattice has been completed, double occupancies are removed via spin-changing collisions, which occur after transferring the atoms from the $m_F = -7/2$ to the $m_F = -3/2$ state [Krauser *et al.*, 2012]. We verify that this procedure removes all double occupancies but leaves singly occupied sites unaffected by measuring the number of double occupancies and the total number of atoms before and after applying the removal sequence.

SINGLET-TRIPLET OSCILLATIONS

We then apply a magnetic field gradient, which causes spin-dependent energy offsets of $\Delta_{-9/2,-7/2}/h = [1291(1), 1156(1)]$ Hz for atoms of opposite spin on adjacent sites. This gives rise to coherent oscillations between the singlet $|\mathrm{s}\rangle = \big(|\uparrow,\downarrow\rangle - |\downarrow,\uparrow\rangle\big)/\sqrt{2}$ and the triplet $|\mathrm{t}_0\rangle = \big(|\uparrow,\downarrow\rangle + |\downarrow,\uparrow\rangle\big)/\sqrt{2}$ state at a frequency $\nu = \Delta/h$ [Trotzky *et al.*, 2010]. If the initial amount of singlets and triplets is equal, no overall oscillation will be visible, as $|\mathrm{s}\rangle$ and $|\mathrm{t}_0\rangle$ oscillate in antiphase.

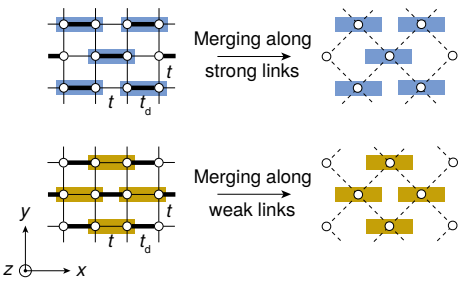

Figure 9.4: *Merging configurations.* The two possible merging configurations in a dimerized lattice. Singlets and triplets are detected on a set of adjacent sites arranged on a checkerboard pattern in the plane.

MERGING ADJACENT SITES

After a certain oscillation time, we remove the gradient and merge two adjacent sites adiabatically into one by linearly reducing $V_{\bar{X}}$ to zero whilst increasing V_X to 25(1) E_R. Owing to the symmetry of the two-particle wave function, the singlet state on neighboring sites evolves to a doubly occupied site with both atoms in the lowest band, while the triplet state transforms into a state with one atom in the lowest and one atom in the first excited band.

Double occupancy detection

The fraction of atoms forming double occupancies in the lowest band of the merged lattice, η_D, is detected by an rf transfer to the previously unpopulated $m_F = -5/2$ spin state [Jördens *et al.*, 2008]. Here, we take into account an independently calibrated detection efficiency of 89(2)%, see Section 8.1.2 on page 151. We verify that merged sites containing two atoms of opposite spin but in different bands are not detected as double occupancies by artificially creating a state containing large amounts of triplets but no singlets and measuring η_D.

Higher-band fraction

The fraction of atoms in the higher band η_{HB} is obtained from a band mapping technique [Esslinger, 2010]. For the final readout we take absorption images after Stern-Gerlach separation of the spin states during ballistic expansion. For an imbalance between the initial singlet and triplet populations, η_D and η_{HB} will show oscillations with opposite amplitudes. As the double occupancy in the lowest band contains only contributions from two particles with opposite spins, we can infer the fraction of atoms forming singlets and triplets from the maxima and minima of a sinusoidal fit to η_D. The higher band fraction η_{HB} has an additional offset caused by dimers containing two atoms with the same spin or one atom with an antisymmetric spatial wave function.

More details on the theoretical framework and the detection scheme can be found in the thesis of Daniel Greif [2013].

9.4 DIMERIZED LATTICE

9.4.1 OBSERVATION OF MAGNETIC CORRELATIONS

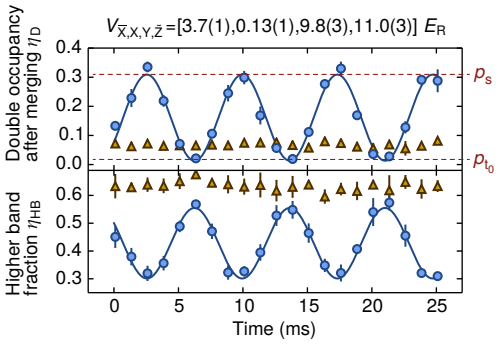

Figure 9.5: *Singlet-triplet oscillations.* Exemplary singlet-triplet oscillation in a strongly dimerized lattice with $U/t = 11.0(8)$ and $t_d/t = 22(2)$. We observe an oscillation in the double occupancy after merging, η_D, and in the higher band fraction, η_{HB}, when merging along the strong links (blue circles), whereas no oscillations are visible for the weak links (ochre triangles). The phase of the oscillation is shifted owing to the double occupancy removal procedure. The red dashed lines denote the extracted singlet and triplet fraction p_s and p_{t_0}. Error bars show the standard deviation of at least five measurements.

When loading atoms into a strongly dimerized lattice and merging along the strong links, we observe oscillations in η_D and η_{HB}, see Fig. 9.5. This reveals an excess number of singlets, corresponding to magnetic order on neighboring sites.

Normalized singlet-triplet imbalance

We quantify this order by the normalized imbalance

$$\mathcal{I} = \frac{p_s - p_{t_0}}{p_s + p_{t_0}}. \tag{9.2}$$

Intra-dimer exchange energy

The order in the strongly dimerized lattice originates from temperatures below the intra-dimer exchange energy

$$J_d = -\frac{U}{2} + \sqrt{16t_d^2 + U^2}/2\,, \tag{9.3}$$

which denotes the singlet-triplet splitting on a single dimer. While such temperatures require very low entropies for isotropic lattices [Fuchs *et al.*, 2011], in our system the access to the regime of magnetic ordering is facilitated by the presence of the weaker inter-dimer exchange energy $J \ll J_d$. This leads to an entropy redistribution from states on the strong to the weak links and gives access to the temperature regime $J < k_B T < J_d$ for experimentally attainable entropies. As expected for strong dimerization, we find no visible oscillations when merging along the weak links, which indicates the absence of magnetic correlations on these links, see Fig. 9.5 on page 168. The observed constant values of $\eta_D = 0.07(1)$ and $\eta_{HB} = 0.63(3)$ are consistent with a state where nearly all singlets are located on neighboring dimer links, with vanishing correlations between them.

Fitting the singlet-triplet oscillations

We apply a sinusoidal fit to the double occupancy, where the frequency and phase are fixed, and take into account the damping of the oscillations. The damping was determined using a measurement of the singlet-triplet oscillations during up to 400 ms and is included by multiplying the amplitude by 1.16 [Greif, 2013]. A phase shift arises from a weak residual magnetic field gradient present during the double occupancy removal procedure, whereas the contribution from switching the singlet-triplet oscillation gradient on and off is negligible. We confirm that the maximum of the oscillation corresponds to its starting point (and hence to the number of singlets) by merging the lattice immediately after it has been ramped to a deep simple cubic structure.

9.4.2 DETAILED EXPERIMENTAL INVESTIGATION

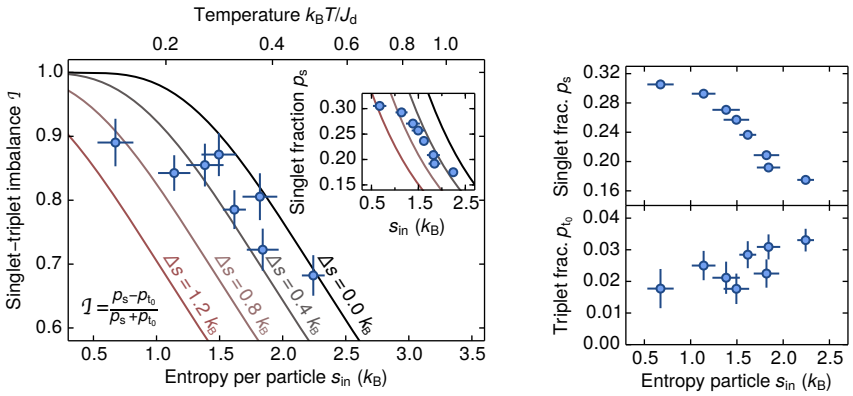

a. Singlet-triplet impalance

b. Singlet and triplet fractions

Figure 9.6: *Entropy scan.* a. Singlet-triplet imbalance on the strong dimer links vs. initial entropy before loading into the lattice s_{in} and vs. relative temperature $k_B T/J_d$ in a dimerized lattice with $U/t = 11.0(8)$ and $t_d/t = 22(2)$. The imbalance and the absolute singlet fraction (inset) decrease with increasing entropy. Solid lines are the prediction of a HTSE taking into account different amounts of added entropy Δs during the lattice loading. b. The separate singlet and triplet fractions, which are used to compute the imbalance $\mathcal{I}$, are shown. Vertical error bars denote the fit error from singlet-triplet oscillations consisting of 63 measurements. The errors in s_{in} are the standard deviation of five measurements.

Effect of temperature

To analyze the effect of temperature on the magnetic correlations, we measure the dependence of the singlet-triplet imbalance on entropy, see Fig. 9.6a. The imbalance $\mathcal{I}$ and the absolute singlet fraction p_s reduce for larger entropies, as triplet states become thermally populated. The singlet fraction is additionally diminished by a shrinking half-filled region in the trapped system [Greif *et al.*, 2011]. Separate curves for p_s and p_{t_0} are shown in Fig. 9.6b. We find good agreement with a second order HTSE of coupled dimers when including an entropy increase

of $\Delta s = 0.4\,k_B$ with respect to the initial entropy in the harmonic trap, s_{in}. This heating is associated to the lattice loading [Jördens *et al.*, 2010] and is larger for the lowest entropies, consistent with previous results [Greif *et al.*, 2011]. From the measured imbalances we infer temperatures below $0.4J_d$.

We additionally measured the fraction of atoms on doubly occupied sites D_{dimer} in the lattice after freezing out the atomic motion but before applying the cleaning procedure and inducing singlet-triplet oscillations. Note that for the dimer lattice, this fraction does not contain any contributions from the admixture of double occupancies present in the initial singlet state. For the entropy scan we find a nearly constant value of $D_{dimer} = 0.026(5)$.

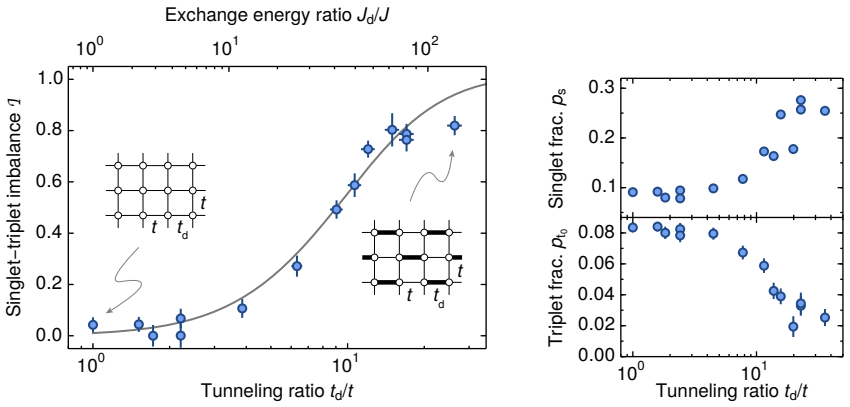

a. Singlet-triplet imbalance b. Singlet and triplet fractions

Figure 9.7: *Changing the dimerization.* a. Imbalance versus dimerization t_d/t and J_d/J, showing an increase for strongly dimerized simple cubic lattices. The solid line is the theory prediction for an entropy per particle of $1.7\,k_B$ in the lattice, which includes the heating during loading. b. The separate singlet and triplet fractions are shown. Vertical error bars denote the fit error from singlet-triplet oscillations consisting of 63 measurements. The errors in t_d/t stem from lattice calibration uncertainties.

Dependence on the dimerization

For reduced dimerizations the coupling between dimers leads to increased inter-dimer correlations. The excitation energy of triplets is then lowered as they delocalize over the lattice, thus changing the nature of the magnetic ordering. In Fig. 9.7a we use the tunable lattice to investigate the dependence of the imbalance $\mathcal{I}$ on the tunneling ratio t_d/t. For this measurement, individual curves for p_s and p_{t_0} are shown in Fig. 9.7b. Additionally, we show the dependence of the interaction energy on the dimerization in Fig. 9.8. For this set of measurements, the double occupancy ranges between 0.066(4) and 0.29(2).

As the dimerization is progressively removed the imbalance $\mathcal{I}$ decreases in good agreement with theory and eventually falls below our experimental resolution. This decrease can be attributed to the inter-dimer exchange energy J_d becoming smaller than the temperature T. For vanishing temperatures the system is expected to undergo a quantum phase transition from a gapped spin liquid state to a long-range ordered antiferromagnet as t_d/t is reduced below a critical value, where the spin gap becomes zero [Sachdev, 2008; Rüegg *et al.*, 2004].

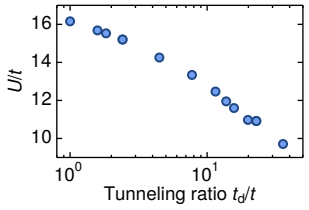

Figure 9.8: *Interactions.* The interaction energy ratio U/t as a function of t_d/t, as calculated from the experimental parameters, is shown for the data points of Fig. 9.7.

9.4.3 HIGH-TEMPERATURE SERIES EXPANSION

OVERVIEW

For sufficiently deep lattices the system is well described by a single band Fermi-Hubbard model. The interaction energy U and nearest-neighbor tunneling $t_{i,j}$ are evaluated from Wannier function integrals [Lewenstein *et al.*, 2007]. The theoretical expectations for the singlet-triplet imbalance in the dimerized lattice are calculated from a perturbative coupling of isolated dimer links with tunneling t. The resulting partition function expansion is then calculated up to second order in $t/k_\mathrm{B}T$. While the dimer link contains 16 states in total and the tunneling operator is non-diagonal between neighboring dimers, the evaluation of the relevant matrix elements is directly analogous to the case of single sites [Henderson *et al.*, 1992]. See [Greif, 2013] for a discussion of the high-temperature series expansion (HTSE) technique for the dimerized lattice.

The harmonic trap is included in a local density approximation, which leads to a quadratically varying chemical potential. All thermodynamic quantities are obtained after integration over the entire trap using independent calibrations of the atom number, trap frequencies and lattice depths [Jördens *et al.*, 2010]. In the limit of very strong dimerization, theory predicts

$$p_{\mathrm{t}_0}/p_\mathrm{s} \propto \exp\left(-J_\mathrm{d}/k_\mathrm{B}T\right), \tag{9.4}$$

which can be used for lattice thermometry.

DETAILS

We start with the definition of the homogeneous single-band Hubbard Hamiltonian in a dimerized cubic lattice with strong and weak links between nearest neighbors $\langle i,j\rangle_{\blacksquare}$ and $\langle i,j\rangle_{\_}$, respectively, see Fig. 9.2 on page 165,

$$\begin{aligned}
\hat{H}_D &= \hat{H}_0 + \hat{H}_1 \\
\hat{H}_0 &= -t_\mathrm{d}\sum_{\sigma,\langle i,j\rangle_{\blacksquare}}(\hat{c}^\dagger_{i,\sigma}\hat{c}_{j,\sigma} + \mathrm{h.c.}) \\
&\quad + U\sum_i \hat{n}_{i,\uparrow}\hat{n}_{i,\downarrow} - \mu\sum_i(\hat{n}_{i,\uparrow}+\hat{n}_{i,\downarrow}) \\
\hat{H}_1 &= -t\sum_{\sigma,\langle i,j\rangle_{_}}(\hat{c}^\dagger_{i,\sigma}\hat{c}_{j,\sigma} + \mathrm{h.c.})\,.
\end{aligned} \tag{9.5}$$

We have split the Hamiltonian into the dimer part $\hat{H}_0$ and the coupling between dimers $\hat{H}_1$. The on-site interaction energy is given by U, the tunneling matrix elements between nearest neighbors by t and t_d and the chemical potential is parametrized with μ. The fermionic creation operator for an atom on the lattice site i is given by $\hat{c}^\dagger_{i,\sigma}$, where $\sigma \in \{\uparrow,\downarrow\}$ denotes the magnetic sublevel and h.c. is the Hermitian conjugate. The particle number operator is $\hat{n}_i = \hat{n}_{i,\uparrow}+\hat{n}_{i,\downarrow}$, $\hat{n}_{i,\sigma} = \hat{c}^\dagger_{i,\sigma}\hat{c}_{i,\sigma}$. Denoting the inverse temperature with $\beta = 1/k_\mathrm{B}T$, the thermal average of an observable $\mathscr{O}$ then reads in the grand canonical potential

Thermal average of an observable

$$\langle\mathscr{O}\rangle = \frac{\mathrm{Tr}\left\{\mathscr{O}\,e^{-\beta\hat{H}_D}\right\}}{\mathrm{Tr}\left\{e^{-\beta\hat{H}_D}\right\}}. \tag{9.6}$$

We now treat the coupling Hamiltonian $\hat{H}_1 = t\hat{T}$ as a perturbation, which leads to an expansion of the above expression in powers of the dimensionless parameter βt [Henderson *et al.*, 1992]. The expansion is expected to be close to the exact result

in the regime $t \ll k_B T \ll t_d, U$. For the partition function up to second order (denominator in Eq. (9.6) on page 171) we find

$$\mathscr{Z} = \mathscr{Z}_0 + (\beta t)^2 \frac{\mathscr{Z}_0}{\beta^2} \int_0^\beta \int_0^{\tau_1} \mathrm{d}\tau_2 \mathrm{d}\tau_1 \langle \hat{T}'(\tau_1)\hat{T}'(\tau_2)\rangle_0 . \tag{9.7}$$

The expression for the numerator is analogous. The partition function of the unperturbed Hamiltonian is denoted by $\mathscr{Z}_0$, whereas $\langle ... \rangle_0$ denotes the thermal average of the unperturbed Hamiltonian

$$\begin{aligned} \langle \hat{T}'(\tau_1)\hat{T}'(\tau_2)\rangle_0 &= \mathrm{Tr}\left\{\exp(-\beta\hat{H}_0)\hat{T}'(\tau_1)\hat{T}'(\tau_2)\right\}\Big/\mathscr{Z}_0 \\ \hat{T}'(\tau) &= e^{\tau\hat{H}_0}\hat{T}e^{-\tau\hat{H}_0} . \end{aligned} \tag{9.8}$$

OBSERVABLES

As the expansion is up to second order in the tunnel coupling, it is sufficient to evaluate all expressions in a two-dimer basis. Denoting the single dimer Hamiltonian in the grand canonical potential with $\hat{H}_0^\mathrm{d}$, the unperturbed partition function then reads

$$\mathscr{Z}_0^\mathrm{d} = \left(\mathrm{Tr}\left\{e^{-\beta\hat{H}_0^\mathrm{d}}\right\}\right)^2 . \tag{9.9}$$

The evaluation of the second order terms is done in a double dimer basis $|\Psi_i^1, \Psi_j^2\rangle$, where $|\Psi_i^1\rangle$ and $|\Psi_j^2\rangle$ each denote one of the 16 possible eigenvectors of the first and second dimer link. This essentially leaves the evaluation of matrix elements of the following kind:

$$\begin{aligned} &\langle \Psi_j^2, \Psi_i^1|\hat{T}'(\tau_1)\hat{T}'(\tau_2)|\Psi_i^1, \Psi_j^2\rangle \qquad \text{and} \\ &\langle \Psi_j^2, \Psi_i^1|\mathscr{O}\,\hat{T}'(\tau_1)\hat{T}'(\tau_2)|\Psi_i^1, \Psi_j^2\rangle , \end{aligned} \tag{9.10}$$

which can be computed either analytically or numerically.

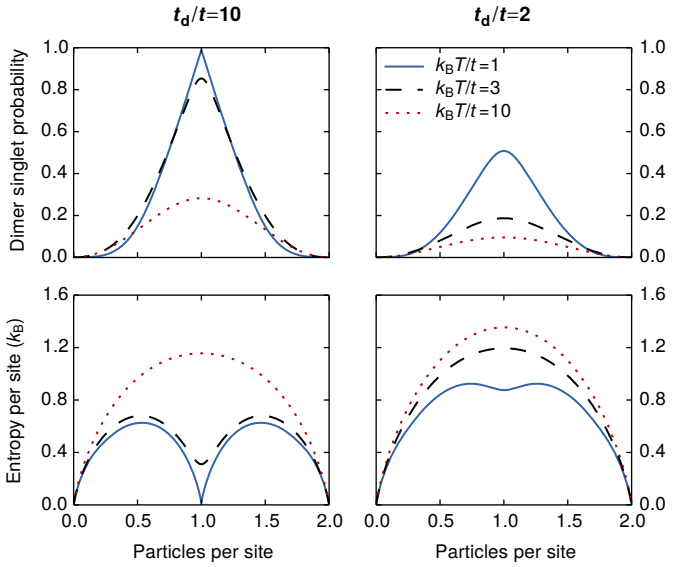

Figure 9.9: *Lattice filling.* HTSE predictions up to second order for the homogeneous dimerized cubic lattice. The dependence on filling of the dimer singlet probability and of the entropy per site is shown. We set $U/t = 5$ and $t_d/t = 10$ or 2 and use different temperatures $k_B T/t$. The entropy at half filling for large dimerization is strongly reduced.

For the singlet and triplet fraction the observable $\mathscr{O}$ takes the form of a projector for the 16 possible states on a dimer. The entropy and particle number per dimer are evaluated from the grand canonical potential $\Omega^{\mathrm{d}} = -k_{\mathrm{B}}T \log \mathscr{Z}^{\mathrm{d}}$ of a single dimer. Figure 9.9 on page 172 shows the dimer singlet probability and the entropy per site versus filling calculated in second order for different temperatures and dimerizations. A comparison between the predictions of lowest order (atomic limit) and second order is shown in Fig. 9.10.

Thermodynamic quantities versus filling

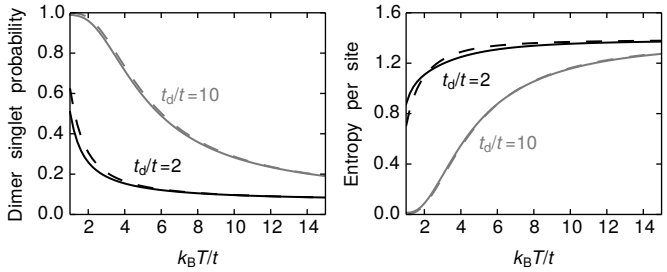

Figure 9.10: *Higher order contributions.* Comparison of the HTSE predictions in lowest and second order (dashed and solid line) for the dimer singlet probability and for the entropy per site in a homogeneous dimerized cubic lattice. The filling is set to one particle per site and the interaction to $U/t = 5$. The second order contributions are expected to be larger for lower temperatures and lead to a reduction of the singlet probability.

SINGLET AND TRIPLET FRACTIONS

The fraction of atoms forming singlets and triplets p_{s} and p_{t_0} are obtained from an integration over the left sites of each merged pair, which we define to be part of the set $\mathscr{A}$ (see Fig. 9.4 on page 167),

$$\begin{aligned} p_{\mathrm{s}} &= 2 \sum_{i \in \mathscr{A}} \langle \hat{P}_i^{\mathrm{s}} \rangle / N \qquad \hat{P}_i^{\mathrm{s}} = |\Psi_i^{\mathrm{s}}\rangle \langle \Psi_i^{\mathrm{s}}| \\ p_{\mathrm{t}_0} &= 2 \sum_{i \in \mathscr{A}} \langle \hat{P}_i^{\mathrm{t}_0} \rangle / N \qquad \hat{P}_i^{\mathrm{t}_0} = |\Psi_i^{\mathrm{t}_0}\rangle \langle \Psi_i^{\mathrm{t}_0}| . \end{aligned} \tag{9.11}$$

Here $\hat{P}_i^{\mathrm{s}}$ and $\hat{P}_i^{\mathrm{t}_0}$ are the projection operators on the singlet and triplet states $|\Psi_i^{\mathrm{s}}\rangle$ and $|\Psi_i^{\mathrm{t}_0}\rangle$ on neighboring sites i and $i+1$, $\langle ... \rangle$ denotes the thermal average and N the total atom number. For the measurements in the anisotropic simple cubic lattice, the projection operators are related to the spin operators $\mathbf{S}_i = {}^1\!/_2 \sum_{s,s'} \hat{c}_{i,s}^\dagger \boldsymbol{\sigma} \hat{c}_{i,s'}$, where $\boldsymbol{\sigma} = (\sigma_x, \sigma_y, \sigma_z)$ are the Pauli matrices,

$$\begin{aligned} \hat{P}_i^{\mathrm{s}} &= \frac{\hat{n}_i \hat{n}_{i+1}}{4} - \mathbf{S}_i \mathbf{S}_{i+1} \\ \hat{P}_i^{\mathrm{t}_0} &= \mathbf{S}_i \mathbf{S}_{i+1} - 2 S_i^z S_{i+1}^z + \frac{\hat{n}_i \hat{n}_{i+1}}{4}. \end{aligned} \tag{9.12}$$

From this the equality of Eq. (9.15) on page 175 is immediately obtained. In the dimerized lattice the projection operator on the triplet reads the same, whereas for the singlet the two-site system needs to be diagonalized.

HARMONIC TRAP

The effect of the harmonic trap is included in a local density approximation with a quadratically varying chemical potential

$$\mu(r) = \mu_0 - \frac{1}{2} m \bar{\omega}^2 \left(\frac{\lambda}{2}\right)^2 r^2, \tag{9.13}$$

Trap averaged observables

where $\bar{\omega}$ is the geometric mean of the trapping frequencies, μ_0 the chemical potential in the center of the trap, λ the wavelength of the optical lattice beam and r the normalized distance of a given site to the trap center. Any trap averaged observable $\mathcal{O}^{\mathrm{trap}}$ is then obtained from an integration of the contributions per site $\mathcal{O}^{\mathrm{hom}}(\mu)$,

$$\mathcal{O}^{\mathrm{trap}} = \int_0^\infty 4\pi r^2 \mathcal{O}^{\mathrm{hom}}(\mu(r))\mathrm{d}r\,. \tag{9.14}$$

Owing to the harmonic trap, the energy offset between neighboring sites on the dimer links changes over the cloud size. The relative correction of this effect to all shown quantities was computed to be less than a few percent.

Figure 9.11 shows the in-trap distribution of the entropy per site and density for a dimerized and simple cubic lattice. Owing to the entropy redistribution, the local entropy per site s_i in the half filled region ($n = 1$) reduces to values below $0.6k_\mathrm{B}$ for the dimerized lattice. In contrast, the entropy per site does not fall below $\log 2$ in the half-filled region in the simple cubic case, which is caused by the spin degree of freedom of the two-component mixture. For a trap-averaged entropy of $s = 1.0k_\mathrm{B}$, the local entropy at half-filling can even fall below $0.1k_\mathrm{B}$ in the dimerized lattice.

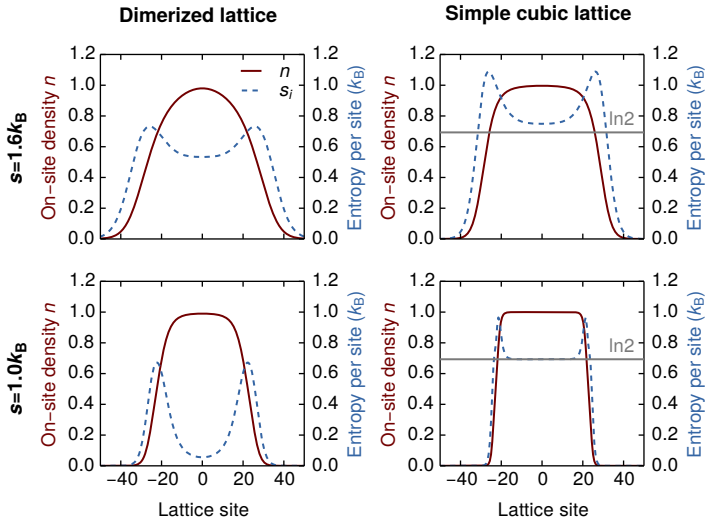

Figure 9.11: *Density and entropy distribution.* Comparison of the density and entropy distribution in the harmonic trap for a simple cubic and dimerized lattice. Top row. Comparison for parameters realized in the experiment, where both systems have the same trap-averaged entropy per particle of $1.6k_\mathrm{B}$. This corresponds to the estimated lowest entropy in the lattice from the highest measured value of the singlet-triplet imbalance $\mathcal{I}$, see Fig. 9.6a on page 169. In both plots the total particle number is set to $N = 100 \times 10^3$ (as in the experiment) with a geometric mean trap frequency of $\bar{\omega} = 2\pi \times 79\,\mathrm{Hz}$, which gives one particle per site in the trap center. The density and entropy distribution are calculated from the second order HTSE. The lattice parameters for the dimerized lattice correspond to the datapoint with the largest dimerization of Fig. 9.7a on page 170: $U/6t = 1.6$ and $t_\mathrm{d}/t = 34$, where $t/h = 67$ Hz. For comparison, the interaction is set to $U/6t = 12.7$ in the simple cubic lattice. Bottom row. Comparison of the local entropy reduction for a lower trap-averaged entropy of $1.0k_\mathrm{B}$ and 50×10^3 particles. The entropy at half-filling in the dimerized lattice falls below $0.1k_\mathrm{B}$.

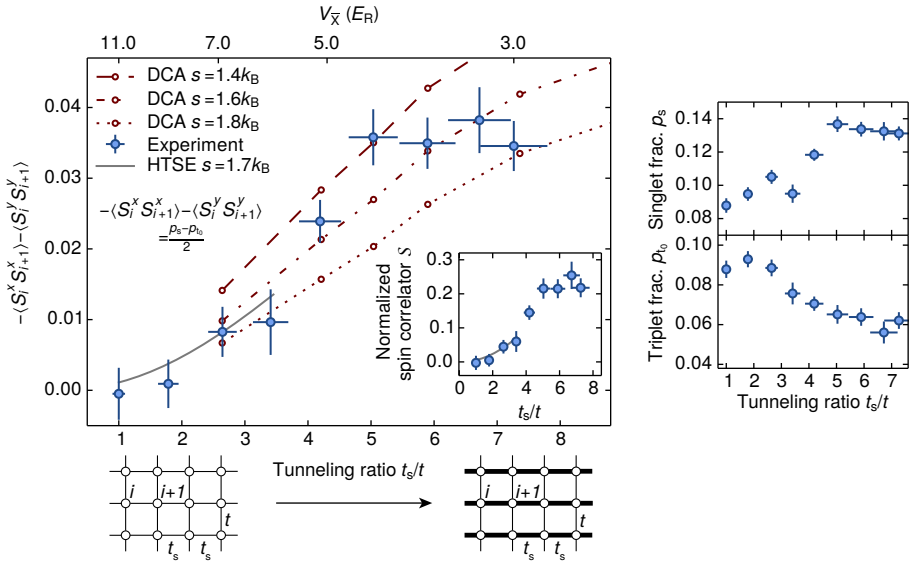

a. Transverse spin correlator

b. Singlet and triplet fraction

Figure 9.12: *Nearest-neighbor antiferromagnetic order.* a. Transverse spin correlator versus tunneling ratio t_s/t and lattice depth $V_{\bar{X}}$ in a 3D anisotropic simple cubic lattice with $V_{Y,\bar{Z}} = 11.0(3)\,E_R$. Positive values correspond to antiferromagnetic ordering. The inset shows the normalized spin correlator $\mathcal{S}$, denoting the fraction of antiferromagnetic ordering at the relevant density. Here U/t decreases from 16(1) to 10.5(8). Solid lines are the prediction of a HTSE for an entropy per particle of 1.7 k_B, as used in Fig. 9.7a on page 170, and are shown up to $t_s/k_BT = 1/2$. The dashed lines are results from the dynamical cluster approximation (DCA) calculation for different entropies. b. The singlet and triplet fractions are shown separately. Error bars as in Fig. 9.7 on page 170.

9.5 ANISOTROPIC LATTICE

9.5.1 *EXPERIMENTAL RESULTS*

The key to the observation of quantum magnetism in our system is the presence of two different exchange energy scales. Without dimerization, this situation also occurs for anisotropic simple cubic lattices with tunneling t along two axes and a stronger tunneling t_s along the third direction. In this case the symmetry between neighboring links is restored and the detected singlet and triplet fractions are the same for both merging configurations. We observe a clear population difference $(p_s - p_{t_0})/2$ after loading a gas with entropies s_{in} below 1.0 k_B into an anisotropic lattice, which increases to 4% for larger tunneling ratios t_s/t, see Fig. 9.12a. Independent curves for p_s and p_{t_0} are shown in Fig. 9.12b. Additionally, we show the dependence of the interaction energy on the anisotropy in Fig. 9.13 on the next page. Measuring the double occupancy immediately after freezing out the atomic motion $D_{anisotropic}$ now corresponds to a direct projection onto doubly occupied sites. We find double occupancies between 0.14(2) and 0.19(2).

Dependence on anisotropy

The population difference $(p_s - p_{t_0})/2$ is equal to the transverse spin correlator between neighboring sites i and $i+1$ along the strong tunneling direction,

Measuring the transverse spin correlator

$$-\langle S_i^x S_{i+1}^x\rangle - \langle S_i^y S_{i+1}^y\rangle = (p_s - p_{t_0})/2\,. \tag{9.15}$$

This quantity hence directly characterizes the fraction of atoms with antiferromagnetic ordering on neighboring sites in the entire atomic cloud. Our observations also extend to weak lattices, where correction terms to the single-band Hubbard model become relevant [Werner *et al.*, 2005]. In this regime a variety of magnetic phases have been predicted [Mathy *et al.*, 2009; Ma *et al.*, 2012].

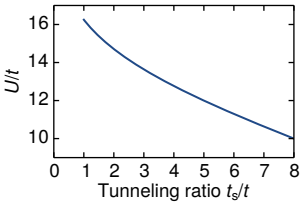

Figure 9.13: *Interactions.* The interaction energy ratio U/t as a function of t_s/t, as calculated from the experimental parameters, is shown for the anisotropy scan of Fig. 9.12 on page 175.

In the regime of small anisotropies, the results can again be compared to a second order HTSE, with which we find good agreement. For larger anisotropies the expansion breaks down, as the strong tunneling and the temperature become comparable. In this regime a dynamical cluster approximation (DCA) [Maier *et al.*, 2005] of the 3D Hubbard model was used to calculate the transverse spin correlator [Imriška *et al.*, 2014a,b], resulting in a good agreement with the experiment for entropies in the range of $s = 1.4k_B$ to $1.8k_B$, see Section 9.5.3 on page 178. In the large anisotropy regime we intuitively expect the temperature to lie between the large and small exchange scales $J < k_B T < J_s$, which is confirmed by the DCA results, see Fig. 9.14.

In this regime, the system behaves as an array of 1D spin-ordered chains without correlations between them [Giamarchi, 2004], where the majority of the entropy is stored in configurations involving the weak links. Low-dimensional systems have been predicted to show enhanced nearest-neighbor correlations [Gorelik *et al.*, 2012].

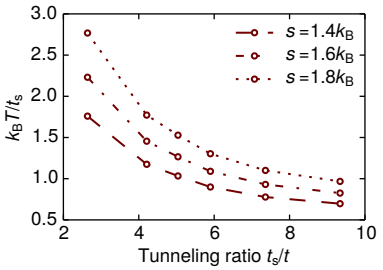

Figure 9.14: *Temperature.* Ratio of temperature T to the strong tunneling t_s versus anisotropy as extracted from the DCA/LDA calculations. Atom numbers and interaction strengths as in Fig. 9.12 on page 175.

Dependence on temperature

For temperatures much larger than the strong exchange energy the magnetic correlations should disappear. In Fig. 9.15a on the facing page and – for a different anisotropy – in Fig. 9.16 on the next page we study the dependence on the initial entropy s_{in}. Separate curves for p_s and p_{t_0} are shown in Fig. 9.15b on the facing page. For this data $D_{anisotropic}$ lies between 0.11(6) and 0.21(1). We find the correlations to vanish for entropies above 2.5 k_B per particle.

The calculated transverse spin correlator obtained using the DCA calculation agrees well with the higher-entropy points, when using the entropy measured before loading into the lattice s_{in} as the lattice entropy. For the lower-entropy data points a heating during the lattice loading of approximately $0.6k_B$ has to be taken into account. This could be because lower-entropy states are subject to larger heating when loading into the lattice, as found in previous work [Greif *et al.*, 2011]. From the calculated temperatures in the lattice we conclude that no correlations are detectable anymore for temperatures $k_B T \gtrsim 2t_s$.

Owing to the presence of the harmonic trap, most spin correlated atoms are located in the center, where the filling is close to one particle per site. The density-normalized fraction of antiferromagnetic ordering is obtained when dividing by the fraction of atoms with two particles of arbitrary spin on adjacent sites. Under the assumption that all spin correlators $\langle S_i^{x,y,z} S_{i+1}^{x,y,z} \rangle$ are equal – which applies if all symmetry breaking fields are much smaller than all other energy scales – the normalized spin correlator $\mathscr{S}$ can be directly obtained from the measurement of

Normalized spin correlator

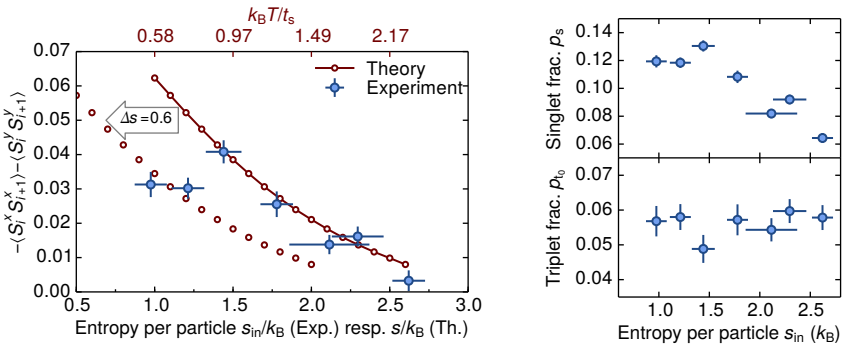

a. Transverse spin correlator b. Singlet and triplet fractions

Figure 9.15: *Scanning the entropy.* a. Transverse spin correlator versus entropy before lattice loading (experiment) or in the lattice (theory) at $U/t = 10.5(8)$ and $t_s/t = 7.3(6)$. The solid line is the result of a DCA calculation. The top axis shows the temperatures obtained from DCA. The shifted theory points show the effect of heating during lattice loading. b. The separate singlet and triplet fractions are shown. Error bars as in Fig. 9.6 on page 169.

singlets and triplets (here n_i^s is one for a single particle of any spin on site i and zero otherwise)

$$\mathscr{S} = \frac{-4\langle S_i^z S_{i+1}^z\rangle}{\langle n_i^s n_{i+1}^s\rangle} = \frac{p_s - p_{t_0}}{p_s + 3p_{t_0}}. \tag{9.16}$$

The normalized antiferromagnetic correlations along the strong tunneling direction reach 25%, see inset Fig. 9.12a on page 175. This corresponds to approximately 5000 ordered atoms.

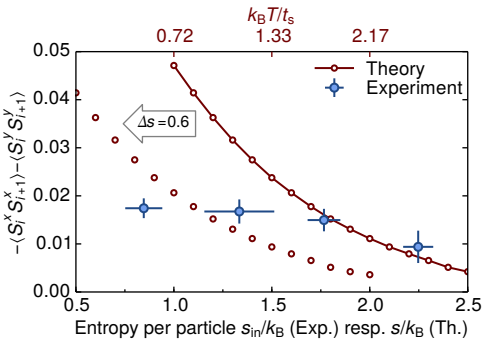

Figure 9.16: *Scanning the entropy at a different anisotropy.* Transverse spin correlator versus entropy before lattice loading (experiment) or in the lattice (theory) at $U/t = 12.5(5)$ and $t_s/t = 4.2(1)$. The solid line is the result of a DCA calculation. The top axis shows the obtained temperatures. The shifted theory points show the effect of heating during lattice loading. Error bars for the experimental data points as in Fig. 9.6.

9.5.2 HIGH-TEMPERATURE SERIES EXPANSION

OVERVIEW

For the anisotropic lattice we evaluate the correlators $\langle S_i^z S_{i+1}^z\rangle$ and $\mathscr{S}$ in a second order series expansion of coupled single sites [Haaf *et al.*, 1992]. The thermodynamic observables are obtained in a similar way as previously described [Jördens *et al.*, 2010], using the average tunneling $\bar{t} = \sqrt{(t_s^2 + 2t^2)/3}$, as discussed in Section 7.3.1 on page 142. Equation (9.15) on page 175 is computed by evaluating the matrix elements of the spin operators.

DETAILS

Similar to the case of the dimerized lattice, we split the Hamiltonian for the homogeneous anisotropic cubic lattice into two parts:

$$\begin{aligned}\hat{H}_A &= \hat{H}_0 + \hat{H}_1 \\ \hat{H}_0 &= U \sum_i \hat{n}_{i,\uparrow}\hat{n}_{i,\downarrow} - \mu \sum_i (\hat{n}_{i,\uparrow} + \hat{n}_{i,\downarrow}) \\ \hat{H}_1 &= -t_s \sum_{\sigma,\langle i,j\rangle_-} (\hat{c}^\dagger_{i,\sigma}\hat{c}_{j,\sigma} + \text{h.c.}) - t \sum_{\sigma,\langle i,j\rangle_-} (\hat{c}^\dagger_{i,\sigma}\hat{c}_{j,\sigma} + \text{h.c.})\,.\end{aligned} \tag{9.17}$$

Notations are analogous to the section on the dimerized lattice. The strong tunneling between nearest neighbors along the x direction is denoted with t_s, whereas the weaker tunneling along the other two axes is given by t. We treat the tunneling Hamiltonian $\hat{H}_1$ as a perturbation to the unperturbed part $\hat{H}_0$, which leads to an expansion of the partition function as in Eq. (9.7) on page 172 in powers of βt_s and βt. Density and entropy per site are then obtained from derivatives of the second order grand canonical potential Ω,

$$\beta\Omega = -\log \mathcal{Z}_0^s - \frac{2(\beta t_s)^2 + 4(\beta t)^2}{(\mathcal{Z}_0^s)^2}\left(\zeta + \zeta^3 w + 2\zeta^2 \frac{1-w}{\beta U}\right). \tag{9.18}$$

Here $\mathcal{Z}_0^s$ is the unperturbed single site partition function, $\zeta = \exp(\beta\mu)$ the fugacity and $w = \exp(-\beta U)$.

The evaluation of the two correlators $\langle S_i^z S_{i+1}^z\rangle$ and $\mathscr{S}$ is slightly more complicated, as it involves two neighboring sites. However, the coefficients for these correlators have already been computed [Haaf *et al.*, 1992], and thus

$$\langle S_i^z S_{i+1}^z\rangle = -\frac{\zeta^2}{(\mathcal{Z}_0^s)^2}\left(\frac{1}{\beta U} + \frac{w-1}{(\beta U)^2}\right)(\beta t_s)^2 \tag{9.19}$$

$$\mathscr{S} = \left(\frac{1}{\beta U} + \frac{w-1}{(\beta U)^2}\right)(\beta t_s)^2. \tag{9.20}$$

9.5.3 DYNAMICAL CLUSTER APPROXIMATION

To get further theoretical insight into our system in the regime of large anisotropies, studies of the anisotropic 3D Hubbard model using DCA [Maier *et al.*, 2005] are conducted. A numerically exact continuous time auxiliary field quantum Monte Carlo impurity solver is used for the numerical simulation [Gull *et al.*, 2008; Gull *et al.*, 2011]. When extrapolating the obtained results in cluster size, the DCA results are exact in the thermodynamic limit [Maier *et al.*, 2002]. To compare the simulations performed for a homogeneous system to the trapped experimental system, LDA is applied, which is still accurate in the experimentally accessible temperature regime [Scarola *et al.*, 2009; Zhou *et al.*, 2011].

Nearest-neighbor spin correlator

In addition to various thermodynamic quantities, the nearest-neighbor spin correlation function $-2\langle S_i^z S_{i+1}^z\rangle$ is calculated. This correlator can be identified with the experimentally measured transverse spin correlator assuming SU(2) invariance of the system,

$$-2\langle S_i^z S_{i+1}^z\rangle = -\langle S_i^x S_{i+1}^x\rangle - \langle S_i^y S_{i+1}^y\rangle = \left(p_s - p_{t_0}\right)/2\,. \tag{9.21}$$

For typical experimental parameters $t_s/t = 7.36$ and $U/t = 10.6$ the correlator is found to have a large increase close to a filling of one particle per site as $k_B T$ is becoming smaller than t_s. When scanning the anisotropy the spin correlations along x, i. e. the axis of anisotropy, are found to be enhanced as the anisotropy is

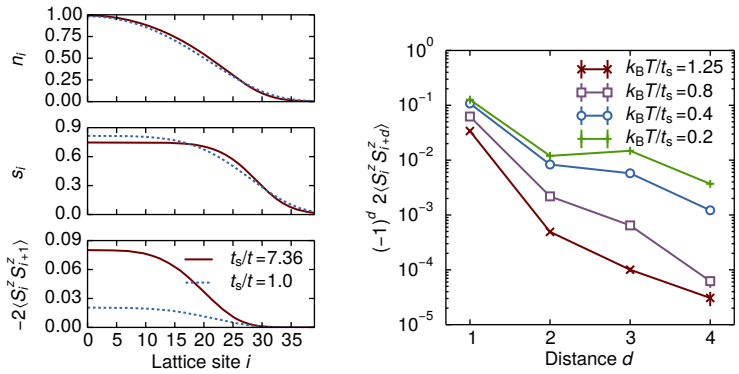

a. Spatial dependence b. Correlation length

Figure 9.17: *Spatial dependence of the thermodynamical quantities and the correlation length.* a. Calculated density n_i, entropy per particle s_i and nearest-neighbor spin correlator as a function of distance to the trap center. Parameters: $U/t = 10.6$, $N = 50 \times 10^3$ and $s = 1.6 k_B$. Half-filling in the center is enforced by the chosen trap frequency. b. The extrapolated spin correlator as a function of the correlation length along the x axis is shown for various temperatures. The sign of the correlator alternates with the distance, indicating antiferromagnetic ordering. Parameters: $t_s/t = 7.36$, $U/t = 10.6$.

increased, with a maximum close to $U/t_s = 5$. This enhancement is at the expense of lowered correlations along the perpendicular axes.

Spatial profiles

The calculated spatial density, entropy, and nearest neighbor spin correlation distributions are shown in Fig. 9.17a for an anisotropic lattice with $t_s/t = 7.36$ and a simple cubic geometry. In contrast to the situation of the dimerized lattice (see Fig. 9.11 on page 174) containing an energy gap, the distributions are all qualitatively similar to the simple cubic case. The spin correlator is however found to be increased by a factor of roughly 4 for the whole trap region.

Longer-range spin correlations

When calculating the spin correlator $-2\langle S_i^z S_{i+d}^z\rangle$ for distances larger than the case studied above for nearest neighbors ($d = 1$), the sign of the correlator is found to alternate, which confirms the existence of antiferromagnetic spin correlations in the system. The magnitude of the correlations, however, is found to decay exponentially, and is already for next-nearest neighbors below the experimental resolution.

Recently, also the 1D Hubbard model was studied using time-dependent density-matrix renormalization group (tDMRG) and analytical arguments [Sciolla *et al.*, 2013] with the aim of comparing to our experimental data. The entropies and temperatures obtained from the experimentally measured correlator agree well with the results obtained from the DCA calculation. Additionally, for $1 \lesssim U/t_s \lesssim 4$ an unexpected doubly non-monotonic behavior in the double occupancy as a function of temperature was found.

9.6 CONCLUSION

In this work, we have demonstrated the observation of short-range quantum magnetism of repulsively interacting ultracold fermions in cubic lattices and investigated the dependence on temperature, lattice dimerization and anisotropy. Our approach is based on a local entropy redistribution scheme within the lattice structure and can be generalized to access the low temperature regime in different geometries, for example 2D systems. The tunable-geometry optical lattice allows the extension of our studies to spin-ladder systems, dimerized 1D chains and zig-zag chains, where the interplay between quantum fluctuations and magnetic ordering plays a particularly important role [Giamarchi, 2004; He *et al.*, 2007]. At even

lower temperatures, the existence of spin liquids in honeycomb or triangular lattices could be investigated [Meng *et al.*, 2010].

TOWARDS LONG-RANGE MAGNETIC ORDER: CORRELATION MEASUREMENTS

10

Going beyond the observation of short-range magnetic order presented in Chapter 9, I will here describe the implementation of a method to detect long-range spin and density correlations based on the correlations of the noise in the atomic momentum distribution in time-of-flight (TOF) absorption images [Altman *et al.*, 2004; Cherng *et al.*, 2007; Bruun *et al.*, 2009]. Additionally, first applications for our tunable-geometry optical lattice are shown. The method, proposed for ultracold atoms in optical lattices in Ref. [Altman *et al.*, 2004][1], is based on the fact that ultracold atoms must be treated as indistinguishable quantum mechanical particles, and therefore either obey bosonic or fermionic particle statistics. TOF imaging can in that context be understood as a simultaneous projective measurement with several detectors, as explained below. The results of detectors measuring the same particle state will then, depending on the quantum statistics of the particle, either show correlated or anti-correlated measurement results. The method can therefore either be used to study emerging correlations or, assuming the correlation signal at a certain detector arrangement as given, to learn about density correlations of the particles beyond those given by just the underlying lattice structure.

Noise correlations

CHAPTER CONTENTS

For optical lattice systems, pioneering experiments employing correlation measurements have studied the emerging correlations in the noise of the momentum distribution of a bosonic Mott insulator [Fölling *et al.*, 2005] and the fermionic antibunching of a spin-polarized gas of ^{40}K released from a simple cubic lattice. Noise correlations have subsequently been used to study the Mott insulator transition of bosons in a 2D lattice [Spielman *et al.*, 2007] and to probe the order in a quantum simulation of antiferromagnetic spin chains [Simon *et al.*, 2011]. Similar experiments investigating correlations in homogeneous systems have studied the atom laser counting statistics [Öttl *et al.*, 2005], pair correlations of fermionic atoms which are dissociated from Feshbach molecules [Greiner *et al.*, 2005], correlations within a bosonic cloud [Schellekens *et al.*, 2005; Estève *et al.*, 2006] and the Berezinskii–Kosterlitz–Thouless (BKT) transition [Hadzibabic *et al.*, 2006]. Moreover, the Hanbury Brown and Twiss (HBT) effect in different isotopes of

Correlation measurements in cold atom systems

1 See also a related proposal for direct detection of the atoms via microchannel plate detectors (MCPs) [Grondalski *et al.*, 1999].

helium [Jeltes *et al.*, 2007], local antibunching in a trapped Fermi gas [Müller *et al.*, 2010; Sanner *et al.*, 2010] and density correlations in *in situ* images [Hung *et al.*, 2011] were studied. A concise discussion of the method and the pioneering experiments is found in Refs. [Bloch *et al.*, 2008; Fölling, 2014], while technical details are discussed in Refs. [Fölling, 2008; Rom, 2009].

In this chapter I will first briefly discuss the two theoretical pictures which can be used to explain the observation of correlations in the momentum distribution of atoms released from an optical lattice. Then I will describe in detail our experimental procedure including the data analysis, which extends upon the method used in previous experiments [Greiner *et al.*, 2005; Fölling *et al.*, 2005; Rom *et al.*, 2006; Spielman *et al.*, 2007]. This will be followed by the results of first experiments confirming that different density ordering patterns in the tunable-geometry optical lattice can be observed.

10.1 THEORY

10.1.1 *HANBURY BROWN AND TWISS PICTURE*

Consider several indistinguishable particles trapped in an optical lattice as sketched in Fig. 10.1a. The atoms are released from the lattice and are detected by independent detectors. Following the intuitive explanation of the Hanbury Brown and Twiss (HBT) effect given by Fano [1961], we will in the following consider two of the atoms that can be seen as sources $S^{A,B}$, from which their wave function expands after release from the lattice.

Measuring the signal emanating from two independent sources simultaneously at two detectors

Let us now assume that the two sources are completely incoherent. The wave function Ψ of the total system is then separable into wave functions for the separate particles ψ^i. The detection probability at one of the detectors, say D_1 can be calculated from the single-particle wave functions as $P_1^i = |\psi^i(\mathbf{x})|^2$. Due to the incoherence of the two particles, the probability of detecting any particle at D_1 is then just the sum of the single-particle detection probabilities: $P_1 = P_1^A + P_1^B = |\psi^A(\mathbf{x})|^2 + |\psi^B(\mathbf{x})|^2$. Therefore, no coherences are seen in the detection process in this case. Surprisingly this does, however, not imply that there are also no coherences for the case where two detectors $D_{1,2}$, spaced by a distance d, simultaneously detect particles.

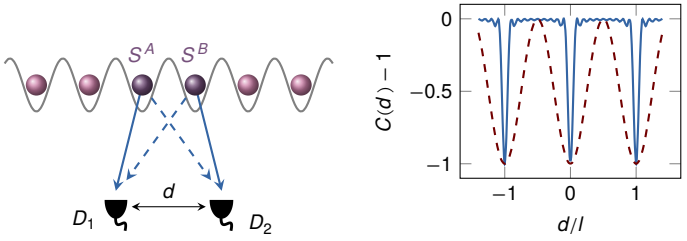

a. Schematics

b. Correlation function for the case of fermions

Figure 10.1: *Hanbury Brown and Twiss (HBT) experiment for particles in a lattice.* a. When calculating the joint detection probability at two detectors $D_{1,2}$ when releasing two atoms $S^{A,B}$ from the lattice, the interference of the two possible combinations of detection paths has to be taken into account. This leads to an interference pattern of the detection probability as the detector distance d is varied. b. The dependence of the correlations $C(d)$ on the detector distance d is shown for 2 (dashed red) and 10 (solid blue) fermions. The distance of the interference maxima is called l. Adapted from [Rom, 2009].

Consider the case where each detector detects one particle. This detection outcome can either be the result of D_1 detecting S^A and D_2 detecting S^B (solid lines) or D_1 detecting S^B and D_2 detecting S^A (dashed lines). To calculate the probability of the detection outcome, the probabilities of all possible two-particle paths must be summed: $P = P(\text{solid + dashed}) \neq P^{AB}(\text{solid}) + P^{AB}(\text{dashed}) = P_1^A P_2^B + P_2^A P_1^B$. Therefore interferences between the two possible combinations of paths have to be taken into account. These interferences of the detection paths lead to an oscillatory dependency of the joint detection probability on the detector distance. This effect can occur both in classical and quantum mechanical systems: actually Hanbury Brown and Twiss first discovered the effect when collecting light from Sirius using photomultiplier tubes [Hanbury Brown *et al.*, 1956]. The outcome of their experiment can be explained by considering a classical electromagnetic wave of which the intensity is measured by two detectors. Due to the spacing of the detectors, the wave arrives with a certain phase difference, giving rise to correlations between the measured intensities, which show an oscillatory behavior as the distance is varied. The related Hong-Ou-Mandel effect showing the bosonic bunching of photons [Hong *et al.*, 1987], however, can only be explained by quantum mechanics. Here, the interference originates from the quantum statistics of the particles (i. e. bosonic or fermionic character). Alternatively, this effect can be seen as the result of the indistinguishability of the particles, requiring an (anti-) symmetrization of the many-body wave function. For fermionic particles, the two possible combinations of detection paths will interfere destructively for certain detector distances. The detection probabilities of the two detectors are then anti-correlated, as shown in Fig. 10.1b on page 182 (dashed red curve), i. e. when D_1 has detected a particle, the probability that D_2 has also detected a particle at the same time is decreased. For bosons the opposite is the case. The argument can be extended to more than two particles. The normalized density correlation function $C(d)$ for the case of a 1D lattice is found to be (for a derivation see Section 10.1.3 on the next page)

Classical effect: light from Sirius

Purely quantum mechanical Hong-Ou-Mandel effect

$$\begin{aligned} C(d) &= 1 \pm \frac{1}{N^2} \sum_{r=1}^{N} \sum_{s=1}^{N} e^{i2\pi rd/l} e^{-i2\pi sd/l} \\ &= 1 \pm \left[\frac{\sin(N\pi d/l)}{N \sin(\pi d/l)} \right]^2 . \end{aligned} \tag{10.1}$$

Here $\pm$ has to be chosen for bosons or fermions, respectively, and l is the distance of the interference maxima. The solid blue curve in the figure shows the correlation function for 10 fermions.

10.1.2 BLOCH PICTURE

The HBT experiment can also be understood in a different physical picture. Consider a 1D lattice containing atoms. When the atoms are released from the optical lattice and evolve freely for a certain time t in a TOF absorption imaging experiment, their initial momenta p in the lattice are converted to a real space position l. The two are related by

$$l = \frac{pt}{m} . \tag{10.2}$$

According to the Bloch theorem the wave function of an atom (the Bloch state) can be written as a superposition of several real momentum states

$$|v, k\rangle = \sum_n c_{v,k}^n \, |p = \hbar(k + 2\pi n/a)\rangle \ . \tag{10.3}$$

Anticorrelations as a result of Pauli's exclusion principle

The measurement of the atomic density after TOF by absorption imaging onto a CCD camera corresponds to a projection onto one of these real momentum basis states $|p = \hbar(k + 2\pi n/a)\rangle$ (note that relating to the Hanbury Brown and Twiss picture discussed above, the pixels of the CCD camera can be seen as an array of independent detectors simultaneously measuring the atomic density at different locations). Because of Pauli's exclusion principle no two fermions can occupy the same quantum state (in that case the same Bloch state $|\nu, k\rangle$). From this it follows that, if a particle is detected at a certain position, another particle cannot be detected at positions with a distance nl (where $n \in \mathbb{Z}$), corresponding to momenta spaced by $2n\hbar k_L$. This statement, illustrated in Fig. 10.2, holds as long as only one band is filled. As a result, we expect anticorrelations in the detected atomic density distribution for the corresponding distances.

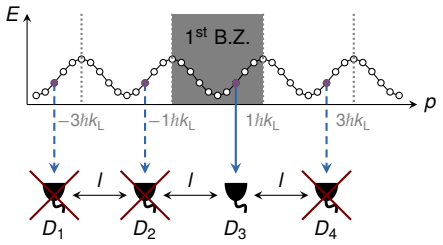

Figure 10.2: *Momentum correlations in the Bloch picture.* The state of a particle in one band of a lattice is a superposition of several real momentum states. If a particle is detected in one of these momentum states, it cannot be detected in momentum states separated by an integer multiple of twice the lattice momentum $\hbar k_L$ (equivalent to $\mathbb{Z}l$ in real space). Adapted from [Rom, 2009].

Effect of the column-integration

The situation is complicated by the fact that the atomic clouds in optical lattices usually have a 3D structure, while the absorption imaging technique is only able to resolve correlations in a 2D plane, as every pixel on the CCD camera records a column-density of the expanded cloud. The correlations are found to persist in the column-integrated density profiles, but are reduced. The detected number of particles N_σ per "momentum bin" σ of the detector will then not be either one or zero depending on which real momentum state has been projected onto, but it will rather fluctuate on the order of $\sqrt{N_\sigma}$ around the mean value N_σ that one would expect when not taking into account the quantum statistics of the particles [Altman *et al.*, 2004]. Hence the name *noise correlations*. The finite cloud size in the trap and the finite TOF duration as well as the optical properties of the imaging system lead to an additional degradation of the signal. Moreover, interactions present during TOF will alter the correlation properties of the particles.

10.1.3 CORRELATION FUNCTIONS

In this section, the correlation function $C(\mathbf{x}_1, \mathbf{x}_2)$ of the density distribution of bosonic or fermionic particles released from an optical lattice is deduced. The following argument is based on the assumption that for a sufficiently long TOF duration, the measured density operator $\hat{n}(\mathbf{x})$ after TOF indeed corresponds to the momentum operator $\hat{n}(\mathbf{k})$ in the trap. The normalized density correlation function for the positions $\mathbf{x}_1$ and $\mathbf{x}_2$ is defined as

$$C(\mathbf{x}_1, \mathbf{x}_2) = \frac{\langle \hat{n}(\mathbf{x}_1)\hat{n}(\mathbf{x}_2)\rangle}{\langle \hat{n}(\mathbf{x}_1)\rangle \langle \hat{n}(\mathbf{x}_2)\rangle} . \tag{10.4}$$

Along the lines of the derivation in [Fölling, 2008], we reorder the field operators:

$$\begin{aligned} \langle \hat{n}(\mathbf{x}_1)\hat{n}(\mathbf{x}_2)\rangle &= \langle \hat{\psi}^\dagger(\mathbf{x}_1)\hat{\psi}(\mathbf{x}_1)\hat{\psi}^\dagger(\mathbf{x}_2)\hat{\psi}(\mathbf{x}_2)\rangle \\ &= \pm \langle \hat{\psi}^\dagger(\mathbf{x}_1)\hat{\psi}^\dagger(\mathbf{x}_2)\hat{\psi}(\mathbf{x}_1)\hat{\psi}(\mathbf{x}_2)\rangle + \delta(\mathbf{x}_1 - \mathbf{x}_2)\langle \hat{n}(\mathbf{x})\rangle \\ &= \langle \hat{n}(\mathbf{x}_1)\rangle \langle \hat{n}(\mathbf{x}_2)\rangle g^{(2)}(\mathbf{x}_1, \mathbf{x}_2) + \delta(\mathbf{x}_1 - \mathbf{x}_2)\langle \hat{n}(\mathbf{x})\rangle . \end{aligned} \tag{10.5}$$

Here, we have written the expectation value $\langle \hat{n}(\mathbf{x}_1)\hat{n}(\mathbf{x}_2)\rangle$ in a form containing the pair distribution function

Pair distribution function

$$g^{(2)}(\mathbf{x}_1, \mathbf{x}_2) = \frac{\langle \hat{\psi}^\dagger(\mathbf{x}_1)\hat{\psi}^\dagger(\mathbf{x}_2)\hat{\psi}(\mathbf{x}_1)\hat{\psi}(\mathbf{x}_2)\rangle}{\langle \hat{n}(\mathbf{x}_1)\rangle \langle \hat{n}(\mathbf{x}_2)\rangle}\,. \tag{10.6}$$

By inserting the field operator in the far field [Fölling, 2008], i. e. where the detector is located,

$$\hat{\psi}(\mathbf{x}, t) = \kappa^{3/2}\tilde{w}(\kappa\mathbf{x})e^{\frac{1}{2}i\kappa\mathbf{x}^2}\sum_j e^{-i\kappa\mathbf{x}\mathbf{X}_j}\hat{a}_j\,, \tag{10.7}$$

where $\hat{a}_j$ is the destruction operator of a particle at position $\mathbf{X}_j$, $\tilde{w}(\mathbf{k})$ is the Fourier transform of the Wannier function and $\kappa = m/(\hbar t)$ (t is the TOF time), we obtain for the correlation function

$$C(\mathbf{x}_1, \mathbf{x}_2) = 1 \pm \frac{1}{N^2}\Big|\sum_j e^{i\kappa\mathbf{X}_j\cdot(\mathbf{x}_1-\mathbf{x}_2)}\langle \hat{n}_j\rangle\Big|^2 + \frac{\delta(\mathbf{x}_1-\mathbf{x}_2)}{\kappa^3\left|\tilde{w}(\kappa\mathbf{x}_1)\right|^2 N}\,, \tag{10.8}$$

where "+" accounts for the bosonic and "−" for the fermionic case. Here we have assumed a deep lattice such that the wave function of the whole system is a product of the particle number (i. e. Fock) states on the single lattice sites. Additionally we have neglected an offset term of order $1/N$. The δ term is the autocorrelation term, which will also be neglected in the quantitative analysis of the obtained data. From the above equation the simplified expression for a 1D lattice given in Eq. (10.1) on page 183 can be deduced.

For large atom numbers N (i. e. $j \to \infty$) the series becomes a Fourier transform and can therefore be written as a sum of δ functions:

$$C(\mathbf{x}_1, \mathbf{x}_2) = 1 \pm \frac{1}{N}\sum_j \delta\Big(\left\{(\mathbf{x}_1-\mathbf{x}_2) - \mathbf{K}_j/\kappa\right\}/l\Big) + \frac{\delta\left(\mathbf{x}_1-\mathbf{x}_2\right)}{\kappa^3\left|\tilde{w}(\kappa\mathbf{x}_1)\right|^2 N}\,, \tag{10.9}$$

where $\mathbf{K}_j$ are the reciprocal lattice vectors. As is obvious from the above equation, the correlation function only depends on $\mathbf{d} = \mathbf{x}_1 - \mathbf{x}_2$ and can therefore be written in the following form:

Form of the correlation function used as the starting point for analyzing the experimental data

$$C(\mathbf{d}) = \frac{\int\langle \hat{n}(\mathbf{x}-\mathbf{d}/2)\hat{n}(\mathbf{x}+\mathbf{d}/2)\rangle \mathrm{d}^2\mathbf{x}}{\int\langle \hat{n}(\mathbf{x}-\mathbf{d}/2)\rangle\langle \hat{n}(\mathbf{x}+\mathbf{d}/2)\rangle \mathrm{d}^2\mathbf{x}}, \tag{10.10}$$

which we will use for the analysis of the data. Column-integration and imperfections of the imaging system will lead to a broadening of the δ functions while retaining the area under the peak. We approximate the broadened peaks by gaussians with a width σ:

$$C(\mathbf{d}) = 1 \pm \frac{1}{4\pi N}\left(\frac{l}{\sigma}\right)^2\sum_j e^{-(\mathbf{d}-\mathbf{K}_j\kappa)^2/4\sigma^2} + \frac{\delta(\mathbf{d})}{\kappa^3\left|\tilde{w}(\kappa\mathbf{d})\right|^2 N}\,. \tag{10.11}$$

The height of the peaks should therefore approximately scale with t^2/N.

Scaling of the peak height

10.2 EXPERIMENTAL PROCEDURE

We have performed tests of the noise correlation algorithm for both $m_F = (-9/2, -7/2)$ and $(-9/2, -5/2)$ spin mixtures as well as spin-polarized gases in the $m_F = -9/2$ Zeeman state of ^{40}K. The spin mixtures are prepared in the usual

way for our experiment, see Section 3.1.4 on page 41. The spin polarized gas is obtained by not producing a spin mixture after performing the spin sweep from $m_F = 9/2$ to $m_F = -9/2$, and instead running the evaporation ramp of the FORT with the spin-polarized gas. The obtained cloud will therefore not be thermalized, leading to a possibly reduced correlation signal. We load about 200×10^3 atoms within 200 ms into the optical lattice structure to be investigated, ensuring thermalization of the spin mixtures by choosing a scattering length on the order of $|a| \gtrsim 300 a_0$.

Freezing the atomic motion

After loading the gas and performing the experiment, the lattice is frozen to a depth which is equivalent to approximately $30\,E_\mathrm{R}$ per lattice beam for the square lattice (i. e. if $V_\mathrm{X} \neq 0$, $V_{\tilde{\mathrm{X}}}$, V_X and V_Y are not set to a depth of $30\,E_\mathrm{R}$ but such that the increased depth by the interference is equal to this value). This freezing ramp is performed within 1 ms. $V_{\tilde{\mathrm{Z}}}$ is ramped to $10\,E_\mathrm{R}$ in this step, independent of the other lattice depths. This avoids an extensively large expansion of the cloud along the column-integration direction during TOF (the absorption images are taken of the $x - y$ plane).

The freezing ramp is necessary to fulfill the condition that the quantum mechanical states on the single lattice sites must be Fock states in order to interpret the noise correlation signal as the density correlator of the system before releasing from the lattice. Additionally, the freezing ramp avoids changes of the density caused by the interaction ramp that follows in the next step. In a non-frozen lattice, changing the interaction can lead to a change of the on-site density caused by both an actual density redistribution or admixture of states with other densities from neighboring sites.

Interactions

The interactions are then tuned to non-interacting (for the $m_F = (-9/2, -7/2)$ spin mixture) or the background scattering length $a_\mathrm{bg} \approx 100 a_0$ (for $m_F = (-9/2, -5/2)$) within 50 ms. Small interactions are chosen in order not to disturb the density correlations during the initial stage of the free expansion of the cloud. Note that our tests with different scattering lengths showed that the correlation signal also persists when large repulsive interactions are chosen. However, a definite conclusion on this issue cannot be drawn as we did not compare the obtained correlation amplitudes with theoretical predictions.

Both the optical lattice and the FORT are then switched off simultaneously, followed by the switch-off of the magnetic offset fields after 1 ms TOF. After a total TOF duration of 10 ms normal absorption images are taken with either the *Andor iXon+* or *Andor iXon Ultra* CCD camera[2]. The pixel size of both cameras is $(16\,\mu\mathrm{m})^2$ and the magnification of the imaging system is approximately 4.

Absorption imaging: imaging light intensity

We have found that the visibility of the correlation signal strongly depends on the intensity of the imaging beam. For our measurements, we increased its intensity with respect to the usual setting to about 20% of the saturation intensity, keeping the normal imaging pulse length of 40 µs. We assume that the increased visibility is due to the more favorable ratio of the relative photon shot noise with respect to the relative atomic shot noise. For the *iXon+* CCD camera an independent noise analysis was performed, from which we conclude that our imaging system is photon shot noise limited.

As discussed in the next section, in order to achieve the signal to noise ratio needed to observe any correlations, the correlation signal from several repetitions of the experiment under equal conditions is averaged. We typically acquire 100 to 200 shots for this averaging procedure.

2 The *Andor iXon Ultra* was used in *fast kinetics* mode, while the *iXon+* showed increased noise levels in the autocorrelation images in this mode (probably due to well spilling during the fast vertical shifts, see Section 3.4 on page 63), and was therefore used in the normal full frame mode.

10.3 DATA ANALYSIS

The images obtained from the CCD camera are processed in the usual way for absorption imaging in order to obtain optical density images (see Section 3.4 on page 63). The optical densities are then converted into column densities. In order to obtain the density-density correlation function (deduced in Eq. (10.10) on page 185) we replace the density operator by the measured density profile $\hat{n}(\mathbf{x}) \longrightarrow n(\mathbf{x})$ and the expectation values $\langle ... \rangle$ by an average over many repeated experiments under the same conditions. Additionally, the average in the numerator is taken after the integration. The correlator therefore reads:

$$C(\mathbf{d}) = \frac{\int \langle n(\mathbf{x}-\mathbf{d}/2) n(\mathbf{x}+\mathbf{d}/2) \rangle \mathrm{d}^2\mathbf{x}}{\int \langle n(\mathbf{x}-\mathbf{d}/2) \rangle \langle n(\mathbf{x}+\mathbf{d}/2) \rangle \mathrm{d}^2\mathbf{x}} = \frac{\left\langle \int n(\mathbf{x}-\mathbf{d}/2) n(\mathbf{x}+\mathbf{d}/2) \mathrm{d}^2\mathbf{x} \right\rangle}{\int \langle n(\mathbf{x}-\mathbf{d}/2) \rangle \langle n(\mathbf{x}+\mathbf{d}/2) \rangle \mathrm{d}^2\mathbf{x}} . \quad (10.12)$$

Inspecting the numerator and denominator, they are actually both found to correspond to the autocorrelation function of a certain variable. The autocorrelation function $R(\mathbf{d})$ of a signal $S(\mathbf{x})$ is defined as

Autocorrelation function

$$R(\mathbf{d}) = \int S(\mathbf{x}-\mathbf{d}/2) S(\mathbf{x}+\mathbf{d}/2) \, \mathrm{d}\mathbf{x} . \quad (10.13)$$

For an efficient calculation of the autocorrelation function, the Wiener–Khinchin theorem [Wiener, 1930] can be used. It relates the autocorrelation function to the power spectral density via the Fourier transform. The autocorrelation function can therefore be calculated using a forward and an inverse discrete Fourier transform,

Wiener-Khinchin theorem

$$R(\mathbf{d}) = \mathfrak{F}^{-1} \left[(\mathfrak{F} S(\mathbf{x}))^* \mathfrak{F} S(\mathbf{x}) \right] . \quad (10.14)$$

Here, ...* denotes the complex conjugate.

Approximations for the numerator and denominator of the correlator

In Eq. (10.12), the numerator corresponds to the mean of the autocorrelation functions of several measured density profiles, while the denominator contains the autocorrelation function of the mean of the measured density profiles. Note that the numerator can in principle also be obtained from the autocorrelation function of only a single density distribution. However, in order to raise the signal above the noise level, several autocorrelation images are usually averaged. By building the fraction of the two quantities, correlations which are present in both the single density images as well as the mean density are theoretically removed. This applies for example to the overall cloud profile: it contains positive correlations between $-\mathbf{x}$ and $\mathbf{x}$ over all length scales (when assuming the atomic cloud to be centered at $\mathbf{x} = 0$). However, if small fluctuations in the cloud profile or the atom number are present between the experimental runs, these would not be removed by the normalization. In contrast to Refs. [Fölling, 2008; Rom, 2009], we overcome this limitation of the method by assuming that the measured density profiles $n(\mathbf{x})$ are the sum of a gaussian function with added noise, i. e. the density fluctuations of interest,

$$n(\mathbf{x}) = n_g(\mathbf{x}) + \Delta n(\mathbf{x}) = n_0 \, e^{-(x-x_0)^2/w_x^2 - (y-y_0)^2/w_y^2} + \Delta n(\mathbf{x}) . \quad (10.15)$$

Here, $\mathbf{x} = (x, y)$. Then,

$$C(\mathbf{x}_1, \mathbf{x}_2) = \frac{\langle n(\mathbf{x}_1) n(\mathbf{x}_2)\rangle}{\langle n(\mathbf{x}_1)\rangle \langle n(\mathbf{x}_2)\rangle} = \frac{\langle n_g(\mathbf{x}_1) n_g(\mathbf{x}_2)\rangle + \langle n_g(\mathbf{x}_1)\Delta n(\mathbf{x}_2)\rangle + \langle \Delta n(\mathbf{x}_1) n_g(\mathbf{x}_2)\rangle + \langle \Delta n(\mathbf{x}_1)\Delta n(\mathbf{x}_2)\rangle}{\langle n_g(\mathbf{x}_1) + \Delta n(\mathbf{x}_1)\rangle \langle n_g(\mathbf{x}_2) + \Delta n(\mathbf{x}_2)\rangle}. \tag{10.16}$$

Assuming that the mean density profile is well fitted by a gaussian and that all experimental runs have approximately the same atom number, we can make the following approximations: $\langle n_g(\mathbf{x}_1) n_g(\mathbf{x}_2)\rangle = \langle n_g(\mathbf{x}_1)\rangle \langle n_g(\mathbf{x}_2)\rangle$, $\langle n_g(\mathbf{x}_1)\Delta n(\mathbf{x}_2)\rangle = \langle \Delta n(\mathbf{x}_1) n_g(\mathbf{x}_2)\rangle = 0$ and $\langle n_g(\mathbf{x}_i) + \Delta n(\mathbf{x}_i)\rangle = \langle n_g(\mathbf{x}_i)\rangle$. Using these, we arrive at

$$C(\mathbf{x}_1, \mathbf{x}_2) = 1 + \frac{\langle \Delta n(\mathbf{x}_1)\Delta n(\mathbf{x}_2)\rangle}{\langle n(\mathbf{x}_1)\rangle \langle n(\mathbf{x}_2)\rangle} \tag{10.17}$$

or, equivalently,

$$C(\mathbf{d}) = 1 + \frac{\langle \int \Delta n(\mathbf{x} - \mathbf{d}/2)\Delta n(\mathbf{x} + \mathbf{d}/2)\mathrm{d}^2\mathbf{x}\rangle}{\int \langle n(\mathbf{x} - \mathbf{d}/2)\rangle \langle n(\mathbf{x} + \mathbf{d}/2)\rangle \mathrm{d}^2\mathbf{x}}. \tag{10.18}$$

This is the form which we will use for the data processing. In detail, the procedure consists of the following steps:

1. Optionally, certain measured density profiles are rejected based on observed excess noise in the CCD image of the probe beam (*bright* picture). We typically reject between none and 30% of the images.
2. A gaussian with independent amplitude, position and width along x and y is fitted to $n(\mathbf{x})$ and subsequently subtracted. The result is a noise distribution with an essentially flat envelope.

Camera readout noise

3. The electronic readout process in the CCD camera introduces correlations of the electron count between neighboring pixels along the horizontal shift direction of the camera. We also measured some correlations along the vertical shift direction, which are, however, weaker than the horizontal ones. To eliminate these correlations, which appear as one pixel spaced stripes in the autocorrelation images, $\Delta n(\mathbf{x})$ (in the form of a matrix as originally obtained from the CCD camera pixels) is convoluted with a 3×3 matrix $\mathbf{M}$ of the following form:

$$\mathbf{M} = \frac{\mathbf{m}}{\sum_{i,j} m_{i,j}} \quad \text{with} \quad \mathbf{m} = \begin{pmatrix} 0 & 0.5 & 0 \\ 1 & \kappa & 1 \\ 0 & 0.5 & 0 \end{pmatrix}, \tag{10.19}$$

   where κ is usually set to a value in the range 1.2 to 2.0, depending on the camera model and the experimental situation. For processing speed considerations, a fast Fourier transform (FFT) based convolution method is chosen instead of a direct integration. The resulting image will be called $\Delta n'(\mathbf{x})$ in the following.
4. To remove residual long-wavelength modulations disturbing the flatness of $\Delta n'(\mathbf{x})$, a high-pass filter with an inverted gaussian weight is applied, see Listing 10.1 on the next page for the corresponding implementation in the programming language *Python*. The frequency weighting function is $1 - \exp(-f^2/w^2)$, where $w \approx 20(\mathrm{px})^{-1}$, thereby excluding approximately the 20 lowest spatial frequencies from the spectrum. The result is called $\Delta n''(\mathbf{x})$.

Listing 10.1: *High-pass filter with a gaussian weight.*

```
# s defines the spatial frequency up to which to cut out from the
    freq. spectrum
def hp_gauss_filter(p, s):
    w = fftshift(equal_gauss_window(p,s))

    fp = fft2(p)
    fp *= (1-w)
    return ifft2(fp).real
```

Listing 10.2: *Calculation of the autocorrelation function.*

```
def acf(r):
    k = fft2(r)
    p = np.abs(k)**2
    a = ifft2(p)
    return fftshift(a.real)
```

5. The autocorrelation function $c(\mathbf{d})$ of $\Delta n''(\mathbf{x})$ is now calculated. The implementation of this calculation in *Python*[3] is shown in Listing 10.2.
6. The density profiles of all experimental runs are processed according to the recipe above and the resulting $c(\mathbf{d})$ are averaged. This is the numerator of the correlation function.

The denominator of $C(\mathbf{d})$ is obtained as follows:

1. All obtained $n(\mathbf{x})$ are averaged and fitted with a gaussian.
2. All $\Delta n''(\mathbf{x})$ obtained while processing the single density images are averaged as well and added to the fitted gaussian obtained in the previous step.
3. The autocorrelation function of the above sum is calculated in the same way as described above, resulting in the denominator $\bar{c}(\mathbf{d})$.

The final correlation function $C(\mathbf{d})$ is then obtained as $C(\mathbf{d}) = \langle c(\mathbf{d}) \rangle / \bar{c}(\mathbf{d})$. Additionally, if the lattice structure along x and y is the same, this symmetry can be used to improve the signal by averaging $C(\mathbf{d})$ with rotations and reflections of itself making use of both point symmetry (which is already given in the original $C(\mathbf{d})$) and reflection symmetry along x and y. Additionally, the analysis code features the option of automatically averaging several correlation functions $C_i(\mathbf{d})$ that have been obtained by processing the same set of data using varying filter parameters, in order to remove filter artifacts.

The dips are then fitted with independent gaussians to obtain their volume, which is a useful measure for theory comparisons, see Eq. (10.11) on page 185.

10.4 VALIDATION

We have measured the correlation functions of Fermi gases prepared in different spin mixtures loaded into the tunable-geometry optical lattice set to square, checkerboard and honeycomb geometries.

3 For optimal performance the `FFTW` library (*"Fastest Fourier Transform in the West"*) via the *Python* interface `anfft` is used.

10.4.1 SQUARE AND CHECKERBOARD LATTICES

We validate our preparation and detection method by loading a balanced (50:50) $m_F = (-9/2, -7/2)$ spin mixture into a lattice of either square or checkerboard geometry in the $x-y$ plane. For both configurations, an additional lattice along z is used. For the square geometry, the lattice is ramped directly to a partly frozen lattice with potential depths $V_{\tilde{\mathrm{X}},\mathrm{X},\mathrm{Y},\tilde{\mathrm{Z}}} = [20, 0, 20, 10]\, E_\mathrm{R}$ at a scattering length of $-310a_0$ to allow for thermalization during the ramp. The scattering length is then ramped to $0a_0$ within 50 ms, followed by 10 ms of TOF. The dataset consists of 110 experimental runs. The obtained correlation pattern is shown in Fig. 10.3a. As expected, clear anticorrelation dips are visible at the spatial positions related to the momenta $\mathbf{p} = (\pm 1|0, \pm 1|0)2\hbar k_\mathrm{L}$ via TOF. Line sums in the vicinity of the dips along $p_{(x,y)}$ and the two diagonals are shown in Fig. 10.3b. The dip depths are on a similar order as those reported in [Rom *et al.*, 2006] for a spin-polarized gas of ^{40}K.

Square geometry

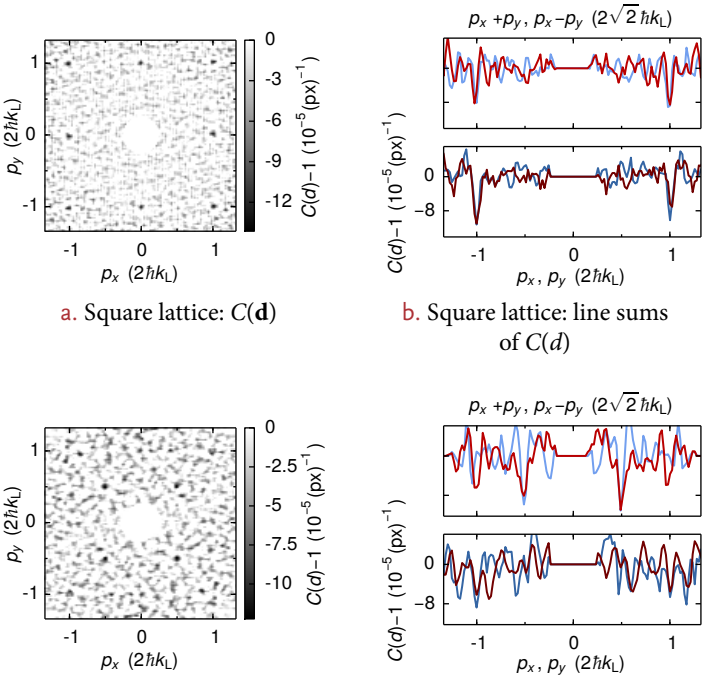

a. Square lattice: $C(\mathbf{d})$

b. Square lattice: line sums of $C(d)$

c. Checkerboard lattice: $C(\mathbf{d})$

d. Checkerboard lattice: line sums of $C(d)$

Figure 10.3: *Measured correlation functions in the square and checkerboard lattice.* In the square lattice anticorrelation dips are visible at $\mathbf{p} = (\pm 1|0, \pm 1|0)2\hbar k_\mathrm{L}$, reflecting the underlying lattice periodicity. In the checkerboard lattice, a similar pattern appears, but rotated by 45° and shrunk by a factor of $\sqrt{2}$. The line sums shown on the right are taken over three pixel rows. The bottom panel shows cuts along p_x (red) and p_y (blue) and the top panel along the first (red) and second diagonal (blue).

Checkerboard geometry

In a second experiment we load a cloud prepared in the same way as above into the checkerboard lattice with potential depths $V_{\tilde{\mathrm{X}},\mathrm{X},\mathrm{Y},\tilde{\mathrm{Z}}} = [0, 15, 15, 20]\, E_\mathrm{R}$, using a scattering length of $a = 770a_0$. The interactions are then tuned to zero, followed by a ramp of the lattice intensities to a final depth of $V_{\tilde{\mathrm{X}},\mathrm{X},\mathrm{Y},\tilde{\mathrm{Z}}} = [0, 7, 7, 10]\, E_\mathrm{R}$ within 10 ms. The dataset again contains 110 separate runs. For the checkerboard lattice, $C(\mathbf{d})$ contains clearly visible dips at $\mathbf{p} = (\pm 1/2, \pm 1/2)2\hbar k_\mathrm{L}$, see Fig. 10.3c. This is a result of the rotation of the unit vectors of the underlying lattice structure in the

$x - y$ plane by 45° combined with an enlargement by a factor of $\sqrt{2}$ with respect to those of the square lattice structure.

10.4.2 HONEYCOMB LATTICE

We test the feasibility of noise correlation measurements in more complex lattice geometries in the strongly interacting regime by loading an $m_F = (-9/2, -5/2)$ spin mixture into a honeycomb lattice. The lattice is set to the following depths: $V_{\tilde{X},X,Y,\tilde{Z}} = [14, 0.79, 6.45, 7]\, E_R$, at which the tunnel couplings in the honeycomb lattice are the same along the horizontal and the vertical bonds. The scattering length is set to $a = 530 a_0$.

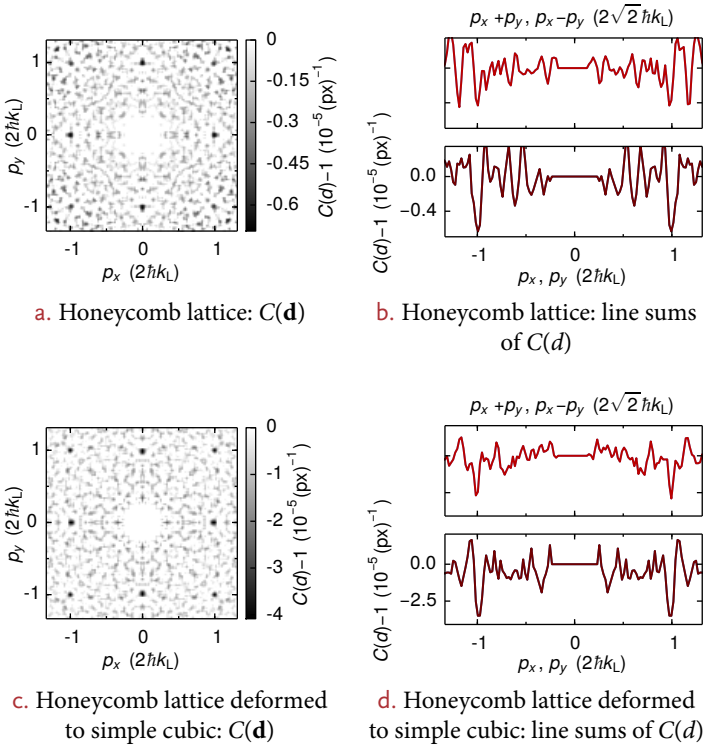

a. Honeycomb lattice: $C(\mathbf{d})$

b. Honeycomb lattice: line sums of $C(d)$

c. Honeycomb lattice deformed to simple cubic: $C(\mathbf{d})$

d. Honeycomb lattice deformed to simple cubic: line sums of $C(d)$

Figure 10.4: *Measured correlation functions for the honeycomb lattice.* To increase the visibility, the obtained correlation patterns have been rotated by 90° and then averaged with themselves.

In a first experiment, the beam intensities are ramped up to $V_{\tilde{X},X,Y,\tilde{Z}} = [28, 1.43, 12.9, 10]\, E_R$ within 10 ms after the lattice loading. Before releasing the atoms, the scattering length is lowered to $280 a_0$. The obtained correlation pattern is shown in Fig. 10.4a. For increased visibility, in this set of measurements, the correlation pattern has been averaged with rotations and reflections of itself. Contrary to the naive expectation, the additional dips attributed to the checkerboard contribution to the honeycomb lattice are not visible, although the Brillouin zone of the lattice structure is actually rotated and resized due to the presence of the X lattice beam. The dips are in fact expected to be present but with an amplitude that is well below the noise level. Intuitively, the magnitude of the dips located at uneven multiples of $(\pm\hbar k_L, \pm\hbar k_L)$ is related to the displacement of the lattice sites with respect to the positions in the square lattice. For the present lattice geometry, this shift is only about 5% of the site distance. The resulting dip amplitude can be estimated by a simple numerical model: we assemble a 2D array with lattice sites located at the minima of the real potential. Instead of the real maximally localized Wannier

Simple model to calculate the dip amplitude

functions we place small gaussian wave packets at the well positions and numerically calculate the Fourier transform of this arrangement, see Fig. 10.5. Therefore this model neglects effects which are due to the structure of the Wannier functions. According to the model, the dips located at $(\pm\hbar k_L, \pm\hbar k_L)$ are about a factor of 6 smaller than those located along the p_x or p_y axes.

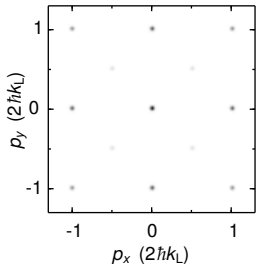

Figure 10.5: *Simple model to obtain the dip amplitudes of the honeycomb lattice.* The absolute value of a Fourier transform of an array of small gaussian wave packets placed at the minimum positions of the honeycomb lattice potential is shown. The number of sites is 50 per axis and the width of the gaussians was chosen to be 1/5 of the lattice spacing.

The noise correlation signal depends both on the relative position of the lattice sites as well as their occupation. To separate the two effects, it can be useful to deform the lattice to, for example, a simple cubic structure for detection after the actual experiment. In Fig. 10.4c on page 191, we load the honeycomb lattice in the same way as described above, but ramp V_Y to 20 E_R and V_X to zero within 1 ms after the freezing ramp. The local density distribution in the lattice follows this change of lattice geometry as long as the ramp is slower than the on-site harmonic oscillator frequencies, which are on the order of several 10 kHz for typical lattice depths. The noise correlation measurement is then performed in the usual way, with the inarguably expected result of a correlation pattern equivalent to that of directly loaded square lattice, but with a larger correlation amplitude.

CONCLUSION We have successfully demonstrated the measurement of momentum correlations of different spin mixtures loaded into square, checkerboard and honeycomb lattices via noise correlations. In agreement with theoretical expectations, the method gives access to the in-trap density distribution and allows for tuning of the interactions and lattice geometry without corrupting the correlation signal. Noise correlations could be a useful tool to detect CDWs and possibly also SDWs[4] in our tunable-geometry optical lattice, which can either be prepared artificially or may emerge naturally due to interactions at low enough entropies.

4 See [Bruun *et al.*, 2009] for a calculation of the noise correlation signal amplitude for an antiferromagnetically ordered state.

OUTLOOK

11

In the following I will present some ideas for future experiments, building upon the work addressing either the non-interacting or the interacting properties of the honeycomb lattice presented in this thesis. The main focus lies on the characterization of the topology of the honeycomb band structure and the implementation of topological insulators. A few possible experiments in other lattice geometries which are accessible using the lattice of tunable geometry are briefly discussed as well.

PROPERTIES OF THE BAND STRUCTURE

While we have thoroughly investigated the two Dirac points with their associated linear dispersion relation of our artificial graphene system, the emerging non-trivial topology of the band structure was not directly addressed so far. Here, a direct measurement of the Berry phase pickup when encircling one of the Dirac points or the observation of the effect of the associated Berry curvature would be desirable. The main difficulty here is the separation of the dynamical phase accumulated when moving through the band structure from the phase purely associated with the topology. Different proposals to resolve this problem have been brought forward. For example, Abanin *et al.* [2013] proposed a direct measurement of the Berry phase of one of the Dirac points using a combination of Ramsey interferometry and Bloch oscillations.

Measuring Berry's phase using a combination of Ramsey interferometry and Bloch oscillations

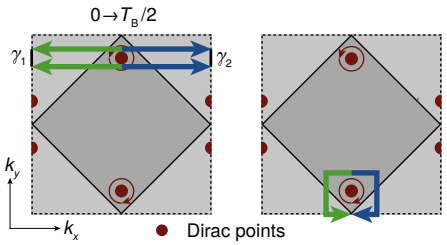

Figure 11.1: *Detecting the Berry phase.* A combination of Ramsey interferometry and Bloch oscillations of two Zeeman states (green and blue arrows) allows for a band-effect free detection of the Berry phase picked up when passing in the vicinity of a Dirac point. Two possible Bloch oscillation paths are shown (left and right panel). The chirality of the Dirac points is indicated by the circular arrows.

The starting point of such an experiment is an ensemble of bosonic or fermionic spin-polarized atoms in the lowest band, such that at least the vicinity of one of the Dirac points is populated, see Fig. 11.1, left panel. A $\frac{\pi}{2}$ rf pulse is then used to create a coherent superposition of two Zeeman states with opposite magnetic moments, shown in green and blue. Using a magnetic field gradient aligned with the x axis, Bloch oscillations along k_x with opposite directions for the two Zeeman states are driven. After a time $t = T_B/2$ the two states meet again and another $\frac{\pi}{2}$ pulse is applied. The population in the two spin states is then measured by separating the two spin components using a magnetic field gradient. The relative population then varies as a function of the difference in phase pickup along the two paths. As the band structure is symmetric with respect to k_y, the dynamical phase pickups for the two spin states will exactly cancel, leaving the geometric phase – called Zak phase in this context – as the only contribution. Comparing the phases picked up by trajectories passing above ($k_y > k_y^D$) and below ($k_y < k_y^D$) the Dirac point (shown in the figure), their difference is found to be equal to the Berry phase pickup for a closed loop around the point, i. e. π. This is because the Berry phase contributions along the two short paths $\gamma_{1,2}$ (see figure) connecting the colored trajectories cancel. This is due to the fact that these two paths are equal (they are

identified by Bragg reflections), but traversed in opposite direction when encircling the Dirac point. A similar scheme has so far allowed for the observation of the Zak phase in 1D optical lattices [Atala *et al.*, 2013].

Alternative Bloch oscillation trajectory to measure Berry's phase

In the right panel of the figure, an alternative pair of trajectories is shown. From the initial position, the two spin states are first separated by a magnetic field gradient along x, followed by a short period of Bloch oscillations along y, driven by gravity. A magnetic field gradient in the opposite direction along x is used to rejoin the two trajectories, which have by now fully encircled the lower Dirac point. The Ramsey interference phase is then equal to the Berry phase of π. Special attention has to be paid that the symmetry between the two paths is only broken by the chirality of the Dirac points. For instance, spin-echo schemes might be necessary to compensate for fluctuating magnetic fields. Alternatively, instead of moving the atomic cloud, also the Dirac points could be moved around the atoms by dynamically changing the lattice beam intensities.

Detecting the Berry curvature based on the perpendicular real space displacement during Bloch oscillations

For the case of broken inversion symmetry, i. e. if the energies of A and B sites are unequal, the Berry curvature associated with the Berry phase spreads over a finite area in the vicinity of the massive Dirac points. This can be a more favorable situation to perform Bloch oscillations in order to probe the topology of one of the bands, since transfer to the second band is suppressed due to the band gap. According to the semiclassical equations of motion (see Section 5.1.1 on page 102), the Berry curvature is found to give rise to a displacement in the real space position perpendicular to the Bloch oscillation direction as the atoms pass through regions of non-zero Berry curvature [Price *et al.*, 2012]. This is equivalent to a Hall current. In the absence of an external confinement, this effect, however, cancels for a full Bloch oscillation along y, since the Berry curvature for the two points is exactly opposite, see Fig. 11.2, left panel. When stopping the oscillations already at $t = T_B/2$, the effect of one of the points should be detectable, but is most likely below the experimental resolution of an *in situ* position measurement. For sequential diagonal oscillations through one of the points on the other hand (right panel), the effect would amplify during the course of several Bloch oscillation periods. However, the situation is complicated by the presence of the harmonic confinement, which leads to a non-periodic movement in real space even without a Berry curvature. This makes an interpretation in terms of this simple picture difficult.

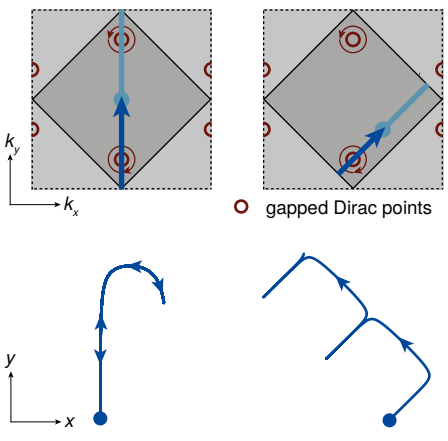

Figure 11.2: *Detecting the Berry curvature.* The semiclassical trajectory of the cloud oscillating through gapped (massive) Dirac points is affected by the Berry curvature, leading to a perpendicular displacement in the real space position (shown below the B.Z. in the figure). For oscillations along y (left panel) the effect is canceled by the opposite chirality of the Dirac points for a full Bloch oscillation period. For diagonal oscillations through one point, the effect accumulates over several oscillation periods (right). The chirality of the Dirac points is indicated by the circular arrows.

Signature of the Berry curvature in the quasimomentum distribution of a trapped system

Numerical time evolution of the trapped system has on the other hand shown that the trap might also be advantageous for the detection of the Berry curvature for oscillations through both Dirac points, see Fig. 11.3 on the next page. In the figure, the numerically calculated quasimomentum evolution of a fermionic atom cloud is shown over the course of two Bloch oscillation cycles for the case of mass-

less (top) and massive (bottom) Dirac points. For the case of the gapped Dirac points, the displacement in real space caused by the Berry curvature is converted into an asymmetry of the momentum space distribution along k_x. Even though the two Dirac points have opposite Berry curvature, their effect does not cancel anymore, owing to the presence of the trap (and possibly the finite transfer to the second band).

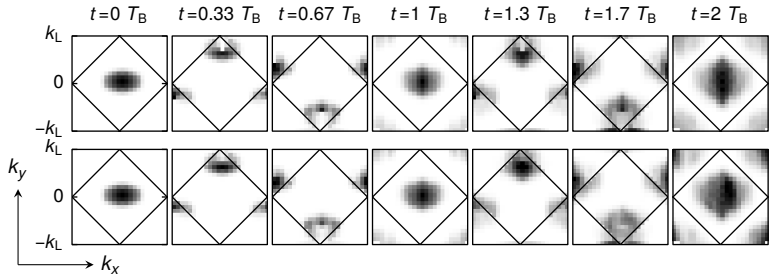

Figure 11.3: *Detecting the Berry curvature through Bloch oscillations in the presence of a trap.* Numerical simulation of Bloch oscillations of a trapped 2D system for $N = 20$ atoms using a force aligned with the positive k_y direction. The quasimomentum distributions during the course of two Bloch oscillation cycles are shown for the case of gapless (top) and gapped (bottom) Dirac points. In the gapless case, the Berry curvature is fully localized at the Dirac points, leading to no observable asymmetry during the Bloch oscillation. In the gapped case, the Berry curvature has as finite extent, leading to a perpendicular movement of the atoms traversing through the respective region in quasimomentum space. At $t = 2T_B$, a clear asymmetry along k_x is visible. Simulation parameters: $t_{1,2,3} = [t_0, t_0, 0]$, $\gamma_{x,y}/t_0 = [0.01, 0.01]$, $\Delta/t_0 = 0$ (top), $\Delta/t_0 = -0.4$ (bottom). $F\lambda/t_0 = 1$. Data courtesy Lei Wang, ETH Zurich.

The origin of the asymmetry in the momentum distribution in the Berry curvature is confirmed when inverting the chirality or the force in the numerical simulation, see Fig. 11.4 on the following page. In the top simulation, the direction of the force causing the Bloch oscillations is inverted. In this case, the asymmetry is the same since both the oscillation direction and the chirality of the Dirac point first seen by the oscillating cloud are inverted. If the force is unchanged but the chirality of the points is switched, the quasimomentum distribution becomes displaced in the other direction. In fact, we have experimentally observed this displacement when re-analyzing the momentum distributions recorded for the data presented in Fig. 6.2 on page 119: the center of mass of the distribution (as determined by a gaussian fit) is either slightly shifted to larger or smaller k_x depending on whether $\Delta > 0$ or < 0.

Stückelberg interferometry

Another effect that could be investigated in more depth using Bloch oscillations along y is the presence of Stückelberg interference [Stückelberg, 1932; Shevchenko *et al.*, 2010] as the two Dirac points are subsequently passed. As discussed in Section 6.2.3 on page 122, the absence of the characteristic Stückelberg oscillations in the transfer efficiency as a function of the dynamic phase difference between the paths in the 1st and 2nd band might be caused by the effectively different Bloch oscillation gradients in the trap. By making use of the deconfinement beams (see Section 3.3.3 on page 58) the effect of the trap can be weakened or even partially canceled, which could allow for the study of Stückelberg oscillations in our system. This might also open new possibilities for the characterization of the topological properties of the band structure, as explained below.

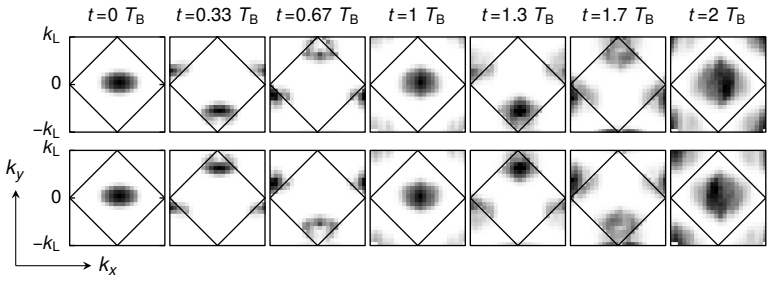

Figure 11.4: *Detecting the Berry curvature through Bloch oscillations: inverting the chirality and force.* Numerical simulation of Bloch oscillations of a trapped 2D system for $N = 20$ atoms using a force aligned with the negative (top) or positive (bottom) k_y direction. The quasimomentum distributions during the course of two Bloch oscillation cycles are shown for the case of gapped Dirac points with normal (top) and inverted (bottom) chirality. Simulation parameters: $t_{1,2,3} = [t_0, t_0, 0]$, $\gamma_{x,y}/t_0 = [0.01, 0.01]$, $\Delta/t_0 = -0.4$ (top), $\Delta/t_0 = 0.4$ (bottom). $F\lambda/t_0 = -1$ (top), $F\lambda/t_0 = 1$ (bottom). Data courtesy Lei Wang, ETH Zurich.

TOPOLOGICAL INSULATORS

Building upon the artificial graphene system studied in this thesis, simulations of topological insulators might be possible. Topological insulators are a fascinating new class of materials, characterized by an insulating bulk enclosed by topologically protected conducting edge channels, which allow for dissipationless current flow and are resilient upon variations of the system parameters [Hasan *et al.*, 2010]. The materials discovered so far showing this behavior can be classified into three categories:

Topological insulators are characterized by an insulating bulk enclosed by conducting edge channels.

- 2D materials (like MOSFETs, where the effect was discovered by Klitzing *et al.* [1980]), show, when applying a strong perpendicular magnetic field a quantized Hall conductance $\sigma_{xy} = \pm Ne^2/h$ (where $N \in \mathbb{N}$). This is called the (integer[1]) quantum Hall effect (QHE). It can be explained by the existence of chiral edge states, of which the direction of current is defined by the magnetic field direction and is independent of the electron spin. The bulk of the material is insulating due to the emerging band structure which contains discrete Landau levels. Apart from the topological properties, the energy level structure at very large magnetic field strengths (on the order of one flux quantum per unit cell, corresponding to thousands of Tesla) exhibits a fractal structure as a function of the magnetic field strength. This structure, named the Hofstadter butterfly, is caused by the splitting of the Bloch and Landau bands into several sub-bands. Signatures of this phenomenon, theoretically studied by Harper [1955] and Hofstadter [1976], have been observed in artificial superlattices. As a first step towards an observation in cold atoms systems, the respective Hamiltonians have recently been implemented using bosonic atoms loaded into specifically-tailored optical lattices [Aidelsburger *et al.*, 2013; Miyake *et al.*, 2013].

(Integer) quantum Hall effect

Hofstadter's butterfly

- In quantum spin Hall insulators (named after the quantum spin Hall effect (QSHE)), first experimentally investigated in HgTe/CdTe quantum wells [König *et al.*, 2007], edge channels are present even in the absence of an external magnetic field, owing to the large spin-orbit coupling of the material. As an additional consequence of the spin-orbit coupling, the current has an opposite direction for the two spin states. They are the first (and

Quantum spin Hall effect

1 Fractional topological insulators have also been proposed [Levin *et al.*, 2009]. They are expected to show similar features as the fractional quantum Hall effect (FQHE), which appears as a consequence of inter-particle interactions. These will, however, not be discussed here.

classical) type of topological insulators at zero magnetic field studied so far. Later, also 3D topological insulators were investigated theoretically [Fu *et al.*, 2007] and experimentally [Hsieh *et al.*, 2008]. In such systems, the edge states have a 2D band structure containing an odd number of Dirac points.

- The third category is that of systems exhibiting the quantum anomalous Hall effect (QAHE) (also called Chern insulators). They are essentially quantum spin Hall insulators with one of the spin channels suppressed, for example by magnetic ordering. Such systems therefore contain edge states with current flowing in only one direction like in the quantum Hall effect, but without applying an external magnetic field (and therefore also without Landau levels). This effect was only recently observed for the first time in experiments, in ferromagnetic $(Bi_{1-x}Sb_x)_2Te_3$ [Chang *et al.*, 2013]. The quantum anomalous Hall effect (QAHE) is not to be confused with what is called the unconventional or anomalous quantum Hall effect in graphene, which refers to its shifted Hall conductivity in a magnetic field $\sigma_{xy} = \pm 4(N + 1/2)e^2/h$ [Novoselov *et al.*, 2005], as compared to materials showing the normal QHE, where $\sigma_{xy} = \pm Ne^2/h$.

Quantum anomalous Hall effect

In all these systems, the appearance of the edge channels either relates to the broken time-reversal symmetry as a result of a magnetic field or to the spin-orbit coupling which gives rise to the opposite chirality of the two spin states (without breaking time-reversal symmetry). As the atoms used to mimic the electrons in our simulations of solids are neutral and unbound particles, they are as such not subject to a Lorentz force in a magnetic field and do not exhibit coupling of their momentum to their (pseudo-)spin. However, these effects can be modeled for example by using laser beams addressing Raman transitions or by time-dependent variations of the lattice potential. In this way spin-orbit coupling [Wang, Yu, *et al.*, 2012; Cheuk *et al.*, 2012] as well as abelian or non-abelian gauge fields [Dalibard *et al.*, 2011] can be emulated. An overview of the schemes to create such gauge fields by optical means and of the measurement techniques for the emerging topological states can be found in [Goldman, Juzeliūnas, *et al.*, 2013].

Implementing gauge fields for neutral atoms

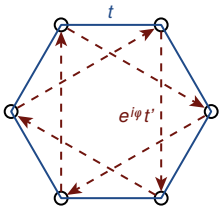

Figure 11.5: *Haldane model.* Introducing complex next-nearest-neighbor tunnelings $e^{i\varphi}t'$ in a honeycomb lattice leads to an effective "magnetic" flux through the plaquettes defined by the additional tunneling links within the unit cell. The total flux through the whole unit cell, however, sums up to zero, realizing a staggered flux lattice. The direction of the phase contributions is indicated by the arrows.

In view of realizing a topological insulator in our experiment, one possible route is the implementation of the Haldane model [1988]. It comprises a (locally time-reversal breaking) Hamiltonian that captures the essential physics of a quantum anomalous spin Hall insulator for spinless particles in a 2D lattice system with honeycomb geometry. Haldane concluded that "[the] particular model presented here is unlikely to be directly physically realizable, [...]", because of the difficulty of engineering the required staggered magnetic fluxes. Surprisingly, the model can actually be realized in our experimental setup with only a few modifications. Besides the normal honeycomb structure, the key ingredient to this Hamiltonian are next-nearest-neighbor tunnel couplings t' with a complex phase $e^{i\varphi}$, see Fig. 11.5. As a particle moves around the plaquettes defined by the complex tunneling links, it acquires a non-zero phase (modulo 2π) reminiscent of the Peierls phase in a magnetic field. As the nearest-neighbor tunneling links remain real, the total phase pickup when encircling the whole hexagon, however, remains zero. This tunneling arrangement thus realizes what is called a staggered flux lattice, i. e. the

Haldane model

emulated "magnetic" flux is non-zero in certain regions of the unit cell, but zero when considering the whole unit cell or even the whole lattice. The staggered flux leads to a gap opening at the Dirac points and induces chiral edge currents.

Possibilities to create complex tunnel couplings in our experiment include [Lebrat, 2013]:

Techniques to obtain complex tunneling amplitudes in our experiment

- Amplitude modulation of the different lattice laser beam intensities, such that the tunneling along the honeycomb bonds alternates periodically in time in a circular manner [Kitagawa *et al.*, 2010]. The circular modulation requires both a modulation of the intensities of the forward and back-reflected laser beams. While the AOMs used for intensity regulation can be employed for the former, the latter can be achieved by placing amplitude-modulation EOMs in front of the retro-reflection mirrors.
- A circular movement of the whole lattice potential by phase modulation of the retro-reflected lattice beams, which can be either obtained using phase-modulating EOMs or by mounting the retro-reflecting mirrors onto piezo stages. A phase modulation along two axes with the same frequency but a phase difference of $\frac{\pi}{2}$ leads to a circular movement of the lattice structure.
- Instead of moving the lattice potential, a circular movement of the atoms can be induced by a rotating magnetic field gradient or the combination of an alternating magnetic field gradient with a phase modulation of a perpendicular lattice beam.

The latter two methods are reminiscent of the proposal by Oka and Aoki [2009] for observing a Hall current in graphene when illuminating the material with high-intensity circularly polarized light. The time-dependent Hamiltonians created using the techniques outlined above can be mapped into time-independent Hamiltonians with complex next-nearest-neighbor tunnelings using Floquet theory [Lebrat, 2013]. Additionally, when using a spin mixture instead of a spin-polarized gas, the combination of modulated magnetic field gradients with phase modulation of the lattice allows for the realization of a related model exhibiting the QSHE,

Kane-Mele model

the Kane-Mele model [2005]. This model consists of two copies of the Haldane model associated with the two spin states and therefore does not break time reversal symmetry. Owing to the Zeeman effect, the modulated magnetic field gradient exerts different forces onto the two Zeeman states, allowing for the realization of a Hamiltonian with opposite chirality for the two states.

With respect to the original Hamiltonian, the next-nearest-neighbor tunneling in the Haldane model leads to an additional diagonal mass term with equal sign for the two spinor components. Therefore, in the bulk, gaps will open at the two Dirac points. In contrast to a gap opening related to a mass induced by a sublattice energy offset (leading to a Semenoff insulator [1984]), the gapped Dirac points in the Haldane insulator have the same chirality and therefore have both either a positive or negative Berry phase and curvature. Thus the system has also a non-zero Chern number (± 1), hence the name Chern insulator. If we now add masses with opposite signs by inversion symmetry breaking, one of the Dirac points will be re-closed while the other opens further. Exactly at the parameters where one of the points closes, the system assumes a special semimetallic state which is topological, due to the non-zero Chern number – a situation yet to be observed in real materials. Moreover, at this point the band structure has the same topology as that of the edge channels in a 3D topological insulator.

Detecting a non-zero Chern number

The detection of the non-zero Chern number and/or Berry curvatures might be possible with the methods described at the beginning of this chapter for the system with zero Chern number. The signals are expected to be generally larger since for example the effects of the Berry curvature do not compensate (but add up) when passing the two Dirac points. A detection of the topological order using TOF [Alba *et al.*, 2011; Wang *et al.*, 2013] and by Stückelberg oscillations [Lim

et al., 2014] (see Section 6.2.3 on page 122) has also been proposed. The latter scheme has recently been experimentally realized with trapped ions [Zhang *et al.*, 2014]. For a direct detection of the chiral edge channels, methods to select certain edge states and image them in a background-free manner using Bragg spectroscopy or by dynamical reshaping of the trapping potential have been proposed [Goldman *et al.*, 2012; Goldman, Dalibard, *et al.*, 2013].

INTERACTIONS IN ARTIFICIAL GRAPHENE

Ionic Hubbard model

Turning to interacting systems, ionic Hubbard models [Egami *et al.*, 1993] can be realized on the honeycomb lattice by use of an A-B on-site energy imbalance Δ. In this model, a transition from a Mott insulator to a band insulator with staggered density is expected when increasing Δ, see Fig. 11.6. However, the nature of the transition between the two states and of possible bond-ordered intermediate states is yet to be clarified [Batista *et al.*, 2004; Hoang, 2010]. When doping the ionic Hubbard model away from half-filling, superconducting states are expected [Watanabe *et al.*, 2013].

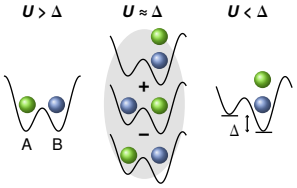

Figure 11.6: *The ionic Hubbard model in 1D.* When increasing the on-site energy imbalance Δ between the A and B sites, a transition from a Mott-insulating to a CDW ordered insulating state occurs. In the regime where $U \approx \Delta$, a bond-ordered state has been predicted.

In our system, the transition between the two states can be characterized by an increasing double occupancy. Additionally, the excitation spectrum of the system changes qualitatively as compared to the situation with $\Delta = 0$. In preliminary measurements, we have observed additional excitations at modulation frequencies corresponding to the energies $U - \Delta$ and $U + \Delta$, see Fig. 11.7.

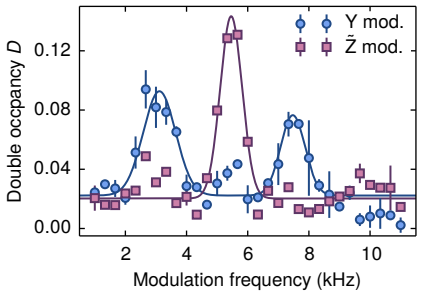

Figure 11.7: *Excitation spectra of an ionic Hubbard model system.* For an arrangement of coupled ionic honeycomb planes (with A-B site energy offset Δ) in-plane lattice amplitude modulation (blue circles) shows excitations with energy $U - \Delta$ and $U + \Delta$. The out-of-plane excitations (purple squares) on the other hand have an energy U, since the A-A type stacking couples sites with the same energy along this direction. Hubbard parameters: $U/h \approx 5.5\,\text{kHz}$ and $\Delta/h \approx 2\,\text{kHz}$.

Long-range quantum magnetism

To advance further into the regime of quantum magnetism, the entropy redistribution scheme presented in Section 9.1 on page 164 could be extended to two dimensions. In combination with global entropy isolation or redistribution schemes the observation of longer-range correlations might be achieved. Possible experimental implementations include the creation of low entropy regions in the trap center using a dimerized lattice, followed by an isolation or removal of the high-entropy regions in the outer region of the trap using a Laguerre-gaussian laser beam [Greif, 2013]. An alternative approach is the creation of a low-temperature state by reducing the confinement using the installed deconfinement laser beams. Here, an additional dimple beam could be used to maintain half-filling in the central region of the trap [Greif, 2013]. Reaching lower temperatures might allow for the observation of antiferromagnetic spin ordering, for example by using noise

correlation measurements (see Chapter 10 on page 181), or shed light on the disputed spin liquid phase [Meng *et al.*, 2010; Sorella *et al.*, 2012; Assaad *et al.*, 2013] in the honeycomb lattice. Alternatively, using the dynamic tunability of the optical lattice, an antiferromagnetically ordered state could be artificially prepared by loading a band insulator into the checkerboard configuration and subsequently dimerizing the lattice [Lubasch *et al.*, 2011].

OTHER LATTICE GEOMETRIES

Triangular, spin ladder and zig-zag chain geometries

Addressing other lattice configurations which can be produced using the tunable optical lattice, the physics of triangular geometries could be studied. Magnetic frustration occurring in the triangular lattice might favor a spin liquid state [Balents, 2010]. In systems of decoupled dimers in the $x-y$ plane, spin ladders can be created by allowing for a coupling along the z direction. Alternatively, zig-zag chains can be obtained by imbalancing the intensities of the retro-reflected with respect to the incoming lattice beams, using a technique similar to that discussed above. Despite the fact that both systems are nearly 1D, the spin configuration is predicted to be still strongly influenced by the remaining coupling along the other spatial dimensions [Greif, 2013]. They thus provide a fruitful ground for the study of exotic spin physics.

Adding additional lattice beams

Adding a second interfering lattice laser beam on the y axis would allow for the detection of spin correlations along that direction. In combination with the existing beams, the spin correlations in a 2D plane, which might emerge by using an extended entropy redistribution scheme, can be fully characterized. By an additional overlapping optical lattice with half the wavelength of the one used presently, *kagome* lattices can be realized, allowing for the study of the emerging physics in flat bands [Green *et al.*, 2010; Balents, 2010]. Lasers to create such a lattice are already in use in our experiment. However, a custom phase stabilization scheme for the two lattice lasers running at $\lambda = 1064\,\mathrm{nm}$ and $\lambda' = \lambda/2 = 532\,\mathrm{nm}$, respectively, will be necessary to avoid drifts of the two lattice potentials with respect to each other.

BIBLIOGRAPHY

Abanin, D. A., T. Kitagawa, I. Bloch, and E. Demler, *Interferometric approach to measuring band topology in 2D optical lattices*, Phys. Rev. Lett. **110**, 165304 (2013), DOI:10.1103/PhysRevLett.110.165304 (cit. on pp. 94, 193).

Adams, C. S. and E. Riis, *Laser cooling and trapping of neutral atoms*, Prog. Quant. Electr. **21**, 1 (1997), DOI:10.1016/S0079-6727(96)00006-7 (cit. on p. 22).

Aidelsburger, M., M. Atala, M. Lohse, J. T. Barreiro, B. Paredes, and I. Bloch, *Realization of the Hofstadter Hamiltonian with ultracold atoms in optical lattices*, Phys. Rev. Lett. **111**, 185301 (2013), DOI:10.1103/PhysRevLett.111.185301 (cit. on p. 196).

Aikawa, K., A. Frisch, M. Mark, S. Baier, R. Grimm, and F. Ferlaino, *Reaching Fermi degeneracy via universal dipolar scattering*, Phys. Rev. Lett. **112**, 010404 (2014), DOI:10.1103/PhysRevLett.112.010404 (cit. on p. 19).

Alba, E., X. Fernandez-Gonzalvo, J. Mur-Petit, J. K. Pachos, and J. J. Garcia-Ripoll, *Seeing topological order in time-of-flight measurements*, Phys. Rev. Lett. **107**, 235301 (2011), DOI:10.1103/PhysRevLett.107.235301 (cit. on pp. 94, 198).

Altman, E., E. Demler, and M. D. Lukin, *Probing many-body states of ultracold atoms via noise correlations*, Phys. Rev. A **70**, 013603 (2004), DOI:10.1103/PhysRevA.70.013603 (cit. on pp. 15, 181, 184).

Anderson, B. P. and M. A. Kasevich, *Macroscopic quantum interference from atomic tunnel arrays*, Science **282**, 1686 (1998), DOI:10.1126/science.282.5394.1686 (cit. on p. 98).

Anderson, M. H., J. R. Ensher, M. R. Matthews, C. E. Wieman, and E. A. Cornell, *Observation of Bose-Einstein condensation in a dilute atomic vapor*, Science **269**, 198 (1995), DOI:10.1126/science.269.5221.198 (cit. on pp. 12, 22).

Anderson, P. W., P. A. Lee, M. Randeria, T. M. Rice, N. Trivedi, and F. C. Zhang, *The physics behind high-temperature superconducting cuprates: the plain vanilla version of RVB*, J. Phys.: Condens. Matter **16**, R755 (2004), DOI:10.1088/0953-8984/16/24/R02 (cit. on p. 163).

Arimondo, E., M. Inguscio, and P. Violino, *Experimental determinations of the hyperfine structure in the alkali atoms*, Rev. Mod. Phys. **49**, 31 (1977), DOI:10.1103/RevModPhys.49.31 (cit. on p. 35).

Asano, K. and C. Hotta, *Designing Dirac points in two-dimensional lattices*, Phys. Rev. B **83**, 245125 (2011), DOI:10.1103/PhysRevB.83.245125 (cit. on p. 120).

Ashcroft, N. W. and N. D. Mermin, *Solid State Physics* (Saunders College Publishing, Philadelphia, PA, 1976) (cit. on pp. 76, 98, 100).

Aspuru-Guzik, A. and P. Walther, *Photonic quantum simulators*, Nat. Phys. **8**, 285 (2012), DOI:10.1038/nphys2253 (cit. on p. 18).

Assaad, F. F. and I. F. Herbut, *Pinning the order: The nature of quantum criticality in the Hubbard model on honeycomb lattice*, Phys. Rev. X **3**, 031010 (2013), DOI:10.1103/PhysRevX.3.031010 (cit. on pp. 15, 127, 140, 162, 200).

Atala, M., M. Aidelsburger, J. T. Barreiro, D. Abanin, T. Kitagawa, E. Demler, and I. Bloch, *Direct measurement of the Zak phase in topological Bloch bands*, Nat. Phys. **9**, 795 (2013), DOI:10.1038/nphys2790 (cit. on pp. 94, 127, 194).

Auerbach, A., *Interacting electrons and quantum magnetism* (Springer, 1994), DOI:10.1007/978-1-4612-0869-3 (cit. on pp. 138, 163).

Bakr, W. S., A. Peng, M. E. Tai, R. Ma, J. Simon, J. I. Gillen, S. Fölling, L. Pollet, and M. Greiner, *Probing the superfluid–to–Mott insulator transition at the single-atom level*, Science **329**, 547 (2010), DOI:10.1126/science.1192368 (cit. on pp. 30, 132, 146, 156).

Balents, L., *Spin liquids in frustrated magnets*, Nature (London) **464**, 199 (2010), DOI:10.1038/nature08917 (cit. on pp. 127, 140, 163, 200).

Bartenstein, M., A. Altmeyer, S. Riedl, S. Jochim, C. Chin, J. H. Denschlag, and R. Grimm, *Crossover from a molecular Bose-Einstein condensate to a degenerate Fermi*

gas, Phys. Rev. Lett. **92**, 120401 (2004), DOI:10.1103/PhysRevLett.92.120401 (cit. on p. 28).

Batista, C. D. and A. A. Aligia, *Exact bond ordered ground state for the transition between the band and the Mott insulator*, Phys. Rev. Lett. **92**, 246405 (2004), DOI:10.1103/PhysRevLett.92.246405 (cit. on p. 199).

Battesti, R., P. Cladé, S. Guellati-Khélifa, C. Schwob, B. Grémaud, F. Nez, L. Julien, and F. Biraben, *Bloch oscillations of ultracold atoms: A tool for a metrological determination of h/m_{Rb}*, Phys. Rev. Lett. **92**, 253001 (2004), DOI:10.1103/PhysRevLett.92.253001 (cit. on p. 98).

Becker, C., P. Soltan-Panahi, J. Kronjäger, S. Dörscher, K. Bongs, and K. Sengstock, *Ultracold quantum gases in triangular optical lattices*, New J. Phys. **12**, 065025 (2010), DOI:10.1088/1367-2630/12/6/065025 (cit. on p. 45).

Bellec, M., U. Kuhl, G. Montambaux, and F. Mortessagne, *Topological transition of Dirac points in a microwave experiment*, Phys. Rev. Lett. **110**, 033902 (2013), DOI:10.1103/PhysRevLett.110.033902 (cit. on p. 123).

Ben Dahan, M., E. Peik, J. Reichel, Y. Castin, and C. Salomon, *Bloch oscillations of atoms in an optical potential*, Phys. Rev. Lett. **76**, 4508 (1996), DOI:10.1103/PhysRevLett.76.4508 (cit. on pp. 98, 109, 110).

Bernier, J.-S., C. Kollath, A. Georges, L. De Leo, F. Gerbier, C. Salomon, and M. Köhl, *Cooling fermionic atoms in optical lattices by shaping the confinement*, Phys. Rev. A **79**, 061601 (2009), DOI:10.1103/PhysRevA.79.061601 (cit. on p. 164).

Berry, M. V., *Quantal phase factors accompanying adiabatic changes*, Proc. R. Soc. Lond. A **392**, 45 (1984), DOI:10.1098/rspa.1984.0023 (cit. on pp. 86, 92).

Berry, M. V. and M. Wilkinson, *Diabolical points in the spectra of triangles*, Proc. R. Soc. Lond. A **392**, 15 (1984), DOI:10.1098/rspa.1984.0022 (cit. on p. 86).

Birkl, G., M. Gatzke, I. H. Deutsch, S. L. Rolston, and W. D. Phillips, *Bragg scattering from atoms in optical lattices*, Phys. Rev. Lett. **75**, 2823 (1995), DOI:10.1103/PhysRevLett.75.2823 (cit. on pp. 23, 30).

Bissbort, U., *Dynamical effects and disorder in ultracold bosonic matter*, PhD thesis (Johann Wolfgang Goethe-Universität, Frankfurt am Main, 2012) (cit. on p. 82).

Blanch, G., *Mathieu Functions*, in *Handbook of Mathematical Functions with Formulas, Graphs, and Mathematical Tables*, edited by M. Abramowitz and I. A. Stegun (Dover Publications, New York, 1972) Chap. 20 (cit. on p. 76).

Blatt, R. and C. F. Roos, *Quantum simulations with trapped ions*, Nat. Phys. **8**, 277 (2012), DOI:10.1038/nphys2252 (cit. on p. 18).

Bloch, F., *Über die Quantenmechanik der Elektronen in Kristallgittern*, Z. Phys. **52**, 555 (1929), DOI:10.1007/BF01339455 (cit. on pp. 71, 97, 98).

Bloch, I., J. Dalibard, and S. Nascimbène, *Quantum simulations with ultracold quantum gases*, Nat. Phys. **8**, 267 (2012), DOI:10.1038/nphys2259 (cit. on p. 18).

Bloch, I., J. Dalibard, and W. Zwerger, *Many-body physics with ultracold gases*, Rev. Mod. Phys. **80**, 885 (2008), DOI:10.1103/RevModPhys.80.885 (cit. on pp. 12, 182).

Bourdel, T., L. Khaykovich, J. Cubizolles, J. Zhang, F. Chevy, M. Teichmann, L. Tarruell, S. J. J. M. F. Kokkelmans, and C. Salomon, *Experimental study of the BEC-BCS crossover region in lithium 6*, Phys. Rev. Lett. **93**, 050401 (2004), DOI:10.1103/PhysRevLett.93.050401 (cit. on p. 28).

Breid, B. M., D. Witthaut, and H. J. Korsch, *Bloch–Zener oscillations*, New J. Phys. **8**, 110 (2006), DOI:10.1088/1367-2630/8/7/110 (cit. on pp. 97, 98, 102).

Breid, B. M., D. Witthaut, and H. J. Korsch, *Manipulation of matter waves using Bloch and Bloch–Zener oscillations*, New J. Phys. **9**, 62 (2007), DOI:10.1088/1367-2630/9/3/062 (cit. on p. 98).

Brinkman, W. F. and T. M. Rice, *Single-particle excitations in magnetic insulators*, Phys. Rev. B **2**, 1324 (1970), DOI:10.1103/PhysRevB.2.1324 (cit. on p. 155).

Bruun, G. M., O. F. Syljuåsen, K. G. L. Pedersen, B. M. Andersen, E. Demler, and A. S. Sørensen, *Antiferromagnetic noise correlations in optical lattices*, Phys. Rev. A **80**, 033622 (2009), DOI:10.1103/PhysRevA.80.033622 (cit. on pp. 181, 192).

Busch, T., B.-G. Englert, K. Rzażewski, and M. Wilkens, *Two cold atoms in a harmonic trap*, Found. Phys. **28**, 549 (1998), DOI:10.1023/A:1018705520999 (cit. on p. 29).

Cahn, S. B., A. Kumarakrishnan, U. Shim, T. Sleator, P. R. Berman, and B. Dubetsky, *Time-domain de Broglie wave interferometry*, Phys. Rev. Lett. **79**, 784 (1997), DOI:10.1103/PhysRevLett.79.784 (cit. on p. 50).

Castin, Y., *Basic theory tools for degenerate Fermi gases*, in Proceedings of the International School of Physics "Enrico Fermi", Vol. 164: Ultra-cold Fermi Gases, edited by M. Inguscio, W. Ketterle, and C. Salomon, Varenna Summer School Enrico Fermi (IOS Press, Amsterdam, 2006), DOI:10.3254/978-1-58603-846-5-289 (cit. on pp. 13, 27, 28).

Castro Neto, A. H., F. Guinea, N. M. R. Peres, K. S. Novoselov, and A. K. Geim, *The electronic properties of graphene*, Rev. Mod. Phys. **81**, 109 (2009), DOI:10.1103/RevModPhys.81.109 (cit. on pp. 87, 89–92, 95, 141).

Chang, C.-Z. *et al.*, *Experimental observation of the quantum anomalous Hall effect in a magnetic topological insulator*, Science **340**, 167 (2013), DOI:10.1126/science.1234414 (cit. on p. 197).

Cherng, R. W. and E. Demler, *Quantum noise analysis of spin systems realized with cold atoms*, New J. Phys. **9**, 7 (2007), DOI:10.1088/1367-2630/9/1/007 (cit. on p. 181).

Cheuk, L. W., A. T. Sommer, Z. Hadzibabic, T. Yefsah, W. S. Bakr, and M. W. Zwierlein, *Spin-injection spectroscopy of a spin-orbit coupled Fermi gas*, Phys. Rev. Lett. **109**, 095302 (2012), DOI:10.1103/PhysRevLett.109.095302 (cit. on p. 197).

Chin, C., R. Grimm, P. Julienne, and E. Tiesinga, *Feshbach resonances in ultracold gases*, Rev. Mod. Phys. **82**, 1225 (2010), DOI:10.1103/RevModPhys.82.1225 (cit. on pp. 13, 28).

Cladé, P., E. de Mirandes, M. Cadoret, S. Guellati-Khélifa, C. Schwob, F. Nez, L. Julien, and F. Biraben, *Determination of the fine structure constant based on Bloch oscillations of ultracold atoms in a vertical optical lattice*, Phys. Rev. Lett. **96**, 033001 (2006), DOI:10.1103/PhysRevLett.96.033001 (cit. on p. 98).

Cohen-Tannoudji, C., J. Dupont-Roc, and G. Grynberg, *Atom – Photon Interactions: Basic Process and Applications* (Wiley-VCH Verlag GmbH, 2008), DOI:10.1002/9783527617197 (cit. on p. 12).

Cosens, C. R., *A balance-detector for alternating-current bridges*, Proc. Phys. Soc. **46**, 818 (1934), DOI:10.1088/0959-5309/46/6/310 (cit. on p. 50).

Cristiani, M., O. Morsch, J. H. Müller, D. Ciampini, and E. Arimondo, *Experimental properties of Bose-Einstein condensates in one-dimensional optical lattices: Bloch oscillations, Landau-Zener tunneling, and mean-field effects*, Phys. Rev. A **65**, 063612 (2002), DOI:10.1103/PhysRevA.65.063612 (cit. on p. 98).

Daley, A. J., C. Kollath, U. Schollwöck, and G. Vidal, *Time-dependent density-matrix renormalization-group using adaptive effective Hilbert spaces*, J. Stat. Mech. **2004**, P04005 (2004), DOI:10.1088/1742-5468/2004/04/P04005 (cit. on p. 142).

Dalibard, J. and C. Cohen-Tannoudji, *Dressed-atom approach to atomic motion in laser light: the dipole force revisited*, J. Opt. Soc. Am. B **2**, 1707 (1985), DOI:10.1364/JOSAB.2.001707 (cit. on p. 23).

Dalibard, J. and C. Cohen-Tannoudji, *Laser cooling below the Doppler limit by polarization gradients: simple theoretical models*, J. Opt. Soc. Am. B **6**, 2023 (1989), DOI:10.1364/JOSAB.6.002023 (cit. on p. 22).

Dalibard, J., F. Gerbier, G. Juzeliūnas, and P. Öhberg, *Colloquium: Artificial gauge potentials for neutral atoms*, Rev. Mod. Phys. **83**, 1523 (2011), DOI:10.1103/RevModPhys.83.1523 (cit. on pp. 15, 197).

Davis, K. B., M.-O. Mewes, M. R. Andrews, N. J. van Druten, D. S. Durfee, D. M. Kurn, and W. Ketterle, *Bose-Einstein condensation in a gas of sodium atoms*, Phys. Rev. Lett. **75**, 3969 (1995), DOI:10.1103/PhysRevLett.75.3969 (cit. on pp. 12, 22).

DeMarco, B. and D. S. Jin, *Onset of Fermi degeneracy in a trapped atomic gas*, Science **285**, 1703 (1999), DOI:10.1126/science.285.5434.1703 (cit. on pp. 12, 18).

DeMarco, B., *Quantum behavior of an atomic Fermi gas*, PhD thesis (University of Colorado, 2001) (cit. on p. 66).

Derevianko, A. and H. Katori, *Colloquium: Physics of optical lattice clocks*, Rev. Mod. Phys. **83**, 331 (2011), DOI:10.1103/RevModPhys.83.331 (cit. on p. 12).

DeSalvo, B. J., M. Yan, P. G. Mickelson, Y. N. Martinez de Escobar, and T. C. Killian, *Degenerate Fermi gas of ^{87}Sr*, Phys. Rev. Lett. **105**, 030402 (2010), DOI:10.1103/PhysRevLett.105.030402 (cit. on p. 19).

Diener, R. B. and T.-L. Ho, *The condition for universality at resonance and direct measurement of pair wavefunctions using rf spectroscopy*, ArXiv e-prints (2004), arXiv: cond-mat/0405174 (cit. on p. 27).

Diener, R. B. and T. Ho, *Fermions in optical lattices swept across Feshbach resonances*, Phys. Rev. Lett. **96**, 010402 (2006), DOI:10.1103/PhysRevLett.96.010402 (cit. on p. 133).

Diep, H. T., G. Misguich, and C. Lhuillier, *Two-dimensional quantum antiferromagnets*, in *Frustrated spin systems* (World Scientific, 2005), pp. 229–306 (cit. on p. 164).

Dreisow, F., A. Szameit, M. Heinrich, T. Pertsch, S. Nolte, A. Tünnermann, and S. Longhi, *Bloch-Zener oscillations in binary superlattices*, Phys. Rev. Lett. **102**, 076802 (2009), DOI:10.1103/PhysRevLett.102.076802 (cit. on p. 98).

Duchon, E., Y. L. Loh, and N. Trivedi, in *Novel superfluids*, Vol. 2, edited by K.-H. Bennemann and J. B. Ketterson (Oxford University Press, Nov. 2013) Chap. Optical Lattice Emulators: Bose and Fermi Hubbard Models, arXiv: 1311.0543 [cond-mat.quant-gas] (cit. on p. 142).

Egami, T., S. Ishihara, and M. Tachiki, *Lattice effect of strong electron correlation: Implication for ferroelectricity and superconductivity*, Science **261**, 1307 (1993), DOI:10.1126/science.261.5126.1307 (cit. on pp. 15, 132, 199).

Esaki, L. and R. Tsu, *Superlattice and negative differential conductivity in semiconductors*, IBM J. Res. Dev. **14**, 61 (1970), DOI:10.1147/rd.141.0061 (cit. on p. 73).

Esslinger, T., *Fermi-Hubbard physics with atoms in an optical lattice*, Annu. Rev. Cond. Mat. Phys. **1**, 129 (2010), DOI:10.1146/annurev-conmatphys-070909-104059 (cit. on pp. 107, 168).

Esslinger, T., I. Bloch, and T. W. Hänsch, *Bose-Einstein condensation in a quadrupole-Ioffe-configuration trap*, Phys. Rev. A **58**, R2664 (1998), DOI:10.1103/PhysRevA.58.R2664 (cit. on p. 39).

Estève, J., J.-B. Trebbia, T. Schumm, A. Aspect, C. I. Westbrook, and I. Bouchoule, *Observations of density fluctuations in an elongated Bose gas: Ideal gas and quasicondensate regimes*, Phys. Rev. Lett. **96**, 130403 (2006), DOI:10.1103/PhysRevLett.96.130403 (cit. on p. 181).

Fano, U., *Quantum theory of interference effects in the mixing of light from phase-independent sources*, Am. J. Phys. **29**, 539 (1961), DOI:10.1119/1.1937827 (cit. on p. 182).

Fattori, M., C. D'Errico, G. Roati, M. Zaccanti, M. Jona-Lasinio, M. Modugno, M. Inguscio, and G. Modugno, *Atom interferometry with a weakly interacting Bose-Einstein condensate*, Phys. Rev. Lett. **100**, 080405 (2008), DOI:10.1103/PhysRevLett.100.080405 (cit. on p. 98).

Fedichev, P. O., Y. Kagan, G. V. Shlyapnikov, and J. T. M. Walraven, *Influence of nearly resonant light on the scattering length in low-temperature atomic gases*, Phys. Rev. Lett. **77**, 2913 (1996), DOI:10.1103/PhysRevLett.77.2913 (cit. on p. 28).

Feldmann, J., K. Leo, J. Shah, D. A. B. Miller, J. E. Cunningham, T. Meier, G. von Plessen, A. Schulze, P. Thomas, and S. Schmitt-Rink, *Optical investigation of Bloch oscillations in a semiconductor superlattice*, Phys. Rev. B **46**, 7252 (1992), DOI:10.1103/PhysRevB.46.7252 (cit. on p. 98).

Ferlaino, F., D'Errico, G. Roati, M. Zaccanti, M. Inguscio, G. Modugno, and A. Simoni, *Feshbach spectroscopy of a K-Rb atomic mixture*, Phys. Rev. A **73**, 040702 (2006a), DOI:10.1103/PhysRevA.73.040702 (cit. on p. 35).

Ferlaino, F., D'Errico, G. Roati, M. Zaccanti, M. Inguscio, G. Modugno, and A. Simoni, *Erratum: Feshbach spectroscopy of a K-Rb atomic mixture [Phys. Rev. A73, 040702 (2006)]*, Phys. Rev. A **74**, 039903 (2006b), DOI:10.1103/PhysRevA.74.039903 (cit. on p. 35).

Ferrari, G., N. Poli, F. Sorrentino, and G. M. Tino, *Long-lived Bloch oscillations with bosonic Sr atoms and application to gravity measurement at the micrometer scale*, Phys. Rev. Lett. **97**, 060402 (2006), DOI:10.1103/PhysRevLett.97.060402 (cit. on p. 98).

Feshbach, H., *Unified theory of nuclear reactions*, Ann. Phys. **5**, 357 (1958), DOI:10.1016/0003-4916(58)90007-1 (cit. on p. 27).

Feynman, R. P., *Simulating physics with computers*, Int. J. Theor. Phys. **21**, 467 (1982), DOI:10.1007/BF02650179 (cit. on pp. 12, 17).

Feynman, R. P., *Quantum mechanical computers*, Found. Physics **16**, 507 (1986), DOI:10.1007/BF01886518 (cit. on pp. 12, 17).

Fölling, S., *Probing strongly correlated states of ultracold atoms in optical lattices*, PhD thesis (Johannes Gutenberg-Universität Mainz, 2008) (cit. on pp. 77, 182, 184, 185, 187).

Fölling, S., *Quantum noise correlation experiments with ultracold atoms*, ArXiv e-prints (2014), arXiv:1403.6842 [cond-mat.quant-gas] (cit. on p. 182).

Fölling, S., S. Trotzky, P. Cheinet, M. Feld, R. Saers, A. Widera, T. Müller, and I. Bloch, *Direct observation of second-order atom tunnelling*, Nature (London) **448**, 1029 (2007), DOI:10.1038/nature06112 (cit. on p. 45).

Fölling, S., F. Gerbier, A. Widera, O. Mandel, T. Gericke, and I. Bloch, *Spatial quantum noise interferometry in expanding ultracold atom clouds*, Nature (London) **434**, 481 (2005), DOI:10.1038/nature03500 (cit. on pp. 181, 182).

Freilich, D. V., D. M. Bianchi, A. M. Kaufman, T. K. Langin, and D. S. Hall, *Real-time dynamics of single vortex lines and vortex dipoles in a Bose-Einstein condensate*, Science **329**, 1182 (2010), DOI:10.1126/science.1191224 (cit. on p. 31).

Freimund, D. L. and H. Batelaan, *Bragg scattering of free electrons using the Kapitza-Dirac effect*, Phys. Rev. Lett. **89**, 283602 (2002), DOI:10.1103/PhysRevLett.89.283602 (cit. on p. 50).

Fu, L., C. L. Kane, and E. J. Mele, *Topological insulators in three dimensions*, Phys. Rev. Lett. **98**, 106803 (2007), DOI:10.1103/PhysRevLett.98.106803 (cit. on p. 197).

Fuchs, J. N., F. Piéchon, M. O. Goerbig, and G. Montambaux, *Topological Berry phase and semiclassical quantization of cyclotron orbits for two dimensional electrons in coupled band models*, Eur. Phys. J. B **77**, 351 (2010), DOI:10.1140/epjb/e2010-00259-2 (cit. on p. 94).

Fuchs, J.-N., L.-K. Lim, and G. Montambaux, *Interband tunneling near the merging transition of Dirac cones*, Phys. Rev. A **86**, 063613 (2012), DOI:10.1103/PhysRevA.86.063613 (cit. on p. 92).

Fuchs, S., E. Gull, L. Pollet, E. Burovski, E. Kozik, T. Pruschke, and M. Troyer, *Thermodynamics of the 3D Hubbard model on approaching the Néel transition*, Phys. Rev. Lett. **106**, 030401 (2011), DOI:10.1103/PhysRevLett.106.030401 (cit. on p. 169).

Fukuhara, T., Y. Takasu, M. Kumakura, and Y. Takahashi, *Degenerate Fermi gases of ytterbium*, Phys. Rev. Lett. **98**, 030401 (2007), DOI:10.1103/PhysRevLett.98.030401 (cit. on p. 19).

Fukuyama, H., R. A. Bari, and H. C. Fogedby, *Tightly bound electrons in a uniform electric field*, Phys. Rev. B **8**, 5579 (1973), DOI:10.1103/PhysRevB.8.5579 (cit. on p. 98).

Gaebler, J. P., J. T. Stewart, T. E. Drake, D. S. Jin, A. Perali, P. Pieri, and G. C. Strinati, *Observation of pseudogap behaviour in a strongly interacting Fermi gas*, Nat. Phys. **6**, 569 (2010), DOI:10.1038/nphys1709 (cit. on p. 29).

Gao, B., *Quantum-defect theory of atomic collisions and molecular vibration spectra*, Phys. Rev. A **58**, 4222 (1998), DOI:10.1103/PhysRevA.58.4222 (cit. on p. 27).

Gasparinetti, S., P. Solinas, and J. P. Pekola, *Geometric Landau-Zener interferometry*, Phys. Rev. Lett. **107**, 207002 (2011), DOI:10.1103/PhysRevLett.107.207002 (cit. on p. 122).

Georges, A., *Condensed Matter Physics With Light And Atoms: Strongly Correlated Cold Fermions in Optical Lattices*, in Proceedings of the International School of Physics "Enrico Fermi", Vol. 164: Ultra-cold Fermi gases, edited by M. Inguscio, W. Ketterle, and C. Salomon, Varenna Summer School Enrico Fermi (IOS Press, Amsterdam, 2007), DOI:10.3254/978-1-58603-846-5-477 (cit. on p. 133).

Georgescu, I. M., S. Ashhab, and F. Nori, *Quantum simulation*, Rev. Mod. Phys. **86**, 153 (2014), DOI:10.1103/RevModPhys.86.153 (cit. on pp. 12, 17).

Gericke, T., F. Gerbier, A. Widera, S. Fölling, O. Mandel, and I. Bloch, *Adiabatic loading of a Bose-Einstein condensate in a 3D optical lattice*, J. Mod. Opt. **54**, 735 (2007), DOI:10.1080/09500340600777730 (cit. on p. 156).

Gerritsma, R., G. Kirchmair, F. Zahringer, E. Solano, R. Blatt, and C. F. Roos, *Quantum simulation of the Dirac equation*, Nature (London) **463**, 68 (2010), DOI:10.1038/nature08688 (cit. on p. 90).

Giamarchi, T., *Quantum physics in one dimension* (Oxford University Press, 2004) (cit. on pp. 176, 179).

Giorgini, S., L. P. Pitaevskii, and S. Stringari, *Theory of ultracold atomic Fermi gases*, Rev. Mod. Phys. **80**, 1215 (2008), DOI:10.1103/RevModPhys.80.1215 (cit. on pp. 12, 27, 28).

Goldman, N., E. Anisimovas, F. Gerbier, P. Öhberg, I. B. Spielman, and G. Juzeliūnas, *Measuring topology in a laser-coupled honeycomb lattice: from Chern insulators to topological semi-metals*, New J. Phys. **15**, 013025 (2013), DOI:10.1088/1367-2630/15/1/013025 (cit. on p. 94).

Goldman, N., G. Juzeliūnas, P. Öhberg, and I. B. Spielman, *Light-induced gauge fields for ultracold atoms*, ArXiv e-prints (2013), arXiv:1308.6533 [cond-mat.quant-gas] (cit. on p. 197).

Goldman, N., J. Beugnon, and F. Gerbier, *Detecting chiral edge states in the Hofstadter optical lattice*, Phys. Rev. Lett. **108**, 255303 (2012), DOI:10.1103/PhysRevLett.108.255303 (cit. on p. 199).

Goldman, N., J. Dalibard, A. Dauphin, F. Gerbier, M. Lewenstein, P. Zoller, and I. B. Spielman, *Direct imaging of topological edge states in cold-atom systems*, Proc. Natl. Acad. Sci. U.S.A. **110**, 6736 (2013), DOI:10.1073/pnas.1300170110 (cit. on p. 199).

Gomes, K. K., W. Mar, W. Ko, F. Guinea, and H. C. Manoharan, *Designer Dirac fermions and topological phases in molecular graphene*, Nature (London) **483**, 306 (2012), DOI:10.1038/nature10941 (cit. on pp. 12, 96).

Gorelik, E. V., D. Rost, T. Paiva, R. Scalettar, A. Klümper, and N. Blümer, *Universal probes for antiferromagnetic correlations and entropy in cold fermions on optical lattices*, Phys. Rev. A **85**, 061602 (2012), DOI:10.1103/PhysRevA.85.061602 (cit. on p. 176).

Gould, P. L., G. A. Ruff, and D. E. Pritchard, *Diffraction of atoms by light: The near-resonant Kapitza-Dirac effect*, Phys. Rev. Lett. **56**, 827 (1986), DOI:10.1103/PhysRevLett.56.827 (cit. on p. 50).

Green, D., L. Santos, and C. Chamon, *Isolated flat bands and spin-1 conical bands in two-dimensional lattices*, Phys. Rev. B **82**, 075104 (2010), DOI:10.1103/PhysRevB.82.075104 (cit. on p. 200).

Greif, D., *Quantum magnetism with ultracold fermions in an optical lattice*, PhD thesis (ETH Zurich, 2013), DOI:10.3929/ethz-a-010008097 (cit. on pp. 34, 40, 46, 47, 49, 51, 53, 54, 58, 145, 160, 168, 169, 171, 199, 200).

Greif, D., L. Tarruell, T. Uehlinger, R. Jördens, and T. Esslinger, *Probing nearest-neighbor correlations of ultracold fermions in an optical lattice*, Phys. Rev. Lett. **106**, 145302 (2011), DOI:10.1103/PhysRevLett.106.145302 (cit. on pp. 34, 155, 169, 170, 176, 237).

Greif, D., T. Uehlinger, G. Jotzu, L. Tarruell, and T. Esslinger, *Short-range quantum magnetism of ultracold fermions in an optical lattice*, Science **340**, 1307 (2013), DOI:10.1126/science.1236362 (cit. on pp. 34, 162, 164, 237).

Greiner, M., *Ultracold quantum gases in three-dimensional optical lattice potentials*, PhD thesis (LMU München, 2003) (cit. on p. 45).

Greiner, M., C. A. Regal, J. T. Stewart, and D. S. Jin, *Probing pair-correlated fermionic atoms through correlations in atom shot noise*, Phys. Rev. Lett. **94**, 110401 (2005), DOI:10.1103/PhysRevLett.94.110401 (cit. on pp. 181, 182).

Greiner, M., O. Mandel, T. Esslinger, T. W. Hänsch, and I. Bloch, *Quantum phase transition from a superfluid to a Mott insulator in a gas of ultracold atoms*, Nature (London) **415**, 39 (2002), DOI:10.1038/415039a (cit. on pp. 13, 132).

Grimm, R. and M. Weidemüller, *Optical dipole traps for neutral atoms*, Adv. At. Mol. Opt. Phys. **42**, 95 (2000), DOI:10.1016/S1049-250X(08)60186-X (cit. on pp. 22, 41).

Grondalski, J., P. Alsing, and I. Deutsch, *Spatial correlation diagnostics for atoms in optical lattices*, Opt. Express **5**, 249 (1999), DOI:10.1364/OE.5.000249 (cit. on p. 181).

Grynberg, G., B. Lounis, P. Verkerk, J.-Y. Courtois, and C. Salomon, *Quantized motion of cold cesium atoms in two- and three-dimensional optical potentials*, Phys. Rev. Lett. **70**, 2249 (1993), DOI:10.1103/PhysRevLett.70.2249 (cit. on pp. 23, 45).

Guerlin, C., K. Baumann, F. Brennecke, D. Greif, R. Jördens, S. Leinss, N. Strohmaier, L. Tarruell, T. Uehlinger, H. Moritz, and T. Esslinger, *Synthetic quantum many-body systems*, in Proceedings of the XIX International Conference on Laser Spectroscopy (ICOLS) (World Scientific, 2009) Chap. 20, pp. 212–221, DOI:10.1142/9789814282345_0020 (cit. on p. 237).

Guinea, F., M. I. Katsnelson, and A. K. Geim, *Energy gaps and a zero-field quantum Hall effect in graphene by strain engineering*, Nat. Phys. **6**, 30 (2010), DOI:10.1038/nphys1420 (cit. on p. 96).

Gull, E., P. Werner, O. Parcollet, and M. Troyer, *Continuous-time auxiliary-field Monte Carlo for quantum impurity models*, Europhys. Lett. **82**, 57003 (2008), DOI:10.1209/0295-5075/82/57003 (cit. on p. 178).

Gull, E., P. Staar, S. Fuchs, P. Nukala, M. S. Summers, T. Pruschke, T. C. Schulthess, and T. Maier, *Submatrix updates for the continuous-time auxiliary-field algorithm*, Phys. Rev. B **83**, 075122 (2011), DOI:10.1103/PhysRevB.83.075122 (cit. on p. 178).

Günter, K., *Interacting Fermi gases and Bose-Fermi mixtures in optical lattices*, PhD thesis (ETH Zurich, 2007), DOI:10.3929/ethz-a-005553376 (cit. on pp. 33, 37, 39).

Günter, K., T. Stöferle, H. Moritz, M. Köhl, and T. Esslinger, *p-wave interactions in low-dimensional fermionic gases*, Phys. Rev. Lett. **95**, 230401 (2005), DOI:10.1103/PhysRevLett.95.230401 (cit. on p. 33).

Günter, K., T. Stöferle, H. Moritz, M. Köhl, and T. Esslinger, *Bose-Fermi mixtures in a three-dimensional optical lattice*, Phys. Rev. Lett. **96**, 180402 (2006), DOI:10.1103/PhysRevLett.96.180402 (cit. on p. 33).

Gustavsson, M., E. Haller, M. J. Mark, J. G. Danzl, G. Rojas-Kopeinig, and H.-C. Nägerl, *Control of interaction-induced dephasing of Bloch oscillations*, Phys. Rev. Lett. **100**, 080404 (2008), DOI:10.1103/PhysRevLett.100.080404 (cit. on pp. 98, 102).

Haaf, D. F. B. ten and J. M. J. van Leeuwen, *High-temperature series expansions for the Hubbard model*, Phys. Rev. B **46**, 6313 (1992), DOI:10.1103/PhysRevB.46.6313 (cit. on pp. 142, 177, 178).

Hackermüller, L., U. Schneider, M. Moreno-Cardoner, T. Kitagawa, T. Best, S. Will, E. Demler, E. Altman, I. Bloch, and B. Paredes, *Anomalous expansion of attractively interacting fermionic atoms in an optical lattice*, Science **327**, 1621 (2010), DOI:10.1126/science.1184565 (cit. on p. 133).

Hadzibabic, Z., P. Kruger, M. Cheneau, B. Battelier, and J. Dalibard, *Berezinskii-Kosterlitz-Thouless crossover in a trapped atomic gas*, Nature (London) **441**, 1118 (2006), DOI:10.1038/nature04851 (cit. on p. 181).

Haken, H. and H. C. Wolf, *Atom- und Quantenphysik* (Springer DE, 2003) (cit. on p. 19).

Haldane, F. D. M., *Model for a quantum Hall effect without Landau levels: Condensed-matter realization of the "parity anomaly"*, Phys. Rev. Lett. **61**, 2015 (1988), DOI:10.1103/PhysRevLett.61.2015 (cit. on p. 197).

Hamilton, W. R., *Third supplement to an essay on the theory of system of rays*, Trans. R. Irish Acad. **17**, 1 (1837) (cit. on p. 86).

Hanbury Brown, R. and R. Q. Twiss, *A test of a new type of stellar interferometer on Sirius*, Nature (London) **178**, 1046 (1956), DOI:10.1038/1781046a0 (cit. on p. 183).

Hänsch, T. and A. Schawlow, *Cooling of gases by laser radiation*, Opt. Comm. **13**, 68 (1975), DOI:10.1016/0030-4018(75)90159-5 (cit. on pp. 22, 37).

Harper, P. G., *Single band motion of conduction electrons in a uniform magnetic field*, Proc. Phys. Soc. A **68**, 874 (1955), DOI:10.1088/0370-1298/68/10/304 (cit. on p. 196).

Hartmann, T., F. Keck, H. J. Korsch, and S. Mossmann, *Dynamics of Bloch oscillations*, New J. Phys. **6**, 2 (2004), DOI:10.1088/1367-2630/6/1/002 (cit. on p. 100).

Hasan, M. Z. and C. L. Kane, *Colloquium: Topological insulators*, Rev. Mod. Phys. **82**, 3045 (2010), DOI:10.1103/RevModPhys.82.3045 (cit. on p. 196).

Hasegawa, Y. and K. Kishigi, *Merging Dirac points and topological phase transitions in the tight-binding model on the generalized honeycomb lattice*, Phys. Rev. B **86**, 165430 (2012), DOI:10.1103/PhysRevB.86.165430 (cit. on p. 104).

Hasegawa, Y., R. Konno, H. Nakano, and M. Kohmoto, *Zero modes of tight-binding electrons on the honeycomb lattice*, Phys. Rev. B **74**, 033413 (2006), DOI:10.1103/PhysRevB.74.033413 (cit. on p. 119).

Haynes, W. M., *Handbook of chemistry and physics*, 94th edition (CRC Press, 2013) (cit. on p. 35).

He, P.-B., Q. Sun, P. Li, S.-Q. Shen, and W. M. Liu, *Magnetic quantum phase transition of cold atoms in an optical lattice*, Phys. Rev. A **76**, 043618 (2007), DOI:10.1103/PhysRevA.76.043618 (cit. on p. 179).

Hemmerich, A. and T. W. Hänsch, *Two-dimensional atomic crystal bound by light*, Phys. Rev. Lett. **70**, 410 (1993), DOI:10.1103/PhysRevLett.70.410 (cit. on p. 45).

Hemmerich, A., C. Zimmermann, and T. W. Hänsch, *Sub-kHz Rayleigh resonance in a cubic atomic crystal*, Europhys. Lett. **22**, 89 (1993), DOI:10.1209/0295-5075/22/2/003 (cit. on p. 45).

Henderson, J. A., J. Oitmaa, and M. C. B. Ashley, *High-temperature expansion for the single-band Hubbard model*, Phys. Rev. B **46**, 6328 (1992), DOI:10.1103/PhysRevB.46.6328 (cit. on pp. 142, 171).

Herbut, I. F., *Interactions and phase transitions on graphene's honeycomb lattice*, Phys. Rev. Lett. **97**, 146401 (2006), DOI:10.1103/PhysRevLett.97.146401 (cit. on p. 141).

Hirsch, J. E., *Two-dimensional Hubbard model: Numerical simulation study*, Phys. Rev. B **31**, 4403 (1985), DOI:10.1103/PhysRevB.31.4403 (cit. on p. 139).

Ho, A. F., M. A. Cazalilla, and T. Giamarchi, *Quantum simulation of the Hubbard model: The attractive route*, Phys. Rev. A **79**, 033620 (2009), DOI:10.1103/PhysRevA.79.033620 (cit. on p. 140).

Ho, T.-L. and Q. Zhou, *Squeezing out the entropy of fermions in optical lattices*, Proc. Natl. Acad. Sci. U.S.A. **106**, 6916 (2009), DOI:10.1073/pnas.0809862105 (cit. on p. 164).

Hoang, A. T., *Metal–insulator transitions in the half-filled ionic Hubbard model*, J. Phys.: Condens. Matter **22**, 095602 (2010), DOI:10.1088/0953-8984/22/9/095602 (cit. on p. 199).

Hodby, E., S. T. Thompson, C. A. Regal, M. Greiner, A. C. Wilson, D. S. Jin, E. A. Cornell, and C. E. Wieman, *Production efficiency of ultracold Feshbach molecules in bosonic and fermionic systems*, Phys. Rev. Lett. **94**, 120402 (2005), DOI:10.1103/PhysRevLett.94.120402 (cit. on p. 66).

Hofstadter, D. R., *Energy levels and wave functions of Bloch electrons in rational and irrational magnetic fields*, Phys. Rev. B **14**, 2239 (1976), DOI:10.1103/PhysRevB.14.2239 (cit. on p. 196).

Hofstetter, W., J. I. Cirac, P. Zoller, E. Demler, and M. D. Lukin, *High-temperature superfluidity of fermionic atoms in optical lattices*, Phys. Rev. Lett. **89**, 220407 (2002), DOI:10.1103/PhysRevLett.89.220407 (cit. on p. 162).

Holthaus, M., *Bloch oscillations and Zener breakdown in an optical lattice*, J. Opt. B: Quantum Semiclass. Opt. **2**, 589 (2000), DOI:10.1088/1464-4266/2/5/306 (cit. on p. 97).

Honerkamp, C., *Density waves and Cooper pairing on the honeycomb lattice*, Phys. Rev. Lett. **100**, 146404 (2008), DOI:10.1103/PhysRevLett.100.146404 (cit. on p. 141).

Hong, C. K., Z. Y. Ou, and L. Mandel, *Measurement of subpicosecond time intervals between two photons by interference*, Phys. Rev. Lett. **59**, 2044 (1987), DOI:10.1103/PhysRevLett.59.2044 (cit. on p. 183).

Horowitz, P. and H. Winfield, *The Art of Electronics*, 2nd edition (Cambridge University Press, 1989) (cit. on p. 50).

Houck, A. A., H. E. Türeci, and J. Koch, *On-chip quantum simulation with superconducting circuits*, Nat. Phys. **8**, 292 (2012), DOI:10.1038/nphys2251 (cit. on p. 18).

Hsieh, D., D. Qian, L. Wray, Y. Xia, Y. S. Hor, R. J. Cava, and M. Z. Hasan, *A topological Dirac insulator in a quantum spin Hall phase*, Nature (London) **452**, 970 (2008), DOI:10.1038/nature06843 (cit. on p. 197).

Hubbard, J., *Electron correlations in narrow energy bands*, Proc. R. Soc. Lond. A **276**, 238 (1963), DOI:10.1098/rspa.1963.0204 (cit. on pp. 13, 131).

Hung, C.-L., X. Zhang, N. Gemelke, and C. Chin, *Slow mass transport and statistical evolution of an atomic gas across the superfluid–Mott-insulator transition*, Phys. Rev. Lett. **104**, 160403 (2010), DOI:10.1103/PhysRevLett.104.160403 (cit. on p. 156).

Hung, C.-L., X. Zhang, L.-C. Ha, S.-K. Tung, N. Gemelke, and C. Chin, *Extracting density–density correlations from in situ images of atomic quantum gases*, New J. Phys. **13**, 075019 (2011), DOI:10.1088/1367-2630/13/7/075019 (cit. on p. 182).

Hunt, B., J. D. Sanchez-Yamagishi, A. F. Young, M. Yankowitz, B. J. LeRoy, K. Watanabe, T. Taniguchi, P. Moon, M. Koshino, P. Jarillo-Herrero, and R. C. Ashoori, *Massive Dirac fermions and Hofstadter butterfly in a van der Waals heterostructure*, Science **340**, 1427 (2013), DOI:10.1126/science.1237240 (cit. on p. 96).

Hussey, N. E., *Low-energy quasiparticles in high-T_c cuprates*, Adv. Phys. **51**, 1685 (2002), DOI:10.1080/00018730210164638 (cit. on p. 91).

Ibañez-Azpiroz, J., Eiguren, A. Bergara, G. Pettini, and M. Modugno, *Tight-binding models for ultracold atoms in honeycomb optical lattices*, Phys. Rev. A **87**, 011602 (2013a), DOI:10.1103/PhysRevA.87.011602 (cit. on pp. 81, 133).

Ibañez-Azpiroz, J., Eiguren, A. Bergara, G. Pettini, and M. Modugno, *Self-consistent tight-binding description of Dirac points moving and merging in two-dimensional optical lattices*, Phys. Rev. A **88**, 033631 (2013b), DOI:10.1103/PhysRevA.88.033631 (cit. on pp. 77, 79–81, 133).

Imriška, J., Iazzi, L. Wang, E. Gull, D. Greif, T. Uehlinger, G. Jotzu, L. Tarruell, T. Esslinger, and M. Troyer, *Thermodynamics and magnetic properties of the anisotropic 3D Hubbard model*, Phys. Rev. Lett. **112**, 115301 (2014a), DOI:10.1103/PhysRevLett.112.115301 (cit. on pp. 164, 176, 237).

Imriška, J., Iazzi, L. Wang, E. Gull, D. Greif, T. Uehlinger, G. Jotzu, L. Tarruell, T. Esslinger, and M. Troyer, *Erratum: Thermodynamics and magnetic properties of the anisotropic 3D Hubbard model [Phys. Rev. Lett. 112, 115301 (2014)]*, Phys. Rev. Lett. **112**, 159903 (2014b), DOI:10.1103/PhysRevLett.112.159903 (cit. on pp. 164, 176, 237).

Inouye, S., M. R. Andrews, J. Stenger, H.-J. Miesner, D. M. Stamper-Kurn, and W. Ketterle, *Observation of Feshbach resonances in a Bose-Einstein condensate*, Nature (London) **392**, 151 (1998), DOI:10.1038/32354 (cit. on p. 28).

Jaksch, D., C. Bruder, J. I. Cirac, C. W. Gardiner, and P. Zoller, *Cold bosonic atoms in optical lattices*, Phys. Rev. Lett. **81**, 3108 (1998), DOI:10.1103/PhysRevLett.81.3108 (cit. on pp. 13, 132).

Jaksch, D. and P. Zoller, *The cold atom Hubbard toolbox*, Ann. Phys. **315**, 52 (2005), DOI:10.1016/j.aop.2004.09.010 (cit. on pp. 12, 133).

Jeltes, T., J. M. McNamara, W. Hogervorst, W. Vassen, V. Krachmalnicoff, M. Schellekens, A. Perrin, H. Chang, D. Boiron, A. Aspect, and C. I. Westbrook, *Comparison of the Hanbury Brown-Twiss effect for bosons and fermions*, Nature (London) **445**, 402 (2007), DOI:10.1038/nature05513 (cit. on p. 182).

Jessen, P. S., C. Gerz, P. D. Lett, W. D. Phillips, S. L. Rolston, R. J. C. Spreeuw, and C. I. Westbrook, *Observation of quantized motion of Rb atoms in an optical field*, Phys. Rev. Lett. **69**, 49 (1992), DOI:10.1103/PhysRevLett.69.49 (cit. on p. 23).

Jo, G.-B., J. Guzman, C. K. Thomas, P. Hosur, A. Vishwanath, and D. M. Stamper-Kurn, *Ultracold atoms in a tunable optical Kagome lattice*, Phys. Rev. Lett. **108**, 045305 (2012), DOI:10.1103/PhysRevLett.108.045305 (cit. on p. 45).

Jones, K. M., E. Tiesinga, P. D. Lett, and P. S. Julienne, *Ultracold photoassociation spectroscopy: Long-range molecules and atomic scattering*, Rev. Mod. Phys. **78**, 483 (2006), DOI:10.1103/RevModPhys.78.483 (cit. on p. 28).

Jördens, R., *A radio frequency source for the preparation of quantum states*, Diploma thesis (ETH Zürich, 2006), DOI:10.3929/ethz-a-005280348 (cit. on p. 40).

Jördens, R., *Metallic and Mott-insulating phases in fermionic quantum gases*, PhD thesis (ETH Zurich, 2010), DOI:10.3929/ethz-a-006278918 (cit. on pp. 27–29, 34, 38, 42, 53, 73, 76, 132, 149).

Jördens, R., N. Strohmaier, K. Günter, H. Moritz, and T. Esslinger, *A Mott insulator of fermionic atoms in an optical lattice*, Nature (London) **455**, 204 (2008), DOI:10.1038/nature07244 (cit. on pp. 13, 14, 33, 132, 148, 149, 153, 155, 163, 165, 168).

Jördens, R. *et al.*, *Quantitative determination of temperature in the approach to magnetic order of ultracold fermions in an optical lattice*, Phys. Rev. Lett. **104**, 180401 (2010), DOI:10.1103/PhysRevLett.104.180401 (cit. on pp. 14, 34, 148, 149, 153, 158, 160, 170, 171, 177, 237).

Kane, C. L. and E. J. Mele, *Quantum spin Hall effect in graphene*, Phys. Rev. Lett. **95**, 226801 (2005), DOI:10.1103/PhysRevLett.95.226801 (cit. on p. 198).

Kapitza, P. L. and P. A. M. Dirac, *The reflection of electrons from standing light waves*, Math. Proc. Cambridge Philos. Soc. **29**, 297 (1933), DOI:10.1017/S0305004100011105 (cit. on p. 50).

Katsnelson, M. I., K. S. Novoselov, and A. K. Geim, *Chiral tunnelling and the Klein paradox in graphene*, Nat. Phys. **2**, 620 (2006), DOI:10.1038/nphys384 (cit. on pp. 11, 90, 95).

Ketterle, W., D. S. Durfee, and D. M. Stamper-Kurn, *Making, probing and understanding Bose-Einstein condensates*, in Proceedings of the International School of Physics "En-

rico Fermi", Vol. 140: Bose-Einstein condensation in atomic gases, edited by M. Inguscio, S. Stringari, and C. Wieman, Varenna Summer School Enrico Fermi (IOS Press, Amsterdam, 1999), pp. 67–176, DOI:10.3254/978-1-61499-225-7-67 (cit. on p. 12).

Ketterle, W. and M. W. Zwierlein, *Making, probing and understanding ultracold Fermi gases*, in Proceedings of the International School of Physics "Enrico Fermi", Vol. 164: Ultra-cold Fermi gases, edited by M. Inguscio, W. Ketterle, and C. Salomon, Varenna Summer School Enrico Fermi (IOS Press, Amsterdam, 2008), pp. 95–287, DOI:10.3254/978-1-58603-846-5-95 (cit. on pp. 12, 66).

Kiesel, M. L., C. Platt, W. Hanke, D. A. Abanin, and R. Thomale, *Competing many-body instabilities and unconventional superconductivity in graphene*, Phys. Rev. B **86**, 020507 (2012), DOI:10.1103/PhysRevB.86.020507 (cit. on p. 140).

Kitagawa, T., E. Berg, M. Rudner, and E. Demler, *Topological characterization of periodically driven quantum systems*, Phys. Rev. B **82**, 235114 (2010), DOI:10.1103/PhysRevB.82.235114 (cit. on pp. 127, 198).

Kivelson, S., *Wannier functions in one-dimensional disordered systems: Application to fractionally charged solitons*, Phys. Rev. B **26**, 4269 (1982), DOI:10.1103/PhysRevB.26.4269 (cit. on pp. 81, 82).

Klein, O., *Die Reflexion von Elektronen an einem Potentialsprung nach der relativistischen Dynamik von Dirac*, Z. Phys. **53**, 157 (1929), DOI:10.1007/BF01339716 (cit. on p. 90).

Kling, S., T. Salger, C. Grossert, and M. Weitz, *Atomic Bloch-Zener oscillations and Stückelberg interferometry in optical lattices*, Phys. Rev. Lett. **105**, 215301 (2010), DOI:10.1103/PhysRevLett.105.215301 (cit. on pp. 98, 100, 113).

Klitzing, K. v., G. Dorda, and M. Pepper, *New method for high-accuracy determination of the fine-structure constant based on quantized Hall resistance*, Phys. Rev. Lett. **45**, 494 (1980), DOI:10.1103/PhysRevLett.45.494 (cit. on p. 196).

Köhl, M., H. Moritz, T. Stöferle, C. Schori, and T. Esslinger, *Superfluid to Mott insulator transition in one, two, and three dimensions*, J. Low Temp. Phys. **138**, 635 (2005), DOI:10.1007/s10909-005-2273-4 (cit. on p. 33).

Köhl, M., T. Stöferle, H. Moritz, C. Schori, and T. Esslinger, *1D Bose gases in an optical lattice*, Appl. Phys. B **79**, 1009 (2004), DOI:10.1007/s00340-004-1662-8 (cit. on p. 33).

Köhl, M., K. Günter, T. Stöferle, H. Moritz, and T. Esslinger, *Strongly interacting atoms and molecules in a 3D optical lattice*, J. Phys. B: At. Mol. Opt. Phys. **39**, S47 (2006), DOI:10.1088/0953-4075/39/10/S05 (cit. on p. 33).

Köhl, M., H. Moritz, T. Stöferle, K. Günter, and T. Esslinger, *Fermionic atoms in a three dimensional optical lattice: observing Fermi surfaces, dynamics, and interactions*, Phys. Rev. Lett. **94**, 080403 (2005), DOI:10.1103/PhysRevLett.94.080403 (cit. on pp. 33, 107).

Kolovsky, A. R., *Transport of cold atoms in optical lattices*, Eur. Phys. J. Special Topics **151**, 103 (2007), DOI:10.1140/epjst/e2007-00366-5 (cit. on p. 103).

König, M., S. Wiedmann, C. Brüne, A. Roth, H. Buhmann, L. W. Molenkamp, X.-L. Qi, and S.-C. Zhang, *Quantum spin Hall insulator state in HgTe quantum wells*, Science **318**, 766 (2007), DOI:10.1126/science.1148047 (cit. on p. 196).

Kozik, E., K. V. Houcke, E. Gull, L. Pollet, N. Prokof'ev, B. Svistunov, and M. Troyer, *Diagrammatic Monte Carlo for correlated fermions*, Europhys. Lett. **90**, 10004 (2010), DOI:10.1209/0295-5075/90/10004 (cit. on p. 145).

Krauser, J. S., J. Heinze, N. Fläschner, S. Götze, O. Jürgensen, D.-S. Lühmann, C. Becker, and K. Sengstock, *Coherent multi-flavour spin dynamics in a fermionic quantum gas*, Nat. Phys. **8**, 813 (2012), DOI:10.1038/nphys2409 (cit. on p. 167).

Krueckl, V. and K. Richter, *Bloch-Zener oscillations in graphene and topological insulators*, Phys. Rev. B **85**, 115433 (2012), DOI:10.1103/PhysRevB.85.115433 (cit. on p. 98).

Kuhl, U., S. Barkhofen, T. Tudorovskiy, H.-J. Stöckmann, T. Hossain, L. de Forges de Parny, and F. Mortessagne, *Dirac point and edge states in a microwave realization of tight-binding graphene-like structures*, Phys. Rev. B **82**, 094308 (2010), DOI:10.1103/PhysRevB.82.094308 (cit. on p. 12).

Landau, L. D., *On the theory of transfer of energy at collisions I*, Phys. Z. Sowjetunion **1** (1932a) (cit. on p. 113).

Landau, L. D., *On the theory of transfer of energy at collisions II*, Phys. Z. Sowjetunion **2** (1932b) (cit. on p. 113).

LeBlanc, L. J., M. C. Beeler, K. Jiménez-García, A. R. Perry, S. Sugawa, R. A. Williams, and I. B. Spielman, *Direct observation of zitterbewegung in a Bose–Einstein condensate*, New J. Phys. **15**, 073011 (2013), DOI:10.1088/1367-2630/15/7/073011 (cit. on p. 90).

Lebrat, M., *Electro-optic modulation in an optical lattice*, Semester thesis (ETH Zürich, 2012) (cit. on p. 85).

Lebrat, M., *Engineering artificial gauge fields in time-modulated optical lattices*, Master thesis (ETH Zürich, 2013) (cit. on p. 198).

Lee, K. L., K. Bouadim, G. G. Batrouni, F. Hébert, R. T. Scalettar, C. Miniatura, and B. Grémaud, *Attractive Hubbard model on a honeycomb lattice: Quantum Monte Carlo study*, Phys. Rev. B **80**, 245118 (2009), DOI:10.1103/PhysRevB.80.245118 (cit. on p. 140).

Lee, K. L., *Ultracold fermions in a honeycomb optical lattice*, PhD thesis (National University of Singapore, 2010) (cit. on p. 89).

Lee, K. L., B. Grémaud, R. Han, B.-G. Englert, and C. Miniatura, *Ultracold fermions in a graphene-type optical lattice*, Phys. Rev. A **80**, 043411 (2009), DOI:10.1103/PhysRevA.80.043411 (cit. on pp. 89, 119).

Lee, P. A., N. Nagaosa, and X.-G. Wen, *Doping a Mott insulator: Physics of high-temperature superconductivity*, Rev. Mod. Phys. **78**, 17 (2006), DOI:10.1103/RevModPhys.78.17 (cit. on p. 140).

Leo, K., P. H. Bolivar, F. Brüggemann, R. Schwedler, and K. Köhler, *Observation of Bloch oscillations in a semiconductor superlattice*, Solid State Commun. **84**, 943 (1992), DOI:10.1016/0038-1098(92)90798-E (cit. on p. 98).

Letokhov, V. S., *Narrowing of the Doppler width in a standing wave*, Sov. J. Exp. Theor. Phys. Lett. **7**, 272 (1968) (cit. on p. 23).

Letokhov, V. and V. Minogin, *Trapping and storage of atoms in a laser field*, Appl. Phys. **17**, 99 (1978), DOI:10.1007/BF00885037 (cit. on pp. 23, 76).

Letokhov, V. and V. Minogin, *Quantum motions of ultracooled atoms in resonant laser field*, Phys. Lett. A **61**, 370 (1977), DOI:10.1016/0375-9601(77)90335-8 (cit. on p. 23).

Levin, M. and A. Stern, *Fractional topological insulators*, Phys. Rev. Lett. **103**, 196803 (2009), DOI:10.1103/PhysRevLett.103.196803 (cit. on p. 196).

Lewenstein, M., A. Sanpera, and V. Ahufinger, *Ultracold Atoms in Optical Lattices, Simulating quantum many-body systems* (Oxford University Press, 2012) (cit. on p. 13).

Lewenstein, M., A. Sanpera, V. Ahufinger, B. Damski, A. Sen(De), and U. Sen, *Ultracold atomic gases in optical lattices: mimicking condensed matter physics and beyond*, Adv. Phys. **56**, 243 (2007), DOI:10.1080/00018730701223200 (cit. on pp. 12, 13, 171).

Li, G. and E. Y. Andrei, *Observation of Landau levels of Dirac fermions in graphite*, Nat. Phys. **3**, 623 (2007), DOI:10.1038/nphys653 (cit. on p. 90).

Lieb, E. H. and F. Y. Wu, *Absence of Mott transition in an exact solution of the short-range, one-band model in one dimension*, Phys. Rev. Lett. **20**, 1445 (1968), DOI:10.1103/PhysRevLett.20.1445 (cit. on p. 138).

Lim, L.-K., J.-N. Fuchs, and G. Montambaux, *Bloch-Zener oscillations across a merging transition of Dirac points*, Phys. Rev. Lett. **108**, 175303 (2012), DOI:10.1103/PhysRevLett.108.175303 (cit. on pp. 104, 114, 116, 122, 126, 148, 162).

Lim, L.-K., J.-N. Fuchs, and G. Montambaux, *Mass and chirality inversion of a Dirac cone pair in Stückelberg interferometry*, Phys. Rev. Lett. **112**, 155302 (2014), DOI:10.1103/PhysRevLett.112.155302 (cit. on pp. 122, 198).

Lin, Y.-J., R. L. Compton, K. Jiménez-García, J. V. Porto, and I. B. Spielman, *Synthetic magnetic fields for ultracold neutral atoms*, Nature (London) **462**, 628 (2009), DOI:10.1038/nature08609 (cit. on p. 127).

Lu, M., N. Q. Burdick, and B. L. Lev, *Quantum degenerate dipolar Fermi gas*, Phys. Rev. Lett. **108**, 215301 (2012), DOI:10.1103/PhysRevLett.108.215301 (cit. on p. 19).

Lubasch, M., V. Murg, U. Schneider, J. I. Cirac, and M.-C. Bañuls, *Adiabatic preparation of a Heisenberg antiferromagnet using an optical superlattice*, Phys. Rev. Lett. **107**, 165301 (2011), DOI:10.1103/PhysRevLett.107.165301 (cit. on pp. 127, 200).

Ma, L.-S., P. Jungner, J. Ye, and J. L. Hall, *Delivering the same optical frequency at two places: accurate cancellation of phase noise introduced by an optical fiber or other time-varying path*, Opt. Lett. **19**, 1777 (1994), DOI:10.1364/OL.19.001777 (cit. on p. 49).

Ma, P. N., S. Pilati, M. Troyer, and X. Dai, *Density functional theory for atomic Fermi gases*, Nat. Phys. **8**, 601 (2012), DOI:10.1038/nphys2348 (cit. on p. 175).

Maier, T. A. and M. Jarrell, *Comparison of two-quantum-cluster approximations*, Phys. Rev. B **65**, 041104 (2002), DOI:10.1103/PhysRevB.65.041104 (cit. on p. 178).

Maier, T., M. Jarrell, T. Pruschke, and M. H. Hettler, *Quantum cluster theories*, Rev. Mod. Phys. **77**, 1027 (2005), DOI:10.1103/RevModPhys.77.1027 (cit. on pp. 176, 178).

Makogon, D., R. van Gelderen, R. Roldán, and C. M. Smith, *Spin-density-wave instability in graphene doped near the van Hove singularity*, Phys. Rev. B **84**, 125404 (2011), DOI:10.1103/PhysRevB.84.125404 (cit. on p. 140).

Mañes, J. L., F. Guinea, and M. A. H. Vozmediano, *Existence and topological stability of Fermi points in multilayered graphene*, Phys. Rev. B **75**, 155424 (2007), DOI:10.1103/PhysRevB.75.155424 (cit. on p. 96).

Marzari, N., A. A. Mostofi, J. R. Yates, I. Souza, and D. Vanderbilt, *Maximally localized Wannier functions: Theory and applications*, Rev. Mod. Phys. **84**, 1419 (2012), DOI:10.1103/RevModPhys.84.1419 (cit. on p. 77).

Marzari, N. and D. Vanderbilt, *Maximally localized generalized Wannier functions for composite energy bands*, Phys. Rev. B **56**, 847 (1997), DOI:10.1103/PhysRevB.56.12847 (cit. on pp. 77, 81).

Mathy, C. J. M. and D. A. Huse, *Accessing the Néel phase of ultracold fermionic atoms in a simple-cubic optical lattice*, Phys. Rev. A **79**, 063412 (2009), DOI:10.1103/PhysRevA.79.063412 (cit. on p. 175).

McNamara, J. M., T. Jeltes, A. S. Tychkov, W. Hogervorst, and W. Vassen, *Degenerate Bose-Fermi mixture of metastable atoms*, Phys. Rev. Lett. **97**, 080404 (2006), DOI:10.1103/PhysRevLett.97.080404 (cit. on p. 19).

Meng, Z. Y., T. C. Lang, S. Wessel, F. F. Assaad, and A. Muramatsu, *Quantum spin liquid emerging in two-dimensional correlated Dirac fermions*, Nature (London) **464**, 847 (2010), DOI:10.1038/nature08942 (cit. on pp. 15, 127, 140, 162, 180, 200).

Michels, W. C. and N. L. Curtis, *A pentode lock-in amplifier of high frequency selectivity*, Rev. Sci. Instrum. **12**, 444 (1941), DOI:10.1063/1.1769919 (cit. on p. 50).

Miyake, H., G. A. Siviloglou, C. J. Kennedy, W. C. Burton, and W. Ketterle, *Realizing the Harper Hamiltonian with laser-assisted tunneling in optical lattices*, Phys. Rev. Lett. **111**, 185302 (2013), DOI:10.1103/PhysRevLett.111.185302 (cit. on p. 196).

Moerdijk, A. J., B. J. Verhaar, and A. Axelsson, *Resonances in ultracold collisions of ^{6}Li, ^{7}Li, and ^{23}Na*, Phys. Rev. A **51**, 4852 (1995), DOI:10.1103/PhysRevA.51.4852 (cit. on pp. 27, 28).

Montambaux, G., F. Piéchon, J.-N. Fuchs, and M. O. Goerbig, *A universal Hamiltonian for motion and merging of Dirac points in a two-dimensional crystal*, Eur. Phys. J. B **72**, 509 (2009a), DOI:10.1140/epjb/e2009-00383-0 (cit. on pp. 116, 126).

Montambaux, G., F. Piéchon, J.-N. Fuchs, and M. O. Goerbig, *Merging of Dirac points in a two-dimensional crystal*, Phys. Rev. B **80**, 153412 (2009b), DOI:10.1103/PhysRevB.80.153412 (cit. on pp. 81, 119).

Morandotti, R., U. Peschel, J. S. Aitchison, H. S. Eisenberg, and Y. Silberberg, *Experimental observation of linear and nonlinear optical Bloch oscillations*, Phys. Rev. Lett. **83**, 4756 (1999), DOI:10.1103/PhysRevLett.83.4756 (cit. on p. 98).

Moritz, H., *One-dimensional atomic gases*, PhD thesis (ETH Zurich, 2006), DOI:10.3929/ethz-a-005195815 (cit. on p. 33).

Moritz, H., T. Stöferle, K. Günter, M. Köhl, and T. Esslinger, *Confinement induced molecules in a 1D Fermi gas*, Phys. Rev. Lett. **94**, 210401 (2005), DOI:10.1103/PhysRevLett.94.210401 (cit. on p. 33).

Moritz, H., T. Stöferle, M. Köhl, and T. Esslinger, *Exciting collective oscillations in a trapped 1D gas*, Phys. Rev. Lett. **91**, 250402 (2003), DOI:10.1103/PhysRevLett.91.250402 (cit. on p. 33).

Morsch, O., J. H. Müller, M. Cristiani, D. Ciampini, and E. Arimondo, *Bloch oscillations and mean-field effects of Bose-Einstein condensates in 1D optical lattices*, Phys. Rev. Lett. **87**, 140402 (2001), DOI:10.1103/PhysRevLett.87.140402 (cit. on p. 98).

Morsch, O. and M. Oberthaler, *Dynamics of Bose-Einstein condensates in optical lattices*, Rev. Mod. Phys. **78**, 179 (2006), DOI:10.1103/RevModPhys.78.179 (cit. on p. 98).

Mostofi, A. A., J. R. Yates, Y.-S. Lee, I. Souza, D. Vanderbilt, and N. Marzari, *Wannier90: A tool for obtaining maximally-localised Wannier functions*, Comput. Phys. Commun. **178**, 685 (2008), DOI:10.1016/j.cpc.2007.11.016 (cit. on p. 81).

Mott, N. F., *The basis of the electron theory of metals, with special reference to the transition metals*, Proc. Phys. Soc. A **62**, 416 (1949), DOI:10.1088/0370-1298/62/7/303 (cit. on pp. 14, 132).

Mottl, R., *Towards a square – superlattice transition*, Semester thesis (ETH Zürich, 2009) (cit. on p. 46).

Müller, T., B. Zimmermann, J. Meineke, J.-P. Brantut, T. Esslinger, and H. Moritz, *Local observation of antibunching in a trapped Fermi gas*, Phys. Rev. Lett. **105**, 040401 (2010), DOI:10.1103/PhysRevLett.105.040401 (cit. on p. 182).

Nandkishore, R., G.-W. Chern, and A. V. Chubukov, *Itinerant half-metal spin-density-wave state on the hexagonal lattice*, Phys. Rev. Lett. **108**, 227204 (2012), DOI:10.1103/PhysRevLett.108.227204 (cit. on p. 140).

Nandkishore, R., L. S. Levitov, and A. V. Chubukov, *Chiral superconductivity from repulsive interactions in doped graphene*, Nat. Phys. **8**, 158 (2012), DOI:10.1038/nphys2208 (cit. on pp. 140, 162).

Nascimbène, S., Y.-A. Chen, M. Atala, M. Aidelsburger, S. Trotzky, B. Paredes, and I. Bloch, *Experimental realization of plaquette resonating valence-bond states with ultracold atoms in optical superlattices*, Phys. Rev. Lett. **108**, 205301 (2012), DOI:10.1103/PhysRevLett.108.205301 (cit. on p. 163).

Nielsen, H. and M. Ninomiya, *The Adler-Bell-Jackiw anomaly and Weyl fermions in a crystal*, Phys. Lett. B **130**, 389 (1983), DOI:10.1016/0370-2693(83)91529-0 (cit. on p. 86).

Novoselov, K. S., V. I. Fal'ko, L. Colombo, P. R. Gellert, M. G. Schwab, and K. Kim, *A roadmap for graphene*, Nature (London) **490**, 192 (2012), DOI:10.1038/nature11458 (cit. on p. 11).

Novoselov, K. S., A. K. Geim, S. V. Morozov, D. Jiang, M. I. Katsnelson, I. V. Grigorieva, S. V. Dubonos, and A. A. Firsov, *Two-dimensional gas of massless Dirac fermions in graphene*, Nature (London) **438**, 197 (2005), DOI:10.1038/nature04233 (cit. on pp. 11, 94, 95, 197).

Novoselov, K. S., A. K. Geim, S. V. Morozov, D. Jiang, Y. Zhang, S. V. Dubonos, I. V. Grigorieva, and A. A. Firsov, *Electric field effect in atomically thin carbon films*, Science **306**, 666 (2004), DOI:10.1126/science.1102896 (cit. on p. 11).

Novoselov, K. S., Z. Jiang, Y. Zhang, S. V. Morozov, H. L. Stormer, U. Zeitler, J. C. Maan, G. S. Boebinger, P. Kim, and A. K. Geim, *Room-temperature quantum Hall effect in graphene*, Science **315**, 1379 (2007), DOI:10.1126/science.1137201 (cit. on p. 11).

Novoselov, K. S., E. McCann, S. V. Morozov, V. I. Fal'ko, M. I. Katsnelson, U. Zeitler, D. Jiang, F. Schedin, and A. K. Geim, *Unconventional quantum Hall effect and Berry's phase of 2π in bilayer graphene*, Nat. Phys. **2**, 177 (2006), DOI:doi:10.1038/nphys245 (cit. on p. 157).

Oitmaa, J., C. Hamer, and W. Zheng, *Series expansion methods for strongly interacting lattice models* (Cambridge University Press, Cambridge, 2006) (cit. on pp. 142, 145, 153).

Oka, T. and H. Aoki, *Photovoltaic Hall effect in graphene*, Phys. Rev. B **79**, 081406 (2009), DOI:10.1103/PhysRevB.79.081406 (cit. on p. 198).

Oliver, W., Y. Yu, J. Lee, K. Berggren, L. Levitov, and T. Orlando, *Mach-Zehnder interferometry in a strongly driven superconducting qubit*, Science **310**, 1653 (2005), DOI:10.1126/science.1119678 (cit. on p. 112).

Orzel, C., A. K. Tuchman, M. L. Fenselau, M. Yasuda, and M. A. Kasevich, *Squeezed states in a Bose-Einstein Condensate*, Science **291**, 2386 (2001), DOI:10.1126/science.1058149 (cit. on p. 132).

Ospelkaus, S., K.-K. Ni, D. Wang, M. H. G. de Miranda, B. Neyenhuis, G. Quemener, P. S. Julienne, J. L. Bohn, D. S. Jin, and J. Ye, *Quantum-state controlled chemical reactions of ultracold potassium-rubidium molecules*, Science **327**, 853 (2010), DOI:10.1126/science.1184121 (cit. on p. 27).

Öttl, A., S. Ritter, M. Köhl, and T. Esslinger, *Correlations and counting statistics of an atom laser*, Phys. Rev. Lett. **95**, 090404 (2005), DOI:10.1103/PhysRevLett.95.090404 (cit. on p. 181).

Paiva, T., R. T. Scalettar, W. Zheng, R. R. P. Singh, and J. Oitmaa, *Ground-state and finite-temperature signatures of quantum phase transitions in the half-filled Hubbard model on a honeycomb lattice*, Phys. Rev. B **72**, 085123 (2005), DOI:10.1103/PhysRevB.72.085123 (cit. on p. 140).

Park, T. J. and J. C. Light, *Unitary quantum time evolution by iterative Lanczos reduction*, J. Chem. Phys. **85**, 5870 (1986), DOI:10.1063/1.451548 (cit. on p. 104).

Pathak, S., V. B. Shenoy, and G. Baskaran, *Possible high-temperature superconducting state with a d + id pairing symmetry in doped graphene*, Phys. Rev. B **81**, 085431 (2010), DOI:10.1103/PhysRevB.81.085431 (cit. on p. 140).

Pedersen, K. G. L., B. M. Andersen, G. M. Bruun, O. F. Syljuåsen, and A. S. Sørensen, *Measuring spin correlations in optical lattices using superlattice potentials*, Phys. Rev. A **84**, 041603 (2011), DOI:10.1103/PhysRevA.84.041603 (cit. on p. 44).

Peleg, O., G. Bartal, B. Freedman, O. Manela, M. Segev, and D. N. Christodoulides, *Conical diffraction and gap solitons in honeycomb photonic lattices*, Phys. Rev. Lett. **98**, 103901 (2007), DOI:10.1103/PhysRevLett.98.103901 (cit. on p. 12).

Peres, N. M. R., M. A. N. Araújo, and D. Bozi, *Phase diagram and magnetic collective excitations of the Hubbard model for graphene sheets and layers*, Phys. Rev. B **70**, 195122 (2004), DOI:10.1103/PhysRevB.70.195122 (cit. on p. 140).

Peres, N. M. R., F. Guinea, and A. H. Castro Neto, *Coulomb interactions and ferromagnetism in pure and doped graphene*, Phys. Rev. B **72**, 174406 (2005), DOI:10.1103/PhysRevB.72.174406 (cit. on p. 141).

Pertsch, T., P. Dannberg, W. Elflein, A. Bräuer, and F. Lederer, *Optical Bloch oscillations in temperature tuned waveguide arrays*, Phys. Rev. Lett. **83**, 4752 (1999), DOI:10.1103/PhysRevLett.83.4752 (cit. on p. 98).

Petrich, W., M. H. Anderson, J. R. Ensher, and E. A. Cornell, *Stable, tightly confining magnetic trap for evaporative cooling of neutral atoms*, Phys. Rev. Lett. **74**, 3352 (1995), DOI:10.1103/PhysRevLett.74.3352 (cit. on p. 39).

Petsas, K. I., A. B. Coates, and G. Grynberg, *Crystallography of optical lattices*, Phys. Rev. A **50**, 5173 (1994), DOI:10.1103/PhysRevA.50.5173 (cit. on p. 45).

Polini, M., F. Guinea, M. Lewenstein, H. C. Manoharan, and V. Pellegrini, *Artificial honeycomb lattices for electrons, atoms and photons*, Nat. Nanotech. **8**, 625 (2013), DOI:10.1038/nnano.2013.161 (cit. on p. 12).

Ponomarev, A. V. and A. R. Kolovsky, *Dipole and Bloch oscillations of cold atoms in a parabolic lattice*, Laser Phys. **16**, 367 (2006), DOI:10.1134/S1054660X06020289 (cit. on pp. 102, 104).

Ponomarev, A. V., *Dynamics of cold Fermi atoms in one-dimensional optical lattices*, PhD thesis (Albert-Ludwigs-Universität, Freiburg im Breisgau, 2008) (cit. on p. 103).

Porto, J. V., *Cold-atom magnetism*, Science **340**, 1297 (2013), DOI:10.1126/science.1239873 (cit. on p. 237).

Price, H. M. and N. R. Cooper, *Mapping the Berry curvature from semiclassical dynamics in optical lattices*, Phys. Rev. A **85**, 033620 (2012), DOI:10.1103/PhysRevA.85.033620 (cit. on pp. 94, 102, 127, 194).

Qu, C., C. Hamner, M. Gong, C. Zhang, and P. Engels, *Observation of zitterbewegung in a spin-orbit-coupled Bose-Einstein condensate*, Phys. Rev. A **88**, 021604 (2013), DOI:10.1103/PhysRevA.88.021604 (cit. on p. 90).

Rachel, S. and K. Le Hur, *Topological insulators and Mott physics from the Hubbard interaction*, Phys. Rev. B **82**, 075106 (2010), DOI:10.1103/PhysRevB.82.075106 (cit. on p. 162).

Regal, C. A., M. Greiner, and D. S. Jin, *Lifetime of molecule-atom mixtures near a Feshbach resonance in ^{40}K*, Phys. Rev. Lett. **92**, 083201 (2004a), DOI:10.1103/PhysRevLett.92.083201 (cit. on p. 29).

Regal, C. A., M. Greiner, and D. S. Jin, *Observation of resonance condensation of fermionic atom pairs*, Phys. Rev. Lett. **92**, 040403 (2004b), DOI:10.1103/PhysRevLett.92.040403 (cit. on p. 29).

Regal, C. A. and D. S. Jin, *Measurement of positive and negative scattering lengths in a Fermi gas of atoms*, Phys. Rev. Lett. **90**, 230404 (2003), DOI:10.1103/PhysRevLett.90.230404 (cit. on p. 29).

Ritsch, H., P. Domokos, F. Brennecke, and T. Esslinger, *Cold atoms in cavity-generated dynamical optical potentials*, Rev. Mod. Phys. **85**, 553 (2013), DOI:10.1103/RevModPhys.85.553 (cit. on p. 12).

Ritt, G., C. Geckeler, T. Salger, G. Cennini, and M. Weitz, *Fourier synthesis of optical potentials for atomic quantum gases*, Phys. Rev. A **74**, 063622 (2006), DOI:10.1103/PhysRevA.74.063622 (cit. on p. 45).

Roati, G., E. de Mirandes, F. Ferlaino, H. Ott, G. Modugno, and M. Inguscio, *Atom interferometry with trapped Fermi gases*, Phys. Rev. Lett. **92**, 230402 (2004), DOI:10.1103/PhysRevLett.92.230402 (cit. on p. 98).

Robertson, J., *Electronic structure and core exciton of hexagonal boron nitride*, Phys. Rev. B **29**, 2131 (1984), DOI:10.1103/PhysRevB.29.2131 (cit. on p. 96).

Rom, T., T. Best, D. van Oosten, U. Schneider, S. Fölling, B. Paredes, and I. Bloch, *Free fermion antibunching in a degenerate atomic Fermi gas released from an optical lattice*, Nature (London) **444**, 733 (2006), DOI:10.1038/nature05319 (cit. on pp. 182, 190).

Rom, T., *Bosonische und fermionische Quantengase in dreidimensionalen optischen Gittern*, PhD thesis (LMU München, 2009) (cit. on pp. 182, 184, 187).

Rüegg, C., A. Furrer, D. Sheptyakov, T. Strässle, K. W. Krämer, H.-U. Güdel, and L. Mélési, *Pressure-induced quantum phase transition in the spin-liquid $TlCuCl_3$*, Phys. Rev. Lett. **93**, 257201 (2004), DOI:10.1103/PhysRevLett.93.257201 (cit. on p. 170).

Sachdev, S., *Quantum magnetism and criticality*, Nat. Phys. **4**, 173 (2008), DOI:10.1038/nphys894 (cit. on pp. 127, 163, 170).

Sakurai, J. J., *Modern Quantum Mechanics (Revised Edition)*, edited by S. F. Tuan (Addison-Wesley Publishing Company, 1994) (cit. on pp. 25, 29).

Salger, T., C. Geckeler, S. Kling, and M. Weitz, *Atomic Landau-Zener tunneling in fourier-synthesized optical lattices*, Phys. Rev. Lett. **99**, 190405 (2007), DOI:10.1103/PhysRevLett.99.190405 (cit. on pp. 14, 86, 98).

Salger, T., C. Grossert, S. Kling, and M. Weitz, *Klein tunneling of a quasirelativistic Bose-Einstein condensate in an optical lattice*, Phys. Rev. Lett. **107**, 240401 (2011), DOI:10.1103/PhysRevLett.107.240401 (cit. on p. 90).

Salger, T., G. Ritt, C. Geckeler, S. Kling, and M. Weitz, *Bloch oscillations of a Bose-Einstein condensate in a subwavelength optical lattice*, Phys. Rev. A **79**, 011605 (2009), DOI:10.1103/PhysRevA.79.011605 (cit. on p. 98).

Sanchis-Alepuz, H., Y. A. Kosevich, and J. Sánchez-Dehesa, *Acoustic analogue of electronic Bloch oscillations and resonant Zener tunneling in ultrasonic superlattices*, Phys. Rev. Lett. **98**, 134301 (2007), DOI:10.1103/PhysRevLett.98.134301 (cit. on p. 98).

Sanner, C., E. J. Su, A. Keshet, R. Gommers, Y.-i. Shin, W. Huang, and W. Ketterle, *Suppression of density fluctuations in a quantum degenerate Fermi gas*, Phys. Rev. Lett. **105**, 040402 (2010), DOI:10.1103/PhysRevLett.105.040402 (cit. on p. 182).

Scarola, V. W., L. Pollet, J. Oitmaa, and M. Troyer, *Discerning incompressible and compressible phases of cold atoms in optical lattices*, Phys. Rev. Lett. **102**, 135302 (2009), DOI:10.1103/PhysRevLett.102.135302 (cit. on pp. 152, 178).

Schellekens, M., R. Hoppeler, A. Perrin, J. V. Gomes, D. Boiron, A. Aspect, and C. I. Westbrook, *Hanbury Brown Twiss effect for ultracold quantum gases*, Science **310**, 648 (2005), DOI:10.1126/science.1118024 (cit. on p. 181).

Schneider, U., L. Hackermüller, S. Will, T. Best, I. Bloch, T. A. Costi, R. W. Helmes, D. Rasch, and A. Rosch, *Metallic and insulating phases of repulsively interacting fermions in a 3D optical lattice*, Science **322**, 1520 (2008), DOI:10.1126/science.1165449 (cit. on pp. 13, 133, 163).

Schori, C., T. Stoferle, H. Moritz, M. Köhl, and T. Esslinger, *Excitations of a superfluid in a three-dimensional optical lattice*, Phys. Rev. Lett. **93**, 240402 (2004), DOI:10.1103/PhysRevLett.93.240402 (cit. on p. 33).

Schreck, F., L. Khaykovich, K. L. Corwin, G. Ferrari, T. Bourdel, J. Cubizolles, and C. Salomon, *Quasipure Bose-Einstein condensate immersed in a Fermi sea*, Phys. Rev. Lett. **87**, 080403 (2001), DOI:10.1103/PhysRevLett.87.080403 (cit. on p. 19).

Schrödinger, E., *Über die kräftefreie Bewegung in der relativistischen Quantenmechanik*, Sitzber. Preuß. Akad. Wiss. Phys.-Math. **24**, 418 (1930) (cit. on p. 90).

Schüler, M., M. Rösner, T. O. Wehling, A. I. Lichtenstein, and M. I. Katsnelson, *Optimal Hubbard models for materials with nonlocal Coulomb interactions: Graphene, silicene, and benzene*, Phys. Rev. Lett. **111**, 036601 (2013), DOI:10.1103/PhysRevLett.111.036601 (cit. on p. 141).

Schwabl, F., *Quantenmechanik (QM I)* (Springer DE, 2002) (cit. on p. 25).

Sciolla, B., A. Tokuno, S. Uchino, P. Barmettler, T. Giamarchi, and C. Kollath, *Competition of spin and charge excitations in the one-dimensional Hubbard model*, Phys. Rev. A **88**, 063629 (2013), DOI:10.1103/PhysRevA.88.063629 (cit. on p. 179).

Sebby-Strabley, J., M. Anderlini, P. S. Jessen, and J. V. Porto, *Lattice of double wells for manipulating pairs of cold atoms*, Phys. Rev. A **73**, 033605 (2006), DOI:10.1103/PhysRevA.73.033605 (cit. on p. 45).

Semenoff, G. W., *Condensed-matter simulation of a three-dimensional anomaly*, Phys. Rev. Lett. **53**, 2449 (1984), DOI:10.1103/PhysRevLett.53.2449 (cit. on pp. 96, 198).

Sensarma, R., D. Pekker, E. Altman, E. Demler, N. Strohmaier, D. Greif, R. Jördens, L. Tarruell, H. Moritz, and T. Esslinger, *Lifetime of double occupancies in the Fermi-Hubbard model*, Phys. Rev. B **82**, 224302 (2010), DOI:10.1103/PhysRevB.82.224302 (cit. on p. 34).

Sherson, J. F., C. Weitenberg, M. Endres, M. Cheneau, I. Bloch, and S. Kuhr, *Single-atom-resolved fluorescence imaging of an atomic Mott insulator*, Nature (London) **467**, 68 (2010), DOI:10.1038/nature09378 (cit. on pp. 30, 132, 146).

Shevchenko, S., S. Ashhab, and F. Nori, *Landau–Zener–Stückelberg interferometry*, Phys. Rep. **492**, 1 (2010), DOI:10.1016/j.physrep.2010.03.002 (cit. on pp. 112, 122, 195).

Shimada, Y., N. Sekine, and K. Hirakawa, *Terahertz emission due to interminiband resonant Zener tunneling in wide-miniband GaAs/Al0.3Ga0.7As superlattices*, Appl. Phys. Lett. **84**, 4926 (2004), DOI:10.1063/1.1759382 (cit. on p. 98).

Simon, J., W. S. Bakr, R. Ma, M. E. Tai, P. M. Preiss, and M. Greiner, *Quantum simulation of antiferromagnetic spin chains in an optical lattice*, Nature (London) **472**, 307 (2011), DOI:10.1038/nature09994 (cit. on pp. 163, 181).

Simon, J. and M. Greiner, *Condensed-matter physics: A duo of graphene mimics*, Nature (London) **483**, 282 (2012), DOI:10.1038/483282a (cit. on p. 237).

Singha, A., M. Gibertini, B. Karmakar, S. Yuan, M. Polini, G. Vignale, M. I. Katsnelson, A. Pinczuk, L. N. Pfeiffer, K. W. West, and V. Pellegrini, *Two-dimensional Mott-Hubbard electrons in an artificial honeycomb lattice*, Science **332**, 1176 (2011), DOI:10.1126/science.1204333 (cit. on p. 12).

Soltan-Panahi, P., J. Struck, P. Hauke, A. Bick, W. Plenkers, G. Meineke, C. Becker, P. Windpassinger, M. Lewenstein, and K. Sengstock, *Multi-component quantum gases in spin-dependent hexagonal lattices*, Nat. Phys. **7**, 434 (2011), DOI:10.1038/nphys1916 (cit. on p. 45).

Sorella, S. and E. Tosatti, *Semi-metal–insulator transition of the Hubbard model in the honeycomb lattice*, Europhys. Lett. **19**, 699 (1992), DOI:10.1209/0295-5075/19/8/007 (cit. on p. 140).

Sorella, S., Y. Otsuka, and S. Yunoki, *Absence of a spin liquid phase in the Hubbard model on the honeycomb lattice*, Sci. Rep. **2** (2012) DOI:10.1038/srep00992 (cit. on pp. 15, 127, 140, 162, 200).

Souza, I., N. Marzari, and D. Vanderbilt, *Maximally localized Wannier functions for entangled energy bands*, Phys. Rev. B **65**, 035109 (2001), DOI:10.1103/PhysRevB.65.035109 (cit. on p. 81).

Spielman, I. B., W. D. Phillips, and J. V. Porto, *Mott-insulator transition in a two-dimensional atomic Bose gas*, Phys. Rev. Lett. **98**, 080404 (2007), DOI:10.1103/PhysRevLett.98.080404 (cit. on pp. 132, 181, 182).

Staudt, R., M. Dzierzawa, and A. Muramatsu, *Phase diagram of the three-dimensional Hubbard model at half filling*, Eur. Phys. J. B **17**, 411 (2000), DOI:10.1007/s100510070120 (cit. on p. 139).

Steck, D., *Rubidium 87 D line data*, version 2.1.4 (2010), http://steck.us/alkalidata/rubidium87numbers.pdf (visited on 08/21/2013) (cit. on pp. 35, 38).

Stöferle, T., *Exploring atomic quantum gases in optical lattices*, PhD thesis (ETH Zurich, 2005), DOI:10.3929/ethz-a-005068694 (cit. on pp. 24, 33, 36).

Stöferle, T., H. Moritz, K. Günter, M. Köhl, and T. Esslinger, *Molecules of fermionic atoms in an optical lattice*, Phys. Rev. Lett. **96**, 030401 (2006), DOI:10.1103/PhysRevLett.96.030401 (cit. on p. 33).

Stöferle, T., H. Moritz, C. Schori, M. Köhl, and T. Esslinger, *Transition from a strongly interacting 1D superfluid to a Mott insulator*, Phys. Rev. Lett. **92**, 130403 (2004), DOI:10.1103/PhysRevLett.92.130403 (cit. on pp. 33, 34, 58, 132).

Strohmaier, N., *Exploring the Hubbard model with ultracold fermionic atoms in an optical lattice*, PhD thesis (ETH Zurich, 2010), DOI:10.3929/ethz-a-006278918 (cit. on pp. 34, 42, 66).

Strohmaier, N., D. Greif, R. Jördens, L. Tarruell, H. Moritz, T. Esslinger, R. Sensarma, D. Pekker, E. Altman, and E. Demler, *Observation of elastic doublon decay in the Fermi-Hubbard model*, Phys. Rev. Lett. **104**, 080401 (2010), DOI:10.1103/PhysRevLett.104.080401 (cit. on p. 34).

Strohmaier, N., Y. Takasu, K. Günter, R. Jördens, M. Köhl, H. Moritz, and T. Esslinger, *Interaction-controlled transport of an ultracold Fermi gas*, Phys. Rev. Lett. **99**, 220601 (2007), DOI:10.1103/PhysRevLett.99.220601 (cit. on p. 33).

Struck, J., C. Ölschläger, R. L. Targat, P. Soltan-Panahi, A. Eckardt, M. Lewenstein, P. Windpassinger, and K. Sengstock, *Quantum simulation of frustrated classical magnetism in triangular optical lattices*, Science **333**, 996 (2011), DOI:10.1126/science.1207239 (cit. on p. 163).

Stückelberg, E. C. G., *Theorie der unelastischen Stösse zwischen Atomen*, Helv. Phys. Acta **5**, 369 (1932), DOI:10.1007/978-3-7643-8878-2_9 (cit. on pp. 112, 122, 195).

Szymańska, M. H., K. Góral, T. Köhler, and K. Burnett, *Conventional character of the BCS-BEC crossover in ultracold gases of ^{40}K*, Phys. Rev. A **72**, 013610 (2005), DOI:10.1103/PhysRevA.72.013610 (cit. on p. 28).

Tarruell, L., D. Greif, T. Uehlinger, G. Jotzu, and T. Esslinger, *Creating, moving and merging Dirac points with a Fermi gas in a tunable honeycomb lattice*, Nature (London) **483**, 302 (2012), DOI:10.1038/nature10871 (cit. on pp. 34, 108, 117, 119, 148, 237).

Taylor, R. and C. A. Coulson, *Studies in graphite and related compounds III: Electronic band structure in boron nitride*, Proc. Phys. Soc. A **65**, 834 (1952), DOI:10.1088/0370-1298/65/10/307 (cit. on p. 96).

Tey, M. K., S. Stellmer, R. Grimm, and F. Schreck, *Double-degenerate Bose-Fermi mixture of strontium*, Phys. Rev. A **82**, 011608 (2010), DOI:10.1103/PhysRevA.82.011608 (cit. on p. 19).

Theis, M., G. Thalhammer, K. Winkler, M. Hellwig, G. Ruff, R. Grimm, and J. H. Denschlag, *Tuning the scattering length with an optically induced Feshbach resonance*, Phys. Rev. Lett. **93**, 123001 (2004), DOI:10.1103/PhysRevLett.93.123001 (cit. on pp. 28, 35).

Ticknor, C., C. A. Regal, D. S. Jin, and J. L. Bohn, *Multiplet structure of Feshbach resonances in nonzero partial waves*, Phys. Rev. A **69**, 042712 (2004), DOI:10.1103/PhysRevA.69.042712 (cit. on p. 35).

Tiecke, T. G., *Properties of potassium*, version 1.0 (2010), http://staff.science.uva.nl/~tgtiecke/PotassiumProperties.pdf (visited on 08/21/2013) (cit. on pp. 35, 38).

Tiesinga, E., B. J. Verhaar, and H. T. C. Stoof, *Threshold and resonance phenomena in ultracold ground-state collisions*, Phys. Rev. A **47**, 4114 (1993), DOI:10.1103/PhysRevA.47.4114 (cit. on p. 27).

Tokuno, A. and T. Giamarchi, *Spin correlations and doublon production rate for fermionic atoms in modulated optical lattices*, Phys. Rev. A **85**, 061603 (2012), DOI:10.1103/PhysRevA.85.061603 (cit. on p. 155).

Trotzky, S., P. Cheinet, S. Fölling, M. Feld, U. Schnorrberger, A. M. Rey, A. Polkovnikov, E. A. Demler, M. D. Lukin, and I. Bloch, *Time-resolved observation and control of superexchange interactions with ultracold atoms in optical lattices*, Science **319**, 295 (2008), DOI:10.1126/science.1150841 (cit. on p. 163).

Trotzky, S., Y.-A. Chen, U. Schnorrberger, P. Cheinet, and I. Bloch, *Controlling and detecting spin correlations of ultracold atoms in optical lattices*, Phys. Rev. Lett. **105**, 265303 (2010), DOI:10.1103/PhysRevLett.105.265303 (cit. on pp. 166, 167).

Truscott, A. G., K. E. Strecker, W. I. McAlexander, G. B. Partridge, and R. G. Hulet, *Observation of Fermi pressure in a gas of trapped atoms*, Science **291**, 2570 (2001), DOI:10.1126/science.1059318 (cit. on p. 19).

Tscherbul, T. V., T. Calarco, I. Lesanovsky, R. V. Krems, A. Dalgarno, and J. Schmiedmayer, *Rf-field-induced Feshbach resonances*, Phys. Rev. A **81**, 050701 (2010), DOI:10.1103/PhysRevA.81.050701 (cit. on p. 28).

Uehlinger, T., D. Greif, G. Jotzu, L. Tarruell, and T. Esslinger, *Bloch-Zener oscillations in a tunable optical honeycomb lattice*, in The Physics of Semiconductors: Proceedings of the 31st International Conference on the Physics of Semiconductors (ICPS) 2012, Vol. 1566 (AIP Conference Proceedings, 2013), pp. 534–535, DOI:10.1063/1.4848521 (cit. on p. 237).

Uehlinger, T., D. Greif, G. Jotzu, L. Tarruell, T. Esslinger, L. Wang, and M. Troyer, *Double transfer through Dirac points in a tunable honeycomb optical lattice*, Eur. Phys. J. Special Topics **217**, 121 (2013), DOI:10.1140/epjst/e2013-01761-y (cit. on pp. 34, 109, 117, 148, 162, 237).

Uehlinger, T., G. Jotzu, M. Messer, D. Greif, W. Hofstetter, U. Bissbort, and T. Esslinger, *Artificial graphene with tunable interactions*, Phys. Rev. Lett. **111**, 185307 (2013), DOI:10.1103/PhysRevLett.111.185307 (cit. on pp. 34, 81, 148, 237).

Verkerk, P., B. Lounis, C. Salomon, C. Cohen-Tannoudji, J.-Y. Courtois, and G. Grynberg, *Dynamics and spatial order of cold cesium atoms in a periodic optical potential*, Phys. Rev. Lett. **68**, 3861 (1992), DOI:10.1103/PhysRevLett.68.3861 (cit. on p. 23).

Wallace, P. R., *The band theory of graphite*, Phys. Rev. **71**, 622 (1947), DOI:10.1103/PhysRev.71.622 (cit. on pp. 89, 91).

Walters, R., G. Cotugno, T. H. Johnson, S. R. Clark, and D. Jaksch, *Ab initio derivation of Hubbard models for cold atoms in optical lattices*, Phys. Rev. A **87**, 043613 (2013), DOI:10.1103/PhysRevA.87.043613 (cit. on pp. 81, 133).

Wang, G., M. O. Goerbig, C. Miniatura, and B. Grémaud, *Emergent spin liquids in the Hubbard model on the anisotropic honeycomb lattice*, Europhys. Lett. **95**, 47013 (2011), DOI:10.1209/0295-5075/95/47013 (cit. on p. 141).

Wang, L., A. A. Soluyanov, and M. Troyer, *Proposal for direct measurement of topological invariants in optical lattices*, Phys. Rev. Lett. **110**, 166802 (2013), DOI:10.1103/PhysRevLett.110.166802 (cit. on p. 198).

Wang, P., Z.-Q. Yu, Z. Fu, J. Miao, L. Huang, S. Chai, H. Zhai, and J. Zhang, *Spin-orbit coupled degenerate Fermi gases*, Phys. Rev. Lett. **109**, 095301 (2012), DOI:10.1103/PhysRevLett.109.095301 (cit. on p. 197).

Wang, W.-S., Y.-Y. Xiang, Q.-H. Wang, F. Wang, F. Yang, and D.-H. Lee, *Functional renormalization group and variational Monte Carlo studies of the electronic instabilities in graphene near 1/4 doping*, Phys. Rev. B **85**, 035414 (2012), DOI:10.1103/PhysRevB.85.035414 (cit. on p. 140).

Wannier, G. H., *The structure of electronic excitation levels in insulating crystals*, Phys. Rev. **52**, 191 (1937), DOI:10.1103/PhysRev.52.191 (cit. on p. 77).

Waschke, C., H. G. Roskos, R. Schwedler, K. Leo, H. Kurz, and K. Köhler, *Coherent submillimeter-wave emission from Bloch oscillations in a semiconductor superlattice*, Phys. Rev. Lett. **70**, 3319 (1993), DOI:10.1103/PhysRevLett.70.3319 (cit. on p. 98).

Watanabe, K., T. Taniguchi, and H. Kanda, *Direct-bandgap properties and evidence for ultraviolet lasing of hexagonal boron nitride single crystal*, Nat. Mater. **3**, 404 (2004), DOI:10.1038/nmat1134 (cit. on p. 96).

Watanabe, T. and S. Ishihara, *Band and Mott insulators and superconductivity in honeycomb-lattice ionic-Hubbard model*, J. Phys. Soc. Jpn. **82**, 034704 (2013), DOI:10.7566/JPSJ.82.034704 (cit. on p. 199).

Weidemüller, M., A. Görlitz, T. W. Hänsch, and A. Hemmerich, *Local and global properties of light-bound atomic lattices investigated by Bragg diffraction*, Phys. Rev. A **58**, 4647 (1998), DOI:10.1103/PhysRevA.58.4647 (cit. on p. 30).

Weidemüller, M., A. Hemmerich, A. Görlitz, T. Esslinger, and T. W. Hänsch, *Bragg diffraction in an atomic lattice bound by light*, Phys. Rev. Lett. **75**, 4583 (1995), DOI:10.1103/PhysRevLett.75.4583 (cit. on pp. 23, 30).

Weitenberg, C., M. Endres, J. F. Sherson, M. Cheneau, P. Schauß, Peter, T. Fukuhara, I. Bloch, and S. Kuhr, *Single-spin addressing in an atomic Mott insulator*, Nature (London) **471**, 319 (2011), DOI:10.1038/nature09827 (cit. on p. 30).

Werner, F., O. Parcollet, A. Georges, and S. R. Hassan, *Interaction-induced adiabatic cooling and antiferromagnetism of cold fermions in optical lattices*, Phys. Rev. Lett. **95**, 056401 (2005), DOI:10.1103/PhysRevLett.95.056401 (cit. on p. 175).

White, S. R. and A. E. Feiguin, *Real-time evolution using the density matrix renormalization group*, Phys. Rev. Lett. **93**, 076401 (2004), DOI:10.1103/PhysRevLett.93.076401 (cit. on p. 142).

Wiener, N., *Generalized harmonic analysis*, Acta Math. **55**, 117 (1930), DOI:10.1007/BF02546511 (cit. on p. 187).

Wilkinson, S. R., C. F. Bharucha, K. W. Madison, Q. Niu, and M. G. Raizen, *Observation of atomic Wannier-Stark ladders in an accelerating optical potential*, Phys. Rev. Lett. **76**, 4512 (1996), DOI:10.1103/PhysRevLett.76.4512 (cit. on p. 98).

Witthaut, D., F. Keck, H. J. Korsch, and S. Mossmann, *Bloch oscillations in two-dimensional lattices*, New J. Phys. **6**, 41 (2004), DOI:10.1088/1367-2630/6/1/041 (cit. on p. 102).

Wunsch, B., F. Guinea, and F. Sols, *Dirac-point engineering and topological phase transitions in honeycomb optical lattices*, New J. Phys. **10**, 103027 (2008), DOI:10.1088/1367-2630/10/10/103027 (cit. on pp. 86, 92, 110, 119, 123).

Würtz, P., T. Langen, T. Gericke, A. Koglbauer, and H. Ott, *Experimental demonstration of single-site addressability in a two-dimensional optical lattice*, Phys. Rev. Lett. **103**, 080404 (2009), DOI:10.1103/PhysRevLett.103.080404 (cit. on p. 30).

Xiao, D., M.-C. Chang, and Q. Niu, *Berry phase effects on electronic properties*, Rev. Mod. Phys. **82**, 1959 (2010), DOI:10.1103/RevModPhys.82.1959 (cit. on pp. 93, 94).

Young, A. F. and P. Kim, *Quantum interference and Klein tunnelling in graphene heterojunctions*, Nat. Phys. **5**, 222 (2009), DOI:10.1038/nphys1198 (cit. on p. 90).

Zak, J., *Berry's phase for energy bands in solids*, Phys. Rev. Lett. **62**, 2747 (1989), DOI:10.1103/PhysRevLett.62.2747 (cit. on p. 92).

Zener, C., *Non-adiabatic crossing of energy levels*, Proc. R. Soc. Lond. A **137**, 696 (1932), DOI:10.1098/rspa.1932.0165 (cit. on pp. 97, 113).

Zener, C., *A theory of the electrical breakdown of solid dielectrics*, Proc. R. Soc. Lond. A **145**, 523 (1934), DOI:10.1098/rspa.1934.0116 (cit. on pp. 97, 98).

Zenesini, A., D. Ciampini, O. Morsch, and E. Arimondo, *Observation of Stückelberg oscillations in accelerated optical lattices*, Phys. Rev. A **82**, 065601 (2010), DOI:10.1103/PhysRevA.82.065601 (cit. on pp. 98, 113).

Zenesini, A., H. Lignier, G. Tayebirad, J. Radogostowicz, D. Ciampini, R. Mannella, S. Wimberger, O. Morsch, and E. Arimondo, *Time-resolved measurement of Landau-Zener tunneling in periodic potentials*, Phys. Rev. Lett. **103**, 090403 (2009), DOI:10.1103/PhysRevLett.103.090403 (cit. on p. 98).

Zhang, D.-W., Z.-D. Wang, and S.-L. Zhu, *Relativistic quantum effects of Dirac particles simulated by ultracold atoms*, Front. of Phys. **7**, 31 (2012), DOI:10.1007/s11467-011-0223-y (cit. on p. 90).

Zhang, J., *Private communication*, 2013 (cit. on p. 29).

Zhang, J., J. Zhang, X. Zhang, and K. Kim, *Realization of geometric Landau-Zener-Stückelberg interferometry*, Phys. Rev. A **89**, 013608 (2014), DOI:10.1103/PhysRevA.89.013608 (cit. on p. 199).

Zhang, Y., Y.-W. Tan, H. L. Stormer, and P. Kim, *Experimental observation of the quantum Hall effect and Berry's phase in graphene*, Nature (London) **438**, 201 (2005), DOI:10.1038/nature04235 (cit. on p. 94).

Zhao, E. and A. Paramekanti, *BCS-BEC crossover on the two-dimensional honeycomb lattice*, Phys. Rev. Lett. **97**, 230404 (2006), DOI:10.1103/PhysRevLett.97.230404 (cit. on pp. 141, 162).

Zhou, Q. and T.-L. Ho, *Universal thermometry for quantum simulation*, Phys. Rev. Lett. **106**, 225301 (2011), DOI:10.1103/PhysRevLett.106.225301 (cit. on p. 178).

Zhou, S. Y., G.-H. Gweon, A. V. Fedorov, P. N. First, W. A. de Heer, D.-H. Lee, F. Guinea, A. H. Castro Neto, and A. Lanzara, *Substrate-induced bandgap opening in epitaxial graphene*, Nat. Mater. **6**, 770 (2007), DOI:10.1038/nmat2003 (cit. on p. 96).

Zhu, S.-L., B. Wang, and L.-M. Duan, *Simulation and detection of Dirac fermions with cold atoms in an optical lattice*, Phys. Rev. Lett. **98**, 260402 (2007), DOI:10.1103/PhysRevLett.98.260402 (cit. on pp. 119, 123).

Zwerger, W., *Mott-Hubbard transition of cold atoms in optical lattices*, J. Opt. B **5**, S9 (2003), DOI:10.1088/1464-4266/5/2/352 (cit. on pp. 134, 137).

Zwierlein, M. W., J. R. Abo-Shaeer, A. Schirotzek, C. H. Schunck, and W. Ketterle, *Vortices and superfluidity in a strongly interacting Fermi gas*, Nature (London) **435**, 1047 (2005), DOI:10.1038/nature03858 (cit. on p. 28).

ACRONYMS

1D one-dimensional. 13, 14, 24, 45, 53, 55, 56, 61, 76, 82, 83, 94, 98–100, 103, 124, 132, 134, 138, 140, 142, 163, 176, 179, 183, 185, 194, 199, 200
2D two-dimensional. 11, 24, 31, 45, 61, 74, 75, 83, 84, 86, 90, 97, 102, 110, 112, 116, 120, 123, 132, 140, 141, 143, 144, 146–149, 153, 155, 157–159, 161, 162, 179, 181, 184, 191, 195–197, 200
2DEG two-dimensional electron gas. 12
3D three-dimensional. 24, 33, 45, 61, 76, 86, 114, 122, 139, 165, 175, 176, 178, 184, 197, 198

AC alternating current. 22, 41
AF antiferromagnetic. 140
AOM acousto-optic modulator. 41, 45, 47, 49, 50, 52, 53, 58, 59, 63, 198
AR anti-reflection. 41, 47, 48, 64, 65

BCS Bardeen-Cooper-Schrieffer. 28, 139, 141
BEC Bose-Einstein condensate. 28, 52–54, 59–61, 98, 105, 118, 119, 139, 141
BKT Berezinskii–Kosterlitz–Thouless. 181
B.Z. Brillouin zone. 11, 71–73, 75, 77, 86–88, 94, 97–99, 101, 102, 107–111, 115, 116, 119–121, 123, 125, 126, 194

CAD computer-aided design. 36
CCD charge-coupled device. 34, 36, 40, 59, 63–65, 184, 186–188
CDW charge density wave. 139–141, 192, 199

DC direct current. 50, 61
DCA dynamical cluster approximation. 175–179
DDS direct digital synthesizer. 40
DMD digital mirror device. 23
DMFT dynamical mean field theory. 142, 145

EMCCD electron multiplying charge coupled device. 64
EOM electro-optic modulator. 45, 53, 198

FFT fast Fourier transform. 188
FM frequency modulation. 50
FORT far-off resonance trap. 37, 41–44, 47–49, 57–61, 105, 137, 146, 150, 152, 162, 186
FQHE fractional quantum Hall effect. 196

GPS global positioning system. 40

HBT Hanbury Brown and Twiss. 181, 183
HTSE high-temperature series expansion. 14, 142–145, 154, 156–161, 169, 172–176

LDA local density approximation. 24, 145, 176, 178
LO local oscillator. 50

MCP microchannel plate detector. 181
MFD mode-field diameter. 47, 59
MOSFET metal–oxide–semiconductor field-effect transistor. 61, 196
MOT magneto-optical trap. 36–39

NA numerical aperture. 23
Nd:YAG neodymium-doped yttrium aluminum garnet. 46, 47
NIR near infrared. 64
NMR nuclear magnetic resonance. 18

PEPS projected entangled pair states. 142
PID proportional-integral-derivative. 41, 52, 53
PLL phase-locked loop. 40, 49

QAHE quantum anomalous Hall effect. 197
QHE quantum Hall effect. 196, 197
QMC quantum Monte Carlo. 141, 145
QSHE quantum spin Hall effect. 196, 198
QUIC quadrupole-Ioffe-configuration. 36, 39, 40, 60, 62

rf radio frequency. 12, 14, 28, 30, 34, 40, 43, 47, 49, 50, 52, 53, 58, 68, 147, 149–152, 168, 193

SDW spin density wave. 140, 141, 192
SF superfluid. 139
SLM spatial light modulator. 23

tDMRG time-dependent density-matrix renormalization group. 142
TOF time-of-flight. 30, 42, 52, 60, 61, 65–67, 105, 107, 146, 150, 152, 181, 183–186, 190, 198

LIST OF FIGURES

LIST OF TABLES

INDEX

DANKSAGUNG

Viele Personen haben mich während dem nun zu Ende gehenden Lebensabschnitt «Doktorat» begleitet. Unentbehrlich war dabei in erster Linie die Unterstützung durch die Forschungsgruppe. Bereits während meiner Diplomarbeit in der Quantenoptik-Gruppe lernte ich diese als ein eingespieltes und eingeschworenes Team kennen, in dem jeder einzelne mit seinen ganz persönlichen Qualitäten die übrigen immer wieder zu inspirieren und anzuspornen vermag.

Zuerst möchte ich mich bei Tilman Esslinger bedanken. Er hat mein Interesse für das Gebiet der ultrakalten Quantengase geweckt und mich dazu ermuntert, meine Diplomarbeit und später die Doktorarbeit in seiner Gruppe auszuführen. Mit Rat und Tat war er immer zur Stelle, wenn ich einmal nicht mehr weiter wusste. Tilman vermag für jedes physikalische Phänomen ein intuitives Bild zu finden und die Dinge auch einmal aus einem anderen Blickwinkel zu betrachten. Er sorgt für die richtige Balance zwischen individueller Freiheit und gemeinsamem Ziel, zwischen Spass und harter Arbeit und zwischen Chaos und Ordnung im Forscheralltag. Die Leichtfüssigkeit, mit der er diese Gratwanderung stets meisterte, hat mich beeindruckt. Nicht zuletzt seinen Humor und sein herzhaftes Lachen werde ich in bleibender Erinnerung behalten. Gianni Blatter danke ich für die Übernahme des Koreferats und sein Interesse an der vorliegenden Arbeit.

Schon während meiner Diplomarbeit unterstützt und betreut haben mich vom *Gitter*-Team Niels Strohmaier, Robert Jördens, Henning Moritz und Daniel Greif, welcher mittlerweile als Post-Doc das *Gitter*-Experiment lenkt. Niels und Robert haben mich von der ersten Spiegel-Justage am *SOLACE*-Experiment bis zu den ersten Schritten auf eigenen Beinen an der grossen Apparatur betreut. Von Robert habe ich viel über das Programmieren dazugelernt. Sein messerscharfer Verstand macht jede Unterhaltung mit ihm zu einer Bereicherung. Henning, ebenso schnell im Denken, Sprechen und auch Handeln, wusste aus jeder experimentellen Zwickmühle einen Ausweg. Mit Daniel zusammen habe ich meine ganze Doktorandenzeit am *Gitter*-Experiment verbracht. Sein experimentelles Wissen und Können, immer kombiniert mit der nötigen Intuition und auch Ausdauer, haben mich beeindruckt. Dabei ging ihm nie der Blick für das grosse Ganze verloren. Seine offene Art machte es eine Freude, mit ihm zusammenzuarbeiten. Gerne erinnere ich mich auch an die gemeinsamen Outdooraktivitäten, sei es beim Wandern oder Iglu-Bauen, zurück.

Ebenfalls in den Anfangsjahren begleitet haben mich Torben Müller, Bruno Zimmermann, Jakob Meineke, Kristian Baumann, Christine Guerlin, Stephan Ritter sowie Silvan Leinß. Sie alle haben mit Freude ihr Wissen und ihre Erfahrung mit mir geteilt. Ich kann mich noch gut an meine erste Konferenz mit Jakob in Florenz, die politischen Diskussionen und das Zeltabenteuer mit Bruno sowie die Technik-Fachsimpeleien mit Kristian erinnern.

Schon vor Beginn meiner Doktorarbeit stiess Leticia Tarruell als Post-Doc zum *Gitter*-Experiment, welches dann über die Jahre weiter durch Gregor Jotzu, Martin Lebrat, Michael Messer und Rémi Desbuquois ergänzt wurde. Leticia leitete über vier Jahre mit viel Engagement und Herz die Geschicke des *Gitter*-Experiments – und wurde von uns manchmal liebevoll die «*Lattice-Mom*» genannt. Sie lebte für unser Experiment und trieb es mit grossem Elan vorwärts. An Gregor bewundere ich sein *thinking out of the box*. Sein Verständnis für die physikalischen Zusammenhänge weit über unser Forschungsgebiet hinaus, kombiniert mit seiner Kreativität, haben einen wichtigen Teil zum Erfolg der Expe-

rimente beigesteuert. Während seiner Semester- und späteren Masterarbeit hat sich Martin mit Hingabe mit den theoretischen und experimentellen Grundlagen für die zukünftigen Experimente auseinandergesetzt. Michael hat mit seiner aufgestellten und anpackenden Art schon nach kurzer Einarbeitungszeit entscheidend zum Fortkommen der Experimente beigetragen. Vielen Dank für die eingelegten Nachtschichten und die Begleitung bei der Durchsteigung der Uetliberg-Nordwand! Auch Rémi als neuer Post-Doc wird dem Experiment sicherlich viele neue Impulse geben – *bonne chance!* Vielen Dank Euch allen auch fürs Korrekturlesen und vor allem viel Erfolg mit den weiteren Experimenten!

Vertieft in die eigenen Experimente passiert es bekanntlich leicht, dass man sich einmal in einer Sackgasse verrennt. In solchen Situationen lernte ich es zu schätzen, dass unsere Arbeit von den übrigen Gruppenmitgliedern mit grossem Interesse verfolgt wurde und wir immer auf ein offenes Ohr für den Erfahrungsaustausch (und manchmal auch Geräteaustausch) stiessen.

So möchte ich mich beim aktuellen *Cavity*-Team, Rafael Mottl, Renate Landig, Lorenz Hruby und Ferdinand Brennecke bedanken. Ebenso gilt mein Dank dem *Lithium*-Team mit David Stadler, Sebastian Krinner, Dominik Husmann, Charles Grenier und Jean-Philipp Brantut. In bester Erinnerung bleiben mir die Schneeschuhtouren und die netten Abende mit David und Nathalie. Vielen Dank für die anregenden Diskussionen und den Erfahrungsaustausch bezüglich Zukunftsplanung – «*the future is bright!*». Beeindruckt hat mich Renates und Nathalies Wagemut auf den Braunwalder Klettersteigen – auf ein nächstes Mal!

Dem Team vom neuen *IMPACT*-Experiment, Julian Leonard, Andrea Morales, Moonjoo Lee und Tobias Donner, wünsche ich gutes Gelingen beim weiteren Aufbau der Apparatur und spannende erste Experimente. Danke für die Gastfreundschaft im Büro währen dem Schreiben meiner Arbeit, das Bei-Laune-Halten, und Julian für das Korrekturlesen. Moonjoo hat mich immer wieder mit geistreichem Fragen überrascht, und so für den einen oder anderen heiteren Moment während des Schreibens gesorgt. Ihm und seiner neu gegründeten Familie wünsche ich alles Gute.

Unserem Elektroniker, Alexander Frank, bin ich zu einem grossen Dank für seine Geduld verpflichtet. Ich habe von ihm viel über Elektronik gelernt und konnte jederzeit auf seine Unterstützung zählen, ganz nach seinem Slogan «der Kunde ist König!». Veronica Bürgisser und Stephanie Ebert kümmerten sich zuverlässig und mit dem nötigen Nachdruck um alle administrativen und kaufmännischen Belange, und hielten mir so den Rücken frei. Zu meiner Freude kam dabei aber der eine oder andere «Schwatz» oder auch mal ein tiefergehendes Gespräch nie zu kurz. Stephanie wünsche ich für die Zukunft das nötige Durchhaltevermögen im steten Kampf gegen die Bürokratie, und Veronica Erfüllung im wohlverdienten (Un)Ruhestand.

Ein grosser Dank geht an unsere Semester-, Bachelor- und Masterstudenten, welche alle mit viel Einsatz zur Forschungsarbeit beigetragen haben. Nicht auslassen möchte ich an dieser Stelle auch die interessanten und stimulierenden Gespräche im Rahmen von wissenschaftlichen Kollaborationen. Besonders bedanken möchte ich mich diesbezüglich bei Lei Wang, Ulf Bissbort, Sebastian Huber, Lode Pollet, Dario Poletti und Corinna Kollath.

Zuletzt möchte ich mich bei meinen Freunden, meiner ganzen Familie und speziell meinen Eltern Max und Elisabeth und meinem Bruder Patrick bedanken. Sie haben mir den Weg geebnet und mich stets unterstützt, wo sie nur konnten, damit ich es dahin geschafft habe, wo ich jetzt stehe. Ein spezieller Dank gebührt hier auch Berthy für den Rückhalt. Danke, Regula, für das Verständnis, die Geduld, Beratung, Unterstützung, Aufmunterung, Ablenkung über all die Jahre – kurzum für die Liebe in all ihren Facetten, die Du mir entgegengebracht hast.

Zürich, im Dezember 2013 *Thomas Uehlinger*

THOMAS UEHLINGER — PUBLICATION LIST

PUBLICATIONS

1. J. Imriška, Iazzi, L. Wang, E. Gull, D. Greif, T. Uehlinger, G. Jotzu, L. Tarruell, T. Esslinger, and M. Troyer, *Thermodynamics and magnetic properties of the anisotropic 3D Hubbard model*, Phys. Rev. Lett. **112**, 115301 (2014a), DOI:10.1103/PhysRevLett.112.115301 (erratum at [Imriška *et al.*, 2014b])
2. T. Uehlinger, G. Jotzu, M. Messer, D. Greif, W. Hofstetter, U. Bissbort, and T. Esslinger, *Artificial graphene with tunable interactions*, Phys. Rev. Lett. **111**, 185307 (2013), DOI:10.1103/PhysRevLett.111.185307
3. D. Greif, T. Uehlinger, G. Jotzu, L. Tarruell, and T. Esslinger, *Short-range quantum magnetism of ultracold fermions in an optical lattice*, Science **340**, 1307 (2013), DOI:10.1126/science.1236362[1]
4. T. Uehlinger, D. Greif, G. Jotzu, L. Tarruell, T. Esslinger, L. Wang, and M. Troyer, *Double transfer through Dirac points in a tunable honeycomb optical lattice*, Eur. Phys. J. Special Topics **217**, 121 (2013), DOI:10.1140/epjst/e2013-01761-y[2]
5. L. Tarruell, D. Greif, T. Uehlinger, G. Jotzu, and T. Esslinger, *Creating, moving and merging Dirac points with a Fermi gas in a tunable honeycomb lattice*, Nature (London) **483**, 302 (2012), DOI:10.1038/nature10871[3]
6. D. Greif, L. Tarruell, T. Uehlinger, R. Jördens, and T. Esslinger, *Probing nearest-neighbor correlations of ultracold fermions in an optical lattice*, Phys. Rev. Lett. **106**, 145302 (2011), DOI:10.1103/PhysRevLett.106.145302
7. R. Jördens *et al.*, *Quantitative determination of temperature in the approach to magnetic order of ultracold fermions in an optical lattice*, Phys. Rev. Lett. **104**, 180401 (2010), DOI:10.1103/PhysRevLett.104.180401

CONFERENCE PROCEEDINGS

1. T. Uehlinger, D. Greif, G. Jotzu, L. Tarruell, and T. Esslinger, *Bloch-Zener oscillations in a tunable optical honeycomb lattice*, in The Physics of Semiconductors: Proceedings of the 31st International Conference on the Physics of Semiconductors (ICPS) 2012, Vol. 1566 (AIP Conference Proceedings, 2013), pp. 534–535, DOI:10.1063/1.4848521
2. C. Guerlin, K. Baumann, F. Brennecke, D. Greif, R. Jördens, S. Leinss, N. Strohmaier, L. Tarruell, T. Uehlinger, H. Moritz, and T. Esslinger, *Synthetic quantum many-body systems*, in Proceedings of the XIX International Conference on Laser Spectroscopy (ICOLS) (World Scientific, 2009) Chap. 20, pp. 212–221, DOI:10.1142/9789814282345_0020

1 See also Science Perspective by Porto [2013].
2 Featured on the cover.
3 Featured on the cover. See also Nature News & Views by Simon *et al.* [2012].

1. Workshop on frontiers between atomic and solid state physics, Ecole Normale Superieure and CNRS, Paris. *Engineering Dirac points with ultracold fermions in a tunable optical lattice*, 2013.
2. NCCR Quantum Science and Technology (QSIT) General Meeting, Arosa, Switzerland, *Engineering Dirac points with cold fermions in optical lattices*, 2012.

COLOPHON

The design of this thesis is largely inspired by Robert Bringhurst's seminal book on typography *"The Elements of Typographic Style"*. It was typeset in XeLaTeX with a style that is partly based on `classicthesis.sty` by André Miede and `arsclassica.sty` by Lorenzo Pantieri. The main text is set in *Minion Pro*. The *Scala Sans*, *TeX Gyre Heros*, *Consolas*, *Asana Math*, *TeX Gyre Pagella Math* and *Zapfino* fonts are used for headings, labels, code and mathematics.